The Infrared Spectrum of Massive Protostars: Circumstellar Disks and High Mass Star Formation

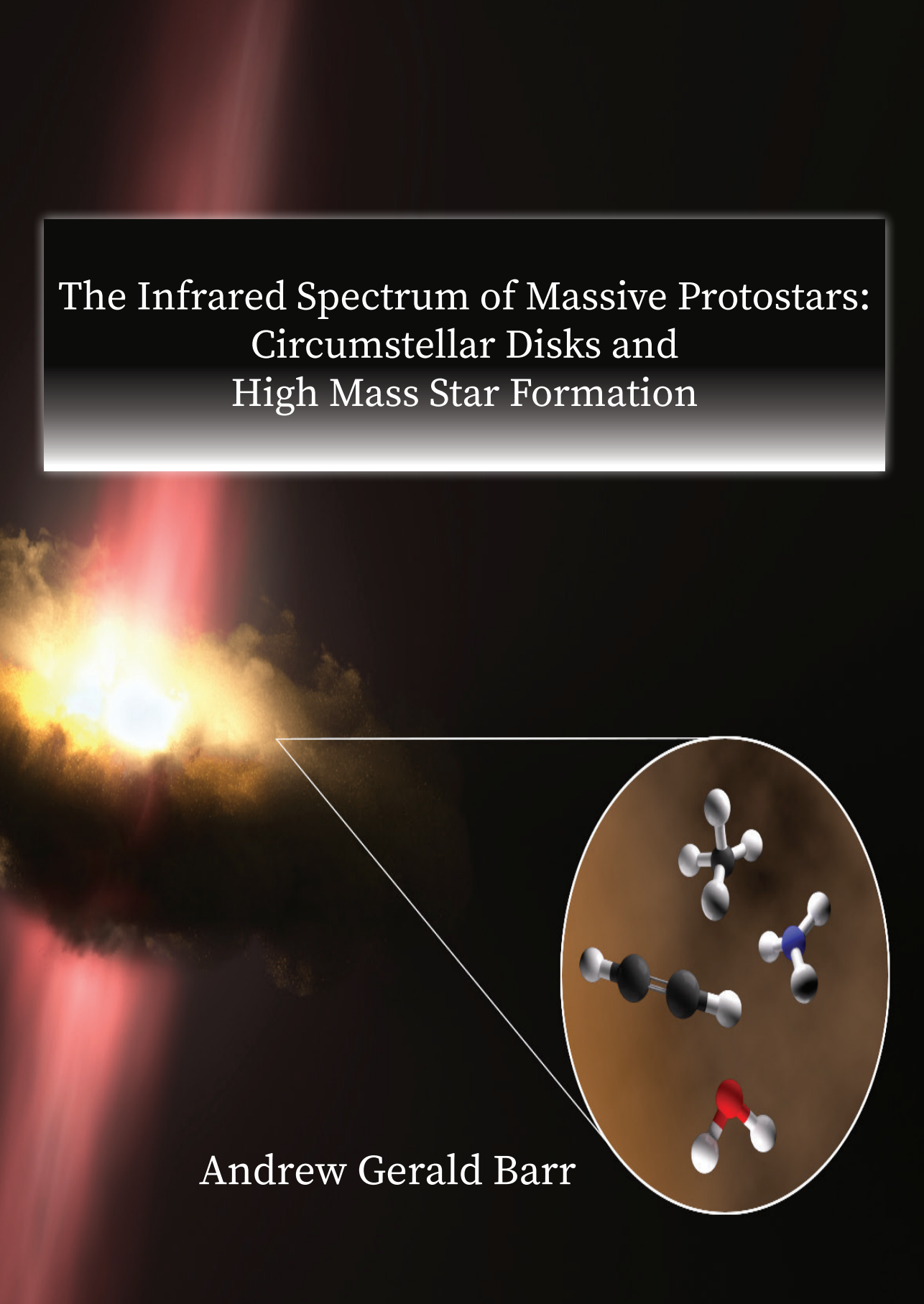

Andrew Gerald Barr

The Infrared Spectrum of Massive Protostars:

Circumstellar Disks and High Mass Star Formation

The Infrared Spectrum of Massive Protostars:
Circumstellar Disks and High Mass Star Formation

Proefschrift

ter verkrijging van
de graad van doctor aan de Universiteit Leiden,
op gezag van rector magnificus prof. dr. ir. Hester Bijl,
volgens besluit van het college voor promoties
te verdedigen op dinsdag 12 april 2022 klokke 11:15 uur

door

Andrew Gerald Barr

geboren te
Paisley, Scotland
in 1993

Promotor: Prof. dr. A. G. G. M. Tielens
Co-promotor: Dr. A. C. A. Boogert

Promotiecommissie

Prof. dr. H. J. A. Röttgering (Universiteit Leiden)
Prof. dr. E. F. van Dishoeck (Universiteit Leiden)
Prof. dr. J. C. Tan (Chalmers University Gothenburg)
Prof. dr. K. I. Öberg (Harvard University)
Prof. dr. F. F. S. van der Tak (Universiteit Groningen)

ISBN 978-94-6419-397-8

Cover design: An artist's impression of the circumstellar accretion disk around a massive protostar. Molecules in the callout are water, ammonia, methane, and acetylene. This illustration was made specifically for chapter 3 of this thesis, as part of the article published on NASA.gov: *'Massive Stars Are Factories for Ingredients to Life'.*
Image credit: NASA / Ames Research Center / Daniel Rutter.

To my little one

When I consider your heavens,
the work of your fingers,
the moon and the stars,
which you have set in place,
what is mankind that you are mindful of them,
human beings that you care for them?

Psalm 8:3-4 *NIV* version

Contents

1 | Introduction

The quote at the start of this book expresses man's wonder at his place in the universe. It reveals how this wonder has existed for many years, the quote being taken from a poem written some 3000 years ago. Indeed humanity's curiosity towards the universe is evident from the earliest of discovered civilisations. The scale of the universe is so grand, and our occupation of it so small, that today it is scarcely possible not to have an increased sense of wonder in relation to the poem's author, as science unravels more and more of the mysteries surrounding the universe. But as more are resolved, yet more are revealed, and the wonder seems rather to increase than to disappear. From exoplanets that we can easily relate to, to clusters of galaxies and supermassive black holes, our little planet begins to feel rather insignificant; a small speck lost in a vast sea of strange and wonderful objects.

Closer to home, the ever increasing chemical complexity beheld e.g. the discovery of glycine on the comet 67-P/Churyumov-Gerasimenko, proves that there are many interesting puzzles that we can, quite literally, get our hands on. With continuously improving facilities and computational capabilities, astronomers have never been better equipped to answer all of the enthralling questions that the universe poses.

Centrally, the question as to our own origin has intrigued humanity for millennia. How did we get here? The chemical complexity observed in star forming regions presents the question: did these molecules have a role to play? Consequently understanding what the organic inventory of regions of planet formation is, and what are the processes involved in their formation, become key questions.

1.1 Star Formation

The formation of stars and planets is one of the key areas of modern day astronomy. Understanding how these objects came to be, which have been visible to humanity across all generations, is not as easy as it would seem to appear. The current understanding, which has come a long way in recent years, is that stars are born in cold, tenuous clouds of dust and gas called giant molecular clouds (GMCs) (Shu et al. 1987). As areas of these clouds become gravitationally unstable, they begin to collapse leading to increasing amounts of dust and gas infalling into a concentrated region called a pre-stellar core (Shu 1977). As this proceeds, the material begins to heat up, forming a protostar. At this point the star is still deeply embedded in the cloud which envelopes it in such a way that the star is invisible at optical wavelengths.

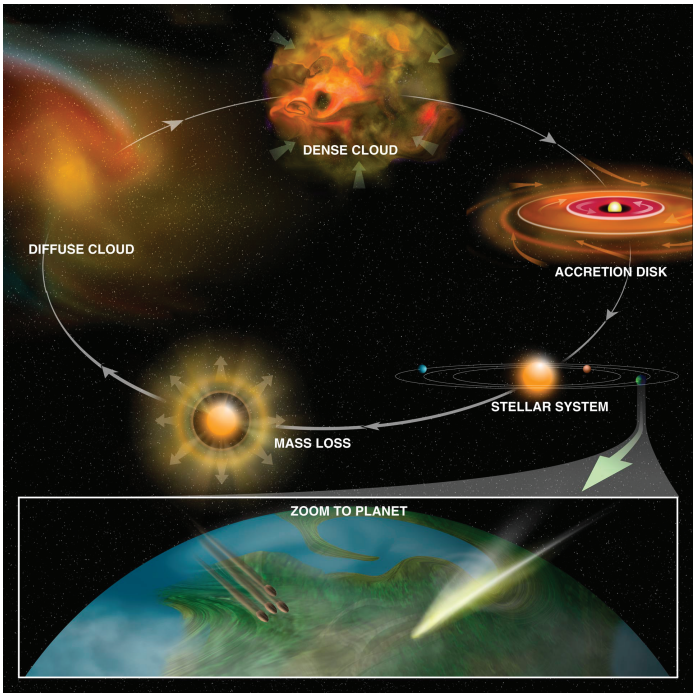

Figure 1.1: The life cycle of stars; from their birth in dense clouds to their death in supernovae. The planet formation process occurs during this cycle, extricably linking these two processes. The material dispensed in supernovae is recycled back into the surrounding cloud where it can once again be used for star formation. Acknowledgement: Bill Saxton (NRAO/AUI/NSF)

In Figure 1.1 we see that the next stage in the evolution involves a circumstellar disk, through which material can accrete onto the protostar, thus it increases in mass and continues to grow (Stahler & Palla 2005). The disk is a consequence of the conservation of angular momentum, as rotating, infalling material spreads out in a flattened structure around the star (Turner et al. 2014). Large outflows and winds perpendicular to the plane of the disk also form as material is ejected from the star-disk system; so the envelope and molecular cloud begin to be dispersed (Stahler & Palla 2005). While this takes place, dust in the disk agglomerates and begins to form planetesimals. Eventually these grow to larger and larger sizes, also acquiring the gas that is in the disk to eventually form planets, resulting in a stellar-planetary system. Eventually the star will begin to fuse hydrogen in its core and, after millions to billions of years, it will exhaust its supply of fuel and will die, shedding its outer layers back into the interstellar medium (Figure 1.1). And so the life cycle of the star is complete; the loop is closed, and the cycle repeats.

This general sequence of star formation does not apply equally to both low ($M < 8M_{\odot}$) and high mass stars ($M \geq 8M_{\odot}$). The fusion of hydrogen in the core of massive stars occurs when the star is still deeply embedded in its envelope, whereas in low mass stars this occurs when the star reaches the main sequence (after $\sim 5 \times 10^7$ yr)

and the disk has been dispersed (after $\sim 1 \times 10^7$ yr). Also planets have yet to be detected around O-type stars with the most massive host stars observed with a planet being 3-5 $M_\odot$, and less discoveries are made as the stellar mass increases (Reffert et al. 2015; Grunblatt et al. 2019; Hollands et al. 2021). This likely reflects the short Kelvin-Helmholtz and disk dispersal timescales of massive stars compared to low mass stars, thus planets have much less time to form, as well as the high radiation fields of massive stars (Veras et al. 2020).

1.1.1 Low Mass Star Formation

With this flavour of the star formation cycle, let us look more closely into the details of this complex process.

The GMCs in which stars form are gravitationally bound structures that exist within even larger clouds of HI gas in the cold interstellar medium (ISM), and range from $>10^4$ $M_\odot$ up to 10^7 $M_\odot$, observed in other galaxies (Vogel, Kulkarni & Scoville 1988; Sakamoto et al. 1999) and have densities of 10^2-10^3 cm^{-3}. GMCs are turbulent and energy injection via internal and external mechanisms replenish this turbulence leading to support against gravitational collapse, and lifetimes estimated ranging from 1-3$\times 10^7$ years (Krumholz, Matzner & McKee 2006).

Within GMCs, intricate cloud structure is observed in the form of web-like networks of filaments and fibres, formed through supersonic flows which compress the gas into either bound or unbound structures (André et al. 2014). Such structure is shown in Figure 1.2. Filaments can be from ~ 1 pc to ~ 30 pc in size and are significantly more dense compared to their environment. The distribution of filaments varies from cloud to cloud, and even within GMCs themselves, where the filaments are aligned in regions of high column density and more disorganised in regions of lower column density (Hill et al. 2011; Palmeirim et al. 2013). These are the sites of star formation where filaments gravitationally fragment into clumps and pre-stellar cores.

The cores can be either bound or unbound structures, with the most massive almost certainly bound (Bertoldi & McKee 1992). They are observed as local maxima in the column density distribution of filaments seen in submillimeter/millimetre continuum emission, or molecular species such as NH_3 and N_2H^+. Pre-stellar cores have subsonic turbulence and thermal motions that exceed non-thermal motions. There is a sharp transition however between the quiescent core and the gas in the surrounding cloud where the opposite is true, on scales of filament widths (0.1 pc) (Pineda et al. 2010). The cores are isothermal, of temperatures 10-20 K, and, being in an unstable hydrostatic equilibrium, eventually collapse forming a $1/r^2$ density distribution, in the approximation of negligible turbulence (Hunter 1977; Shu 1977). Due to an increase in opacity, the core becomes adiabatic in the centre and eventually the collapse is halted in the innermost region where the temperature continues to rise. Once hydrogen fusion can begin, a zero-age main-sequence (ZAMS) star is formed.

Figure 1.2: Herschel image of the star forming region RCW106 in the Southern constellation of Norma, taken as part of Herschel's Hi-GAL key project. The three colours in the image correspond to 70 μm (blue), 160 μm (green) and 250 μm (red). Very bright, young stars are illuminating the surrounding cloud causing dust radiation seen in these three colours. The powerful winds of these stars blow bubbles and excavate the surrounding cloud. Filamentary structures of dust and gas can be seen as web-like networks extending across the entire image. Stars are forming all along these filaments, which signify the densest regions of the cloud. Acknowledgement: UNIMAP / L. Piazzo, La Sapienza-Universitá di Roma; E. Schisano / G. Li Causi, IAPS/INAF, Italy)

1.1.2 Circumstellar Disks

Disks are typically modelled as viscous fluids in which turbulence redistributes angular momentum (Shakura & Sunyaev 1973), rather than particle collisions, as in the case for a standard fluid. Loss of angular momentum is the driving force behind the evolution of the disk and occurs in the perpendicular direction to disk rotation. Conservation of angular momentum requires the spreading out of the disk, where most of the disk mass flows radially towards the star, and a small fraction of the disk mass carries angular momentum outwards, thus spreading out the surface density. This is predicted but has not yet been observed.

Disk evolution also occurs through disk winds. The presence of stellar magnetic field lines which thread the disk allow for a sufficiently ionised disk to form a magneto-hydrodynamic (MHD) disk wind, removing material from the disk. Magnetic tension and magnetic pressure gradients dominate the thermal pressure in a region above the disk surface and, in this way, disk winds can also remove angular momentum from the disk as the magnetic field exerts a torque on the disk while material that is accelerated along field lines gain angular momentum.

Powerful winds driven by the protostar result in the production of jets and outflows perpendicular to the disk axis. Jets have higher velocities than the outflows and are more collimated because they are primarily due to the stellar wind, whereas outflows consist of entrained material from the envelope that is swept up by the winds resulting in wide angles which surround the jet at the centre. In some cases, if the jet is powerful enough, it may drive the outflow. The launching point of the wind may vary radially from the star, with the launching point spread over a range of radii. Winds are thought to be magneto-centrifugally driven due to the presence of magnetic fields in circumstellar disks, thus driving MHD winds and jets. These come in the form of the disk wind model (see above) and X-wind model. X-winds are launched closer to the star compared to disk winds, with the possibility of both types being present driving different velocity components.

Disks in High Mass Young Stellar Objects

The role of disks in the process of massive star formation is a hotly debated topic (Beltrán & de Wit 2016). From a theoretical standpoint, some sort of non-spherical accretion is needed to overcome the strong stellar winds and radiation pressure from the star for it to continue growing, most likely in the form of a disk (Nakano 1989; Jijina & Adams 1996). However non-spherical accretion may also come in the form of multidirectional accretion flows for the more massive objects (Liu et al. 2015; Maud et al. 2017; Goddi et al. 2020). B-type sources are described as being scaled-up versions of their low mass counterparts in terms of the disk (Beltrán & de Wit 2016), however only a few examples of observations of very clear Keplerian disks around O-type stars stars are known, showing that stable disks can form around the most massive protostars but may be rare (Patel et al. 2005; Kraus et al. 2010; Johnston et al. 2015; Maud et al. 2019; Zapata et al. 2019). Protostars of mass $> 30\ M_{\odot}$ typically show rotating non-equilibrium structures often named 'toroids', on scales of >1000 AU (Beltrán et al. 2005; Cesaroni et al. 2007). The lack of ubiquity of disks in massive young stellar objects (MYSOs) may be an observational bias as

massive stars lie systematically further away compared to low mass stars, therefore higher spatial resolution is required to detect these disks (milliarcsecond resolution is required to resolve these structures). Further evidence for disks comes from near infrared observations of CO emission in Keplerian rotation which derive very high temperatures (up to 4500 K) and column densities ($\sim 10^{21}$ cm^{-2}), consistent with the inner regions of a circumstellar disk (Bik & Thi 2004; Ilee et al. 2013). The question as to how massive stars actually form is still very much open, particularly for O-type stars above 30 $M_{\odot}$, and much remains to be answered. Very high spatial resolution studies are required to properly address this and firmly establish the different accretion mechanisms of massive star formation.

1.1.3 Massive Star Formation

While the mass distribution of galaxies necessitates that most stars that form will be low mass stars, massive stars have a far more significant role to play in the universe on galactic and extra-galactic scales, extending their influence to many different areas of astrophysics. The distribution of mass is described by the initial mass function, which is a probability distribution with a negative slope, stating that the number of stars in a given mass range decreases with mass. Visually, the very high ionising flux that comes from massive stars, and their strong winds, means that fantastic images of these star forming regions can be obtained, such as the Cygnus-X region, a large field of view image of which is shown in 1.3, where many different physical structures are formed. One of the massive stars central to this thesis, AFGL 2591, lies, impossible to discern, somewhere in this star forming region. Massive stars act simultaneously as catalysts and inhibitors of star formation, as stellar feedback both appeases and disrupts this process. Powerful winds and ionising gas from massive stars, and shocks from supernovae, sweep up material into dense shells, promoting further gravitational collapse to form new stars; these also disrupt molecular clouds injecting turbulence into quiescent clouds preventing the formation of new stars or dispersing them entirely. The strong radiation from massive stars also regulates the phases of the ISM via heating, ionisation and dissociation. Finally the enrichment of the ISM in atoms ranging in mass from carbon to rubidium is important with this being the sole production process for a handful of these elements. In this thesis we aim to shed some light onto how these important stars come to be, and the processes that occur during their formation.

A sequence of massive star formation can be made for high mass star formation, and is expected to span around 10^5 yr (Beuther et al. 2007). A cartoon illustration of the widely accepted process is given in Figure 1.4 and is based on Cesaroni et al. (2005b). High mass stars also are born in GMCs and they play an important role in the life cycle of GMCs where ionised hydrogen (HII) regions and outflows from OB associations can inject energy on large enough scales to support the clouds, however simultaneously, photoevaporation from HII regions is the dominant destruction mechanism (Zinnecker & Yorke 2007). Thus stellar feedback from massive stars is of fundamental importance to the galactic ecosystem on local scales. The pre-stellar cores of massive stars are themselves contained in infrared dark clouds (Rathborne, Jackson & Simon 2006) which are seen in absorption against mid-infrared continuum

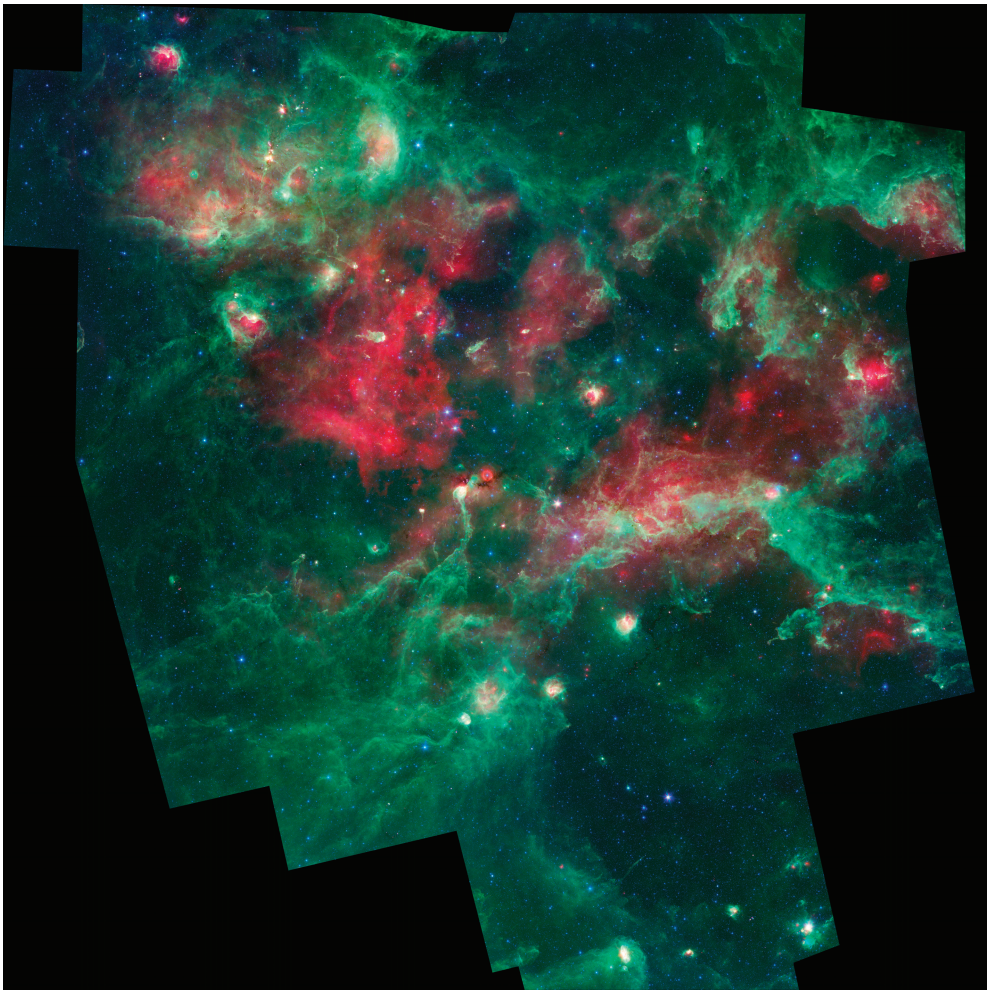

Figure 1.3: Full size mosaic image of the Cygnus-X massive star forming region in the constellation Cygnus, taken with NASA's *Spitzer* space telescope. The three colours in the image correspond to 3.6/4.5 μm (blue), 8 μm (green) and 24 μm (red). Cool dust and ionised gas can be seen in red. The ionising stars are seen as blue dots as clusters of forming massive stars irradiate their surroundings and sweep up gas and dust into bubbles and pillars. This image fully portrays the violent and chaotic environment of massive star formation. Portions of the cloud have been completely dispersed while filamentary structures are created promoting the further formation of stars, resulting in stars in different stages of their evolution, including young stars with planet-forming disks, deeply embedded embryonic stars and stars in the final stages of their life. Acknowledgement: NASA/JPL-Caltech/Harvard-Smithsonian CfA.

emission. These have masses of a few hundred to a few thousand $M_{\odot}$, and will eventually form many massive stars in a clustered manner (Lada & Lada 2003); thus massive protostars are almost exclusively observed to form in clusters. The role of filaments in allowing this kind of clustered star formation may be vital as merging filaments provide regions of very high density (Schneider et al. 2012). Evidence for such intersecting filaments has been seen in the Cygnus-X star forming region (Hennemann et al. 2012), shown in Figure 1.3.

Temperatures in the envelope quickly rise to above 100 K, initiating the onset of the hot molecular core phase (van der Tak 2003; Cesaroni et al. 2005b; Beuther 2006). This phase being the main focus of this thesis, the hot core will be discussed more extensively in its own section below. After the star has evolved enough to produce a high enough EUV flux to ionise hydrogen, it will begin to ionise the surrounding gas forming a very confined hypercompact HII region (Fig 1.4), characterised by broad hydrogen recombination lines (Zinnecker & Yorke 2007). This will continue to expand and evolve to an ultracompact HII region and eventually a classical HII region. During the hypercompact HII region phase, the disk of the massive star is likely still present whereas by the ultracompact HII region phase, the disk has most likely been fully dispersed (Keto 2007; Nielbock et al. 2007).

There are three main models for how massive stars form, and potentially all three contribute to the observed massive stars in the universe. The first is the most similar to the formation of a low mass star, and is called monolithic collapse (Tan & McKee 2003). This involves the collapse of an individual core, and the subsequent build-up of the star through an accretion disk (Yorke & Sonnhalter 2002; Krumholz, Klein & McKee 2005). An alternative way of stellar growth is competitive accretion (Bonnell et al. 1997). In this scenario, specific regions of the stellar cluster are more prone to accreting material depending on the distribution of the stars, therefore stars in these advantageous regions may accrete material easier than their neighbours. This has a feedback loop characteristic to it since, as the star grows, its force of gravitational attraction increases and the advantaged star can accrete still more material with respect to its neighbours. Competitive accretion is also expected to involve an accretion disk. The third process is stellar mergers in which stars collide to form larger mass stars (Bonnell, Bate & Zinnecker 1998). This theory is not as commonly considered as it faces a variety of challenges; most important the pre-requisite of a high stellar density. However it may be the cause of the formation of a very low number of very massive stars.

At first look, low mass and high mass star formation may appear rather similar when considering monolithic collapse, with many of the same emerging global structures, however under the surface there are important details in the physics which significantly distinguish these two evolutionary processes. For example the formation of both types of star most likely involves the role of a disk, however in high mass stars the extreme luminosities involved (10^4-10^5 $L_{\odot}$) leads to the radiation pressure from massive stars exceeding the gravitational force, which should halt collapse and the subsequent build up of the star (Wolfire & Cassinelli 1986; Zinnecker & Yorke 2007). This high radiation pressure also leads to very strong bipolar stellar winds and outflows which are magneto-centrifugally driven in low mass stars. Furthermore, the high levels of EUV photons photoevaporate the disk early on, whereas in low mass

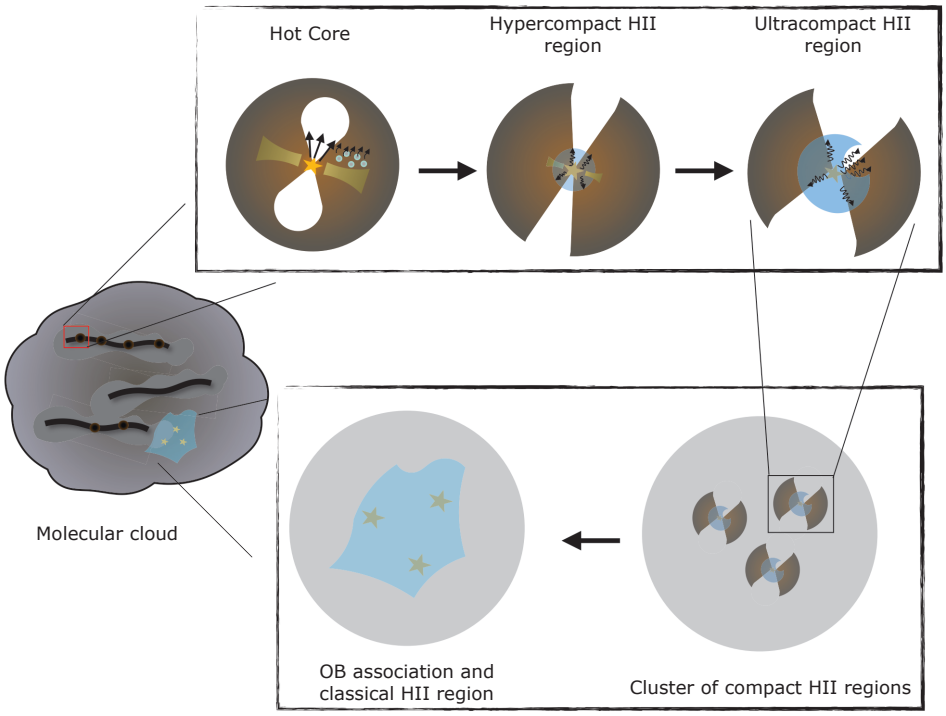

Figure 1.4: Cartoon depicting the evolutionary sequence for the formation of massive stars.

stars this occurs in the disk dispersal phase. The impact of the high flux of ionising photons is not the only source of differences between the two stellar groups, because the ionising photons are able to dissociate H_2 and CO in the nearby environment as well as ionising hydrogen resulting in the formation of HII regions. These complications do not exist in low mass star formation. A particularly striking outcome of this is that ionising radiation from the star can escape through cavities in the polar directions that are blown by these winds resulting in the so-called flashlight effect (Nakano 1989; Yorke & Bodenheimer 1999; Kuiper et al. 2016). Here infrared and UV photons, which exert radiation pressure, interact with the accretion flow through the disk and are absorbed by the innermost region of the disk, the most fundamental zone being the dust sublimation front. This heated region of the disk will then cool through the optically thin layers of the disk photosphere in the vertical direction via the bipolar outflow cavity, and thus the rest of the disk is strongly shielded in the radial direction from the stellar radiation (Kuiper et al. 2010; Tanaka et al. 2016, 2017).

Hot Cores

As mentioned above, hot molecular cores are intermediate objects in the high mass star formation process. They can be characterised as regions which are greater than

100 K in temperature, less than 0.1 pc in size, and have densities greater than 10^7 cm^{-3} (Kurtz et al. 2000). The temperature and density structure is such that these increase towards the centre of the core, located in a larger scale molecular clump, consistent with these objects being the sites of star formation. Methanol and OH masers are unique to massive star forming regions, and are generally associated with the Hot Core phase, likely probing the sites of disks or outflows, whereas water masers are characteristic of both low and high mass star forming regions. The Hot Core phase has been associated with the disk accretion phase (Patel et al. 2005; Kraus et al. 2010; Moscadelli & Goddi 2014; Johnston et al. 2015; Ilee et al. 2016; Moscadelli et al. 2019; Zapata et al. 2019; Maud et al. 2019), with several disks observed at the centres of hot cores, although to what extent this is the case remains to be established. This is supportive of the core accretion model for massive star formation. There is also evidence that Hot Cores are collapsing strengthening the relation to the disk accretion phase (Hofner, Peterson, & Cesaroni 1999; Osorio et al. 2009; Beltrán et al. 2018).

Another very important feature of hot cores is their chemical diversity with high temperatures providing ideal conditions for the formation of complex organic molecules (COMs). These are defined as molecules with six or more atoms, and many of theses have been detected for the first time towards Hot Cores (Herbst & van Dishoeck 2009). Some COMs are formed on dust grain surfaces in the colder, preceding stages of star formation as ices. Once the Hot Core reaches temperatures of above ∼100 K, these ices evaporate leading to a rich gas-phase chemistry where many more COMs are produced with increasing complexity, depicted in Figure 1.4. The high temperatures (100-300 K) allow new energy barriers to be overcome, facilitating chemical reactions that cannot take place in colder environments. The presence of COMs is not unique to high mass objects however, as Hot Cores also have low mass analogues called Hot Corinos (Cazaux et al. 2003; Bottinelli et al. 2004; Ceccarelli 2008), such as the Class 0 binary IRAS 16293-2422.

1.2 Chemistry of Circumstellar Disks

Disks associated with Herbig AeBe stars and T-Tauri stars are considered to be externally illuminated, thus the temperature profile of the disk is such that the surface layer of the disk is much hotter than the mid-plane of the disk. Deviations from this scenario come in the form of FU Orionis variables. In these objects very high accretion rates in the disk occur in bursts leading to an inversion of the temperature structure such that the mid-plane is much hotter than the surface, as the disk heating becomes dominated by dissipation of gravitational potential energy. Thus molecular transitions are observed to be in absorption towards these kinds of disks. The result of the temperature stratification of externally illuminated disks is that a chemical stratification also occurs, with different molecular species dominating at different temperatures, and therefore different locations in the disk.

The chemistry of the hot upper layers is controlled by UV and X-ray photons, and in the case of massive stars EUV photons will also contribute. Temperatures exceed 1000 K in both the gas and the dust (although decoupled) making it difficult for most molecules to survive in this region of the disk. Some molecules that can survive are

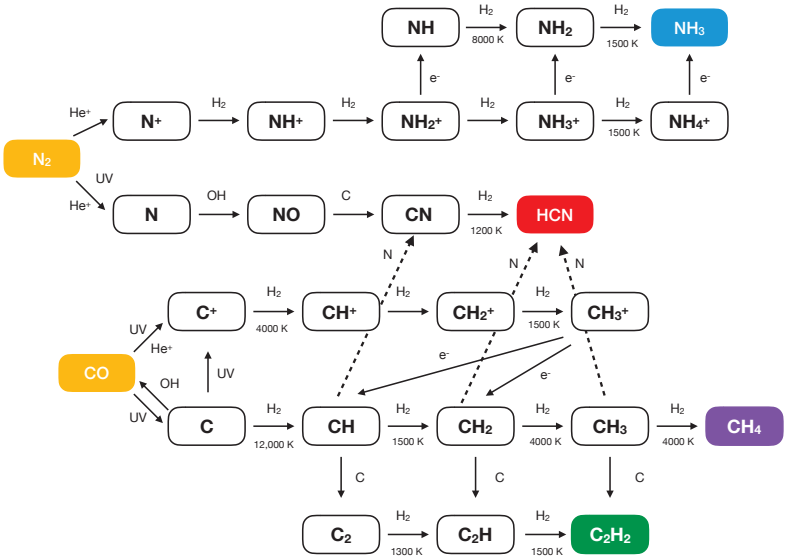

Figure 1.5: Chemical network of the main reactions with high activation energies to produce HCN, C_2H_2, CH_4 and NH_3. The reactions with the highest energy barriers have this quantified where appropriate. Adapted from Bast et al. (2013) and Agúndez et al. (2008).

H_2, CO, and N_2, as these molecules form rapidly at high temperatures and are hard to dissociate, meaning that they can self-shield (van Dishoeck & Black 1988; Visser et al. 2009). The rest of the gas will mostly consist of atoms and ions. Close to the mid-plane, the radiation field of the star is strongly attenuated by the upper layers of the disk. Therefore the majority of the gas-phase chemistry will depend on cosmic rays to be triggered. Temperatures are below 100 K in this part of the disk. Cosmic rays can produce H_3^+ and He^+ which can initiate ion-molecule chemistry, as well as a UV field due to the interaction with H_2 molecules. These weak energy sources can further process ices that reside on dust grain mantles to produce species such as NH_3 and CH_4, as well as more complex species such as CH_3OH and CH_3OCH_3 (Öberg et al. 2008; Öberg 2016). Some of the solid-state chemical products from the dark cloud stage preceding the disk stage, as well as gas-phase products from the cloud warm-up stage, may be incorporated into the disk (Visser et al. 2009), however it is possible that the chemistry is reset by accretion shocks as material accretes from the envelope to the disk (Jørgensen, Belloche & Garrod 2020).

The warm region of the disk has temperatures between 100 K and 1000 K and is the production site of simple species such as HCN, C_2H_2, NH_3, CH_4 and H_2O in high abundances. In contrast to hot cores, CH_3OH (Walsh et al. 2016), CH_3CN (Öberg et al. 2015) and t-HCOOH (Favre et al. 2018) are the only COMs to be detected in disks. This apparent difference may result from chemistry involving evaporating ices inherited from the dark cloud phase and the warm chemistry initiated in the gas phase, or the column densities of COMs in disks may simply be too low for current instrumentation to detect. The UV and X-ray flux from the star allow C and N to

be broken free from the parent bearing species CO and N_2, which can then react through a network of chemical reactions to form these species outlined in Figure 1.5. The high temperatures facilitate the initial reactions to form C-bearing species from CO, which have very high energy barriers, and HCN, C_2H_2 and CH_4 can be formed. CO_2 may also be produced, however the abundance of this species peaks between 100 K and 200 K because the main reaction to form CO_2 is OH + CO, and OH is driven rapidly into H_2O at temperatures above 250 K. The high temperatures also allow the reactions of CN + H_2 and NH + H_2 to form HCN and NH_3 respectively. CS is another molecule that can be formed in high abundances in disks (Agúndez et al. 2018).

1.3 Absorption Lines at Infrared Wavelengths

1.3.1 Ro-vibrational Spectroscopy

Molecular transitions provide an excellent tool for studying star formation, as the discrete frequencies of these transitions allow specific molecules to be uniquely identified. With the large amount of knowledge of the behaviour of astrophysically relevant molecules readily obtained from the highly controlled environment of laboratories here on Earth, molecules can provide information on the physical conditions of star forming regions, as well as on the chemical process taking place.

At mid-infrared wavelengths molecular lines are predominantly due to ro-vibrational transitions. These involve transitions between a rotational level in a certain vibrational level, to a rotational level in another vibrational level, altering the vibrational energy of the molecules. The result is complex spectra such as those illustrated in Figure 1.6. Linear molecules such as CS exhibit a relatively simple spectrum, with lines evenly spaced, whereas non-linear molecules such as H_2O and NH_3 show complex patterns that are difficult to identify. HCN and C_2H_2 have P, R and Q branches, which are ro-vibrational bands that are formed due to transitions that change rotational quantum number, J, by 1, -1 and 0 respectively. H_2O and NH_3 are described by quantum numbers J, K_a and K_c. The ro-vibrational levels are split into ortho and para states with para states having both K_a and K_c odd or even, and ortho states with either K_a or K_c odd or even. Transitions between ortho and para states are not allowed, however transitions may occur between two ortho or two para states. The reader is referred to Papousek (1982) and Mihalas (1978) for more information on ro-vibrational spectroscopy and absorption line formation, respectively.

1.3.2 Absorption Line Formation

Towards massive protostars ro-vibrational transitions in the infrared are typically seen in absorption against the bright infrared continuum. Thus absorption lines at infrared wavelengths allow for the determination of the physical conditions of these regions. To understand the formation of absorption lines we begin with the absorption coefficient, α_ν, and its relation to the optical depth, τ_ν, of a molecular transition. The absorption coefficient can be defined as such in equation 1.1:

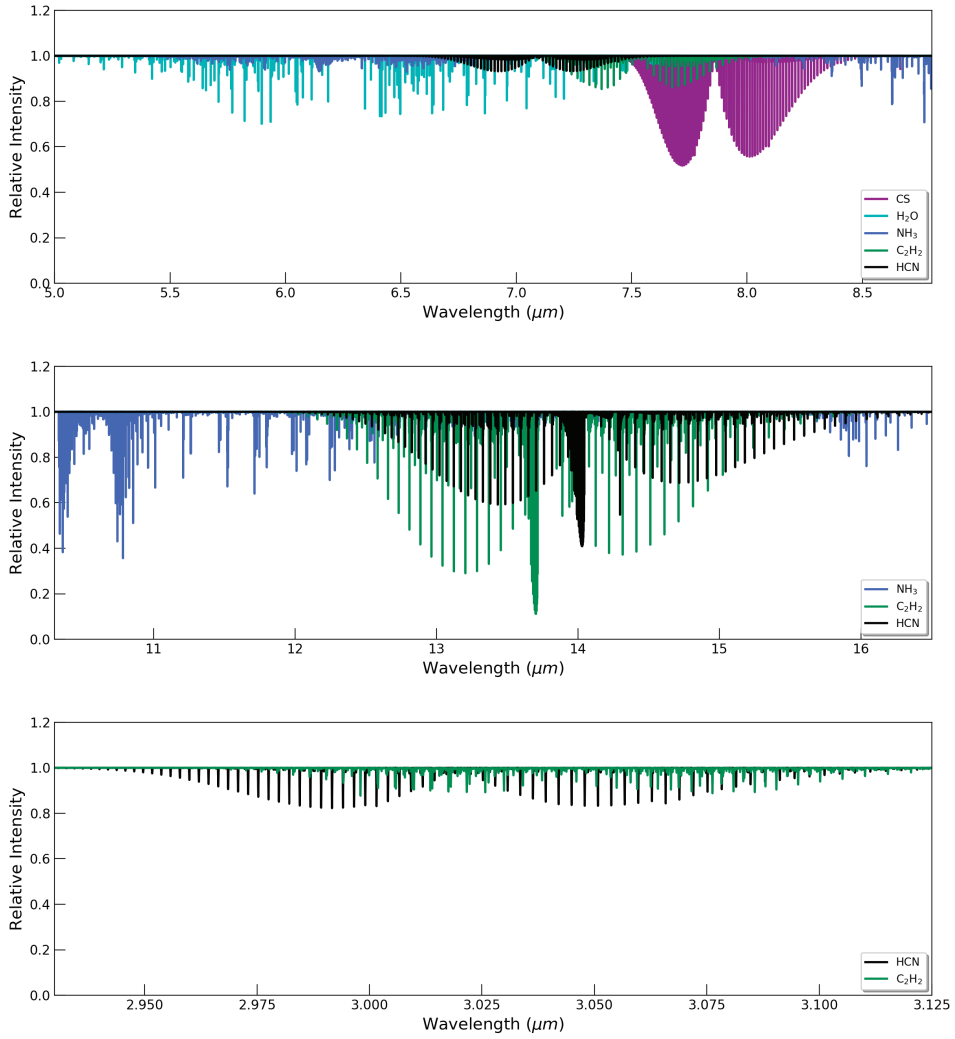

Figure 1.6: Model absorption line spectra of H_2O, HCN, C_2H_2, NH_3 and CS at a column density of $1{\times}10^{17}$ cm^{-2} and a temperature of 500 K. The H_2O lines are relatively weak compared to the other species, however in practice, these lines are observed to be the strongest due to the large column density in star forming regions (10^{18} cm^{-2}). The bands at 13 μm are stronger relative to the bands at other wavelengths for HCN, C_2H_2 and NH_3.

$$\tau_\nu = \int \alpha_\nu ds = \int \frac{h\nu}{4\pi}\phi(\nu)(n_u B_{ul} - n_l B_{lu})ds \tag{1.1}$$

where ν is the frequency, n_u and n_l are the density of particles in the upper and lower state energy levels respectively, B_{ul} and B_{lu} are the Einstein B coefficients, and $\phi(\nu)$ is the line profile. Under molecular cloud conditions $\phi(\nu)$ is best described by

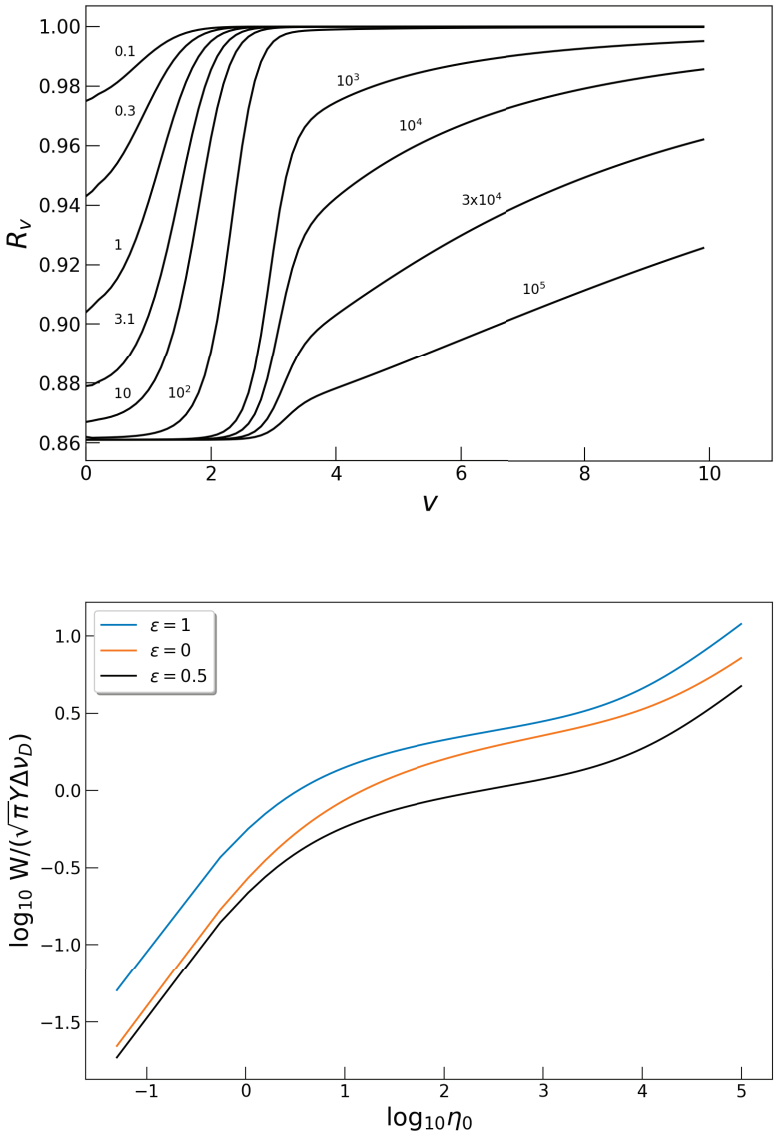

Figure 1.7: *top:* The calculated profile of an absorption line as a function of the opacity η_0. v is the the frequency-parameter describing the Voigt profile, and R_v is the residual flux of the absorption line, and can be described as 1 - Y, where Y is the line depth. Values for η_0 are indicated for the corresponding curves. Taken from Mihalas (1978). *bottom:* The theoretical curve of growth for three different assumptions of line formation. ϵ equal to 1, 0 and 0.5 represents line formation via pure absorption, pure scattering and a combination of the two, respectively (see Appendix of chapter 3 for more details). W is the equivalent width and $\Delta\nu_D$ the Doppler parameter.

a Voigt profile (a combination of a Lorentzian and Gaussian line profile), however often simply a Gaussian profile is a very good approximation. The relation derived by Einstein for B_{ul} is:

$$B_{ul} = \frac{A_{ul}c^2}{2h\nu^3} \tag{1.2}$$

and the expression for the level populations in local thermodynamic equilibrium (LTE) is:

$$\frac{n_u}{n_l} = \frac{g_u}{g_l} \exp\left[\frac{-h\nu}{kT_{ex}}\right] \tag{1.3}$$

where g_u and g_l are the upper and lower state statistical weights, A_{ul} is the Einstein A coefficient and T_{ex} is the excitation temperature. After some simple algebraic manipulation, and integrating over the distance, ds, we arrive at the expression for the optical depth of a line:

$$\tau_\nu = \frac{A_{ul}c^2}{8\pi\nu^2} \frac{g_u}{g_l} (1 - e^{-h\nu/kT_{ex}}) \phi(\nu) N_l \tag{1.4}$$

Thus we see that the optical depth is directly proportional to the column density in the lower level of the transition, N_l. The column density in the lower level of a transition is related to the total column density, N, of a molecule via:

$$N_l = g_l e^{-E_l/kT} \frac{N}{Q(T)} \tag{1.5}$$

where E_l is the energy of the transition and $Q(T)$ is the partition function at any given temperature. Thus the resulting optical depth will be exponentially dependent on the temperature. The relative intensity is related to the optical depth as $I = e^{-\tau_\nu}$. Then adopting a line profile, and using the line information from the HITRAN database (Rothman et a. 2013) we can construct synthetic spectra for molecules of interest, such as those shown in Figure 1.6.

In the limit of high optical depth, absorption lines will begin to broaden. When this happens the column density is no longer linearly related to the optical depth, but rather these two parameters become logarithmically related, and equation 1.5 no longer holds. This is a consequence of the Gaussian component of the line profile (for a Voigt profile) becoming saturated, and the strength of the line scales logarithmically with the column density. Eventually the Lorentzian component of the line profile takes over, and the line broadens due to absorption in the wings. The integrated strength will then scale with the square root of the column density (see top panel of Figure 1.7). The behaviour of the transition can be described by the curve of growth, which is a measure of the equivalent width of an absorption line, W, in relation to its opacity, η_0. Examples of the curve of growth are shown in Figure 1.7 for three different types of line formation. The equivalent width of a line is defined as the width of a rectangle that has the height of the continuum and the area of the line profile. For a continuum normalised absorption line the equivalent width of the absorption line will be equal to its area.

Figure 1.8: NASA's SOFIA observatory in full flight with the telescope door open taking data.

Absorbing gas can be seen in the foreground against the infrared continuum source, however the continuum emitting dust and absorbing gas can also be mixed, coming from the same physical space. A consequence of the latter is that an absorption line at a specific wavelength will typically probe the gas to the point where the line plus continuum optical depth becomes equal to 2/3. This follows directly from the Eddington approximation where the temperature equals the effective temperature where the optical depth equals 2/3 (Mihalas 1978). The result is that the absorption lines will probe to varying depths in the gas, leading to discrepancies in the absolute and relative column densities. Furthermore, the simple curve of growth analysis assumes that the absorption coefficient is constant with depth, and ignores any temperature or density gradients in the absorbing gas, which is generally not realistic.

1.3.3 Observations of Gas-phase Absorption Lines

This thesis continues a long study of absorption lines towards MYSOs in the infrared regime, presenting results from the first full spectral survey of the 4-13 μm wavelength region at high spectral resolution, as well as the first L band observations of organics in MYSOs. By combining ground based surveys from the Infrared Telescope Facility (IRTF) and the Gemini telescope in the L, M and N bands, with SOFIA observations in the 5-8 μm region, at high spectral resolution (3-6 km/s), we obtain velocity resolved line profiles of individual ro-vibrational transitions across the mid-IR regime.

The first molecule detected in absorption in the infrared way was CO in the late 1970's towards Orion BN (Hall et al. 1978). This was followed up by Scoville et al. (1983), and Mitchell et al. (1989, 1990) extended this research to a survey of many

different objects. A recurring finding was that CO absorption was observed to be offset in velocity compared to the systemic velocity of the cloud. Velocity differences were generally of the order of 5 km s^{-1}, and occurred both in either the blue- or red-shifted directions, depending on the source. Furthermore many different velocity components were detected as well as multiple temperature components, including very hot gas. The first detection of C_2H_2 in interstellar clouds followed (Lacy et al. 1989), which was shortly succeeded by CH_4 (Lacy et al. 1991), both towards massive protostars. Evans, Lacy & Carr (1991) then detected HCN, C_2H_2 and NH_3, again towards Orion, this time in IRc2 and IRc7, with OCS also detected towards IRc2 (Mitchell et al. 1989, 1990; Black et al. 1990; Mitchell et al. 1991).

With the advent of the Infrared Space Observatory (ISO), the possibility to detect H_2O without interference from the Earth's atmosphere allowed spectral surveys of MYSOs at low spectral resolution (Boonman et al. 2003a; Boonman & van Dishoeck 2003). The first detection of H_2O in the interstellar medium at infrared wavelengths was towards AFGL 2591, one of the main objects in this thesis (Helmich et al. 1996). Water gas was found to be in absorption, and very abundant in the hot gas close to the protostars. ISO also saw the detection of gas phase CO_2 and SO_2 in the infrared towards a sample of massive protostars (Boonman et al. 2000; Keane et al. 2001; Boonman et al. 2003b), as well as the first interstellar detection of CH_3 (Feuchtgruber et al. 2000). Lahuis & van Dishoeck (2000) detected very hot and abundant HCN and C_2H_2 in absorption with ISO towards a sample of massive protostars. Boonman et al. (2001) found that sub-mm observations of the high energy J=9-8 rotational lines from the $\nu_2 = 0$ and $\nu_2 = 1$ levels of HCN, probed the same gas in emission towards AFGL 2591. The abundance measured was two orders of magnitude higher than the envelope, suggesting a jump in the abundance of HCN in the hot gas very close to the protostar. High spectral resolution cross-echelle spectrographs such as the Texas Echelon Cross Echelle Spectrograph (TEXES; Lacy et al. 2002) improved observations at infrared wavelengths beginning studies at a resolving powers above R=50,000. Knez et al. (2009) detected many species towards NGC 7538 IRS1 with TEXES, including first detections of HNCO and CS in the infrared.

The observation of absorption lines at infrared wavelengths offers many essential differences for studying star forming regions compared to sub-mm emission line studies. Due to the nature of absorption lines, beam size variations with wavelength are not an issue since the beam size is set by the size of the infrared continuum source, the observer only seeing everything along the line of sight between them and the continuum. As a consequence of this, very high spatial resolution is a given. Star forming regions, and particularly circumstellar disks, are very bright at these wavelengths - they are the main infrared continuum source - therefore absorption lines at infrared wavelengths naturally probe material very close to the protostar. A typical observational setting covers 0.2-0.3 μm, therefore many lines can be observed in a single setting (Fig 1.6). Finally specific molecules that do not have permanent dipoles, and yet are important members of the organic inventory, are not observable at sub-mm wavelengths but have strong transitions in the infrared (such as CH_4, C_2H_2 and CO_2).

These advantages do not come for free however, and there are several challenges associated with this method (Lacy 2013). In the case that the absorbing gas is physically separated from the emitting dust, if the foreground gas does not fully cover

the continuum, the derived column density of the gas will be underestimated. Along with absorbing material in the foreground, absorbing gas is often found to be mixed with the emitting dust however, leading to radiative transfer effects which complicate the analysis. Furthermore, realistically the continuum source also has a temperature gradient that increases towards the protostar, therefore the dust emission may arise from hotter regions closer to the star than where the gas probes. Finally, observationally, many of these species are very abundant in the Earth's atmosphere, therefore absorption by telluric lines can be difficult to correct for, often resulting in residual absorption features that are hard to distinguish from real features, or removing parts of real features, however large Doppler shifts can mitigate this. Removing the Earth's atmosphere generally involves the use of a featureless star (or standard star) that will then only contain the telluric lines, and this greatly increases observing time. Atmospheric models provide an efficient way to remove the atmosphere from science spectra, often resulting in a better solution.

1.4 SOFIA

The Stratospheric Observatory for Infrared Astronomy (SOFIA) is a modified Boeing 747-SP aeroplane that has been adapted to the purpose of infrared astronomy and is a joint project of NASA and the German Aerospace Center (DLR). Within the aircraft is a telescope with a 2.7 m mirror that can be exposed via a door in the side of the plane. SOFIA is unique in the sense that it can fly at altitudes of up to 45,000 ft to take data, however unlike space telescopes, can be continually upgraded and repaired when it lands again. Thus data can be taken at altitudes where transmission through the atmosphere is much better, particularly in the infrared. Figure 1.9 compares the atmospheric transmission at altitudes typical of SOFIA with that of ground based observatories. SOFIA is based at NASA's Armstrong Flight Research Centre in Palmdale California and also in Christchurch International Airport in New Zealand. In this thesis we use the Echelon-cross-Echelle Spectrograph (EXES) on-board SOFIA, making use of the high resolution mode which can achieve a spectral resolution of 5×10^4-1×10^5. The combination of echelon and echelle gratings as primary and secondary dispersers, respectively, produces spectra that are split into orders, the number of which depends on the spectral resolution mode. EXES operates between 4.5-28.3 μm allowing the study of ro-vibrational transitions of many molecules of astrophysical interest.

1.4.1 Data Reduction

There are a number of steps required to turn an observation into a usable spectrum. Firstly a flat field is taken and used to correct for unequal spectral and spatial gains as well as calibrating the intensity. The spectrum is also wavelength calibrated using bright sky lines. The removal of sky emission is achieved by nodding either on or off the slit and subtracting each B nod from each A nod. The spectrum must then be extracted from the aperture within a given spatial range of the slit. The various cycles of the observation can then be combined. The final stage in obtaining a complete

spectrum is to merge the different Echelle orders, however this requires that the atmosphere has first been removed, either by dividing by a standard star or using an atmospheric model.

1.5 This Thesis

With the use of EXES on-board SOFIA to obtain data in the 5-8 μm wavelength region, combined with ground based facilities using TEXES to obtain 8-13 μm, this thesis presents the first spectral survey of the mid-IR regime of two hot cores, AFGL 2591 and AFGL 2136, at high spectral resolution. iSHELL observations in the L and M bands complete the survey providing much needed information on CO (at high spectral resolution), and also the HCN and C_2H_2 stretching modes at 3 μm. The stretching mode of HCN in MonR2 IRS 3 is also analysed. Resolving powers range from 50,000 - 80,000. These targets are very well studied objects at infrared and sub-mm wavelengths.

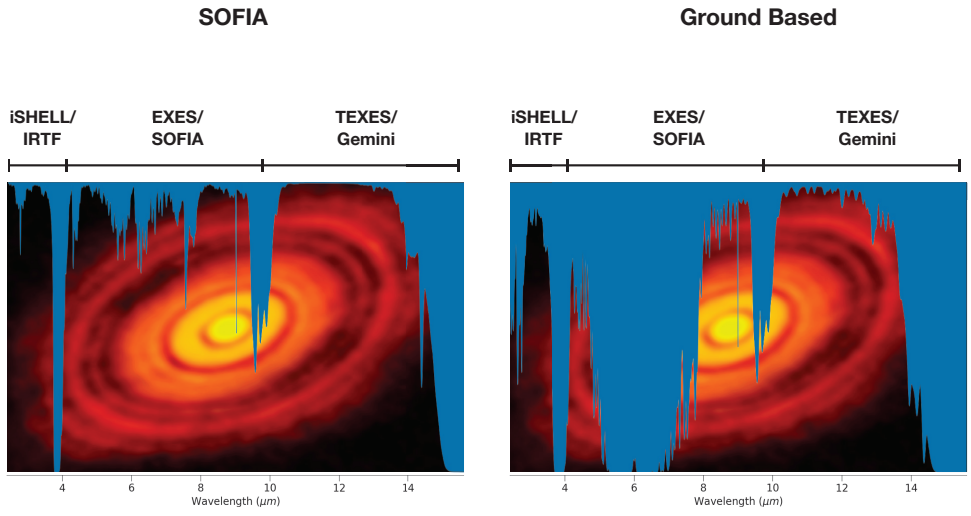

Figure 1.9: Dust continuum emission image of the TTauri disk HL Tau (ALMA Partnership et al. 2015) overlaid with the atmospheric transmission of SOFIA (left) and the IRTF on Mauna Kea (right) in the 3 to 15 μm range calculated using the ATRAN model (Lord 1992). Water vapours are 7.6 μm and 1.3 mm for SOFIA and IRTF respectively.

Chapter 2 presents the detection of CS with EXES in AFGL 2591 at high spectral resolution, constituting the second detection of CS in this way. These data are complemented by iSHELL observations of CO, and both CS and CO are observed in absorption. ^{12}CO lines are highly optically thick and saturated, therefore we limit the discussion to the optically thin isotopologue ^{13}CO, which shows five blended velocity components. We discern two temperature components in CO at the velocity of CS, where a narrow component is superimposed on a broad underlying component, which disappears above J=6. The temperature of the hot CO component is in agreement with the temperature of CS, and is ∼700 K. The column density, and abundance with respect to CO, of CS is two orders of magnitude higher than derived from sub-mm observations which detect CS in emission. This points towards a large reservoir of warm sulphur-bearing gas that is not detectable at sub-mm wavelengths, which might help alleviate the low fraction of accounted-for sulphur in dense regions.

Chapter 3 expands the detection of CS in AFGL 2591 to the other simple organics detected in the spectral survey including HCN, C_2H_2 and NH_3, as well as the detection of all these species in AFGL 2136. All species are observed in absorption and derived temperatures are high (400-700 K). Column density variations are observed in HCN and C_2H_2 with wavelength between vibrational bands that trace the same lower level, where the column at 13 μm is a factor of 4-10 lower than the column at 7 μm. Furthermore ortho-to-para ratios of C_2H_2 are found to be below the expected value of 3 for a hot gas formation. Supplementary data in the L-band at 3 μm for AFGL 2591 find HCN and C_2H_2 in emission. The mid-IR continuum of these two sources originates in a circumstellar disk (Monnier et al. 2009; Frost et al. 2021), therefore we associate the absorbing gas to arise from the disk. We develop a model based on stellar atmosphere theory to account for the temperature gradient in the disk, which is heated from the mid-plane by viscous processes resulting in a temperature gradient that decreases with scale height. We find that the disk model can account for all of the above observational results.

Chapter 4 extends the discussion to H_2O, with hundreds of absorption lines being detected in both AFGL 2591 and AFGL 2136 from the v=1-0 and v=2-1 bands. Two velocity components are observed in each source. A rotation diagram analysis shows large scatter as lines with high opacity are underestimated compared to low opacity ones. We find that absorption lines saturate at non-zero flux, a direct prediction of the stellar atmosphere model developed in chapter 3. We therefore carry out a curve of growth analysis in this regime, and find that lines with high opacity have transitioned onto the logarithmic part of the curve of growth. The temperatures derived are of the order 400-600 K. The model of an absorbing slab of gas associated with foreground absorption is found to be incompatible with the results; namely the absence of H_2O emission lines, chemical abundance ratios and unexpected covering factors. The internally heated disk model also has challenges as absorption lines are offset in velocity from the cloud and line widths are narrower than would be expected based on a disk origin, requiring a specific geometry. A velocity gradient is observed with opacity in AFGL 2591 indicative of a disk wind along the observer's line of sight. We conclude that the disk model best explains all of the observational results, includ-

ing the other species detected.

Chapter 5 presents the detections, in the 3 μm spectral window, of HCN towards the high mass protostar MonR2 IRS 3 in emission, and HCN and C_2H_2 towards AFGL 2136 in absorption. MonR2 IRS 3 is a binary, and our observations allow us to separate the contributions from each source in the binary. HCN is confidently detected in MonR2 IRS 3A and tentatively detected in MonR2 IRS 3B. A rotation diagram analysis reveals hot gas associated in velocity with the red-shifted emission feature of P-cygni profiles seen up to high J levels (J=26) in CO. We attribute the HCN emission either to the back-side of an expanding shell of gas that is moving away from the observer, or to the upper layers of a circumstellar disk photosphere. We explore two options for the absorption lines of AFGL 2136: a foreground absorbing slab model and an internally heated circumstellar disk. For the foreground model, partial covering of the continuum source at 13 μm must be invoked in order to explain the equivalent widths, with a covering factor 0.3 of that at 3 and 7 μm. An important conclusion of this model is that HCN and C_2H_2 must cover the source more than H_2O. For the disk model, consistent physical conditions are measured across all wavelengths for HCN, however C_2H_2 shows a trend of increasing temperature/abundance with decreasing wavelength, indicative of a radial abundance gradient. Both of these sources differ from AFGL 2591 in that no P-Cygni profiles are observed towards AFGL 2591 or AFGL 2136, and AFGL 2591 and MonR2 IRS 3 show emission lines rather than absorption lines.

1.6 Future Outlook

The detection of hundreds of ro-vibratioanl transitions towards massive protostars offers the potential to study in detail the physical structure of the inner regions of MYSOs, offering insights that are not possible with sub-mm astronomy. The lack of spatial information (or difficulty in extracting it) in absorption studies presents a challenge in interpreting the results, however, and for that reason very high spatial resolution observations with sub-mm interferometers such as the Atacama Large Millimetre Array (ALMA) are extremely useful in complementing these studies. A particular example is the detection and velocity mapping of the Keplerian disk of AFGL 2136 seen in vibrationally excited H_2O emission with ALMA (Maud et al. 2019). The James Webb Space Telescope (JWST) will allow the opportunity to study low mass objects at infrared wavelengths due to the high sensitivity, a current limitation to SOFIA studies. The absence of a high resolution spectrometer on JWST means that this thesis will be essential in providing a benchmark for interpreting the lower spectral resolution data, as kinematic information of the different molecular species will not be available. The Mid-Infrared E-ELT Imager and Spectrograph (METIS) on the Extremely Large Telescope (ELT), and NASA's distant future mission Origins Space Telescope, will allow for velocity resolved studies at high sensitivity and will greatly expand this work to fainter high and low mass protostars. This will give the opportunity to determine whether absorption lines are also common in deeply embedded low mass disks, or if this is a characteristic unique to high mass objects,

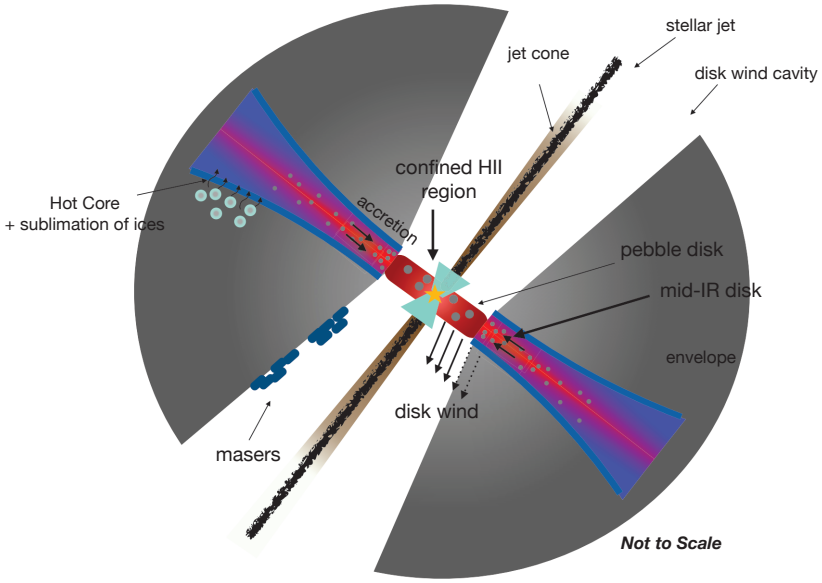

Figure 1.10: Cartoon illustration of the potential environment of MYSOs, taken from chapter 4 of this thesis.

and to understand the different heating mechanisms involved. In the earliest stages of disk evolution of low/intermediate mass stars, we expect that the disk will also be internally heated when the accretion rate is high and stellar luminosity low. Next generation telescopes will help to answer whether this is true or not. Observations of mid-IR absorption lines towards many class 0 disks would be a step toward solidifying this hypothesis, as for now only a few low mass sources show mid-IR absorption lines, which are believed to be due to a rare viewing angle (Gibb et al. 2007; Lahuis et al. 2006; Najita et al. 2021).

On the other side of the coin, of particular importance is the development of theoretical models which are necessary to establish what the temperature and density structures are for disks that are heated internally by viscous dissipation. The complex environment depicted in Figure 1.10 for a MYSO suggests many different physical components that can be modelled and constrained with observations. In this picture, strong winds close to the protostar carve out cavities through which radiation can escape via the flashlight effect, thus shielding the disk from stellar radiation. These winds also excavate the inner disk of small grains, extending the mid-IR continuum origin further out in the disk. From a chemical perspective, chemical models will have to explore what the dominant routes are towards molecules such as HCN and C_2H_2 in these disks, in particular if there are no UV photons available to break carbon out of CO and nitrogen out of N_2.

2 | Infrared Detection of Abundant CS in the Hot Core AFGL 2591 at High Spectral Resolution with SOFIA/EXES

Abstract

We have performed a 5-8 μm spectral line survey of the hot molecular core associated with the massive protostar AFGL 2591, using the Echelon-Cross-Echelle Spectrograph (EXES) on the Stratospheric Observatory for Infrared Astronomy. We have supplemented these data with a ground based study in the atmospheric M band around 4.5 μm using the iSHELL instrument on the Infrared Telescope Facility (IRTF), and the full N band window from 8-13 μm using the Texas Echelon Cross Echelle Spectrograph on the IRTF. Here we present the first detection of ro-vibrational transitions of CS in this source. The absorption lines are centred on average around -10 km s^{-1} and the line widths of CS compare well with the hot component of ^{13}CO (around 10 km s^{-1}). Temperatures for CS, hot ^{13}CO and ^{12}CO v=1-2 agree well and are around 700 K. We derive a CS abundance of 8×10^{-3} and 2×10^{-6} with respect to CO and H_2 respectively. This enhanced CS abundance with respect to the surrounding cloud (1×10^{-8}) may reflect sublimation of H_2S ice followed by gas-phase reactions to form CS. Transitions are in LTE and we derive a density of $>10^7$ cm^{-3}, which corresponds to an absorbing region of $<0.04''$. EXES observations of CS are likely to probe deeply into the hot core, to the base of the outflow. Submillimeter and infrared observations trace different components of the hot core as revealed by the difference in systemic velocities, line widths and temperatures, as well as the CS abundance.

A. G. Barr, A. Boogert, C. N. DeWitt, E. Montiel, M. J. Richter, N. Indriolo, D. A. Neufeld, Y. Pendleton, J. Chiar, R. Dungee, A. G. G. M. Tielens
The Astrophysical Journal Letters, 868, L2 (2018)

2.1 Introduction

Hot cores are objects that are formed during the embedded phase of high mass star formation. They are compact ($\leq$0.1 pc) regions of dense molecular gas with temperatures and densities $\geq$100 K and $\geq 10^7$ cm^{-3} respectively (Kurtz et al. 2000). They are thought to be an intermediary stage in the formation of massive stars, which starts with the formation of an infrared dark cloud, which then collapses. Once a protostar is formed, it will heat its surroundings, evaporating ice mantles accrued during the preceding, cold, dark cloud phase. The resulting rich organic inventory gives rise to a dense forest of spectral lines in the sub-millimeter (sub-mm) of species such as methanol, dimethyl ether, methyl formate and many others (Blake et al. 1987; Plambeck & Wright 1987; Cesaroni 2005a). Regions of warm dense gas with a similarly rich organic inventory have also been observed around low mass stars, where they have been dubbed hot corinos (Ceccarelli 2008).

The physics and chemistry of the hot core phase of massive star formation has been well studied in the sub-mm regime by the analysis of pure rotational line emission at high spectral resolution (Kurtz et al. 2000; van der Tak 2003; Beuther et al. 2007). However this is not the case for the mid-infrared (MIR) spectral range, which contains many strong ro-vibrational transitions of important molecules, such as CH_4 and C_2H_2, which do not have transitions in the sub-mm (Lacy et al. 1991).

High resolution infrared (IR) studies have been carried out before by Mitchell et al. (1990) to analyse CO absorption in a sample of hot cores, including AFGL 2591. Also, Knez et al. (2009) studied the hot core NGC 7538 IRS 1 with TEXES, the Texas Echelon Cross Echelle Spectrograph (Lacy et al. 2002). They detected CS in absorption, however only 6 lines were observed, as well as HNCO and CH_3 for the first time in the IR. Indriolo et al. (2015a) studied H_2O absorption towards AFGL 2591 with the Echelon-Cross-Echelle Spectrograph (EXES; Richter et al. 2010).

The results presented in this paper are part of the first unbiased spectral survey of the 4.5-13 μm region of hot cores, at high spectral resolution (R=50,000). The high velocity resolution (6 km s^{-1}) allows level specific column densities to be determined, and dynamics studied, for the molecules that are detected. This kind of method has come into reach with instruments such as TEXES and iSHELL (Rayner et al. 2016) on the Infrared Telescope Facility (IRTF), and EXES onboard the Stratospheric Observatory for Infrared Astronomy (SOFIA; Young et al. 2012).

In this paper we present the first detection of ro-vibrational transitions of CS in AFGL 2591 at MIR wavelengths. CS is well studied in hot cores at sub-mm wavelengths (Li et al. 2015; Tercero et al. 2010; van der Tak et al. 2003). Sulphur-bearing molecules are very sensitive to the physical conditions in hot cores and therefore provide good tracers for hot core evolution (Hatchell et al. 1998). Sulphur is also known to be heavily depleted in dense regions (Tieftrunk et al. 1994) and large discrepancies exist between abundances derived from IR and sub-mm observations (van der Tak et al. 2003; Keane et al. 2001). CS therefore provides a good candidate for investigating these issues.

2.2 Observations and Data Reduction

AFGL 2591 (RA=20:29:24.80, Dec=+40:11:19.0; J2000) was observed with the EXES spectrometer on the SOFIA flying observatory as part of program `05_0041` using the high resolution echelon with the low resolution cross disperser (in order 4). Two settings were observed to cover the wavelength range (7.57-7.82 μm) containing the absorption lines of CS reported here. The slit length and width were 3.2″ and 2.89″, respectively. The spectral resolving power was R=55,000, and the sampling 16 points per resolution element. The observations were done on flights with mission identifications `2017-03-17_EX_F388` and `2017-03-23_EX_F391` at UT 09:51-10:51, initial latitudes of 45 degrees, initial longitudes of -104 degrees, altitudes of 42,000-44,000 feet, and airmasses of 1.70-1.81. In order to remove background emission, the telescope was nodded between the target position and a position 11″ to the West and 10″ North.

The EXES data were reduced with the SOFIA Redux pipeline (Clarke et al. 2015), which has incorporated routines originally developed for TEXES (Lacy et al. 2002). The science frames were de-spiked and sequential nod positions subtracted, to remove telluric emission lines and telescope/system thermal emission. An internal blackbody source was observed for flat fielding and flux calibration, and the data were divided by the flat field and then rectified, aligning the spatial and spectral dimensions. The wavenumber calibration was carried out from first examining the sky emission spectrum. This allowed for an easier match to the ATRAN wavenumbers in order to calibrate the dispersion and wavenumber zeropoint. There are two wavenumber solutions as the two settings were taken on different days, and they are accurate to 0.42 km s^{-1} and 0.89 km s^{-1}. The spectral orders were not flat as a result of instrument fringes. To correct for this the spectrum was divided over a 201 pixel median-smoothed version of itself. Telluric lines were corrected for using an ATRAN model which was not scaled to the depth of the observed telluric lines. The final signal-to-noise values are 130 and 157 at the native sampling.

AFGL 2591 was observed with iSHELL at the IRTF telescope on Maunakea on UT 2017-07-05 from 13:40 to 15:22 at an airmass range of 1.16-1.50, during good weather conditions as part of program 2017A985. The 0.375″ slit provided a spectral resolving power of 80,000. The combination of the M1 and M2 configurations provide full coverage from 4.51-5.24 μm. The target was nodded along the 15″ long slit to be able to subtract background emission from the sky and hardware. The total on-target time was 20 minutes for M1 and 31 minutes for M2. iSHELL's internal lamp was used to obtain flat field images. The spectra were reduced with the Spextool package version 5.0.1 (Cushing et al. 2004). Correction for telluric absorption lines was not done with a standard star but with the program xtellcor_model [1] newly developed at the IRTF and makes use of the atmospheric models calculated by the Planetary Spectrum Generator (Villanueva et al. 2018). The Doppler shift of AFGL 2591 at the time of the observations was -35 km s^{-1}, and thus telluric and target CO lines are well separated. The blaze shape of the echelle orders were corrected using the flat fields. The final signal-to-noise is 200 at the native sampling of 2 pixels per

[1] http://irtfweb.ifa.hawaii.edu/research/dr_resources/

resolution element.

2.3 Results

2.3.1 CS and CO

CS has a simple ro-vibrational spectrum with approximately equidistant lines separated by 2.0 cm^{-1} in the ground state. We have detected 18 CS absorption lines with excitation energies ranging from 14 to 1317 K. For ^{13}CO, 16 lines were detected with an energy range of 5 to 719 K and 8 lines of the ^{12}CO v=1-2 band are detected spanning an energy range of 3200 to 4234 K. Missing transitions coincide with strong telluric absorption lines or are blended with other hot core lines.

Figure 2.1 compares molecular line profiles between the sub-mm and IR in AFGL 2591. The CS lines reveal the presence of a single component at approximately -10 km s^{-1}. We have fitted those observed lines with a Gaussian line profile leaving the width, peak position and integrated strength as free parameters.

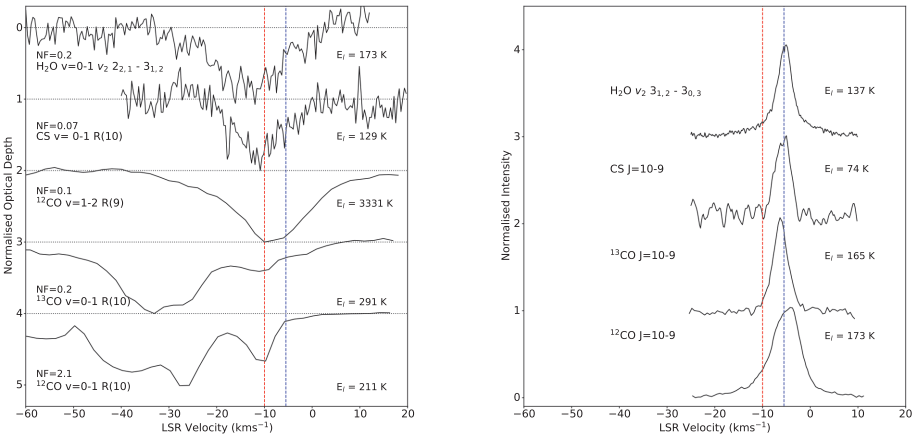

Figure 2.1: Comparison between IR and sub-mm line profiles. The IR lines are shown as optical depth profiles. The sub-mm profiles for CS, ^{13}CO and ^{12}CO are taken from Kaźmierczak-Barthel et al. (2014) and the sub-mm H_2O line is taken from Choi et al. (2015). The IR H_2O line is from our EXES data. The dashed red and blue lines indicate -10 km s^{-1} and -5.5 km s^{-1} respectively. Lines are normalised and lower energy levels given. For the IR lines, normalisation factors (NF) are given and horizontal baselines are shown.

The ^{12}CO v=0-1 ro-vibrational lines are saturated up until J=9, and thus we have elected to focus here on the optically thin ^{13}CO and ^{12}CO v=1-2 transitions. All components in the ^{12}CO v=0-1 line blend into one saturated line except for a broad high velocity component indicative of a high velocity outflow.^{12}CO v=1-2 line profiles also show a single component at -10 km s^{-1}. The line widths have been de-convolved with the instrumental resolution.

The ^{13}CO lines show complex profiles with multiple velocity components (Figure 2.1), one of which coincides in velocity with the CS lines and ^{12}CO v=1-2 transitions. Two temperature components (hot and cold; see Figure 2.2) are observed at this velocity. For the hot component (high J), we adopted the CS line width but the line width for the cold component (low J) had to be reduced (to 4.1 km s^{-1}). Absorption by the narrower cold component overwhelms the contribution by the warm component at the lower J-levels.

The detected, unblended lines of CS and CO are presented in Figure 2.3 in the Appendix. There is a spread in centroid velocity for a given species. The line widths for CS and hot ^{13}CO are in agreement for equivalent energy level.

The rotation diagrams of CS, ^{13}CO and ^{12}CO v=1-2 are shown in Figure 2.2. In all cases the rotation diagrams are straight lines indicating that local thermodynamic equilibrium (LTE) is a good approximation. We have calculated the vibrational excitation temperature of ^{12}CO from the v=1-2 transitions and the warm ^{13}CO column density assuming a ^{12}CO/^{13}CO abundance ratio of 60 (Wilson & Rood 1994). The derived vibrational excitation temperature of 625±56 K agrees well with a similar estimate by Mitchell et al. (1989). The similar values for the rotational and vibrational temperatures suggest vibrational LTE.

The excitation temperature and velocity for all three species (CS, ^{13}CO high J and ^{12}CO v=1-2) are very similar. This supports an origin in the same region. The physical conditions for the detected species are summarised in Table 2.1. An estimate of the column density of hot ^{12}CO from the lines of vibrationally excited ^{12}CO gives

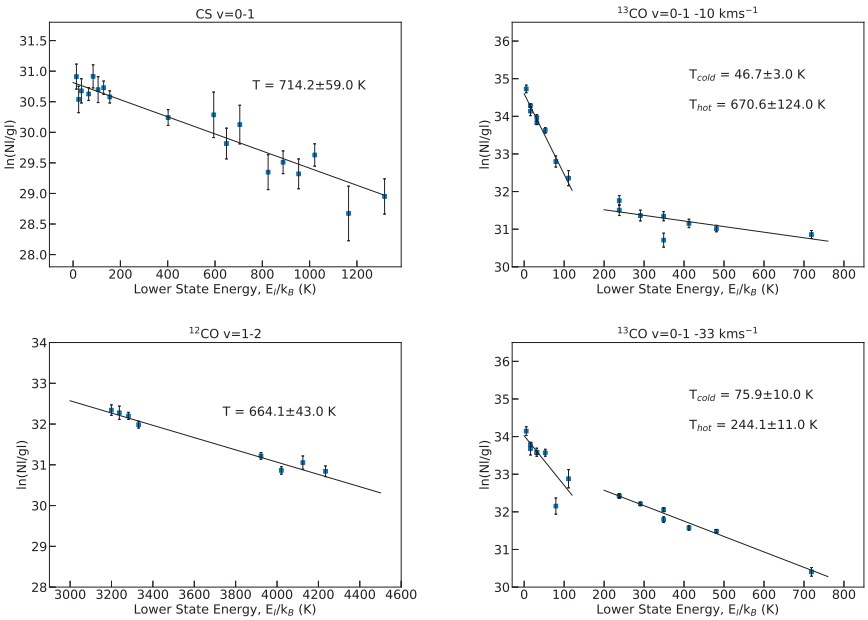

Figure 2.2: CS and CO rotation diagrams. Temperatures for each species are shown, with two temperature components for ^{13}CO.

$1.5\pm0.6\times10^{18}$ cm^{-2}. We derive an upper limit on CS in the -33 km s^{-1} velocity component of $< 8\times10^{14}$ cm^{-2}. The line parameters derived from the Gaussian fits are summarised in Table 2.2.

Table 2.1: Summary of Molecular Species in AFGL 2591.

Species	v_{lsr} (km s^{-1})	T_{ex} (K)	N ($\times10^{16}$cm^{-2})	N/N(^{12}CO)[a]
CS v=0-1	-10 ±0.5	714 ±59	1.6 ±0.1	8.0×10^{-3}
^{12}CO v=1-2	-8.4 ±0.5	664 ±43	1.48 ±0.6	7.4×10^{-3}
^{13}CO v=0-1	-11.95 ±0.6	670 ±124	3.4 ±0.4	0.02
H_2O[b]	-11 ±0.3	640 ±80	370 ±80	1.85
^{13}CO v=0-1	-9.2 ±0.2	47 ±3	3.8 ±0.2	0.02
^{13}CO v=0-1	-33 ±0.8	76 ±10	3.4 ±0.2	0.02
^{13}CO v=0-1	-33 ±0.5	244 ±11	5.9 ± 0.4	0.03
CS v=0-1[c]	-33	244	< 0.08	$< 2.2\times10^{-4}$

[a] N(^{12}CO) = N(^{13}CO)×60 (Wilson & Rood 1994).
[b] Indriolo et al. (2015a) with EXES.
[c] Velocities and temperatures for CS at -33 km s^{-1} are assumed.

2.3.2 CS and CO: Infrared vs Submillimeter

From our observations we derive a different systemic velocity than from sub-mm studies of AFGL 2591 (Figure 2.1) in both CS, ^{13}CO and ^{12}CO v=1-2 (-10 km s^{-1} compared to -5.5 km s^{-1}, Bally & Lada 1983). van der Tak et al. (1999) studied AFGL 2591 at sub-mm, radio and IR wavelengths, at lower resolution, and derive a centroid velocity for ^{13}CO absorption of -5.5 km s^{-1}, in agreement with the systemic velocity of rotational emission lines, including CS (Boonman et al. 2001; Benz et al. 2007; Kaźmierczak-Barthel et al. 2014). However their IR transitions show a spread in velocity of -3.5 to -12.4 km s^{-1} which they attribute to atmospheric interference, picking only a few lines to derive their value of -5.5 km s^{-1}.

The intrinsic line widths that we observed are broader than for sub-mm studies (Figure 2.1). As an example, the CS J=10-9 transition has a width of 3.5 km s^{-1} whereas our CS rovibrational transition v=0-1 R(10) has a width of 10.4 km s^{-1}. The H_2O 3(1,2)-3(0,3) line has a width of 3.1 km s^{-1} in the sub-mm compared to 16.5 km s^{-1} for the ν_2=0-1 2(2,1)-3(1,2) IR line.

We suggest our higher temperature, higher velocity IR observations trace more turbulent gas closer to the central source, probing deep into the base of the outflow, whereas sub-mm observations trace more extended gas at the velocity of the quiescent envelope.

The CS, ^{13}CO v=0-1 and ^{12}CO v=1-2 temperatures are very similar and given the difference in critical densities, suggest gas in LTE. The critical densities for J=7-6 are 2×10^5 cm^{-3} (Yang et al. 2010) and 3×10^7 cm^{-3} (Lique et al. 2006) for CO and CS respectively. Therefore we estimate that the density must exceed 10^7 cm^{-3} in order to maintain LTE. The critical density of ^{12}CO v=1-2 cannot be used due to the high optical depth of the ^{12}CO v=0-1 transitions, which may lead to line trapping and tends to increase the vibrational excitation temperature.

Assuming a ^{12}CO/H$_2$ abundance of 2x10^{-4} (Lacy et al. 1994) and constant density of 10^7 cm^{-3}, we derive a physical size for the absorbing region of $<$ 130 AU. At a distance of 3.3 kpc (Rygl et al. 2012) this corresponds to $<0.04''$.

The velocity structure of the inner region (down to 500 AU) of the hot core in AFGL 2951 has been well resolved and modelled by Wang et al. (2012). A high velocity gradient is found for SO_2 and the velocity field of the blue shifted component is observed to have the highest negative velocities towards the centre on the source. However the highest velocity that is reached is $\sim$ -7 km s^{-1}, at the very centre. This further indicates that CS at -10 km s^{-1} would not be observed at sub-mm wavelengths. Combined with the fact that SO_2 is a molecular tracer for shocks or outflows (Schilke et al. 1997), Wang et al. (2012) conclude that the SO_2 emission originates in an interactive layer between the upper parts of a disk-like structure and the outflow.

van der Tak et al. (1999) conclude that the outflow of AFGL 2591 points towards us along the line of sight. In order to explain CS (7-6) emission, Bruderer et al. (2009) propose that their observations trace dense walls of the outflow, at a velocity of around -5.5 km s^{-1}. Given that the extreme velocities originate in the centre of the source, and that our EXES observations show an average velocity around -10 km s^{-1}, we propose that we are looking into the outflow, probing deeply towards the protostar to the base of the outflow. Also the broad line profiles of CS are indicative of a shocked region. The high temperature implies that the gas lies close to the protostar, further supporting the proposed origin as the base of the outflow.

2.3.3 Chemistry of CS

We derive a CS/^{12}CO abundance of 8x10^{-3} and CS/H$_2$ abundance of 2×10^{-6}, assuming a CO/H$_2$ ratio of 2×10^{-4}. This abundance is two orders of magnitude higher than sub-mm observations of the hot core and envelope (van der Tak et al. 2003; Jiménez-Serra et al. 2012). This, once again, illustrates that the IR observations probe a very different region in this source. Consequently hot CS contains 6$\pm$0.8 % of the cosmic sulphur budget, assuming an S/H ratio of 1.3×10^{-5} (Asplund et al. 2009). Compared to the Orion Hot Core which has a CS/CO abundance of 4.1×10^{-4} derived from sub-mm observations (Tercero et al. 2010), the CS abundance in the gas traced by the IR observations of the hot core in AFGL 2591 is much higher.

Chemical models based on sub-mm observations (Charnley et al. 1997; Doty et al. 2002) derive a CS abundance of the order 1×10^{-8} with respect to H$_2$. A two phase, time-dependent gas-grain model (Viti et al. 2004) has been used to study the sulphur chemistry in the Orion Hot Core, and predicts the abundance of CS as a function of hot core age (Esplugues et al. 2014). The first and second phase simulate depletion onto, and sublimation from, grain surfaces respectively. For a hot core with a mass

of 10 $M_\odot$, solar sulphur abundance and a density of 10^7 cm^{-3}, a CS/CO abundance of around 5×10^{-3} is achieved after 6×10^4 yr.

The abundances of CS, H_2CS and SO_2 increase such that these species become the most abundant sulphur-bearing molecules for an evolved hot core (Esplugues et al. 2014). The main chemical pathway that is responsible for the production of CS in this model is $CH_2 + S \rightarrow CS + H_2$. Chemical models predict large amounts of atomic sulphur at high temperatures (Doty et al. 2002). This arises due to abstraction of H_2S which is efficient at high temperatures. At the same time small hydrocarbons are formed by the breakdown of CO via cosmic ray ionisation.

Therefore we propose two scenarios to interpret the CS abundance. The first is that AFGL 2591 is a more evolved hot core in which all sulphur is converted to H_2S on grain surfaces, and then converted back to S in the gas-phase after ice mantle sublimation. Then, at long timescales, enough CS is produced in the hot inner region of the hot core to explain our observations (Esplugues et al. 2014). These models are not optimised to AFGL 2591 which would likely have an effect on the CS abundance, therefore a more in depth study using chemical models would be necessary to clarify the proposed timescales. We note that H_2S ice has not been observed in absorption towards massive protostars (Smith 1991) at abundance upper limits a factor of 7 lower than that of CS, putting H_2S as a source of the gas phase S into question. Deeper searches for H_2S would be very helpful to asses the sulphur budget in interstellar ices.

The alternative scenario is that our observations trace a disk-wind interaction zone very close to the protostar. In this case the cosmic ray ionisation rate would be high, which would favour the breaking of C out of CO, which could lead to the enhancement of CS production. Again, atomic sulphur is produced via abstraction of H_2S. May et al. (2000) find that grain sputtering becomes important in shocks around 15 km s^{-1}, therefore sulphur could also be released from grain mantles in the presence of shocks.

The conditions and chemical history of AFGL 2591 are clearly favourable for the production of CS. A high CS/CO abundance of $7\pm0.4\times10^{-3}$ has also been observed at MIR wavelengths in NGC 7538 IRS 1 (Knez et al. 2009) with TEXES. Nevertheless, the enhanced CS abundance is still not enough to appoint this molecule as the main reservoir of sulphur in hot cores. A high abundance of warm SO_2 has also been observed with EXES in the hot core MonR2 IRS 3 (Dungee et al. 2018). This also is not observed in the sub-mm suggesting that a large amount of sulphur is visible only at IR wavelengths.

2.4 Conclusions

We present the first detection of ro-vibrational transitions of CS in the hot core of AFGL 2591 with EXES. The CS observations are complemented with high resolution iSHELL CO observations. The CO gas is found to have five velocity components, one of which is consistent with the velocity of CS, -10 km s^{-1}. ^{12}CO v=1-2 is also observed at this velocity. A temperature of 714±59 K is derived from the rotation diagram of CS, and the observation of CS up to J level of 33, along with a similar excitation temperature for the pure rotational CO lines, imply high densities ($> 10^7$ cm^{-3}). The temperature is consistent with hot ^{13}CO and ^{12}CO v=1-2 which have

670±124 K and 664±43 K respectively.

The systemic velocity of AFGL 2591 that we derive is 5 km s^{-1} bluer than that derived from sub-mm observations. We propose that this is because we are observing the base of the blue-shifted outflow very close to the central IR source. This is reflected in the high densities and temperatures derived in our observations.

The abundance of CS is observed to be $8x10^{-3}$ and 2×10^{-6} with respect to CO and H_2 respectively. This is two orders of magnitude above what is derived from sub-mm observations, 1×10^{-8} with respect to H_2. This provides evidence of a large sulphur depository which is detectable more readily at IR wavelengths. IR observations are sensitive to a different region of the hot core than sub-mm observations. IR observations of CS trace gas in the hot core that is much hotter and denser than do sub-mm observations, and that is at a larger systemic velocity. Therefore they probe much deeper into the innermost parts of the hot core, avoiding any contamination by the surrounding envelope.

Chemical models support the derived abundance of CS if AFGL 2591 is an evolved hot core. Alternatively our observations may be tracing the onset of a disk wind at the base of the outflow.

Acknowledgements

Based [in part] on observations made with the NASA/DLR Stratospheric Observatory for Infrared Astronomy (SOFIA). SOFIA is jointly operated by the Universities Space Research Association, Inc. (USRA), under NASA contract NNA17BF53C, and the Deutsches SOFIA Institut (DSI) under DLR contract 50 OK 0901 to the University of Stuttgart. A.G.G.M.T thanks the Spinoza premie of the NWO. D.A.N gratefully acknowledges the support of an USRA SOFIA grant, SOF05-0041.

2.A Appendix

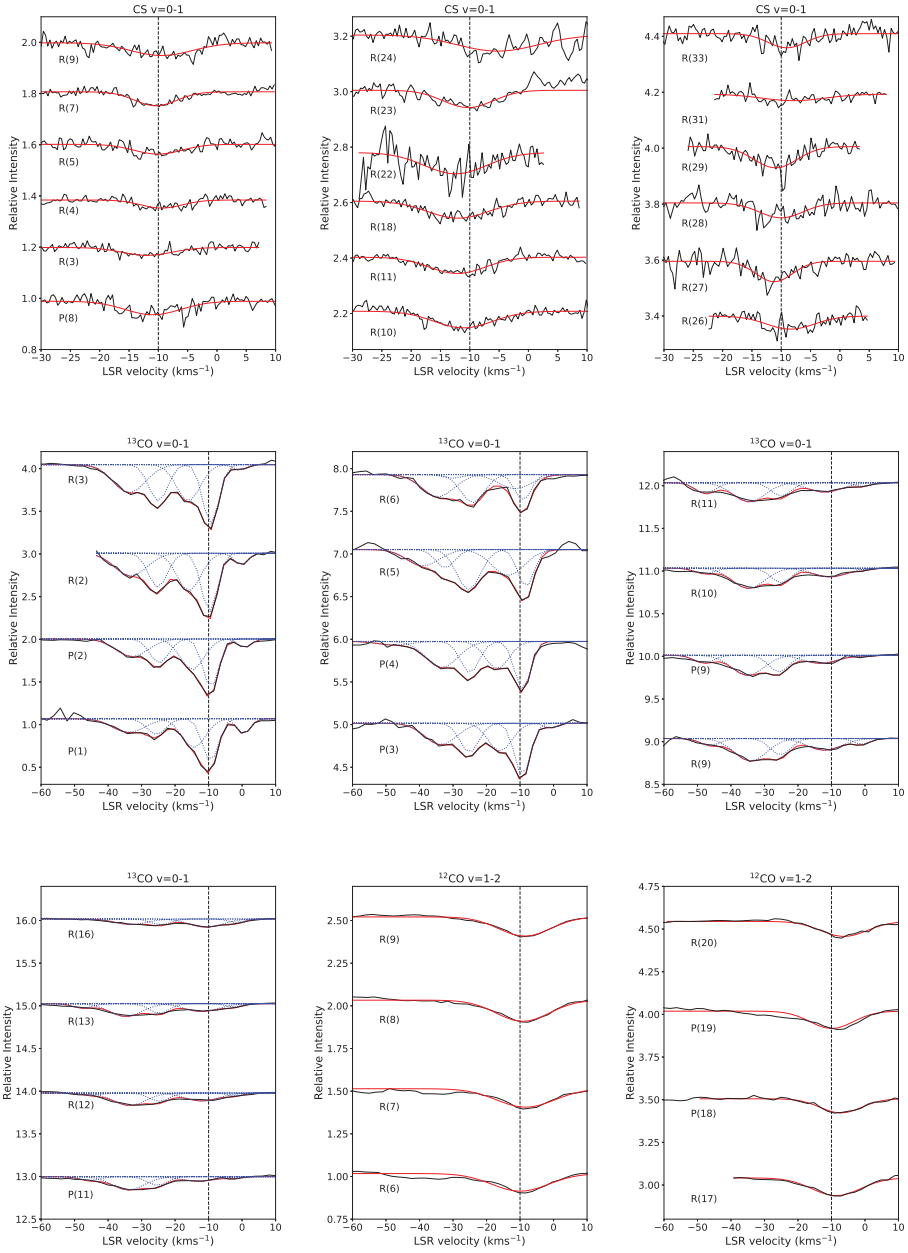

Figure 2.3: All lines of CS, ^{13}CO and ^{12}CO v=1-2. The blue dotted lines represent the individual velocity components and the red solid lines show the overall fit. The black dashed line denotes -10 km s^{-1}.

Table 2.2: CS and CO line parameters. Δv is the line FWHM, τ_0 is the optical depth at line centre and N_l is the column density in the lower energy level of the transition, with energy E_l. A_{ij} is the Einstein A coefficient for the transition and g_l is the statical weight. Line data were taken from the HITRAN database (Gordon et al. 2017).

Species	Transition	λ (μm)	E_l (K)	g_l	A_{ij} (s^{-1})	v_{lsr} (km s^{-1})	Δv (km s^{-1})	τ_0	N_l ($\times 10^{14}$ cm^{-2})
CS v=0-1	R(3)	7.8212	14.1	7	7.2	-11.9 ±0.5	8.3 ±1.5	0.031 ±0.004	1.9 ±0.4
	R(4) *	7.8116	23.5	9	7.4	-9.4 ±0.5	6.1 ±1.3	0.032 ±0.004	1.6 ±0.4
	R(5)	7.8020	35.3	11	7.6	-10.1 ±0.5	7.7 ±1.3	0.039 ±0.004	2.3 ±0.5
	R(7) *	7.7833	65.8	15	7.8	-10.4 ±0.2	6.4 ±0.6	0.056 ±0.003	3.0 ±0.3
	P(8)	7.9443	84.6	17	8.1	-10.9 ±0.5	9.6 ±1.5	0.055 ±0.006	4.5 ±0.9
	R(9)	7.7649	105.8	19	8.0	-9.5 ±0.6	11.2 ±1.8	0.051 ±0.005	4.1 ±0.5
	R(10)	7.7559	129.2	21	8.0	-11.1 ±0.3	10.4 ±0.9	0.061 ±0.004	4.7 ±0.5
	R(11)	7.7469	155.1	23	8.1	-12.1 ±0.3	9.9 ±0.8	0.060 ±0.002	4.4 ±0.4
	R(18)	7.6868	401.8	37	8.5	-12.0 ±0.3	11.0 ±0.8	0.063 ±0.003	5.0 ±0.6
	R(22) *	7.6545	594.5	45	8.7	-12.7 ±0.4	10.7 ±1.2	0.080 ±0.004	6.1 ±2.4
	R(23)	7.6467	648.5	47	8.8	-10.3 ±0.9	8.4 ±3.8	0.016 ±0.003	4.2 ±1.1
	R(24) *	7.6389	704.7	49	8.8	-5.2 ±0.7	15.0 ±1.8	0.060 ±0.003	5.9 ±1.9
	R(26)	7.6237	824.4	53	8.9	-8.4 ±0.6	7.9 ±2.0	0.048 ±0.007	3.0 ±0.7
	R(27) *	7.6162	887.8	55	9.0	-11.2 ±0.6	4.9 ±1.2	0.076 ±0.006	3.6 ±0.8
	R(28)	7.6088	953.4	57	9.0	-10.0 ±0.4	6.8 ±1.0	0.055 ±0.008	3.1 ±0.7
	R(29)	7.6015	1021.5	59	9.1	-10.9 ±0.4	6.7 ±1.2	0.078 ±0.008	4.4 ±0.8
	R(31) *	7.5871	1164.5	63	9.2	-8.0 ±0.9	11.4 ±4.1	0.024 ±0.005	1.8 ±0.8
	R(33)	7.5731	1316.8	67	9.2	-9.0 ±0.6	5.2 ±1.5	0.051 ±0.009	2.5 ±0.7
^{13}CO v=0-1	P(1)	4.7792	5.2	6	32.4	-9.4 ±0.2	4.1	0.50 ±0.04	72.4 ±7.3
	P(2)	4.7877	15.8	10	21.5	-9.3 ±0.1	4.1	0.57 ±0.02	77.5 ±3.6
	R(2)	4.7463	15.8	10	14.2	-9.7 ±0.3	4.1	0.68 ±0.07	67.0 ±8.0
	R(3)	4.7383	31.7	14	14.8	-9.3 ±0.1	4.1	0.70 ±0.02	68.6 ±2.7
	P(3)	4.7963	31.7	14	19.3	-9.3 ±0.2	4.1	0.61 ±0.04	79.0 ±6.2
	P(4)	4.8050	52.8	18	18.2	-9.3 ±0.2	4.1	0.57 ±0.03	72.4 ±5.2

Table 2.2: continued.

Species	Transition	λ (μm)	E_l (K)	g_l	A_{ij} (s^{-1})	v_{lsr} (km s^{-1})	Δv (km s^{-1})	τ_0	N_l ($\times 10^{14}$ cm^{-2})
	R(5)	4.7227	79.3	22	15.5	-8.3 ±0.2	4.1	0.44 ±0.06	38.6 ±5.7
	R(6)	4.7150	111.0	26	15.8	-9.1 ±0.3	4.1	0.31 ±0.06	29.3 ±5.9
	R(9)	4.6927	237.9	38	16.4	-12.1 ±0.7	11.2	0.14 ±0.01	23.6 ±3.1
	P(9)	4.8501	237.9	38	16.4	-13.2 ±0.8	11.2	0.10 ±0.01	18.3 ±2.6
	R(10)	4.6853	290.8	42	16.5	-10.5 ±0.6	11.2	0.10 ±0.01	17.5 ±2.5
	R(11)	4.6782	349.0	46	16.7	-12.0 ±0.5	11.2	0.11 ±0.01	18.9 ±2.3
	P(11)	4.8689	349.0	46	16.1	-13.0 ±0.6	11.2	0.05 ±0.01	10.0 ±1.8
	R(12)	4.6711	412.3	50	16.8	-12.0 ±0.6	11.2	0.09 ±0.01	16.9 ±1.9
	R(13)	4.6641	481.1	54	16.9	-12.0 ±0.4	11.2	0.09 ±0.01	15.9 ±1.4
	R(16)	4.6437	718.8	66	17.3	-10.8 ±0.5	11.2	0.10 ±0.01	16.6 ±1.8
^{12}CO v=1-2	R(6)	4.6675	3199.5	13	33.2	-9.6 ±0.6	17.9 ±1.4	0.102 ±0.006	13.1 ±1.6
	R(7)	4.6598	3237.9	15	33.7	-8.2 ±0.7	19.9 ±1.9	0.108 ±0.008	15.6 ±2.6
	R(8)	4.6522	3281.8	17	34.1	-9.1 ±0.4	18.3 ±0.9	0.124 ±0.006	16.4 ±1.4
	R(9)	4.6448	3331.0	19	34.4	-8.6 ±0.4	17.9 ±0.9	0.113 ±0.005	14.8 ±1.2
	R(17)	4.5887	3922.5	35	36.6	-8.5 ±0.3	16.6 ±0.9	0.104 ±0.005	12.7 ±1.1
	P(18)	4.8948	4020.9	37	31.7	-7.1 ±0.3	13.9 ±0.9	0.083 ±0.004	9.4 ±0.9
	P(19)	4.9054	4124.8	39	31.4	-9.9 ±0.8	14.6 ±3.8	0.010 ±0.009	12.0 ±1.9
	R(20)	4.5694	4234.4	41	37.2	-6.1 ±0.5	16.0 ±1.2	0.088 ±0.005	10.3 ±1.5

*These lines suffer from systematic error such as poor baselines therefore there is a larger uncertainty in the continuum placement.

3 | High Resolution Infrared Spectroscopy of Hot Molecular Gas in AFGL 2591 and AFGL 2136: Accretion in the Inner Regions of Disks Around Massive Young Stellar Objects

Abstract

We have performed a high resolution 4-13 μm spectral survey of the hot molecular gas associated with the massive protostars AFGL 2591 and AFGL 2136, utilising the Echelon-Cross-Echelle-Spectrograph (EXES) on-board the Stratospheric Observatory for Infrared Astronomy, and the iSHELL instrument and Texas Echelon Cross Echelle Spectrograph (TEXES) on the NASA Infrared Telescope Facility (IRTF). Here we present results of this survey with analysis of CO, HCN, C_2H_2, NH_3 and CS, deriving the physical conditions for each species. Also from the IRTF, iSHELL data at 3 μm for AFGL 2591 are presented that show HCN and C_2H_2 in emission. In the EXES and TEXES data, all species are detected in absorption, and temperatures and abundances are found to be high (600 K and 10^{-6}, respectively). Differences of up to an order of magnitude in the abundances of transitions that trace the same ground state level are measured for HCN and C_2H_2. The mid-infrared continuum is known to originate in a disk, hence we attribute the infrared absorption to arise in the photosphere of the disk. As absorption lines require an outwardly decreasing temperature gradient, we conclude that the disk is heated in the mid-plane by viscous heating due to accretion. We attribute the near-IR emission lines to scattering by molecules in the upper layers of the disk photosphere. The absorption lines trace the disk properties at 50 AU where a high temperature gas-phase chemistry is taking place. Abundances are consistent with chemical models of the inner disk of Herbig disks.

A. G. Barr, A. Boogert, C. N. DeWitt, E. Montiel, M. J. Richter, J. H. Lacy, D. A. Neufeld, N. Indriolo, Y. Pendleton, J. Chiar, A. G. G. M. Tielens

The Astrophysical Journal, 900, 104 (2020)

3.1 Introduction

Massive star formation begins with the formation of a dense core, inside a so-called infrared dark cloud (Egan et al. 1998; Carey et al. 1998). This core becomes then gravitationally unstable and collapses, resulting in a central protostar embedded in a dusty cocoon (Zinnecker & Yorke 2007; Tan 2017). Because of excess angular momentum, much of the in-falling material is channeled into an accretion disk, which can feed the central protostar. This disk is heated by viscous dissipation in the mid-plane. For massive stars, hydrogen burning starts already during this accretion phase and the resulting high luminosity heats the gas and dust in the direct environment. This is the so-called Hot Core phase which is rich in complex organic molecules (van der Tak 2003; Beuther et al. 2007; Herbst & van Dishoeck 2009). Eventually, when the central star is hot enough to create ionising photons, a hyper compact HII region will form in the inflating material. Once the cocoon is thin enough, the ionising photons can escape, leading to the ultracompact and compact HII region phases (Beuther et al. 2007).

From an observational perspective, the understanding of these stages is hindered on several accounts. Distances to the nearest massive stars are larger than for low mass stars, meaning that higher angular resolution is required to study them at comparable physical scales as their low mass counterparts (Henning et al. 2002). Furthermore dust extinction is high ($\sim A_v = 200$) as massive stars remain deeply embedded in their natal envelope for a large fraction of their early evolution (Beuther et al. 2007). A 40 $M_\odot$ star will live for around a few million years with an embedded lifetime of around $1{\times}10^5$ yr. This contrasts to low mass stars that have an embedded lifetime of around 10^6 yr but a main sequence lifetime of over 10^9 yr. Therefore it is challenging to disentangle the protostar and its direct environment - circumstellar disk, hot core and surrounding molecular cloud (Zinnecker & Yorke 2007; Cesaroni et al. 2007).

During the star formation process, infalling material onto the central protostar forms a disk, with a bipolar outflow along the perpendicular axis (Zinnecker & Yorke 2007). Angular momentum is transported to the outer parts of the disk via viscous stresses and gravitational torques, and the disk is predicted to expand (Lynden-Bell & Pringle 1974; Cassen & Summers 1983; Dullemond et al. 2007). As a result of this, material moves inward and accretes onto the central protostar. Theoretical models of dust disks come in varying degrees of complexity. One such model combines a hot, flared dust surface layer heated by stellar radiation, and viscous dissipation of gravitational energy due to accretion (D'Alessio et al. 1998). In this model one can see that for high accretion rates (10^{-7} - $10^{-6} M_\odot$/yr), three regimes arise in the disk. The surface region is irradiation dominated, the midplane of the disk is accretion dominated, and the two are connected by an intermediate zone. Here two temperature gradients can be distinguished, with an outwardly decreasing temperature gradient in the vertical direction in the accretion dominated region, and an inwardly decreasing temperature gradient in the vertical direction in the irradiation dominated zone (Dullemond et al. 2007).

Whilst disks around forming low mass young stellar objects (YSOs) are common (Williams & Cieza 2011), the number of detected disks around massive stars remains constrained to a handful, especially in the case of O-type stars (Patel et al. 2005;

Kraus et al. 2010; Moscadelli & Goddi 2014; Johnston et al. 2015; Ilee et al. 2016; Moscadelli et al. 2019; Zapata et al. 2019; Maud et al. 2019). Commonly detected around massive stars are massive rotating toroids likely to host stellar clusters (Cesaroni 2005a; Sandell et al. 2003; Olmi et al. 2003; Beltrán et al. 2004; Sollins et al. 2005). The search for disks around O-B stars is undertaken with sub-millimetre (sub-mm) continuum or specific line tracers and infrared (IR) continuum/line observations, as well as maser studies, in order to penetrate the surrounding obscuring dust in these embedded regions. Sub-mm observations probe preferentially the outer parts of the disk and the envelope, while IR observations are sensitive to the innermost regions of the disk (Cesaroni et al. 2007; Dullemond et al. 2007). Inner regions of TTauri and Herbig disks are observed in molecular *emission* such as CO and H_2O at IR wavelengths (Mandell et al. 2012; Bast et al. 2013, 2011; Pontoppidan et al. 2011, 2019; Setterholm et al. 2019; Adams et al. 2019). These disks are illuminated by UV radiation from the central protostar under an irradiation angle, resulting in a PDR-like layered structure (Tielens & Hollenbach 1985), with a temperature gradient that decreases towards the mid-plane. The inner portions of massive disks have been studied mainly through atomic line and CO bandhead *emission* (Cooper et al. 2013; Ilee et al. 2013; Davies et al. 2010; Bik et al. 2006; Fedriani et al. 2020). In a survey of massive protostars, Ilee et al. (2013) model CO bandhead emission from 20 massive YSOs and find temperatures and densities consistent with emission from an accretion disk, close to the dust sublimation radius. For a further discussion on the inner regions of protoplanetary disks, see the review by Dullemond & Monnier (2010).

Observations of ro-vibrational lines in the mid-infrared (MIR) regime of star forming regions offer a unique view. Towards massive YSOs these lines are typically seen in absorption rather than emission. Since the IR source is very small, a very high angular resolution is achieved, comparable to the highest possible obtainable with emission studies (≈50mas). Furthermore, since the lines lie so close together, it is possible to observe many of these lines in one observational setting. Further details about studies of ro-vibrational lines at IR wavelengths can be found in Lacy (2013) along with the various issues that these kind of observations face. Finally, we emphasise that IR studies allow observations of CH_4, C_2H_2 and CO_2 that have no allowed rotational spectrum in the sub-mm.

We have carried out a high spectral resolution spectral survey of the 4-13 μm region towards AFGL 2591 and AFGL 2136. This article is an follow-up of a chapter 2, where we reported IR observations of CS in absorption towards the hot core AFGL 2591 VLA 3. Here we extend the discussion to other species detected in our spectra of AFGL 2591 VLA 3, as well as those in the hot core AFGL 2136 IRS1. In section 3.2 we present the observational details of the spectral survey, in section 3.3 we outline the analysis techniques used and section 3.4 contains the results for each molecular species identified. Section 3.5 discusses the results in the context of the physical structures of the sources, along with the origin of L-band emission lines and the calculation of the abundances. Finally the chemical implications are discussed as well as extending the discussion to other infrared studies of massive protostars.

3.2 Observations and Data Reduction

3.2.1 Target Sources

AFGL 2591 is a star forming region in the Cygnus X region, at coordinates $\alpha(J2000)$ = 20:29:24.8, $\delta(J2000)$ = +40:11:19.6. It is home to the massive protostar AFGL 2591 VLA 3 (hereafter AFGL 2591) which has a luminosity of 2×10^5 $L_\odot$ at a distance of 3.33±0.11 kpc (Rygl et al. 2012). It is an O-type star with a mass of ∼40 $M_\odot$ (Sanna et al. 2012) and powers a bipolar outflow seen in CO and H_2 (Bally & Lada 1983; Mitchell et al. 1991; Tamura & Yamashiti 1992). Radio continuum emission is observed at 3.6 cm and 1.3 cm towards AFGL 2591 which coincides with a cluster of maser emission in a helical shell around the outflow (Trinidad et al. 2003).

AFGL 2136 IRS1 is an O-type star and is the main IR source, in the star forming region of AFGL 2136, coordinates $\alpha(J2000)$ = 18:22:26.385, $\delta(J2000)$ = -13:30:11.97. The luminosity of AFGL 2136 IRS1 (hereafter AFGL 2136) is 1×10^5 $L_\odot$ at a distance of 2.2 kpc (Lumsden et al. 2013; Urquhart et al. 2012, 2014). AFGL 2136 is one of the few sources that has a clear signature of a Keplerian disk around a proto-O-type star (Maud et al. 2019) with a bipolar outflow in the perpendicular direction to the disk. There is also evidence for a disk wind from Brγ emission and SiO line emission (Murukawa et al. 2013; Maud et al. 2018). The surrounding environment of AFGL 2136 consists of a bipolar reflection nebula in a fan shape (Murakawa et al. 2008) and has deep ice bands associated with ice located in the envelope (Gibb et al. 2004).

3.2.2 EXES

AFGL 2591 and AFGL 2136 were observed with the EXES spectrometer (Richter et al. 2018) onboard the Stratospheric Observatory for Infrared Astronomy (SOFIA) flying observatory (Young et al. 2012) as part of SOFIA program 05_0041. In the full spectral survey of AFGL 2591 and AFGL 2136, EXES covered the range 5.5-8 μm and required 16 wavelength settings in its HIGH-LOW mode, where the high-resolution echelon grating is cross-dispersed with the R 1/2 LOW resolution echelle grating. For AFGL 2136, observations were taken over three EXES flight series. For the analysis in this paper, 8 spectral settings were used, covering wavelengths 6.7-8.0 μm (1249 cm^{-1} - 1494 cm^{-1}). These observations are summarised in Table 5.1. The slit width was 3.2″ for all settings, providing R=55,000 resolution. The fixed slit lengths used were either 3.1″ or 2.2″, depending on the wavelength setting. In order to remove background night sky emission and telescope thermal emission, the telescope was nodded to an off-source position 15″ away from the target coordinates every 1-2 minutes.

The EXES data were reduced with the SOFIA Redux pipeline (Clarke et al. 2015), which has incorporated routines originally developed for the Texas Echelon Cross Echelle Spectrograph (TEXES) (Lacy et al. 2003). The science frames were de-spiked and sequential nod positions subtracted, to remove telluric emission lines and telescope/system thermal emission. An internal blackbody source was observed for flat fielding and flux calibration and then the data were rectified, aligning the spatial and spectral dimensions. The wavenumber solution was calibrated using sky emission

spectra produced for each setting by omitting the nod-subtraction step. We used wavenumber values from HITRAN (Rothman et a. 2013) to set the wavelength scale. The resulting wavelength solutions are accurate to 0.3 km s^{-1}. Where necessary, lines were divided by a local continuum which was fit as a straight line over the transition. This was done in cases where the continuum was uncertain due to fringing or poor atmospheric correction.

3.2.3 TEXES

Spectra were obtained of HCN, C_2H_2, and NH_3 from spectral surveys made with TEXES (Lacy et al. 2002). AFGL 2136 was observed with the Gemini North telescope on 2017 March 17 and 18 (UT) in the TEXES hi-lo spectral mode. In this mode the high resolution echelon grating is cross dispersed with a first order grating, providing a spectral coverage of $\delta\lambda \approx 0.25\mu m$ with typically 20-30 echelon spectral orders. To prevent order overlap on the detector array a short slit was required, which necessitated nodding the source off of the slit to observe the sky background. Between the two nights the 782-904 cm^{-1} region was covered with a total telescope time of 3^h 30^m including time for source acquisition, spectral setups, flat fields, nod delays, and sky observations. The on-source time at each spectral setting was typically 130 s, with some settings extended if clouds interfered. On the night of 2017 March 20 the spectral region of 1157-1195 cm^{-1} was observed in the TEXES hi-med spectral mode, in which the echelon is cross dispersed with an echelle, which was used in 6^{th} order. In this mode the spectral coverage in each setting is less, with $\delta\lambda \approx 0.006\lambda$, but a longer slit can be used so that the source can be nodded along the slit, improving the observing efficiency. The total telescope time was 40^m, and the on-source time at each spectral setting was 260 s. The data are publicly available from the Gemini archive.

AFGL 2591 was observed with TEXES on the NASA Infrared Telescope Facility (IRTF) on 2018 July 7 and 8, and 2018 Sep. 29 and 30. The 728-849 cm^{-1} spectral region was covered on July 7, the 849-999 cm^{-1} region was covered on July 8, and the 727-905 cm^{-1} region was covered on Sep. 18. These observations were in the TEXES hi-lo mode, with a total telescope time of 9^h and an on-source time per spectral setting of 130 s. The 1107-1120 cm^{-1} region was covered on July 8, the 1227-1250 cm^{-1} region on July 12, and the 751-841 cm^{-1} region on Sep. 30, all in hi-med mode. The total telescope time for these observations was 9^h 10^m. The on-source time per spectral setting was 972 s on July 8 and 12, and 583 s for most Sep. 30 observations, except that additional time was spent when clouds interfered.

No comparison sources for correction of telluric and instrumental features were available without spectral features and at least comparable in flux to the primary targets. Consequently, the observed spectra were divided by spectra of an ambient temperature black body and a model of the telluric absorption. The telluric model was based on measurements of atmospheric pressure, temperature, and water vapour from a weather balloon launched from Hilo each night and spectral parameters from the HITRAN database. The balloon data are available from the National Centres for Environmental Information Integrated Global Radiosonde Archive (IGRA) at ncdc.noaa.gov. The HITRAN database is available from https://hitran.org/. The

atmospheric ozone is measured less frequently, and the measurement closest to the observation dates were used. They are available from the NOAA Earth System Research Laboratories at esrl.noaa.gov. The water vapour and ozone abundances in the telluric model were adjusted to give the best correction and the best fit to the observed telluric emission spectrum. Most spectral lines were corrected well, but instrumental fringing was not always removed as well, so the corrected spectra were divided by a polynomial baseline.

3.2.4 iSHELL

AFGL 2591 and AFGL 2136 were observed with iSHELL (Rayner et al. 2016) at the IRTF telescope on Maunakea at a spectral resolving power of 80,000. The observations are summarised in Table 5.1. The observations for AFGL 2591 are described in chapter 2. AFGL 2136 was observed on UT 2018-10-10 from 05:45 to 06:52 at an airmass range of 1.55-1.80, during moderate weather conditions as part of program 2018B095. The target was nodded along the 15″ long slit to be able to subtract background emission from the sky and hardware. Spectra affected by clouds were discarded in the data reduction. iSHELL's internal lamp was used to obtain flat field images. The spectra were reduced with the Spextool package version 5.0.1 (Cushing et al. 2004). Correction for telluric absorption lines was not done with a standard star but with the program Xtellcor model developed at the IRTF and makes use of the atmospheric models calculated by the Planetary Spectrum Generator (Villanueva et al. 2018). The Doppler shift of AFGL 2136 at the time of the observations was +37 km s^{-1} (including an assumed VLSR=+23 km s^{-1}), and thus telluric and target CO lines are well separated. The blaze shape of the echelle orders was corrected for using the flat fields. The continuum signal-to-noise ratio as measured from the scatter in the data points is ∼250 at the native sampling of 3 pixels per resolution element. AFGL 2591 was also observed with iSHELL's L1, L2, and L3 modes at R=80,000 on UT 2018-10-05 at 04:42-08:52 as part of program 2018B095. The airmass range was 1.08-1.20. The data reduction process was the same as for the M-band, although standard stars were used for the telluric absorption correction: BS 8830 (L1), and Vega (L2+L3). The continuum signal-to-noise values between the telluric lines ranges from ∼220 in L1 to ∼400 in the L2 and L3 modes. The Doppler shift of AFGL 2591 at the time of the L-band observations was -13 km s^{-1} (including an assumed VLSR=-6 km s^{-1}).

Table 3.1: Summary of Observations.

Source	Telescope	Instrument	Date (UT)	Wavelength Range (μm)	Mode	Slit Width ($''$)	Resolving Power (R)	Integration Time (min)
AFGL 2591	IRTF	iSHELL	2017-07-05	4.51-5.24	M1 & M2	0.375	80,000	51
	IRTF	iSHELL	2018-10-05	2.750-3.459	L1, L2 & L3	0.375	80,000	93
	SOFIA	EXES	2017-03-17	7.34-7.68	High-low	3.2	55,000	30
	SOFIA	EXES	2017-03-21	6.69-7.05	High-low	3.2	55,000	20
	SOFIA	EXES	2017-03-22	7.19-7.37	High-low	3.2	55,000	14
	SOFIA	EXES	2017-03-23	7.67-8.01	High-low	3.2	55,000	25
	SOFIA	EXES	2017-03-23	7.02-7.21	High-low	3.2	55,000	25
	IRTF	TEXES	2018-07-08	8.93-9.03	High-med	1.4	85,000	65
	IRTF	TEXES	2018-07-12	8.00-8.15	High-med	1.4	85,000	32
	IRTF	TEXES	2018-09-30	11.89-13.32	High-med	1.4	85,000	185
AFGL 2136	IRTF	iSHELL	2018-10-10	4.51-5.24	M1 & M2	0.375	80,000	42
	SOFIA	EXES	2017-03-17	7.34-7.69	High-low	3.2	55,000	53
	SOFIA	EXES	2017-03-21	6.69-6.88	High-low	3.2	55,000	43
	SOFIA	EXES	2017-03-23	7.67-7.85	High-low	3.2	55,000	90
	SOFIA	EXES	2017-03-23	8.87-7.05	High-low	3.2	55,000	90
	SOFIA	EXES	2017-05-25	7.19-7.37	High-low	3.2	55,000	30
	SOFIA	EXES	2019-04-24	7.83-8.01	High-low	3.2	55,000	36
	SOFIA	EXES	2019-04-26	7.19-3.37	High-low	3.2	55,000	41
	Gemini	TEXES	2017-03-17	11.06-12.79	High-low	1.4	85,000	15
	Gemini	TEXES	2017-03-20	8.37-8.64	High-med	1.4	85,000	22

3.3 Analysis

The detected absorption lines were fitted with one Gaussian line profile for each velocity component detected. The free parameters that were allowed to vary were the line strength, line width, line velocity and continuum level. The fitting was conducted in velocity space, therefore the fit was a function of the local standard of rest (LSR) velocity and full width at half maximum (FWHM) both in units of km s^{-1}. The fit was then converted into an optical depth profile, and then into a column density profile via:

$$\tau(v) = -\ln(flux/cont) \tag{3.1}$$

followed by,

$$\frac{dN_l}{dv} = \tau(v)\frac{g_l}{g_u}\frac{8\pi}{A\lambda^3} \tag{3.2}$$

where $\tau(v)$ is the optical depth profile as a function of velocity, g_l and g_u are the statistical weights of the lower and upper states respectively, A is the spontaneous emission coefficient for the transition and λ is the wavelength. The fit was then integrated in velocity space to derive a column density in the lower energy level of the transition.

Each state-specific column density was then plotted in a rotation diagram by plotting $\ln(N_l/g_l)$ against E_l, where N_l is the integrated column density in each transition and E_l is the energy of the lower level in Kelvin. The rotational temperature is given by the Boltzmann equation:

$$\ln\frac{N_l}{g_l} = \ln N - \ln Z(T) - \frac{E_l}{kT} \tag{3.3}$$

where the temperature is -1/gradient of the fit to the rotation diagram. Here Z is the partition function at the rotational temperature and N is the total column density of the species. In this way the excitation temperature of each species was calculated. Initially, column densities were calculated for both absorption and emission lines. However a more extensive analysis of the absorption lines was carried out using stellar atmosphere theory to calculate the abundances with respect to H, assuming a dust/H ratio, and this utilised the excitation temperatures derived from the initial rotation diagrams. The analysis process is discussed further in section 3.5.2. Results from the rotation diagram analysis are presented in Tables 3.2 & 3.3 and parameters of the gaussian fitting are given in Tables 3.4 and 3.5 in the Appendix.

The rotational diagrams reveal different behaviour for the low and high J lines. Averaged line profiles were obtained for high and low energy lines by the mathematical averaging of all normalised, unblended lines of a given species. The distinction between high and low energy was taken as low energy lines having $E_l \leq 90$ K. The weighted average of the line profiles was taken to give the average line profiles which are presented in Figures 3.1 and 3.2.

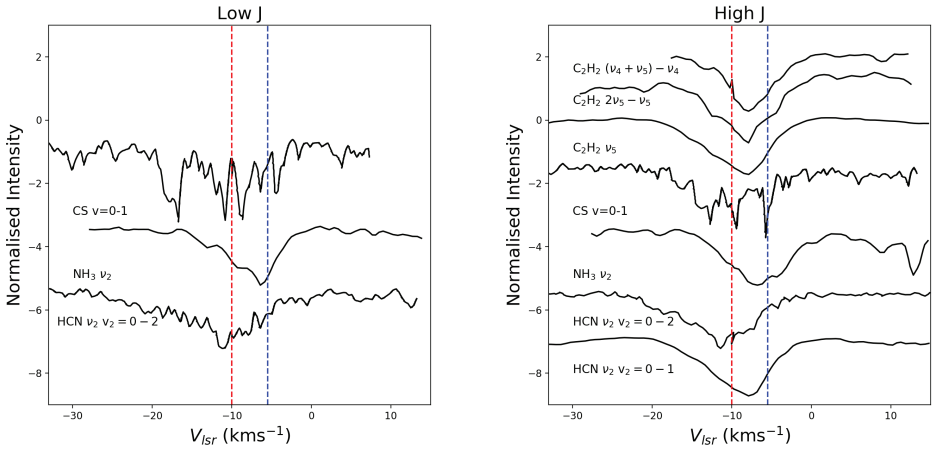

Figure 3.1: Normalised average line profiles for each band detected in AFGL 2591 plotted against the LSR velocity. Transitions are separated into high and low J levels before the average is calculated (high for $E_l > 90$ K). To guide the eye, we mark $v_{lsr} = -10$ km/s with a red dashed line in both panels. The blue dashed line denotes the systemic velocity of the source which is -5.5 km s^{-1}. CS and HCN $v_2 = 0 - 2$ transitions are detected with EXES at 7 μm whilst the other bands/species are detected with TEXES at 13 μm.

3.4 Results

Line widths and centroid velocities quoted in this section are given as weighted averages for the lines detected of a given band. The line widths have been corrected for the resolving power of the different instruments used. In all cases, missing lines of a band are either lost in the wings of deep telluric lines, blended with other hot core lines or additionally, in the case of TEXES data, lost in order gaps. Some lines are affected by systematic error such as proximity to other hot core lines or poor baselines due to fringing or poor atmospheric correction. This makes it harder to put a constraint on the continuum of such lines. The result is that these lines exhibit a greater error in line parameters than that which is portrayed by the fitting routine.

Also, for the TEXES data, it can be the case that lines lie close to the edge of gaps between orders. Therefore these lines will be slightly underproduced as some of their flux gets lost at the edges of the detector. For the TEXES data of AFGL 2591, additional systematic errors affect the data such as spurious emission wings on the shoulders of absorption lines due to the removal of strong fringing, and also CO_2 atmospheric residuals beyond around 13 μm.

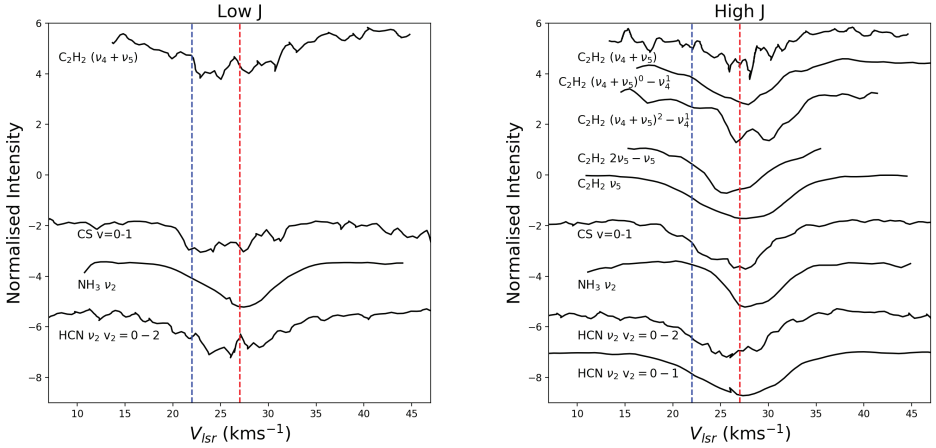

Figure 3.2: Normalised average line profiles for each band detected in AFGL 2136 plotted against the LSR velocity. Transitions are separated into high and low J levels before the average is calculated (high for $E_l > 90$ K). To guide the eye, we mark $v_{lsr} = 27$ km/s with a red dashed line in both panels. The blue dashed line denotes the systemic velocity of the source which is 22 km s^{-1} (van der Tak et al. 2003). CS, HCN $v_2 = 0-2$ and C_2H_2 ($\nu_4 + \nu_5$) transitions are detected with EXES at 7 μm whilst the other bands/species are detected with TEXES at 13 μm. NH_3 transitions are detected from 10 to 13 μm.

3.4.1 AFGL 2591

CO

AFGL 2591 shows a complex structure, with five velocity components of ^{13}CO detected. The scope of this paper will cover only the -10 km s^{-1} component, which has been previously discussed in chapter 2. These results are in agreement with a previous IR study of CO carried out by (Mitchell et al. 1989). We do not discuss the ^{12}CO v=0-1 transitions as they are saturated up until J=9. The rotation diagram for ^{13}CO at -10 km s^{-1} is shown in Figure 3.3. Furthermore, vibrationally excited ^{12}CO is detected with a single temperature component at -10 km s^{-1}, and we derive a vibrational temperature of 623±292 K. A comparison of line profiles from low and high J level is displayed in Figure 3.3 and detected unblended transitions of ^{13}CO v=0-1 and ^{12}CO v=1-2 are presented in Figure 3.4.

The rotation diagram of ^{13}CO in chapter 2 and Mitchell et al. (1989) shows two temperature components at -10 km s^{-1}. These two temperature components are also distinct physical components. This can be seen by comparing low and high J transitions around the dashed line in Figure 3.3. The line profile of the R(3) line is dominated by a narrow velocity component with a width of 1.5 km s^{-1} and peak velocity of -9.2 km s^{-1}. This component disappears past J=6 which is reflected in the R(9) transition (Fig 3.3) where we see a broad component uncovered with a width of 10.5 km s^{-1} centred on a velocity of -12 km s^{-1}. The temperatures of the narrow and broad components are 49 K and 671 K, respectively. Therefore we only

show the hot component in the rotation diagram in Figure 3.3 and discuss only the high temperature component in the rest of the paper, the temperature of which is consistent with that of other species at the same velocity.

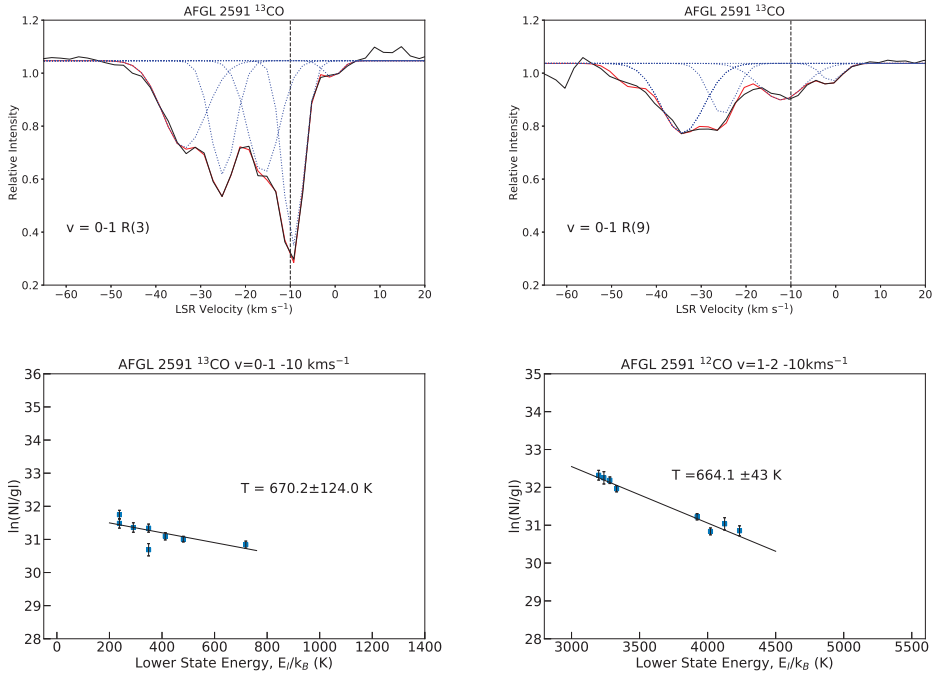

Figure 3.3: Individual line profiles for a high J (right) and low J (left) transition of ^{13}CO for AFGL 2591 detected with iSHELL at 4.5 μm. Blue dotted lines represent the individual gaussian fits and the red solid line is the overall fit. The black dashed line denoted -10 km s^{-1}. Rotation diagrams of ^{13}CO v=0-1 and ^{12}CO v=1-2 are also shown for the -10 km s^{-1} velocity component.

CS

CS is detected towards AFGL 2591 and has been discussed extensively in chapter 2. One velocity component is detected around -10 km s^{-1} and corresponds with one of the velocity components of ^{13}CO and the velocity of vibrationally excited ^{12}CO. Figure 3.5 shows that the rotation diagram reveals a CS temperature of 714±59 K which is consistent with the hot component of ^{13}CO at -10 km s^{-1} and ^{12}CO v=1-2. Line widths are in agreement for CS and hot ^{13}CO for equivalent energy level. Therefore CS and CO trace the same region of the hot core.

HCN

20 lines of the ν_2 band of HCN are detected in the v_2=0-1 transition with TEXES, spanning an energy range of 2500 K. From the rotation diagram, we derive a high

temperature of 675±32 K. All line profile parameters are summarised in Tables 3.2 and 3.3.

A second vibrational transition of HCN is detected at shorter wavelengths with EXES, the v_2=0-2 transition in the ν_2 band. From the 22 lines, the rotation diagram reveals the presence of a temperature gradient (Figure 3.6) by a curving of the rotation diagram at low J level, as line profiles are consistent from low to high J (Fig 3.1). Thus the physical conditions derived from the rotation diagram may not be reflective of the true values for this species. This is observed in the v_2=0-2 transition of HCN while it is not seen in the v_2=0-1 transition. This may be because, in the v_2=0-1 transition, only lines with J≥7 are observed as our observations did not extend to long enough

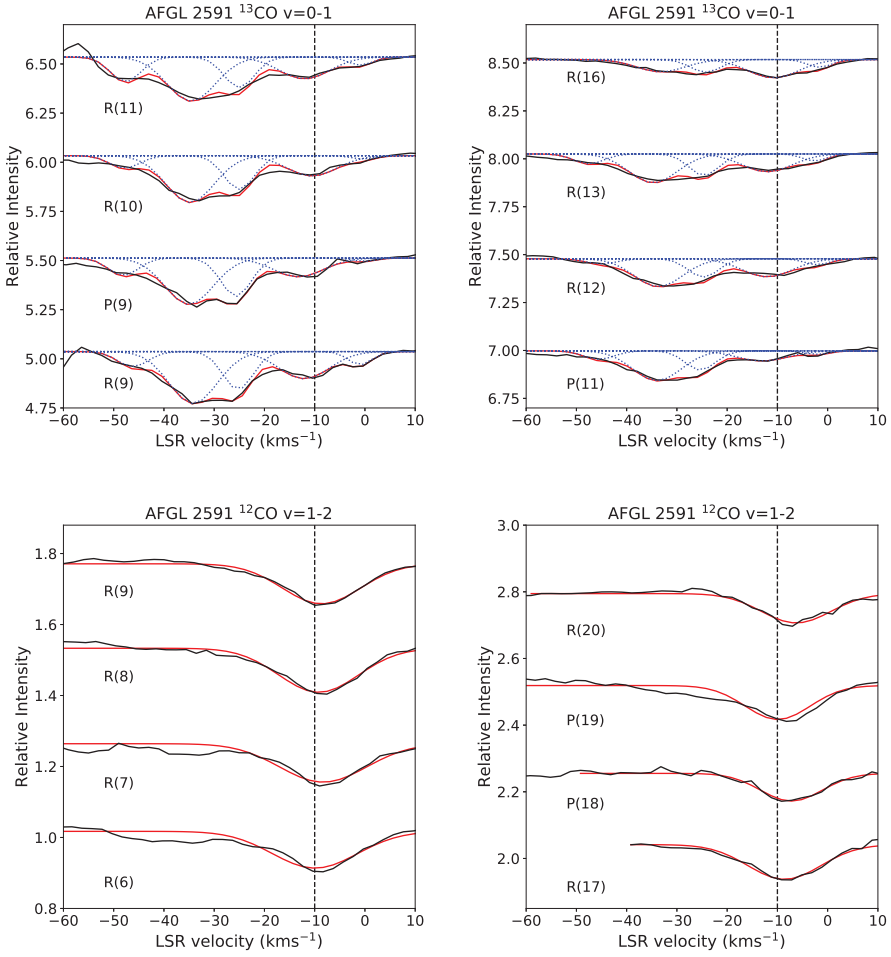

Figure 3.4: Lines of ^{12}CO v=1-2 and high J ^{13}CO v=0-1 in AFGL 2591 detected with iSHELL at 4.5 μm. The blue dotted lines represent the individual velocity components and the red solid lines show the overall fit. The black dashed line denotes -10 km s^{-1}.

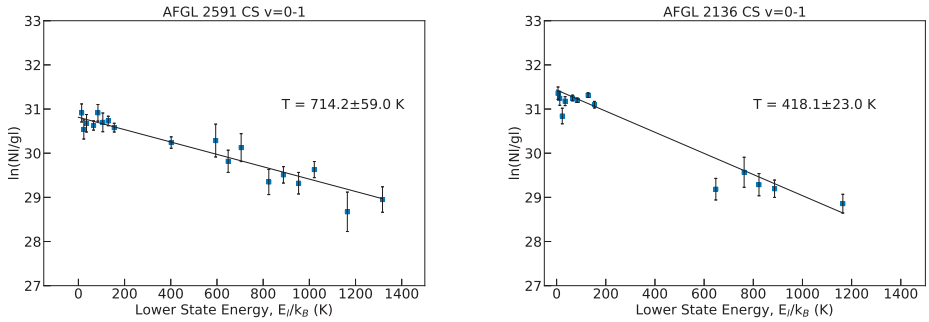

Figure 3.5: CS rotation diagrams for transitions in AFGL 2591 and AFGL 2136 detected with EXES. Rotational temperatures are shown.

wavelengths. As no low J transitions are observed in the HCN v_2=0-1 band, we cannot ascertain the presence (or absence) of an upward curvature in the rotation diagram. Due to the non-linearity of the rotation diagrams, we derive physical conditions from a fit to the flat, or high energy, part of the rotation diagram. A temperature of 670±118 K is found, in good agreement with the rotational temperature derived for the v_2=0-1 transition of HCN, as well as CS and CO. The line widths of CO, CS and HCN are also in agreement.

The column density measured in the v_2=0-2 transition at 7 μm is larger than the column density of the v_2=0-1 transition at 13 μm by one order of magnitude, despite the fact that these two transitions both trace the ground state. Compared to the v_2=0-1 transition, the line widths agree but the velocity is blue-shifted by a few km s^{-1}, which is around the instrumental spectral resolution.

The R(0) line in the HCN v_2=0-2 band is offset in velocity from the other HCN lines and appears to be tracing cold foreground absorption. Hot HCN has been detected towards AFGL 2591 before via MIR absorption with Infrared Space Observatory Short Wavelength Spectrometer (ISO-SWS) (Lahuis & van Dishoeck 2000). The derived temperature of 650^{+75}_{-50} K is in agreement with what we find at high spectral resolution.

HCN has also been detected in emission in the L-band spectrum of AFGL 2591. 21 lines tracing the ν_1 band are detected and the rotation diagram is also plotted in Figure 3.6. The line width is not in agreement with the HCN in absorption, being a factor of ∼2 narrower. The rotation diagram reveals a temperature of only 240±13 K, lower than the other two transitions seen in absorption.

C_2H_2

Several bands of C_2H_2 have been detected in AFGL 2591 with TEXES. Rotation diagrams have been constructed using statistical weights from the HITRAN database, which incorporates a factor of 3 difference between the statistical weights for the ortho- and para- states, due to nuclear spin degeneracy. Therefore the statistical weights of para- lines are 2J+1 however the statistical weights of the ortho- lines are 3(2J+1). We

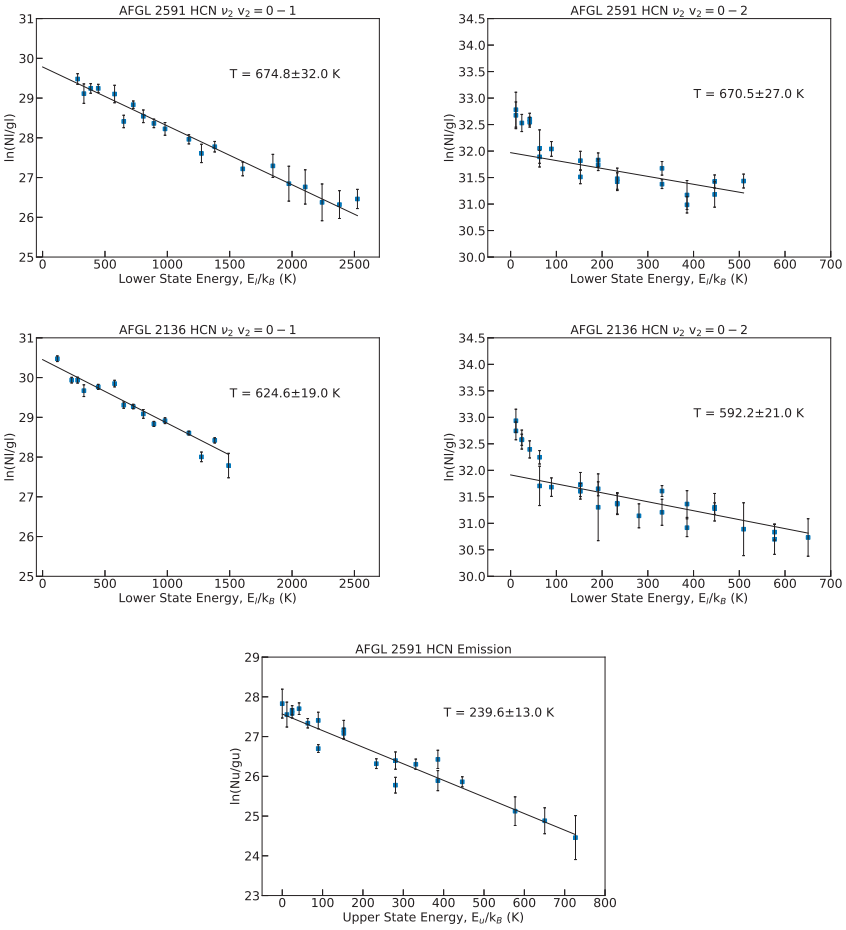

Figure 3.6: HCN rotation diagrams for AFGL 2591 and AFGL 2136. The v_2=0-1 transition is detected at longer wavelengths with TEXES. The v_2=2-0 transition comes from the EXES data. The rotation diagram for the HCN ν_1 band seen in emission is also shown which is detected with iSHELL.

also use the partition function, Q, given in HITRAN, and incorporate the difference in statistical weights by taking Q(ortho) = 3/4 Q and Q(para) = 1/4 Q. Ortho- and para- states have been split up and treated as separate molecular species. All line parameters are summarised in Tables 3.2 and 3.3.

In AFGL 2591, 26 lines of the ν_5 fundamental band of C_2H_2 are detected. The temperature ($\simeq$ 600 K) derived from the rotation diagrams is consistent with the other species. This suggests that o-C_2H_2 and p-C_2H_2 in this band come from the same part of the hot core. We derive an apparent ortho-to-para ratio (OPR) of 2.1±0.3, and this will be discussed further in section 3.5.2. The ortho- lines are seen up to higher J level, which is reflected in the rotation diagram.

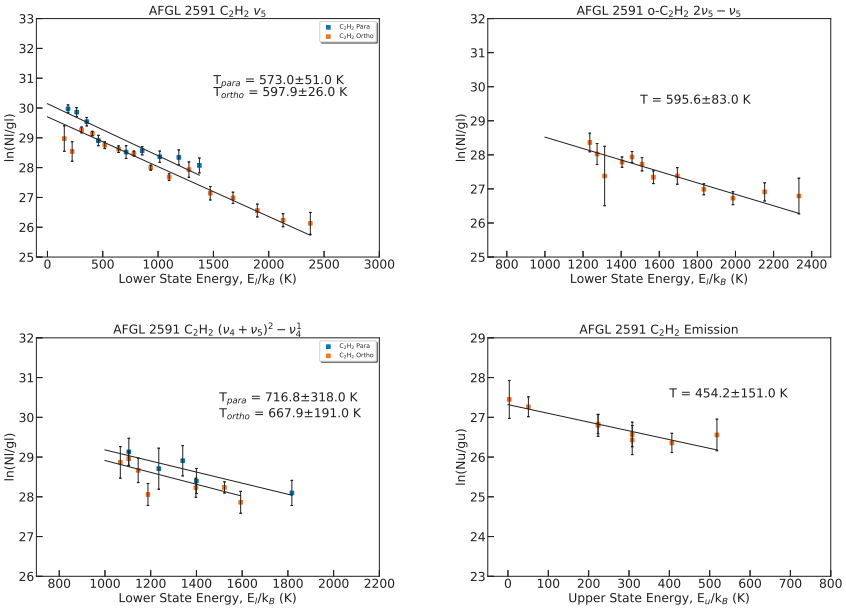

Figure 3.7: Acetylene rotation diagrams for the C_2H_2 bands detected in AFGL 2591 with TEXES. Ortho- and Para-C_2H_2 states are split into their corresponding ladders, and are shown as orange and blue respectively. The rotational temperatures for each are also given.

Two vibrationally excited bands of C_2H_2 are marginally detected in AFGL 2591, the $(\nu_4+\nu_5)^2-\nu_4^1$ and the $2\nu_5^2-\nu_5^1$ band, probing the ν_4 and ν_5 levels respectively. The rotation diagrams are shown in Figure 3.7. For the $(\nu_4+\nu_5)^2-\nu_4^1$ band, the line widths of p-C_2H_2 and o-C_2H_2 agree well however the velocity of p-C_2H_2 is slightly lower than o-C_2H_2. The parameters derived for this band have a large uncertainty due to the weakness of the lines.

For the vibrationally excited $2\nu_5-\nu_5$ band, we only observe o-C_2H_2 lines. We derive a rotational temperature of 596 K, in good agreement with the rotational temperature for the ν_5 band. The line profiles of this vibrationally excited band are consistent with those of the ν_5 fundamental band.

The $\nu_2+(\nu_4+\nu_5)$ band of C_2H_2 was detected in emission in the L-band towards AFGL 2591. The lines are narrower than the other C_2H_2 lines we observe in absorption by 4 km s^{-1}. Also, the velocity is clearly offset from the v_{lsr} of other species. The rotation diagram is shown in Figure 3.7. The rotation diagram gives a temperature of 454±151 K. Only o-C_2H_2 is detected in emission as the p-C_2H_2 lines are too weak.

The blended Q-branch of hot C_2H_2 has been detected in AFGL 2591 with ISO-SWS Lahuis & van Dishoeck (2000). The derived excitation temperature (900 K) is higher than what we observe with TEXES (Table 3.2). This may reflect the limited spectral resolution of ISO-SWS - hampering extraction of physical conditions from this blended line - and the severe fringing inherent to this instrument.

NH_3

For NH_3, we also treat ortho- and para- states as separate molecular species. We also take different partition functions as in the case for C_2H_2. For NH_3 the ortho states have K as a multiple of 3, and the para states have K=3n±1. The statistical weights of the o-NH_3 lines are a factor of 2 higher than the p-NH_3 lines (Šimečková et al. 2006). Since there are twice as many options for J for para states, this results in an equal number of ortho and para molecules. Thus we implement the partition functions as Q(ortho) = Q(para) = Q/2, where Q is the partition function for NH_3 given in HITRAN. For NH_3 the value of the OPR for high temperatures is equal to 1 (Faure et al. 2013).

For AFGL 2591, NH_3 is harder to detect than in AFGL 2136. This reflects the poorer data quality due to fringing and lower signal to noise. AFGL 2136 was observed with TEXES on Gemini and used Orion BN as a standard star to improve atmospheric and standing wave correction, while AFGL 2591 was observed with the IRTF without a standard star. Since the temperature that we measure for NH_3 gas is hotter than in AFGL 2136, the energy spreads out over more, weaker transitions. Then, since the column densities of NH_3 derived for the two sources are the same, the lines in AFGL 2591 will be weaker than those in AFGL 2136.

Both o-NH_3 and p-NH_3 lines are detected in the v_2=0-1 transition of the ν_2 band. The peak velocities are in agreement, however the line width of o-NH_3 is almost twice as large as p-NH_3. Temperatures are in agreement and a high temperature of around 875 K is derived. An OPR=1±0.4 is found for AFGL 2591, consistent with the high rotational temperature. The rotation diagram is shown in Figure 3.8.

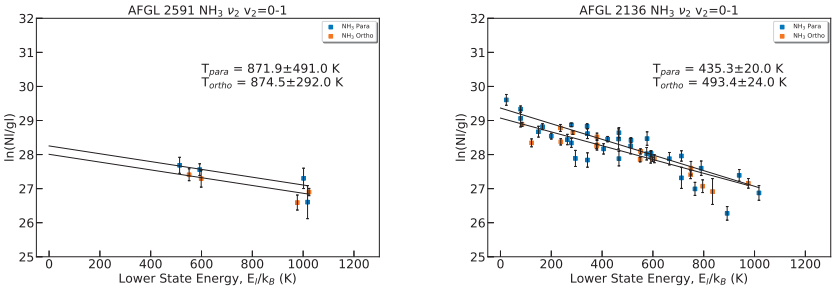

Figure 3.8: Rotation diagrams of the v_2=0-1 transition in the ν_2 band of NH_3 in AFGL 2591 and AFGL 2136 detected with TEXES. Both ortho- and para- states are detected and they are plotted in orange and blue respectively.

3.4.2 AFGL 2136

CO

AFGL 2136 shows a much simpler morphology compared to AFGL 2591, with only two velocity components of CO observed, which correspond to two separate physical components. For ^{13}CO, one velocity component is detected at 22.3±0.2 km s^{-1}

with a line width of 3.4±0.7 km s^{-1}. This velocity component is superimposed on a broader underlying velocity component centred at 26.5±0.3 km s^{-1}, which has a width of 13.2±0.9 km s^{-1}. In $C^{18}O$, the narrow and broad velocity components are also observed, with line widths and velocities consistent with ^{13}CO. ^{12}CO v=0-1 lines are saturated for $J \lesssim 6$.

Separate rotation diagrams are made for each velocity component. Figure 3.10 shows the rotation diagrams for the broad component seen in ^{12}CO, ^{13}CO and $C^{18}O$ plotted in the same panel. The four lines in the ^{12}CO v=0-1 rotation diagram between 1000 and 3000 K are overestimated since they are difficult to disentangle from the component at 22 km s^{-1}. For ^{12}CO v=0-1, the transitions are optically thick since the optical depth at line centre is > 1.

This is also the case for ^{13}CO, where low J lines of ^{13}CO and ^{12}CO overlap in the rotation diagram. For $E_l > 500$ K the ^{12}CO and ^{13}CO rotation diagrams start to separate, however the higher J lines for ^{13}CO remain to have an optical depth above 2/3.

As a result of this, we instead focus on the $C^{18}O$ transitions which are optically thin, and the fits to the $C^{18}O$ lines are shown in Figure 3.9. Comparing the line profiles between high and low J in $C^{18}O$ (Fig 3.10) the broad component centred on the red dashed line is present from low to high J, whilst the narrow component is present only at low J. This is a result of the fact that the two velocity components are also distinct in temperature, with the broad and narrow velocity components being hot and cold respectively. This distinction is seen also in ^{12}CO and ^{13}CO. Therefore the two velocity components trace different physical components. The focus of the rest of this article will be the broad component at 26 km s^{-1}, the line parameters of which are presented in Table 3.5.

$C^{18}O$ exhibits a straight line which suggests that the transitions are optically thin and that local thermodynamic equilibrium (LTE) is a good approximation. A temperature of 27±2 K and 440±15 K is derived for the cold and hot component, respectively. In the rotation diagram, several of the low J level lines in $C^{18}O$ appear overproduced. This is a result of blending between the 22 km s^{-1} and 26 km s^{-1} velocity components which are difficult to disentangle since they are only separated by a small amount in velocity space, whereas for the higher energy lines, the narrow cold component at 22 km s^{-1} is not observed. Therefore these lines give a better handle on the real temperature of the gas.

26 lines of vibrationally excited ^{12}CO are also detected in AFGL 2136, and are presented in Figure 3.9. The transitions show a single velocity component at 27.1±0.3 km s^{-1} with a width of 12.1±0.7 km s^{-1}. This is in good agreement with hot $C^{18}O$. From Figure 3.10 we see that the rotation diagram is a straight line implying that the lines are optically thin and in LTE, with a rotational temperature of 661±9 K. We derive a vibrational temperature of 490±39 K.

The velocity derived from our observations of the hot CO component at 26 km s^{-1} is in agreement with what is found by Mitchell et al. (1990) for the v=0-1 band. They do not resolve the two velocity components in the CO line profiles. Therefore they fit two temperature components at the same velocity in the rotation diagram. The temperature of their hot component is consistent with what we find for fitting the ^{13}CO lines with E_l above 100 K. The temperature that we derive for the narrow

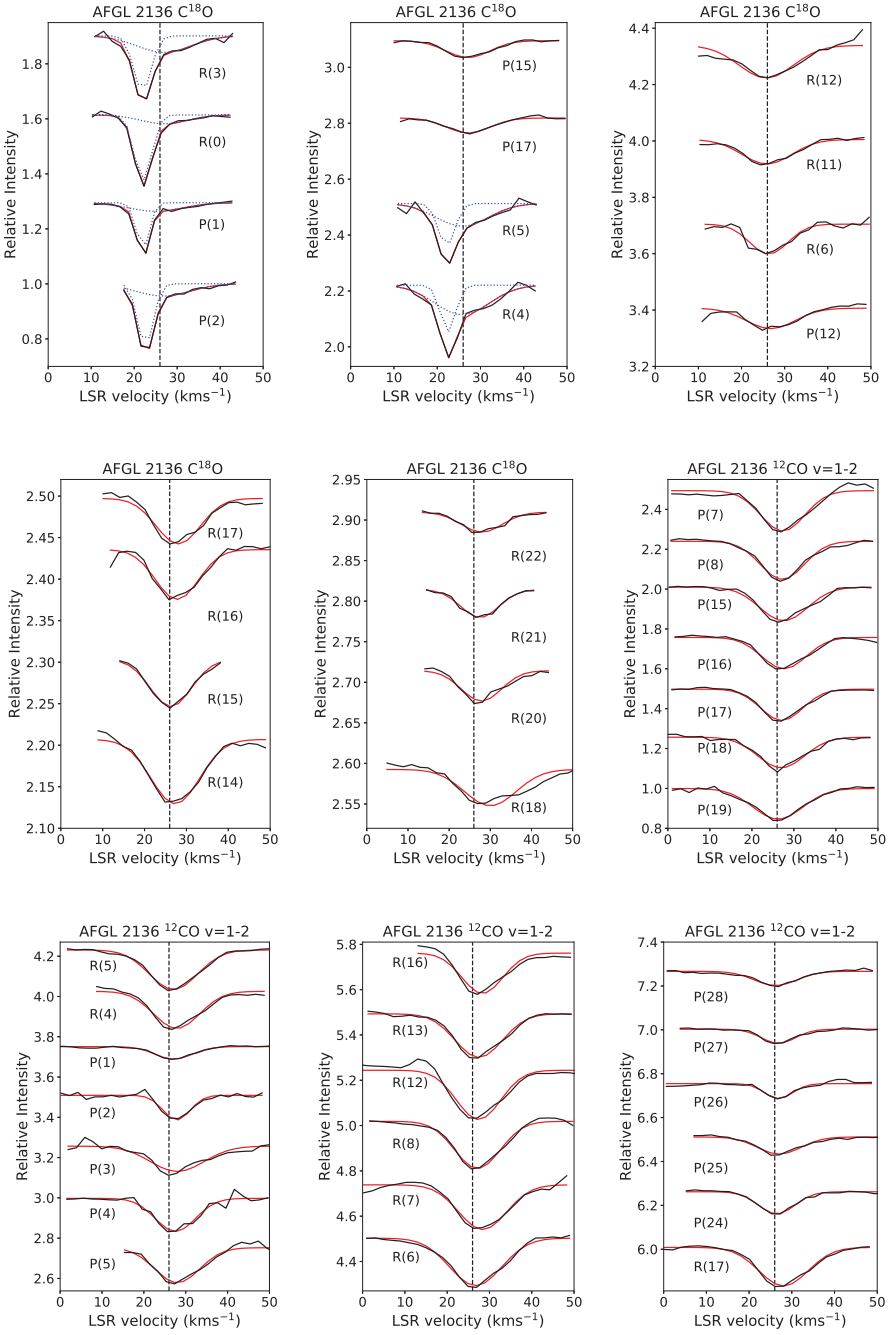

Figure 3.9: Multi-gaussian fitting of $C^{18}O$ v=0-1 and ^{12}CO v=1-2 line profiles in AFGL 2136 detected with iSHELL at 4.5 μm. The dashed line represents 27 km s^{-1}. The overall fit is shown in red and the individual gaussian components are in blue dotted lines.

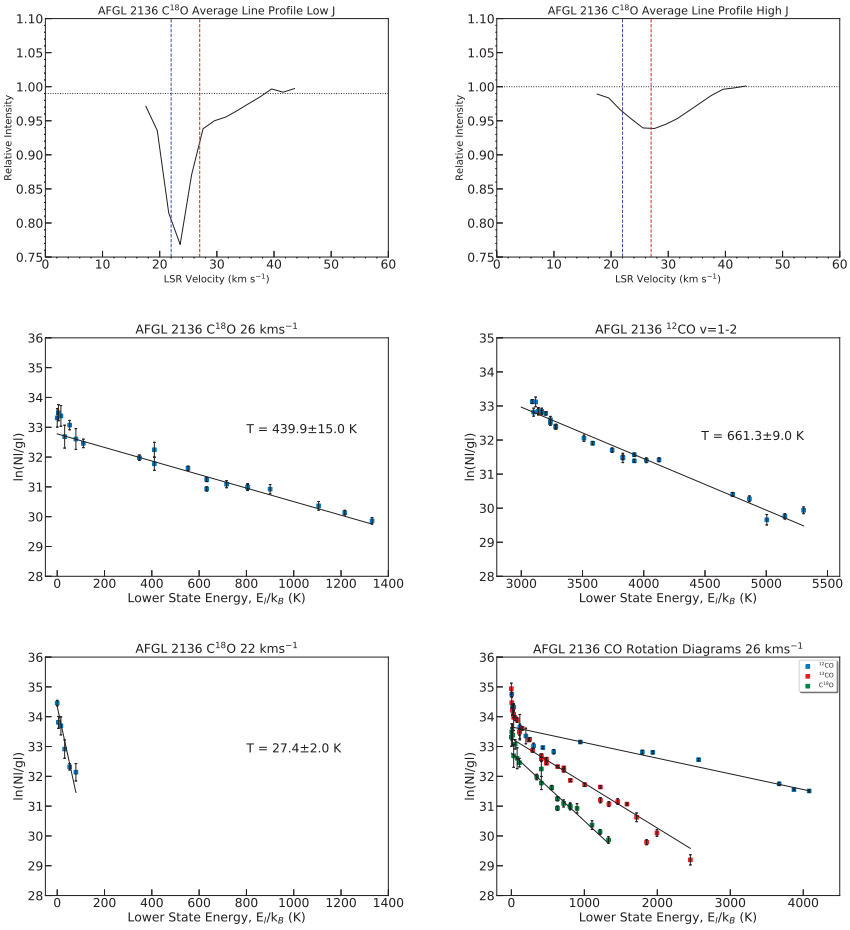

Figure 3.10: $C^{18}O$ v=0-1 rotation diagrams and average line profiles for high and low J, along with the rotation diagram for ^{12}CO v=1-2 in AFGL 2136. An additional plot for the hot component in AFGL 2136 is shown with ^{12}CO v=0-1, ^{13}CO v=0-1 and $C^{18}O$ v=0-1 rotation diagrams plotted on the same panel. Blue and red dashed lines correspond to the systemic velocity of the source and velocity of IR observations, respectively, which are 22 and 27 km s^{-1}, respectively. The black dotted line denotes the continuum level

component at 22 km s^{-1} is higher than the temperature that they derive for their cold component. Mitchell et al. (1990) neglect the ^{12}CO v=0-1 transitions as they are strongly saturated and they do not discuss $C^{18}O$ as it was not detected.

The two velocity components are also observed in the CO v=0-2 band at 2.3-2.4 μm (Goto et al. 2019). The temperatures for the hot component are in agreement within the errors, however for the cold component, Goto et al. (2019) measure a temperature of 16.3±2.4 K while we derive a temperature of 27±2 K for the v=0-1 band. This may be a result of uncertainty in disentangling the two velocity components since they are heavily blended. It is difficult to gauge whether or not the single gaussian

fit to the 26 km s^{-1} component that we use is adequate for deriving state-specific column densities (Figs 3.10 & 3.9). This can be further seen from the line profiles of the CO v=0-2 band, where Goto et al. (2019) fit two velocity components to the hot CO component. In this case the high J CO lines may be doubly peaked as well, which is also true for the H_2O lines at 2.5 μm in this source (Indriolo et al. 2020).

CS

13 lines of CS are detected towards AFGL 2136 spanning an energy range of 7 to 1165 K. It is one of the species most readily detected in our spectra. One velocity component is detected at 26.1±0.4 km s^{-1} with a line width of 8.0±1.1 km s^{-1}. All lines are accounted for from J=2 to J=31 with non-detected lines being lost in strong telluric absorption or blending with other hot core lines. The CS velocity is consistent with that derived in CO, however the line width is narrower for equivalent energy levels.

Temperatures and column densities for CS are derived from the rotation diagram shown in Figure 3.5. A temperature of 418±23 K is measured, in good agreement with the temperature found for $C^{18}O$.

HCN

For AFGL 2136, 15 lines of the ν_2 band in the v_2=0-1 transition are detected spanning an energy range of only 1500 K. The rotation diagram gives a temperature of 625±19 K. 26 lines of HCN of the ν_2 band in the v_2=0-2 transition are detected in AFGL 2136. The linear part of the rotation diagram gives a temperature of 605±96 K. This is in good agreement with the temperature of the v_2=0-1 transition of HCN. The column density derived for the v_2=0-2 transition is a factor of 4 larger than the v_2=0-1 transition. The line profiles for the v_2=0-1 and v_2=0-2 transition are similar in AFGL 2136.

As for AFGL 2591, evidence for a temperature gradient is observed in the v_2=0-2 transition of HCN while it is not seen in the v_2=0-1 transition. The line profiles in the v_2=0-2 transition are consistent from low to high J (Fig 3.2). As in AFGL 2591, the R(0) line of the HCN v_2=0-2 band is offset in velocity from the other HCN lines and appears to be tracing cold foreground absorption. (Lahuis & van Dishoeck 2000) detected HCN with ISO towards AFGL 2136 and the derived temperature of 650^{+75}_{-50} K agrees between low and high spectral resolution.

C_2H_2

For the ν_5 fundamental band of C_2H_2 in AFGL 2136, 16 lines are detected. The temperature and line profiles are consistent with the other species in this source suggesting that they are co-spatial in this hot core. We derive an apparent OPR of 1.8±0.2.

We also detect vibrationally excited C_2H_2 in AFGL 2136 and rotation diagrams are shown in Figure 3.11. Similar to AFGL 2591, we only observe o-C_2H_2 in the $2\nu_5^2 - \nu_5^1$ band. A temperature of 480±41 K is derived, slightly lower than the ν_5 band but within the errors.

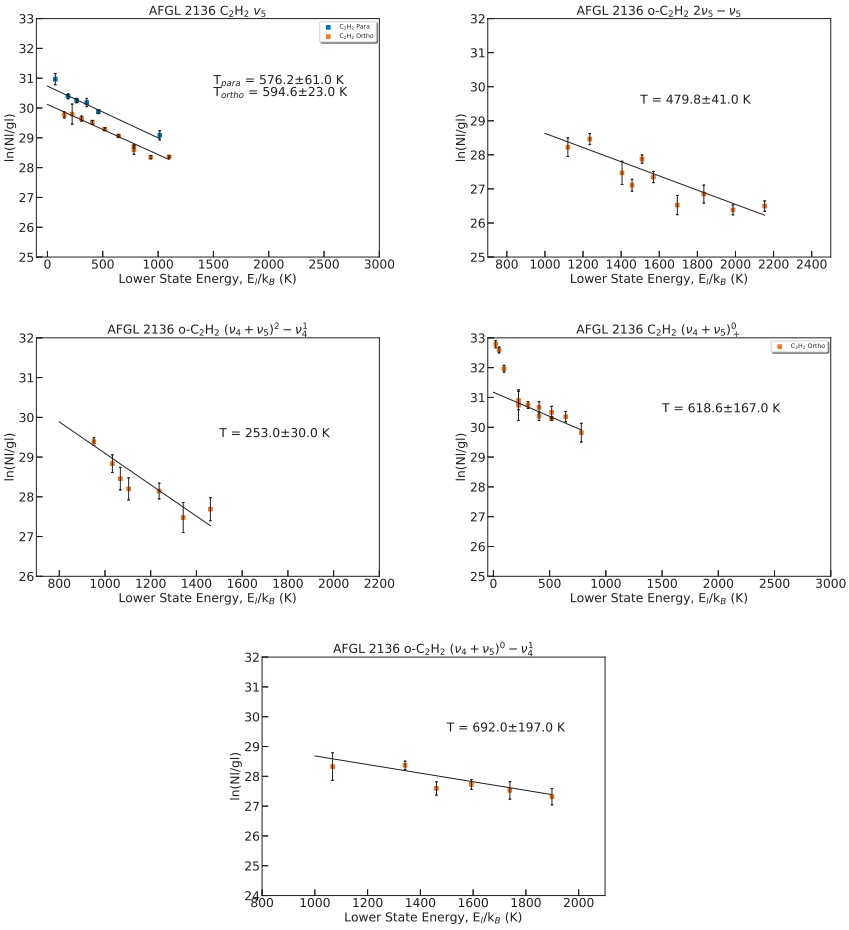

Figure 3.11: Acetylene rotation diagrams for the C_2H_2 bands detected in AFGL 2136 with TEXES. Ortho- and Para-C_2H_2 states are split into their corresponding ladders, and are shown as orange and blue respectively. The rotational temperatures for each are also given.

In AFGL 2136 we see an additional band, the $(\nu_4 + \nu_5)^0 - \nu_4^1$ band. The line parameters are consistent with the $(\nu_4 + \nu_5)^2 - \nu_4^1$ band of C_2H_2. The temperature of this band is comparable to the ν_5 band, with 692±197 K derived from the rotation diagram. The physical conditions derived from this band however are very uncertain.

In AFGL 2136, the $(\nu_4 + \nu_5)$ band of o-C_2H_2 is detected in the EXES data around 7 μm. A column density of $5.0\pm0.1\times10^{16}$ cm^{-2} is derived. This is a factor of 4 higher than expected based on the column density of the ν_5 band, despite the fact that these bands trace the same lower vibrational energy level. The temperature derived for the $(\nu_4 + \nu_5)$ band is measured only from the higher energy lines, since there is non-linearity for the low energy lines, analogous to HCN at 7 μm. The derived temperature is equivalent to that found for the ν_5 band. Similar behaviour is observed

in HCN and the difference of the column density between the 7 and 13 μm C_2H_2 is of the same order as that found for HCN in AFGL 2136 (a factor of 4). We expect that non-linearity is also present in the ν_5 band, however we do not observe to long enough wavelengths to observe this trend. However it does appear that the R(6e) line is slightly overproduced in the ν_5 band. The $(\nu_4 + \nu_5)$ band of C_2H_2 is observed in AFGL 2136, but not in AFGL 2591.

C_2H_2 has been detected in AFGL 2136 with ISO-SWS with a temperature of 800 K (Lahuis & van Dishoeck 2000), higher than what we observe with EXES/TEXES. This may be a reflection of the much lower spectral resolution of ISO-SWS and the fringing inherent to this instrument.

NH_3

Figure 3.8 shows the rotation diagram for the v_2=0-1 transition in the ν_2 band of NH_3 in AFGL 2136. Approximately 50 lines are detected including both ortho and para states and the transitions cover an energy level range of over 1000 K. p-NH_3 and o-NH_3 have peak velocities and line widths that are in agreement, however the temperature derived from the rotation diagrams are slightly different with the o-NH_3 being higher. An OPR of 1$\pm$0.5 is derived, consistent with the high rotational temperature. NH_3 in AFGL 2136 is a very good example of the power of this method to detect many lines by only observing a handful of spectral settings. Another band of NH_3, the ν_4 band at 6 μm is included in our spectral range, but no transitions were apparent, consistent with Indriolo et al. (2020).

Table 3.2: Summary of Species in AFGL 2591.

Species	Band	λ_0 (μm)	# Lines	Temperature (K)	N (cm^{-2})	Abundance (w.r.t H)	v_{lsr} (km s^{-1})	ΔV (km s^{-1})
^{13}CO	v=0-1	–	8	49 ±3	$3.8\pm0.2 \times 10^{16}$	$2.4\pm0.2 \times 10^{-6}$	-9.2±0.3	1.5
	v=0-1	–	8	671 ±124	$3.4\pm0.2 \times 10^{16}$	$2.8\pm1.0 \times 10^{-6}$	-12.0±0.6	10.5
^{12}CO	v=1-2	4.7	8	664 ±43	$1.5\pm0.6 \times 10^{16}$	$1.2\pm0.4 \times 10^{-6}$	-8.4±0.5	16.4±1.6
H_2O	ν_2 v_2=0-1	6.0	8	[a] 640 ± 80	[a] $3.7\pm0.8 \times 10^{18}$	–	-11.0	12.4
HCN	ν_2 v_2=0-2	7.0	16	671 ± 118	$2.4\pm0.2 \times 10^{17}$	$2.0\pm1.0 \times 10^{-5}$	-11.7±0.5	10.8±1.3
	ν_2 v_2=0-1	14.0	20	675 ±32	$2.7\pm0.2 \times 10^{16}$	$3.4\pm0.6 \times 10^{-6}$	-8.9±0.5	8.2±1.3
	ν_1 v=1-0	3.0	21	240±13	$7.9\pm0.5 \times 10^{15}$	–	-9.6±0.5	6.3±1.0
CS	v=0-1	7.8	18	713 ± 59	$1.6\pm0.1 \times 10^{16}$	$1.5\pm0.3 \times 10^{-6}$	-10.4±0.5	8.4±1.7
p-C_2H_2	ν_5	13.7	9	573±51	$4.8\pm0.5 \times 10^{15}$	$5.8\pm2.3 \times 10^{-7}$	-8.8±0.4	7.7±1.1
	$(\nu_4+\nu_5)^2-\nu_4^1$	13.7	5	717±318	$4.2\pm3.8 \times 10^{15}$	$4.9\pm4.4 \times 10^{-7}$	-9.6±0.9	8.8±2.5
o-C_2H_2	ν_5	13.7	15	598±26	$1.0\pm0.1 \times 10^{16}$	$1.2\pm2.3 \times 10^{-6}$	-9.0±0.4	8.7±1.1
	$2\nu_5^2$ - ν_5^1	13.7	12	596±83	$2.7\pm0.4 \times 10^{15}$	$3.5\pm1.5 \times 10^{-7}$	-8.7±0.6	8.3±1.8
	$(\nu_4+\nu_5)^2-\nu_4^1$	13.7	7	668±191	$7.7\pm6.9 \times 10^{15}$	$1.0\pm0.9\times10^{-6}$	-7.7±0.5	7.4±1.4
	$\nu_2+(\nu_4+\nu_5)$	3.0	8	454±151	$6.0\pm0.9 \times 10^{15}$	–	-7.4±0.5	3.7±1.2
p-NH_3	ν_2 v_2=0-1	9.5	4	872±491	$1.3\pm0.7 \times 10^{16}$	$1.6\pm0.9 \times 10^{-6}$	-6.9±0.6	6.2±1.5
o-NH_3	ν_2 v_2=0-1	9.5	4	875±292	$1.0\pm0.4 \times 10^{16}$	$1.4\pm0.5 \times 10^{-6}$	-7.3±0.4	7.8±1.1

No abundances relative to H are given for H_2O because stellar atmosphere theory is not used in the analysis of Indriolo et al. (2015a).

No abundances for the HCN ν_1 and C_2H_2 $\nu_2+(\nu_4+\nu_5)$ emission bands are given since we measure column densities for these bands which are given in section 3.5.3.

[a] (Indriolo et al. 2015a)

Table 3.3: Summary of Species in AFGL 2136.

Species	Band	λ_0 (μm)	# Lines	Temperature (K)	N (cm^{-2})	Abundance (w.r.t H)	v_{lsr} (km s^{-1})	ΔV (km s^{-1})
$C^{18}O$	v=0-1	–	6	27± 2	$8.7\pm0.7 \times 10^{15}$	$2.8\pm0.1 \times 10^{-6}$	22.2±0.3	2±0.8
	v=0-1	–	20	440± 15	$2.9\pm0.2 \times 10^{16}$	$1.9\pm0.1 \times 10^{-6}$	27.1±0.6	12.3±1.5
^{12}CO	v=1-2	4.7	26	661±9	$2.7\pm0.2 \times 10^{16}$	$1.7\pm0.4 \times 10^{-6}$	27.1±0.3	12.1±0.7
H_2O	ν_1 / ν_3	2.5	34	[a]502 ± 12	[a]$8.25\pm0.95\times10^{18}$	–	24.6±1.1	13.2±2.5
HCN	ν_2 v$_2$=0-2	7.0	18	592 ± 21	$1.8\pm0.2 \times 10^{17}$	$1.6\pm0.8 \times 10^{-5}$	26.2±0.5	8.5±1.6
	ν_2 v$_2$=0-1	14.0	15	625±19	$4.6\pm0.2 \times 10^{16}$	$5.3\pm0.4 \times 10^{-6}$	26.1±0.5	11.0±1.5
CS	v=0-1	7.8	13	418 ± 23	$1.6\pm0.1 \times 10^{16}$	$1.2\pm0.1 \times 10^{-6}$	26.1±0.4	8.0±1.1
p-C_2H_2	ν_5	13.7	6	576±61	$8.8\pm0.7 \times 10^{15}$	$1.0\pm0.4 \times 10^{-6}$	27.0±0.3	10.9±1.1
o-C_2H_2	ν_5	13.7	10	595±23	$1.6\pm0.1 \times 10^{16}$	$1.7\pm0.1 \times 10^{-6}$	27.2±0.3	11.3±0.9
	$2\nu_5^2$ - ν_5^1	13.7	10	480±41	$1.6\pm1.0 \times 10^{15}$	$2.3\pm0.1 \times 10^{-7}$	26.6±0.4	7.1±1.2
	$(\nu_4+\nu_5)^2-\nu_4^1$	13.7	7	253±30	$1.7\pm1.5 \times 10^{15}$	$1.3\pm1.3 \times 10^{-7}$	26.9±0.6	8.1±1.8
	$(\nu_4+\nu_5)^0-\nu_4^1$	13.7	6	692±197	$2.1\pm0.2 \times 10^{15}$	$2.3\pm2.0 \times 10^{-7}$	26.8±0.6	8.5±1.9
	$(\nu_4+\nu_5)$	7.5	12	618±176	$5.0\pm0.1 \times 10^{16}$	$7.0\pm0.8 \times 10^{-6}$	26.0±0.5	8.0±1.5
p-NH_3	ν_2 v$_2$=0-1	9.5	32	435±20	$1.0\pm0.5 \times 10^{16}$	$1.0\pm0.1 \times 10^{-6}$	28.1±0.4	6.7±1.0
o-NH_3	ν_2 v$_2$=0-1	9.5	17	493±24	$0.9\pm0.4 \times 10^{15}$	$9.7\pm0.5 \times 10^{-7}$	27.7±0.3	7.7±0.9

No abundances relative to H are given for H_2O because stellar atmosphere theory is not used in the analysis of Indriolo et al. (2020).

[a] Indriolo et al. (2020)

3.4.3 Comparison to Sub-millimetre Observations

Absorption lines at IR wavelengths probe the hot core on very small spatial scales, comparable to the smallest achievable by sub-mm emission line studies (0.02″). On scales as large as 10″, differences in line widths, peak velocities, temperatures and column densities are observed between sub-mm emission and IR absorption studies. This is summarised in Figure 3.12, where we compare the results from our MIR line survey of AFGL 2591 with a line survey by Kaźmierczak-Barthel et al. (2014) from 480-1900 GHz (with respective beam sizes 10-40 ″), with *Herschel*/HIFI.

Temperatures compare on average with 700 K for IR absorption to 50 K in sub-mm emission. The temperature derived from the emission lines corresponds well with the temperature of the cold ^{13}CO absorption component (Table 3.2). For AFGL 2591 the velocity of the sub-mm emission lines agrees with the systemic velocity and is on average -5.5 km s^{-1}, consistent with other studies of this source in the sub-mm (Wang et al. 2012; Gieser et al. 2019; van der Tak et al. 2003). However from the IR absorption lines the velocity observed is -10 km s^{-1}. Furthermore the line widths of the absorption lines are around a factor of 2 higher than those measured in the sub-mm.

Towards AFGL 2591, 6 lines of HCN were detected in emission and a population diagram results in an estimate of the temperature of 35 K (Kaźmierczak-Barthel et al. 2014). In total, we detect 42 lines of HCN from 2 different transitions in the IR spanning an energy range of 0 to 2500 K in AFGL 2591. The large number of lines combined with the large span in energy range gives a good handle on the physical conditions and a temperature of 670 K is derived, although the possibility of a temperature gradient is apparent from the rotation diagram.

Boonman et al. (2001) however, detected emission from the high energy J=9-8 rotational lines of the $\nu_2 = 0$ and $\nu_2 = 1$ levels of HCN in AFGL 2591, with the James Clerk Maxwell Telescope (JCMT). They found a well constrained temperature of 720^{+135}_{-100} K which agreed well with that of Lahuis & van Dishoeck (2000), as well as with what we derive for AFGL 2591 in absorption, suggesting that sub-mm observations of high J level transitions also probe the same region observed by infrared absorption lines. Our high spectral resolution observations allow us also to compare line profiles with the high J sub-mm lines, and we find that the line widths are a factor of 2 lower than the IR absorption lines. Also the peak velocity of the sub-mm lines are at the systemic velocity, whereas the IR absorption lines are shifted to the blue by 5 km s^{-1}. This implies that this hot gas seen with J=9-8 lines is concentrated very close to the protostar, as it can only be detected via high J level transitions, whereas lower J lines are more spatially extended measuring a lower temperature (Wang et al. 2012; Gieser et al. 2019). However IR absorption lines are potentially probing a different region of this high temperature, high abundance region.

Although not many species have been detected towards AFGL 2136 at sub-mm wavelengths, CS has been detected by van der Tak et al. (2003). A velocity of 22.8 km s^{-1} and a line width of 3.1 km s^{-1} are derived for sub-mm emission lines. This contrasts with the IR absorption where we derive a v_{lsr} of 26.1 km s^{-1} and a width of 8 km s^{-1}. This is consistent with the two velocity components we see in CO presented in section 3.4.2 From a rotation diagram analysis we see that the narrow 22 km s^{-1}

component is cold while the broad 26 km s^{-1} component is hot.

As mentioned in section 3.4.2, IR CO line profiles of AFGL 2136 reveal two velocity components in the same line of sight (Figure 3.10); a cold component with narrow lines centred at 22 km s^{-1} and a hot component with broad lines centred at 26 km s^{-1}. Maud et al. (2018) observed this source with the Atacam Large Millimetre Array (ALMA) and detected an unresolved disk-like structure in SiO and dust continuum, at 22 km s^{-1}. SiO emission is observed to be spatially extended at 22 km s^{-1}, which is the systemic velocity of the cloud as derived from previous sub-mm observations (van der Tak et al. 2003), suggesting that the velocity component we detect in the IR at 26 km s^{-1} is not spatially resolved by Maud et al. (2018).

However, recent very high angular resolution (20×15 mas) observations with ALMA by Maud et al. (2019) reveal that sub-mm observations can resolve this velocity component if the spatial resolution is high enough. Velocity maps of the H_2O $5_{5,0} - 6_{4,3}$ $\nu_2 = 1$ line show that a Keplerian disk is resolved which is centred at a velocity of 26 km s^{-1}. Furthermore, since this line lies 3461 K above ground, this gas must be hotter than the temperature estimates given by previous sub-mm studies, which is more consistent with the IR absorption lines.

A recent study of AFGL 2591, (Gieser et al. 2019) analyses chemical complexity in this hot core. The pure rotational CO J=2-1 line profile that is presented in their Figure 7 shows a complex velocity structure, analogous to that which we see in IR absorption. There is a broad, blue-shifted part of the line profile that appears to consist of several velocity components, one of which is centred around -10 km s^{-1}. There is also tentative evidence for this same velocity component being present in the emission line profile of SiO, however the other more blue-shifted velocity components are missing. This further indicates that it is possible to resolve in emission this inner part of the hot core that is so evident in IR absorption.

Overall, IR observations trace hot, dense gas at the centre of the hot core. Sub-mm observations, unless at very high angular resolution ($0.02''$), probe the surrounding envelope and cloud where temperatures are lower.

3.5 Discussion

Summarising the observations presented in Section 3.4, MIR spectra of AFGL 2136 and 2591 show absorption bands of a number of molecular species, which can be analysed in terms of the velocity and temperature of the absorbing gases. There are a number of differences between IR and sub-mm wavelengths that provide further insight into the structure of these sources. The IR lines are typically seen in absorption and the sub-mm lines in emission, there is a peak velocity offset (Fig 3.12), and the line width is typically much larger (Fig 3.12) in the IR than in the sub-mm (van der Tak et al. 2003; Kaźmierczak-Barthel et al. 2014; Gieser et al. 2019). In addition, the IR lines originate from gas that is typically much warmer (400-600 K) than the sub-mm lines (20-200 K).

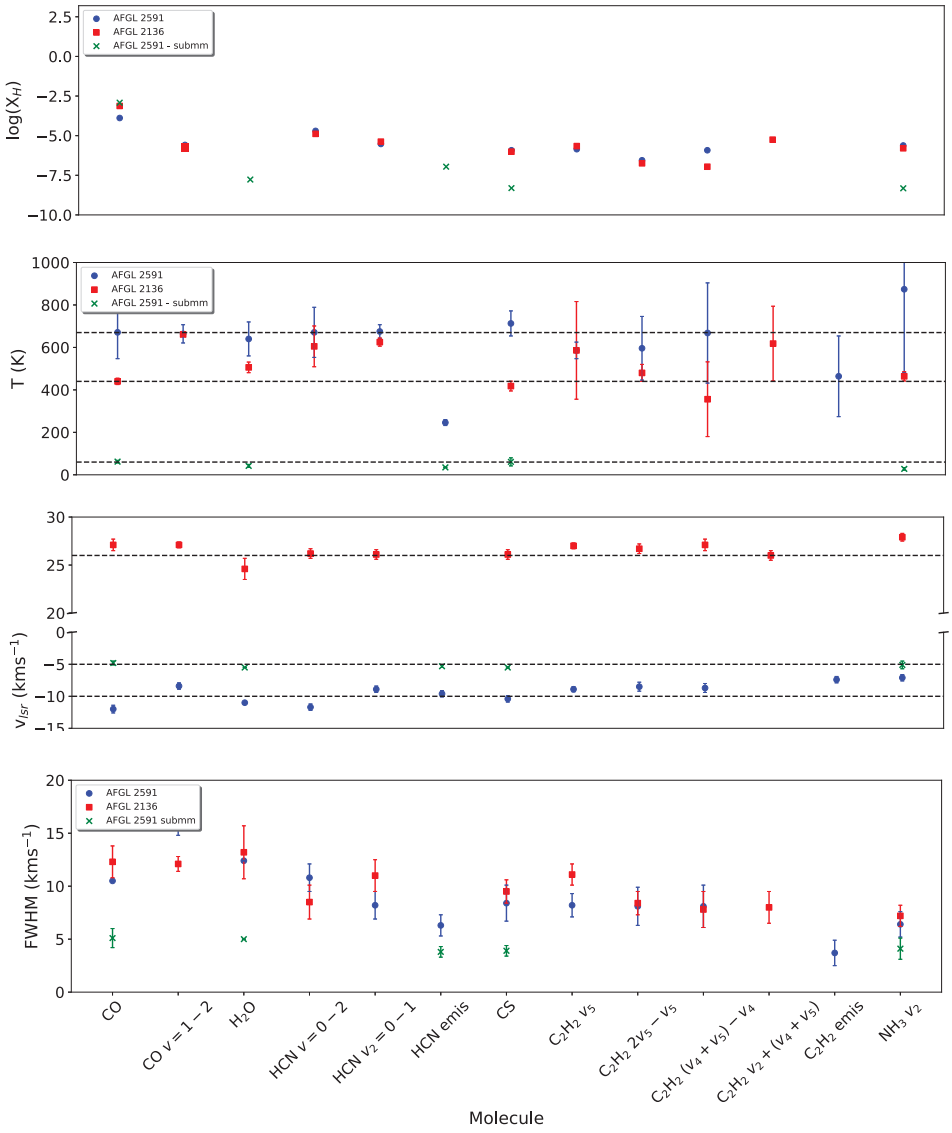

Figure 3.12: Scatter plots comparing the temperature, abundance w.r.t H, velocity and line width of selected molecules observed towards AFGL 2591 (blue circles) and AFGL 2136 (red squares), and also the literature values for AFGL 2591 (green crosses) observed in the sub-mm (Kaźmierczak-Barthel et al. 2014). For the sub-mm abundances, a H column of $\sim 1 \times 10^{22}$ cm^{-2} was assumed following Kaźmierczak-Barthel et al. (2014).

3.5.1 General Structure of the Sources

Very high angular resolution observations of AFGL 2136 in the N band with the mid-infrared interferometer (MIDI) instrument on the Very Large Telescope Interferometer (VLTI), H and K band polarisation studies with the Subaru telescope, sparse aperture Keck interferometry and sub-mm dust emission with ALMA reveal the presence of a geometrically thin circumstellar dust disk with an inner and outer radius of 30 and 120 AU respectively (Murakawa et al. 2008; Monnier et al. 2009; de Wit et al. 2011; Boley et al. 2013; Maud et al. 2019). The whole system is embedded in a dusty envelope. The circumstellar disk is optically thick in the MIR continuum and the N-band emission originates from a radius of ∼100 AU. Inside the dust sublimation radius (≤30 AU), the disk is thought to be gaseous. Recent ALMA observations at high spatial resolution in a highly excited H_2O line (E_u=3461.9 K) reveal the presence of a disk in Keplerian rotation around the central ∼45 $M_\odot$ protostar (Maud et al. 2019). The total disk mass, estimated from the sub-mm continuum, is somewhat sensitive to the adopted temperature but is of the order of 1 $M_\odot$ (Maud et al. 2019).

Both AFGL 2136 and AFGL 2591 have been imaged at 10.7 μm with the Keck telescope (Monnier et al. 2009). The physical structure of both of these sources is very similar at this wavelength. The MIR continuum is asymmetrically extended to the West around the disk, out to around 250 mas. However, the extended emission is an order of magnitude lower in intensity than the continuum emission from the compact disk. For AFGL 2136, the FWHM size of the MIR continuum is 125±5×115±3 mas for the major and minor axes, respectively. This is reasonably consistent with the size of the disk in the ALMA 1.3 mm continuum image, 93×71 mas for the major and minor axes, respectively. This 25 % difference in size, and the somewhat flatter disk seen in the ALMA image, could be due to the fact that at 10 μm the observer looks less deep into the disk than at sub-mm wavelengths, making it appear more spherical and extended at 10 μm. The size of the MIR continuum in AFGL 2591 is 123±3×111±3 mas for the major and minor axes, respectively. Since the MIR continuum is dominated by the disk, we neglect envelope emission contributing to the continuum of our absorption lines.

At MIR wavelengths, both sources are characterised by extended emission incommensurate with the central protostar. The ALMA observations of AFGL 2136 reveal that the MIR emission coincides with a circumstellar disk in Keplerian rotation. In the following, we presume that this is also the case for AFGL 2591 and will discuss this more in section 3.5.6 As the MIR continuum emission is dominated by the disk, the absorption lines have to originate in the photosphere of this disk.

For AFGL 2136, the observed peak velocity of the IR absorption lines is in good agreement with that of the H_2O sub-mm emission line which clearly associates the absorbing gas within the disk (rather than the surrounding envelope or molecular cloud in which the source is embedded). The observed high temperatures also argue for a location in the inner warm regions. The line width of the CO, HCN, C_2H_2 and NH_3 IR absorption lines are narrower than that of the H_2O sub mm emission line. This is also the case for H_2O absorption (Indriolo et al. 2020). Absorption may still be associated with the Keplerian disk if the absorption does not trace the full extent of the disk. This will be discussed in more detail in section 3.5.6.

The fact that the lines are in absorption implies that the disk surface behaves like a photosphere with a temperature which decreases outwards. Hence, rather than heating of the disk surface from the outside by impinging stellar (UV/visible) radiation, the disk is heated from the inside, and radiative diffusion sets up a temperature gradient decreasing outwards in the radial and vertical directions. We attribute the heating to rapid accretion in the mid-plane, which viscously heats the gas to high temperatures.

At the high densities of the disk, the dust and gas temperature will be closely coupled in this situation. Models for viscous disks imply a radial temperature gradient with an exponent in the range of -0.4 to -0.7 (Dullemond et al. 2007). Following the N-band continuum studies, we set the temperature of the dust disk photosphere to the sublimation temperature (1200 K) at 30 AU, which implies a dust temperature at 120 AU of 450 K. Hence, the disk would indeed be bright in mid-IR continuum and, given the much larger surface area, would outshine the dust photosphere of the protostellar cocoon.

As sketched in Figure 3.13, the observed spectrum will originate from "characteristic" regions in the disk, with shorter wavelengths coming from the inner regions and longer wavelengths predominantly from further out. For any region in the disk, at any wavelength, the observed flux will originate from a total optical depth $(\tau_L + \tau_c) = 2/3$, where τ_L and τ_c are the line and continuum optical depth respectively. The decreasing temperature towards the surface will then lead to an absorption line.

3.5.2 Abundance Analysis

Since we are dealing with an internally heated disk, and therefore an outwardly decreasing temperature gradient in the vertical direction, some further insight into the characteristics of these disks can be obtained by standard stellar atmosphere analysis of absorption lines. We will base this analysis on the radiative transfer equation in the grey approximation, $\kappa(\nu) =$ constant. It is likely that the dust has coagulated either during the preceding molecular cloud phase or in the disk and will have a grey-like opacity (Ormel et al. 2011). Using the Milne-Eddington solution to the equation of radiative transfer in a grey atmosphere applied to line formation (Mihalas 1978), the observed flux at any wavelength will originate from a total optical depth $(\tau_L + \tau_c) = 2/3$. This assumes an average over viewing angles through the atmosphere. The outward-decreasing temperature gradient will then give rise to an absorption line and, comparing absorption by different species, lines tend to be stronger when the line opacity is larger. The full details of the derivation of the Milne-Eddington solution, along with further information, can be found in the Appendix section 3.A.

We conclude that for a weak line (relative to the continuum), the central depth (or equivalent width) is a measure of the relative column density in the lower level of the molecule. One important conclusion is then that the measured central depths can still be used in a Boltzmann diagram analysis, and the excitation temperatures used from the initial rotation diagram analysis still applies. The column density is relative to the continuum opacity, which itself is a measure of the hydrogen column density (and the dust absorption properties). In this way the line strength is a measure of the abundance with respect to H of the molecular levels, which can be used in a rotation

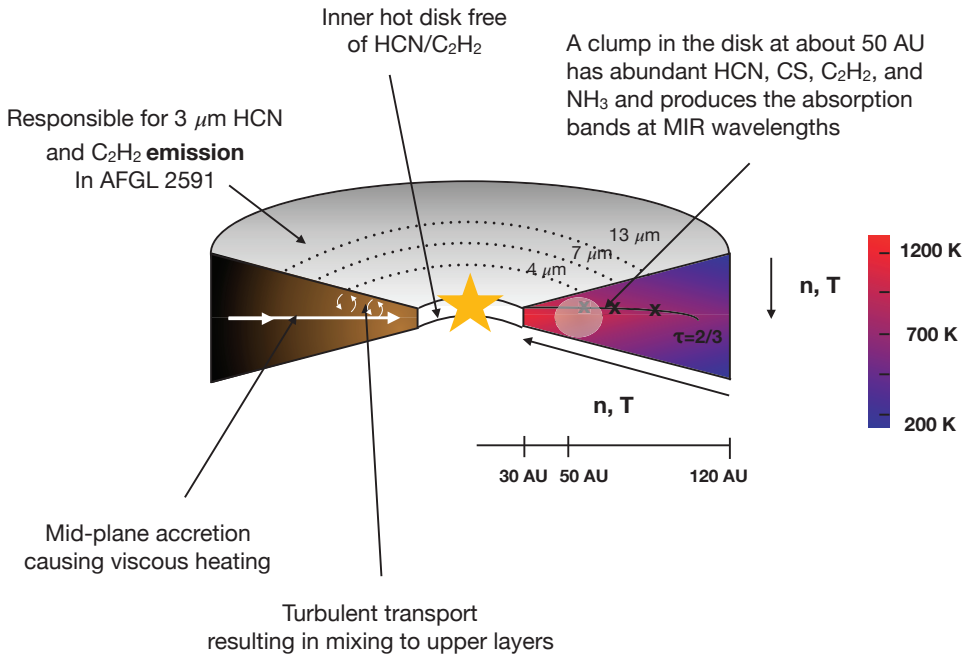

Figure 3.13: Slice of the disk showing the structure of the disk and the physical processes taking place. Dotted lines represent the extent of the disk at the $\tau = 2/3$ dust photospheres at 4, 7 and 13 μm. The black solid line indicates the $\tau = 2/3$ optical depth profile through the disk with wavelength, where crosses indicate the wavelength corresponding to the dotted lines. The blue/red colour scheme shows the temperature of the disk and is represented by the colourbar on the right. A physical scale is given indicating at what radii the given positions are. Temperature and density increase towards the mid-plane, and also towards the star in the centre. The transparent circle represents the dust clump at 50 AU from the protostar, that produces the absorption lines. The innermost region of the disk is free of HCN and C_2H_2 gas and dust. Turbulent mixing results in HCN and C_2H_2 gas being carried up to the cooler, upper layers of the disk where resonant scattering of the disk continuum causes emission lines.

diagram to derive the total abundance of the species. This conversion also involves the temperature gradient in the atmosphere through the coefficients a and b in the source function (see Appendix section 3.A). Since the line opacity is much less than the continuum opacity, the molecules absorb continuum photons therefore coupling the gas and dust.

In the weak line approximation, we can use the curve of growth approach and for the linear portion we arrive at (Mihalas 1978 section 10.3):

$$\frac{W}{2Y\Delta\nu} = \eta_0 \frac{\sqrt{\pi}}{2} \tag{3.4}$$

with W the equivalent width in frequency space, $\Delta\nu$ is the line width in frequency

space and Y a parameter which takes care of the gradient in the source function and is defined in the Appendix section 3.A. Here the peak line-to-continuum ratio at line centre, η_0, is given by

$$\eta_0 = \frac{\kappa_L(\nu = \nu_0)}{\kappa_c} = \frac{A_{ul}\lambda^3}{8\pi\sqrt{2\pi}\sigma_v}\frac{g_u}{g_l}\frac{N_l}{\sigma_c N_H}\left(1 - \frac{g_l N_u}{g_u N_l}\right) \tag{3.5}$$

where A_{ul} is the coefficient for spontaneous emission, g_u and g_l are the statistical weights for the upper and lower levels respectively, ν_0 is the line frequency and κ_L and κ_c are the line and continuum opacities respectively and N_l is the column density in the lower level of the line. σ_v is the dispersion in velocity space and σ_c the dust opacity per H-nucleus. For the latter we will adopt the value 7×10^{-23} cm^2/H-nucleus appropriate for coagulated interstellar dust (Ormel et al. 2011). This value is not very sensitive to the degree of coagulation. Here the expression for stimulated emission (the term in brackets) has been neglected since it is very close to unity.

The optical depth of the absorption lines is thus set against the continuum and therefore the level-specific column densities are calculated relative to the hydrogen column density. We measure the equivalent width of the absorption lines and thus calculate level specific abundances which, using equation 5.8, results in a total abundance for a given species (Tables 3.2 & 3.3).

We note the dependence on the adopted dust characteristics and hence the quoted absolute abundances carry that uncertainty. For lines that originate from the same spatial zone, derived abundances can still be directly compared. As the disk will show a strong radial temperature gradient in addition to the vertical temperature gradient, we recognise that derived abundances for lines that originate from a wide zone in the disk are ill defined without a detailed model for the disk. Dilution by continuum from regions with low molecular abundances will also result in ill-defined averages of the abundance over the emitting disk surface. Thus, abundance comparisons have to be taken with caution. However, as we will argue below, the observations indicate that much of these molecular absorption lines originate from the same region of the disk.

In both hot cores, the measured OPRs for C_2H_2 are less than the statistical equilibrium value of 3 for high temperatures. An ortho to para ratio of 3 is expected for this molecule as the observed (excitation) temperature (600K) is well above the energy difference between these states and, as we will argue in section 3.5.7, the high observed abundance requires formation of this molecule in hot gas. However we measure 2.1±0.3 and 1.8±0.2 for AFGL 2591 and AFGL 2136 respectively. We attribute this slightly lower value for the C_2H_2 OPR to the finite optical depth of these transitions. The observed strength of a line is only a direct measure of the column density in the weak opacity limit. When the opacity increases, the temperature gradient comes into play. Ortho lines will have 3 times the column density of the para lines. Hence, if line optical depth becomes important relative to that of the dust, our observations of the ortho lines will trace gas slightly higher in the photosphere than the para lines, and hence derived abundances will be smaller than those of the para transitions. The fact that the OPR is not equal to 3 is evidence for temperature gradients. Detailed modelling will be necessary to fully disentangle the effects of gradients.

In the above analysis of the abundances of molecular species, several assumptions

are made that are important to emphasise. We assume that the opacity is dominated by dust (weak line limit) and that albedo is small thus $\epsilon = 1$. Furthermore we assume that the dust and the gas are well coupled thermally, the level populations are in LTE and dust properties do not vary as a function of distance to the star. We also take a grey atmosphere, namely that the source function is linear, which has a number of assumptions that result in uncertainties in the abundances. These include the degree of dust-to-gas ratio (settling), the extent to which coagulation has proceeded and compaction (e.g., porosity) of the grains. This results in additional uncertainty in the absolute abundances of the molecules however it does not affect the relative abundances of the species, so the actual abundance relative to H will depend on the adopted value of dust opacity, but abundances between species are directly comparable.

Comparing the abundances to the sub-mm observations at high spatial resolution ($> 0.5''$), we see that the abundances calculated for the IR absorption lines in AFGL 2591 are higher by 2-3 orders of magnitude (Figure 3.12). Boonman et al. (2001) measured an HCN abundance of 10^{-6} for AFGL 2591 from high J level sub-mm emission lines. This is comparable to the abundance we derive for the HCN ν_2=0-1 band, but still an order of magnitude lower than the $\nu_2 = 0 - 2$ band. Larger IR abundances compared to sub-mm studies are also found for of AFGL 2136 where van der Tak et al. (2003) detect CS from single-dish sub-mm observations and derive an abundance of $4{\times}10^{-9}$ with respect to H_2. This compares to an abundance of $1.2{\times}10^{-6}$ with respect to H from the IR absorption lines. For AFGL 2591, the derived abundance for ^{13}CO corresponds to a ^{12}CO abundance of $1.6{\pm}0.5 \times 10^{-4}$, assuming a $^{12}C/^{13}C$ ratio of 60. This agrees well with the typical CO abundance of $1{\times}10^{-4}$(Lacy et al. 1994). Taking a $^{16}O/^{18}O$ ratio of 500 (Asplund et al. 2009) we derive a $C^{16}O$ ratio of $9.4{\pm}5.0{\times}10^{-4}$ with respect to H for AFGL 2136. This is larger than the typical CO abundance which may reflect that the chosen dust opacity per H-atom in this source was too high. We will return to this issue in section 3.5.5

3.5.3 Emission Lines of HCN and C_2H_2 in AFGL 2591

While the 4 to 14 μm window exclusively shows molecular absorption lines, the 3 μm region of the spectrum of AFGL 2591 shows emission lines of HCN and C_2H_2. One major conclusion from these emission lines is that the abundance of HCN and C_2H_2 are very low in the innermost, warm region that is responsible for the 3 μm continuum. The absence of broad HCN and C_2H_2 absorption lines in the 3 μm region implies that there is an HCN/C_2H_2 free region in the innermost parts of the disk (Figure 3.13). This should be contrasted with CO which does show absorption lines in the (v=0-2) overtone in the K band (R. Smith 2020, private communication). Hence, the CO abundance must be high throughout the entire disk and produce absorption features, which greatly overwhelm scattered photons from the cooler portions of the disk.

The emitting gas is characterised by low temperatures (250 K) and small line width (3-6 km s^{-1}). The line profiles in Figure 3.14 reveal that the velocities of the emission and absorption lines of HCN are the same, firmly associating this gas with the disk. This is also true of C_2H_2, suggesting that emission of HCN and C_2H_2 in the disk originates from the same radial part as the corresponding absorption. As the

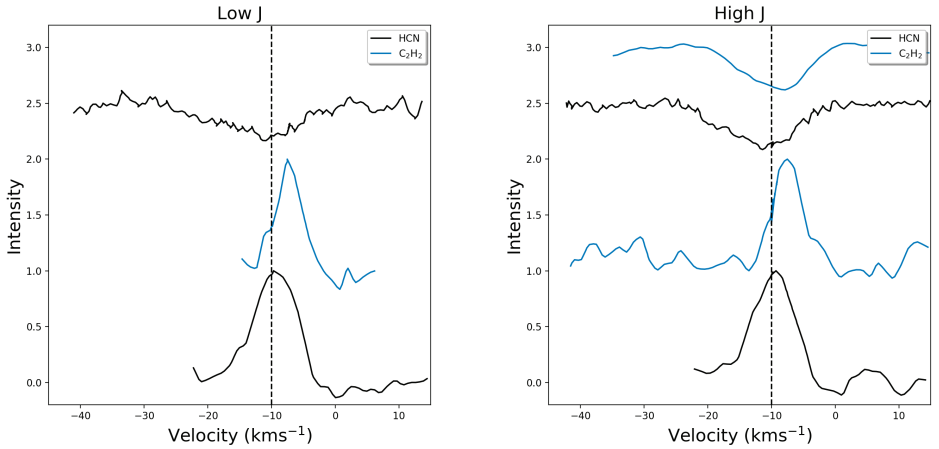

Figure 3.14: Average line profiles comparing HCN and C_2H_2 emission and absorption line profiles in AFGL 2591 plotted in velocity space. The HCN absorption transition is ν_2 v$_2$=0-2 and the C_2H_2 absorption band is the ν_5. Transitions are separated into high and low J levels before the average is calculated (high for $E_l < 90$ K). The black dashed line denotes -10 km s^{-1}.

3 μm continuum emission likely arises from a region of the disk further in than the longer wavelength emission, we attribute these emission lines to resonant scattering by C_2H_2 and HCN molecules high up in the photosphere of the disk at the same radial location that is responsible for the 7 and 13 μm absorption lines. This would in a natural way explain the relatively low temperatures and the small line widths. For this to occur, at 3 μm there must be an optically thin gas layer in the upper photosphere of the disk, indicative of dust settling in the disk. Likely, the disk is flaring at large scale heights and the gas is turbulently brought up to high altitudes where it is exposed to near-IR pumping continuum photons from the warm inner disk.

Consider a disk with size R_{out} which emits continuum (black body) radiation at 3 μm over a small region with surface area A. The flux seen by gas, at a distance R from this continuum source to the gas is then

$$F_R = \frac{L}{2\pi R^2} = \frac{A\pi B}{2\pi R^2} = \frac{AB\,(T)}{2R^2} \quad . \tag{3.6}$$

where we have included an extra factor of 0.5 in the denominator since the disk sees half of the flux, and B is the Planck function. The flux scattered into our direction by gas in an annulus, dR, is then,

$$dF_s = 2\pi R F_R N_s \frac{d\sigma}{d\Omega} dR \quad , \tag{3.7}$$

where N_s is the column density of scattering molecules along the line of sight from the continuum source to the emitting gas, and $d\sigma/d\Omega$ is the differential scattering cross section, approximated by $\sigma/4\pi$. We find then for the line to continuum ratio

that the observer sees,

$$\frac{F_s - F_c}{F_c} = \frac{F_L}{F_c} = \frac{\tau_s}{4\pi} \ln [R_{out}/R_{in}] \tag{3.8}$$

where τ_s is the (scattering) optical depth given by (Tielens 2021),

$$\tau_s = \frac{c^3}{8\pi\sqrt{2\pi}\sigma_v\nu^3} A_{ul} N_u \left(\frac{g_u N_l}{g_l N_u} - 1 \right) \tag{3.9}$$

where σ_v is the line standard deviation of the line in velocity space and N_u is the column density in the upper level. In this derivation, we have assumed that the density is low enough that collisional deactivation and thermalisation of the scattered photon energy is unimportant. We neglect the effect of stimulated emission.

After subtracting the continuum, the required HCN scattering optical depth is 0.03 which results in a total column density of $7.9\pm0.5 \times 10^{15}$ cm^{-2}. This is not relative to the continuum since the continuum origin is not in the same part of the disk. The temperature of the resonant scattering HCN is only 240±13 K which is lower than the temperature derived from the HCN absorption lines (670±118 K). For C_2H_2 we derive a scattering column density of $6.0\pm0.9\times10^{15}$ cm^{-2} and a temperature of 464±190, and again we measure a higher temperature from the absorption lines (600±50 K). If we assume the abundance of HCN as derived from the absorption lines, this column density would result in a H column of 3×10^{22} cm^{-2}. Therefore the optical depth in the continuum of this layer would be a few times 10^{-2}.

3.5.4 Abundance Gradients in the Disk

Consider the energy level diagrams for HCN and C_2H_2 shown in Figure 3.15. For both species, we measure two transitions originating from the same ground state levels, yet the derived abundances are very different, by up to a factor of 10. Specifically, the abundance of HCN derived from the 13 μm transition (v_2=0-1) is much lower than that derived from the 7 μm transition (v_2=0-2). The same holds for C_2H_2 in AFGL 2136 where the abundance derived from the ground state to the $\nu_4 + \nu_5$ level at 7 μm is a factor of 4 higher than the abundance derived from the ground state to the ν_5 level. As the 13 μm continuum originates from further out in the disk than the 7 μm continuum, this suggests the presence of an abundance gradient with higher abundances in the photosphere of the inner, warmer disk, out to 50 AU (Fig 3.13).

However, the excitation temperature derived from the rotational diagram analysis is very similar for the transitions probed at 13 μm and at 7 μm. Most importantly, the observed line profiles are similar (Figs 3.1, 3.2 & 3.12). The observed line width will be dominated by Keplerian rotation and suggests absorption by gas at about the same radial location. Thus we locate the absorption in all of these ro-vibrational transitions from HCN and C_2H_2 to originate from the same gas at about the same depth in the disk photosphere, at about the same radial distance from the protostar. The derived gas temperatures of these transitions are ∼600 K which is higher than the dust temperature that is characteristic for 13 μm continuum, which traces the outer regions of the disk (∼400 K assuming a radial temperature gradient $\propto T^{-0.7}$) This implies a location of the absorbing gas in the warmer inner regions. At 13 μm

however, due to the lack of absorbing species, the outer disk will contribute to the continuum, and only very little to the absorption feature. This dilution by continuum emission will lead to an underestimate of the abundance of the absorbing species (Fig 3.13). Detailed models will be required to assess the importance of this effect.

In their pioneering study of C_2H_2 absorption lines in the spectrum of Orion IRC2, Evans, Lacy & Carr (1991) noted a similar effect with a 3 times higher column density derived from the $\nu_4 + \nu_5$ (7 μm) transition than from the ν_5 (13 μm) transition. They located the absorbing material in the protostellar photosphere and attributed this difference to a higher continuum (dust) opacity at 13 μm than at 7 μm. This would locate the C_2H_2 gas absorbing at 13 μm higher up in the photosphere where the abundance could be lower. This means that extinction can only explain around a factor of 2 difference and not the factor of up to 10 we observe. Furthermore it does not explain the similar line profile and temperatures observed at 7 and 13 μm. Barentine & Lacy (2012) have seen the same effect for C_2H_2 absorption in the spectrum of NGC 7538 IRS9. They attributed this to a filling in of absorption by resonant scattering which would be more important for the fundamental (ν_5) band than for the combination band ($\nu_4 + \nu_5$) (Fig 3.15). However, for material along the line of sight towards the continuum source, resonant scattering does not play a role as this line scattering process emits into 2π steradians. Moreover, even in the depth of the absorption band, the photon emission is dominated by continuum processes rather than line transitions because the continuum opacity is much larger than the line opacity.

The rotation diagrams of HCN and C_2H_2 at 7 μm reveal non-linearity. Line profiles of low and high J of these species are consistent with each other which implies that these lines originate from the same physical component (Figs 3.1 & 3.2). We attribute this to the presence of a temperature gradient in the disk with colder gas higher up in the disk photosphere absorbing more predominantly in the lowest rotational transitions. The fact that this is only observed in these two species, and not, for example, in CS, suggests that these species have a more extended vertical distribution in the disk measuring a relatively steep vertical temperature gradient along the disk photospheres. This could reflect that CS absorption is more concentrated close to $\tau_c = 2/3$ than HCN and C_2H_2. A full chemical and radiative transfer modelling effort would be required to ascertain the exact structure of the disk photospheres, however this is beyond the scope of this paper.

In AFGL 2591, all species are at the same temperature. It is therefore plausible that absorption by all species originates in the same gas. For AFGL 2136 however, a scatter of rotational temperatures of the molecules, indicative of the scatter seen in ISO-SWS studies (Boonman et al. 2003b; Boonman & van Dishoeck 2003; Keane et al. 2001; Lahuis & van Dishoeck 2000), reveals complex temperature variations with wavelength. This is a reflection of the interplay between the vertical and radial temperature gradients which will require radiative transfer modelling to disentangle. As a result of the grey atmosphere in the disk, all wavelengths will probe to the same depth in the disk. However, due to a combination of the disk being larger at longer wavelengths, and a decrease in the density with increasing radius from the central star, the photosphere layer structure is such that longer wavelengths probe to deeper layers of the mid-plane where the temperatures are higher (Figure 3.13)

In contrast to C_2H_2 and HCN, the spectra do not show absorption lines associated with the N-H bending mode of NH_3 in the EXES data range. As the umbrella mode (at 10 μm) is 5 times stronger than the N-H bending mode, the inferred abundance derived from the 10 μm would not give rise to discernible absorption features at 6 μm. However, we can exclude much higher NH_3 abundances in the region responsible for the 6 μm continuum emission. So, unlike for C_2H_2 and HCN, NH_3 does not show a strong increase in abundance in the radial (inwards) direction.

In the discussion of 3 & 6 μm H_2O absorption lines, Indriolo et al. (2020) already emphasised that absorption lines originate from a total optical depth of 2/3 which for strong lines is higher up in the disk photosphere than for weaker lines. Our complete 5-8 μm spectra of these two sources contains hundreds of H_2O lines. This will allow a much more detailed analysis of the origin and distribution of H_2O in the disk photosphere and we will come back to this in chapter 4.

3.5.5 Vibrationally Excited Absorption

As presented in section 3.4.1 and 3.4.2, the vibrational temperatures for ^{12}CO are 623±292 K and 490±39 K for AFGL 2591 and AFGL 2136, respectively. These are in agreement with the rotational temperatures for ^{13}CO and $C^{18}O$ which suggests that CO is in vibrational equilibrium. The vibrational temperatures for the ν_5 band of C_2H_2 are 670±95 K and 494±139 K for AFGL 2591 and AFGL 2136, respectively. Again these are in agreement with the rotational temperatures which suggests that this band is in vibrational equilibrium. Knez et al. (2009) noted the presence of vibrationally excited transitions (C_2H_2 $2\nu_5 - \nu_5$) in their spectrum of NGC 7538 IRS1 and concluded that this must imply very dense gas.

Collisional coupling of the rotational population to the temperature of the gas requires densities in excess of $\sim 10^{10}$ cm^{-3}. This limit is consistent with densities in protoplanetary disks, therefore the presence of such high density gas would further imply the presence of a dust disk that dominates the continuum emission for this

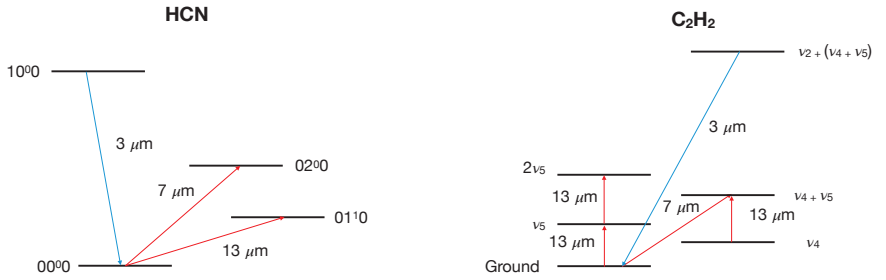

Figure 3.15: Energy level diagrams indicating the observed transitions of HCN (left) and C_2H_2 (right). The wavelength at which each vibrational transition is observed is indicated. Red arrows indicated transitions seen in absorption and blue arrows transitions seen in emission.

source. The scale height of the disk is given by $H = C_s/\Omega_k$ with C_s the sound speed ($\sim$ 2 km s^{-1} for 600 K) and $\Omega_k = v_k/r$ with v_k the Keplerian velocity and r the distance to the star. v_k is 30 km s^{-1} at a distance of 50 AU from a 50 M$_\odot$ star. This scale height would correspond to a dust optical depth of unity or $\sim 7{\times}10^{22}$ H-nuclei/cm^2. This results in a density of $\sim 1{\times}10^9$ cm^{-3}. Hence, the radiation field plays an important role in the population of the molecular gas. As gas in the photosphere of the disk receives only radiation from 2π steradians, the molecular excitation temperature is given by (Tielens 2005),

$$T_x/T_R = 1 + (kT_x/h\nu)\ln[2] \tag{3.10}$$

in the absence of collisions. T_x is the excitation temperature and T_R is the radiation temperature. As a result, the excitation temperature will be about 25 % lower than the radiation field temperature. For a reduced black body, collisional excitation dominates over radiative pumping if:

$$\frac{W}{exp(h\nu/kT_R)} \lesssim \frac{n}{n_{crit}} \tag{3.11}$$

where W is the dilution factor, n is the density and n_{crit} is the critical density (Tielens 2005). For $W = 0.5$, this occurs for $n > 1.7 \times 10^{10}$ cm^{-3} for the species considered here. As the actual density is likely only 10^9 cm^{-3}, the radiation field couples the level populations of these species to the continuum (dust) temperature. This implies that we observe weak scattering lines in our spectra.

In both sources, the ^{12}CO v=0-1 transitions go close to zero, with the low J lines being saturated. Therefore these are strong scattering lines and the ^{12}CO v=0-1 scattering line opacity is strong compared to the continuum opacity. This implies that collisional de-excitation is unimportant and hence the density is much less than the critical density for the v=0-1 ro-vibrational transitions of CO (10^{10} cm^{-3}).

For AFGL 2136, we derived a C^{16}O abundance that was higher than the typical value of $1{\times}10^{-4}$ based on the C^{18}O abundance. Since the ^{12}C^{16}O absorption lines are saturated in this source, we can make an estimate on what the dust opacity per H-atom should be for these values to agree. If we set the line-to-continuum ratio equal to 1, using equation 3.5 we calculate a dust opacity per H-atom of $5.3{\times}10^{-22}$ cm^2/H-nucleus. Taking this value instead of that quoted in section 3.5.2 would reduce the calculated absolute abundances in AFGL 2136 by an order of magnitude.

3.5.6 The Schematic Structure of AFGL 2136 and AFGL 2591

AFGL 2136

In order to place our results in context with respect to the specifics of each source, we outline a proposed schematic in Figure 3.16. For AFGL 2136, as mentioned in section 3.4.3, at a spatial resolution of 0.2″, an unresolved disk-like structure is observed in SiO emission at the systemic velocity, 22 km s^{-1}, which traces a disk wind out to 250 AU (Maud et al. 2018, 2019). At higher spatial resolution however, of 0.02″, SiO kinematics are observed to follow the H_2O Keplerian disk (Maud et al. 2019) on scales <120 AU.

In the H_2O velocity map and position-velocity diagrams that are presented by Maud et al. (2019), this disk is centred at around 26 km s^{-1} and is seen almost edge-on. The IR absorption that we detect at 26 km s^{-1} is associated with gas in the centre of the Keplerian disk. Therefore we propose that our IR absorption observations trace the minor axis of the disk seen in H_2O emission. This is further supported by the high temperatures that we measure of around 400-600 K (Table 3.3) which suggest that gas seen in the IR comes from warm gas close to the protostar.

H_2O emission is present across the entire extent of the dust disk. The width of the 232 GHz H_2O line is broader than the widths of the absorption lines, which would suggest that the absorption actually probes regions further out in the disk. This may be reconciled however by considering the 1.3 mm continuum image in Figure 1b of Maud et al. (2019) where clumps are observed to occur in the disk along the minor axis. These clumps are observed as peaks in the 1.3 mm continuum image. Indriolo et al. (2020) propose that, assuming the continuum structure is the same in the MIR as it is in the sub-mm, locating the H_2O absorption in these clumps would explain the difference in line width between the disk absorption and emission. One of these clumps coincides with the velocity of the absorption lines (26 km s^{-1}) of the species we discuss here and occurs about 50 AU from the protostar. It should be noted that there is no obvious sign of the 33 km s^{-1} clump, which is present in H_2O absorption and 1.3 mm continuum, for any of the other molecules except perhaps CO, as seen from the v=2-0 band at 2 μm (Goto et al. 2019) and marginally in a handful of the lines in Figure 3.9.

Since the sub-mm observations show the H_2O $5_{5,0} - 6_{4,3}$ $\nu_2 = 1$ line is in emission (Maud et al. 2019), the disk will be optically thin at sub-mm wavelengths. For interstellar dust properties at 230 GHz, N_H = N(H) + 2N(H_2) must be less than $2{\times}10^{26}$ cm^{-2} to be in the optically thin regime (Draine 2003). This line provides support for the presence of strong temperature gradients in the disk. It originates from a level $\sim$ 3500 K above the ground and its emission peaks at a radius of about 50 AU. The very high energy required to excite the H_2O emission line requires that it is produced in a very hot environment, if it is excited by collisions. This suggests that the line emission originates in the mid-plane of the disk where viscous heating originates, while the absorption lines that we study at the optically thick, mid-IR wavelengths originate from about the same radial location but then in the much cooler, disk photosphere.

The line width of the 22 km s^{-1} velocity component of CO absorption is narrow (2 km s^{-1}; Fig 3.10). Combined with the low temperature of only 27 K and difference in peak velocity, this suggests that this contribution comes from the cloud or surrounding envelope but not the disk.

AFGL 2591

In the case of AFGL 2591 the picture is less clear. We observe 5 different velocity components of ^{13}CO in absorption. This points to a complex environment in this hot core, which has been previously illustrated by van der Tak et al. (1999). These authors suggest that the different CO components are picked up along the cavity walls excavated by the outflow which points towards the observer, implying that any disk

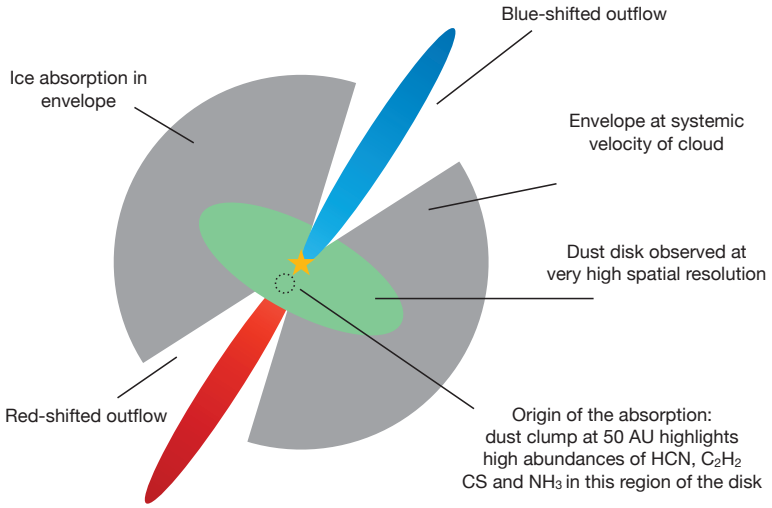

Figure 3.16: Cartoon schematic illustrating the different physical components in the large scale environs of the hot cores discussed. Drawing is not to scale.

in this source would be seen face-on. The main velocity component in the IR at -10 km s^{-1} is seen in all of the species presented in section 3.4.1, not just CO. There have been several studies that point towards the presence of a disk in AFGL 2591, despite no disk being spatially resolved (Wang et al. 2012; van der Tak 2006; Preibisch et al. 2003; van der Tak & Menten 2005). Sub-mm observations at 0.5″ spatial resolution suggest the presence of a disk wind (Wang et al. 2012). Line profiles best match sub-Keplerian motion along with a contribution from expansion which Wang et al. (2012) attribute to a disk structure with a wind blowing across the surface layer. van der Tak (2006) find evidence for a face-on disk in H_2O and dust emission on scales of $<$ 800 AU. In this study, the emission lines are still centred at -5.5 km^{-1} with a line width of up to 5.4 km s^{-1}. The beam size of the observations was 2-0.9″, and combined with the line profiles shows that the -10 km s^{-1} component is not resolved at these scales.

We propose that we are viewing AFGL 2591 down to the base of the blue-shifted outflow close to the protostar, the same as Indriolo et al. (2015a) suggest for H_2O absorption towards AFGL 2591 and in chapter 2 for CS. Due to the similarity in the IR absorption properties of both hot cores, and the tentative evidence for a disk in AFGL 2591, although no disk has been clearly imaged in this source, we propose a similar scenario as for AFGL 2136. The -10 km s^{-1} velocity component seen in IR absorption traces a clump in a circumstellar disk around a high mass protostar(s). It is fortuitous that this clump would also arise from close to the zero point velocity of the disk, as in AFGL 2136, and not at the extreme velocities in the disk, placing the absorption around 50 AU from the protostar. This disk is heated from the inside by

viscous heating due to accretion in the mid-plane. van der Tak & Menten (2005) see tentative evidence for a compact ionised accretion flow onto the protostar for AFGL 2591, although results may also be consistent with dust emission from a disk. We propose that the other velocity components seen in CO are also due to dust clumps in the disk, as in AFGL 2136. These are present only in CO which is omnipresent throughout the disk.

In a recent sub-mm study of rotational transitions of COMs by Gieser et al. (2019), the temperature and density structure of AFGL 2591 is modelled along with chemical complexity. The authors find that, at a spatial resolution of $0.5''$, the source is not resolved below 700 AU. They conclude that no disk structure is observed. Gieser et al. (2019) also show, based on modelling of the temperature distribution in AFGL 2591, that a temperature of around 700 K is reached at a radius of 56 AU from the central star, in agreement with predictions of the source size based on the CS column density and critical density (chapter 2). This is consistent with inner disk extent estimates from chemical modelling of Herbig disks (Agúndez et al. 2018; Walsh et al. 2015). For the many other simple and complex species that are detected by Gieser et al. (2019), low temperatures are derived compared to the results in Table 3.2, with a maximum of 212 K for HC_3N. Furthermore, the systemic velocity of -5.5 km s^{-1} is observed for all species. This would place the emission from these species in the surrounding envelope of the hot core, likely at the location of the sublimation temperature of the ices.

In the line profiles in Figure 3.1, NH_3 absorption is seen to occur at a peak velocity of -7 km s^{-1}, slightly more red-shifted compared to the other absorption lines. This is still blue-shifted with respect to the systemic velocity, associating the NH_3 absorption with the disk. This is supported by the high temperature that we derive for NH_3 absorption, of 870 K. The line width is also observed to be narrower than the other absorption lines. Furthermore, from Figure 3.1, we see that HCN and C_2H_2 absorption are slightly shifted in velocity space with respect to each other. These line profiles point towards compositional gradients in a clumpy distribution in the disk. It is difficult to ascertain the exact kinematical nature of the disk without an image of it from the sub-mm, therefore very high spatial resolution ($\lesssim 0.05$) observations of AFGL 2591 will be necessary for this.

The hot core phase in the evolution of massive stars ends when ionising radiation breaks out of the cocoon around the protostar itself and creates a hypercompact HII region. At that point, EUV and FUV photons will start to illuminate the photosphere of the disk and the temperature gradient can then be reversed. At that point, the absorption lines will disappear and gas in the upper regions of the disk will radiate in emission lines. We note that several sources in the neighbourhood of AFGL 2591 are connected with ionised gas (Johnston et al. 2013) and hence have already entered in this subsequent phase. We surmise that low mass protostars in the class 0 phase will also show molecular absorption lines in their mid-IR disk spectrum. Finally, we note that ultra-luminous infrared galaxies (ULIRGS) show molecular absorption lines in their mid-IR spectrum (Spoon et al. 2013) also indicative of an outwardly decreasing temperature gradient in an optically thick, grey atmosphere.

3.5.7 Chemistry in the Warm and Dense Disk Photosphere

The chemistry of the inner regions of TTauri and Herbig disks has been modelled extensively, including HCN, C_2H_2, NH_3 CH_4, CS and H_2O (Markwick et al. 2002; Willacy & Woods 2009; Walsh et al. 2010; Agúndez et al. 2008, 2018), with high abundances of these species predicted to arise due to high temperature gas phase chemistry (Agúndez et al. 2018; Walsh et al. 2015). For Herbig disks, the high abundance region is expected to be larger and extend to further out regions of the disk than TTauri disks due to the higher temperatures involved, although this is contrary to observations (Pontoppidan et al. 2010; Fedele et al. 2011). Detailed modelling studies of the chemistry of massive disks have not been carried out, yet. These would need to be undertaken to determine the exact nature of the chemistry in these disks which may be quite different due to the much higher masses and luminosities of the central object, and also the different heating mechanism which results in an outwardly decreasing temperature gradient in the vertical direction. However, if the same trend of increasing abundance with mass of the disk applies, we can expect that massive disks will show even larger abundances to further out distances in the disk from the protostar, compared with Herbig and TTauri disks.

High abundances of C_2H_2 and HCN are characteristic of chemistry in warm, dense gas (Agúndez et al. 2008; Bast et al. 2013). When C and N are broken out of their main reservoir, CO and N_2, high temperatures will allow the reaction of C with H_2 to CH to dominate the chemistry and a rich chemistry ensues with high abundances of C_2H_2 and HCN, as well as CH_4 and NH_3. The chemical models of TTAuri and Herbig disks rely on UV and X-ray photons to break the C and N out of their very stable main parent species. That is relevant for these objects where the stellar photons freely impinge on the photosphere of the disk. However, as the presence of absorption lines attests, disks around these massive stars do not have a photon-dominated region (PDR) surface. The destruction of N_2 and CO must therefore rely on cosmic ray ionisation. Cosmic ray ionisation of H_2 will lead to protonated H_2 and this proton can be handed over to CO and N_2. However, dissociative recombination of these protonated species will merely reform the parent species without breaking the strong bonds involved. The formation of C and N atoms requires then cosmic ray ionisation of helium.

We can then derive a minimum timescale for the disk by requiring that each cosmic ray ionised helium atom leads to either C_2H_2 or HCN. This results in

$$\tau_{chem} = \frac{X\left(C2H2\right) + X\left(HCN\right)}{X\left(He\right)\zeta_{CR}} \quad , \tag{3.12}$$

where $X\left(i\right)$ is the abundance of species i and ζ_{CR} is the cosmic ray ionisation rate for which we take the nominal value of 3×10^{-17} s^{-1} commonly adopted for molecular clouds (van der Tak & van Dishoeck 2000; Indriolo et al. 2015b). Adopting a He abundance of 0.06 (Peimbert et al. 2007) we derive a timescale of $7.3\pm0.5 \times 10^5$ yr and $6.2\pm0.5 \times 10^5$ yr for AFGL 2591 and AFGL 2136 respectively. These timescales are consistent with these two objects being similar in evolutionary stage (Boonman & van Dishoeck 2003). With the recently modelled values for the cosmic ray ionisation rate towards hot cores being up to 10 times greater than the value we have adopted

here (Barger & Garrod 2020; Padovani et al. 2015, 2016), we place an upper limit on these calculated chemical timescales. This timescale compares to an age of 2×10^4 yr based on chemical modelling of AFGL 2591 on scales of $> 0.4''$ (Doty et al. 2002; Gieser et al. 2019).

Indriolo et al. (2013, 2020) detect H_2O absorption in the K band in AFGL 2136 which means that this innermost region still has H_2O present. We expect that H_2O and CO will be omnipresent throughout the disk photosphere, tracing the entire extent of the disk seen in H_2O emission at 232 GHz, and do not show abundance gradients. Enhanced abundances of H_2O are predicted to occur for temperatures greater than 250 K (Charnley et al. 1997; Doty et al. 2002).

The abundance of HCN and C_2H_2, however, will be strongly influenced by the temperature. Both HCN and C_2H_2 require high temperature gas for their formation as the first step in the chemical pathway to either of these species (the conversion of C to hydrocarbons through reaction C+H_2 -> CH + H) has a high activation barrier of 12,000 K (Bast et al. 2013). Thus, due to the lower temperature in the outer regions of the disk, chemical enhancement is confined to the inner region only. In the inner dense warm gas regions, however, three body reactions will dissociate H_2 and atomic H will break OH out of H_2O. The OH radical will eventually burn these hydrocarbons to CO (Kress et al. 2008). Hence, we expect that HCN and C_2H_2 will occupy a small region in the disk limited on the inside by this burning process and on the outside by kinetics in the low temperature gas (Fig 3.13).

However, since the apparent size of the dust disk gets larger with wavelength (except for resonances such as the silicate feature), the continuum source will be larger at 13 μm than at 7 μm (Fig 3.13). The longer wavelength continuum will be dominated by lower temperature regions further out in the disk. The consequent abundance gradient will result in a filling in of absorption lines at these wavelengths by dust emission from the photosphere in the outer regions, which has low abundances of absorbing molecules. This results in a dilution of the observed flux at 13 μm, affecting the relative strength of 7 and 13 μm absorption bands (cf., section 3.5.4), hence we infer a strong radial gradient in the HCN and C_2H_2 abundances.

Agúndez et al. (2008, 2018) and Walsh et al. (2015) find that the chemistry of HCN and C_2H_2 in the inner region of disks is similar, therefore it is expected that, since these species exhibit similar chemical behaviour at high temperature, it is likely that they also exhibit similar physical behaviour. Indeed, the derived gas temperatures of these bands are similar ($\sim$600 K), both species show behaviour in the rotation diagrams characteristic of a temperature gradient, and both species exhibit an abundance gradient with wavelength. Furthermore, L-band data of AFGL 2591 show that HCN and C_2H_2 are detected in emission and NH_3 is not detected.

Upper limits of NH_3 emission from the inner disks of TTauri disks suggest that NH_3 is efficiently destroyed in the inner disk and that the main N-carriers are N_2 followed by HCN (Pontoppidan et al. 2019). Disk models, on the other hand, with full nitrogen chemical networks predict gas-phase NH_3 abundances of 10^{-5} or 10^{-6} with respect to H for the majority of N originating in NH_3 or N_2 respectively (Schwarz & Bergin 2014). We have very accurately determined the NH_3 abundance in the disks of both AFGL 2591 and AFGL 2136. High abundances (10^{-6}) suggest that NH_3 is one of the main N-carriers, along with HCN and most likely N_2, in the inner region.

3.5.8 Molecular Absorption Lines in the IR Spectra of Massive Protostars

This study focuses on AFGL 2136 and AFGL 2591, however several other hot cores have been observed before at high spectral resolution at MIR wavelengths using a few specifically chosen settings. These studies reveal MIR transitions in absorption towards hot cores (Mitchell et al. 1989, 1990; Evans, Lacy & Carr 1991; Knez et al. 2009; Barentine & Lacy 2012; Rangwala et al. 2018; Dungee et al. 2018; Indriolo et al. 2013, 2015a, 2020). Hot cores have also been observed at low spectral resolution in the MIR with ISO (Lahuis & van Dishoeck 2000; Keane et al. 2001; Boonman et al. 2003b; Boonman & van Dishoeck 2003).

All theses studies conclude that absorption lines in the IR originate in a region in very close proximity to the illuminating protostar. In the past, molecular absorption lines in the mid-IR spectra of high mass protostars have been interpreted in terms of either a disk, or small foreground blobs along the line of sight towards the star. However, if the continuum emission is associated with a circumstellar disk, as in the case for AFGL 2136, these blobs must by necessity cover a substantial fraction of the disk surface. Moreover, as the rotational temperature is very high, this gas must be located close to a heating source. It is then likely that this gas is really associated with the surface layers of an internally heated disk. This also explains, in a natural way, the observed peak velocity and width of these absorption lines.

In view of the presence of absorption lines, a temperature gradient of the form we proposed in section 3.5.1 must also apply to these other hot cores. Viscous heating from the mid-plane up results in a vertically decreasing temperature gradient. These results are in contrast to TTauri stars and Herbig AeBe stars whose MIR spectra are dominated by strong molecular emission lines (Carr & Najita 2011) indicative of an inwardly decreasing temperature gradient in the vertical direction. The high abundances measured indicate the presence of a hot gas-phase chemistry, which has been discussed in section 3.5.7. This chemistry implies a timescale for these hot cores between 7×10^4 yr and 7×10^5 years. We speculate that during the deeply embedded phase of low mass protostars, the Hot Corino gas (Ceccarelli 2008) is characterised by mid-IR absorption lines with a disk with an outwardly decreasing temperature gradient in the vertical direction.

Several massive YSOs show hot CO v=2-0 emission at NIR wavelengths which is best described as arising from a circumstellar disk. This emission arises from within the dust sublimation radius where the disk is gaseous (Ilee et al. 2013). One of the hot cores in this survey, AFGL 4176, shows CO v=2-0 bandhead emission, as well as H_2O and CO absorption at 2.5 μm and 4.6 μm respectively (A. Karska et al., in preparation). The absorption is indicative of an outwardly decreasing temperature gradient in the vertical direction, therefore this may be a general characteristic possessed by disks around massive stars, which would suggest that these disks are accreting.

3.6 Conclusions

We have presented here results of the first ever full spectral survey of the 4.5-13 μm region at high spectral resolution towards a hot core, which utilises EXES, TEXES

and iSHELL. MIR ro-vibrational lines are observed to be in absorption in CO, CS, HCN, C_2H_2 and NH_3. However HCN and C_2H_2 in the L-band are seen in emission towards AFGL 2591. A rotational diagram analysis reveals that the absorption lines probe high temperature gas of the order of 600 K. Line profiles reveal a difference in line width and peak velocity when compared to the surrounding envelope which is traced by sub-mm emission lines. IR absorption lines are broader and offset by several km s^{-1} with respect to sub-mm lines seen by single-dish telescopes.

A disk around AFGL 2136 has been inferred at MIR wavelengths and has recently been resolved as a Keplerian disk with ALMA. There is also evidence for a potential disk around AFGL 2591. We propose that the IR absorption lines trace this circumstellar disk and due to the presence of absorption lines, we propose that this disk is characterised by an outwardly decreasing temperature gradient in the vertical direction, with viscous heating due to accretion originating in the mid-plane. Temperatures and line profiles are consistent with clumps in these disks at a distance of 50 AU from the protostar.

We have derived vertically averaged abundances for all species detected using stellar atmosphere theory to account for the temperature gradient in the disk. We derive high abundances for all species, of the order 10^{-6} with respect to H. In view of the lower temperature of the emission lines in the L-band, we conclude that these lines trace gas higher up in the photosphere of the disk.

Differences of up to an order of magnitude in the abundances of transitions that trace the same ground state level are measured for HCN and C_2H_2 in both hot cores. The abundance derived from the transition at 7 μm is higher than that at 13 μm, however the temperature and line profiles of the two transitions are in agreement. We conclude that the transitions originate from the same gas, whilst we attribute the abundance difference to filling in of absorption lines by dust continuum emission from the outer part of the disk where the abundance of these species is low. The extent of the outer part of the disk increases with wavelength, thus diluting the gas at 13 μm more than at 7 μm. Thus abundance gradients exist in the disk with the high abundance material constrained to the inner 50 AU of the disk.

The location of the absorption coming from 50 AU from the protostar is supported by chemical models of TTauri and Herbig Ae/Be disks, where high temperatures and abundances are derived for all species observed. Comparison to these models is limited however due to the different physical structure of the disks. In the case of these massive disks, we suggest that C and N are broken out of their main reservoirs by cosmic ray ionisation. The presence of HCN and C_2H_2 emission at 3 μm implies that these species may be destroyed by OH radicals in the innermost regions of the disk resulting in a depleted region of HCN and C_2H_2 gas. Turbulent mixing then transports HCN and C_2H_2 gas to the upper, cooler layers of the disk photosphere where it is illuminated by the warm inner disk and resonant scattering produces emission lines. High abundances of NH_3 implies that this is one of the main N-bearing species at radii of around 50 AU from the central object, along with HCN and likely N_2.

Finally, MIR absorption lines have been observed along sight lines towards several other hot cores. All of these studies observe high abundances of detected species. These observations are consistent with the scenario that we propose in this paper for AFGL 2591 and AFGL 2136. Therefore MIR absorption lines indicating high

rotational temperatures towards hot cores may be an indication of massive disks at the centre of these sources.

Acknowledgements

Based [in part] on observations made with the NASA/DLR Stratospheric Observatory for Infrared Astronomy (SOFIA). SOFIA is jointly operated by the Universities Space Research Association, Inc. (USRA), under NASA contract NNA17BF53C, and the Deutsches SOFIA Institut (DSI) under DLR contract 50 OK 0901 to the University of Stuttgart. A.G.G.M.T thanks the Spinoza premie of the NWO. D.A.N gratefully acknowledges the support of an USRA SOFIA grant, SOF05-0041. The authors also thank Rachel Smith and Agata Karska for their helpful contributions to this paper, as well as the anonymous referee for the constructive suggestions for improving the manuscript.

3.A Derivation of Milne-Eddington Solution

We will adopt a linear source function on the continuum optical depth scale, τ_c:

$$S = a + b\tau_c = a + p_\nu \tau_\nu \tag{3.13}$$

where $p_\nu = b/(1+\eta_\nu)$ transforms the continuum optical depth scale to the total line plus continuum optical depth scale, τ_ν. Here η_ν is the line-to-continuum opacity ratio at frequency ν. Ignoring scattering in the continuum, the Milne-Eddington approximation leads to the residual flux of an absorption line (Mihalas 1978):

$$R_\nu = \frac{F_\nu}{F_c} = \frac{2(p_\nu + \sqrt{3\lambda_\nu}a)}{(1+\sqrt{\lambda_\nu})(b+\sqrt{3}a)} \tag{3.14}$$

Examining this solution we see that, in the case of a pure absorption line, the residual flux will not be equal to 1, even for a strong line. For a pure absorption line, $\epsilon = 1$ and $\lambda_\nu = 1$, where the thermalisation length is:

$$\lambda_\nu = \frac{1+\epsilon\eta_\nu}{1+\eta_\nu} \tag{3.15}$$

where ϵ ranges from 0 to 1 and is a measure of the thermalisation of the line, such that the fraction of scattered and absorbed photons during line formation is $(1-\epsilon)$ and ϵ, respectively (see section 3.B for further definition).

For a weak line the residual flux is given by,

$$R_\nu = \frac{\sqrt{3}a + b/(1+\eta_\nu)}{\sqrt{3}a + b} \tag{3.16}$$

This leads to a central depth of

$$A_0 = 1 - R_\nu = \frac{b(1-(1+\eta_\nu)^{-1})}{b+\sqrt{3}a} \tag{3.17}$$

For weak lines ($\eta_\nu << 1$), we can use the Taylor expansion to arrive at,

$$A_0 \simeq \frac{\eta_\nu}{1+\sqrt{3}a/b} \tag{3.18}$$

Thus the strength of the line scales with η_ν. For a strong line ($\eta_\nu \to \infty$), the central depth of the line is given by,

$$A_0 = \frac{b}{b+\sqrt{3}a} \tag{3.19}$$

Thus, if the column density is large enough, lines will go down to the same value, A_0, independent of the line column density. In this case, the continuum optical depth will be small and hence the stellar atmosphere approximation will break down as the line opacity will be much larger than the continuum opacity.

The expression in eqn 3.18 is the same for the weak line approximation in a pure scattering line (Collins 2003). This is because for weak lines the opacity is dominated by the continuum and a scattered photon is lost to the continuum opacity process (thermalisation). So, line scattered photons do not stray from the place where they initially interacted and we will still measure the flux at a depth of $\tau = \tau_c + \tau_l = 2/3$. Strong scattering lines, however, will go to 0 residual flux as photons at any depth will wander around until they are lost.

If we consider equation 5.6 in section 3.5.2, the source function gradient is given by $Y = (1 + 3a/2b)^{-1}$ (Mihalas 1978). For a we will adopt the Planck function at the temperature derived from the rotation diagram and $b = 3/8X_0a$, where X_0 is given by eqn 3.21 below. For a grey atmosphere, we can evaluate the source function gradient to arrive at (Mihalas 1978, section 10.2),

$$Y = \frac{X_0}{X_0+4} \tag{3.20}$$

with

$$X_0 = \frac{h\nu_0/kT_0}{1-e^{-h\nu_0/kT_0}} \tag{3.21}$$

with T_0 the temperature at the depth where the continuum originates and ν_0 the frequency of the lines. At the frequency of the absorption lines ($\sim 5 \times 10^{13}$ Hz) and the excitation temperature derived from the rotation diagrams, X_0 is in the range 3-19.

3.B Derivation of Stellar Atmosphere Parameters

Let us consider the equation of radiative transfer:

$$\mu \frac{dI_\nu(\mu)}{dx} = (\kappa_\nu^c + \kappa_\nu^L + \sigma)I_\nu - \epsilon_\nu^c - \epsilon_\nu^L - \sigma J_\nu \tag{3.22}$$

where κ_i are the absorption coefficients and ϵ_i are the emission coefficients. σ is the scattering contribution to the total absorption coefficient. Assuming that we

have LTE in the continuum ($\epsilon^c_\nu/\kappa^c_\nu = B_\nu(T)$) and that scattering is negligible in the continuum ($\sigma << \kappa^c_\nu$), we come to:

$$\mu\frac{dI_\nu}{dx} = (\kappa^c_\nu + \kappa^L_\nu)\big[I_\nu - \frac{\kappa^c_\nu}{\kappa^c_\nu + \kappa^L_\nu}B_\nu - \frac{\kappa^L_\nu}{\kappa^c_\nu + \kappa^L_\nu}S^L_\nu\big] \tag{3.23}$$

Now let us define $\eta_\nu = \dfrac{\kappa^L_\nu}{\kappa^c_\nu}$ and $\lambda_\nu = \dfrac{1+\epsilon\eta_\nu}{1+\eta_\nu}$. Making a change of variables from x to τ_ν:

$$d\tau_\nu = (\kappa^c_\nu + \kappa^L_\nu)dx = k^c_\nu(1+\eta_\nu)dx \tag{3.24}$$

for the equation of radiative transfer we arrive at the Milne-Eddington approximation:

$$\mu\frac{dI_\nu}{d\tau_\nu} = I_\nu - \lambda_\nu B_\nu - (1-\lambda_\nu)\int_0^\infty \phi_\nu J_\nu d\nu \tag{3.25}$$

The definition of the thermalisation of the line ϵ used in equations 3.19 and 3.16 is:

$$\epsilon = \frac{\kappa_c}{\kappa_c + \sigma} \tag{3.26}$$

where κ_c is the continuum opacity and σ is the scattering contribution to the total absorption coefficient. Note that the expression for ϵ in equation 3.26 is not the same as the emission coefficient in the equation of radiative transfer, ϵ^c_ν (Eqn 3.22), but rather this ϵ without a subscript is that from section 3.5.2. When scattering is important, $\sigma \to \infty$, thus ϵ becomes 0. When scattering is negligible, $\sigma = 0$ therefore $\epsilon = 1$.

Table 3.4: Line Parameters for AFGL 2591. E_l is the energy of the lower level of the transition, g_l is the statistical weight of the lower level, A_{ij} is the Einstein A coefficient of the transition, v_{lsr} is the centroid velocity of the line, Δv is the FWHM of the line, τ_0 is the optical depth at line centre and N_l/N_H is the abundance in the lower level of the transition. Line data were taken from the HITRAN database (Gordon et al. 2017).

Species	Transition	λ (μm)	E_l (K)	g_l	A_{ij} (s^{-1})	v_{lsr} (km s^{-1})	Δv (km s^{-1})	τ_0	N_l/N_H ($\times 10^{-7}$)
^{13}CO v=0-1	P(1)	4.7792	5.2	6	32.4	-9.4 ±0.2	1.5	0.50 ±0.04	72.4 ±7.3
	P(2)	4.7877	15.8	10	21.5	-9.3 ±0.1	1.5	0.57 ±0.02	77.5 ±3.6
	R(2)	4.7463	15.8	10	14.2	-9.7 ±0.3	1.5	0.68 ±0.07	67.0 ±8.0
	R(3)	4.7383	31.7	14	14.8	-9.3 ±0.1	1.5	0.70 ±0.02	68.6 ±2.7
	P(3)	4.7963	31.7	14	19.3	-9.3 ±0.2	1.5	0.61 ±0.04	79.0 ±6.2
	P(4)	4.8050	52.8	18	18.2	-9.3 ±0.2	1.5	0.57 ±0.03	72.4 ±5.2
	R(5)	4.7227	79.3	22	15.5	-8.3 ±0.2	1.5	0.44 ±0.06	38.6 ±5.7
	R(6)	4.7150	111.0	26	15.8	-9.1 ±0.3	1.5	0.31 ±0.06	29.3 ±5.9
	R(9)	4.6927	237.9	38	16.4	-12.1 ±0.7	10.5	0.14 ±0.01	56.5 ±7.5
	P(9)	4.8501	237.9	38	16.4	-13.2 ±0.8	10.5	0.10 ±0.01	42.7±6.3
	R(10)	4.6853	290.8	42	16.5	-10.5 ±0.6	10.5	0.10 ±0.01	41.4 ±6.3
	R(11)	4.6782	349.0	46	16.7	-12.0 ±0.5	10.5	0.11 ±0.01	39.0 ±5.0
	P(11)	4.8689	349.0	46	16.1	-13.0 ±0.6	10.5	0.05 ±0.01	23.9 ±3.8
	R(12)	4.6711	412.3	50	16.8	-12.0 ±0.6	10.5	0.09 ±0.01	38.9 ±3.8
	R(13)	4.6641	481.1	54	16.9	-12.0 ±0.4	10.5	0.09 ±0.01	37.7 ±3.8
	R(16)	4.6437	718.8	66	17.3	-10.8 ±0.5	10.5	0.10 ±0.01	38.9 ±3.8
^{12}CO v=1-2	R(6)	4.6675	3199.5	13	33.2	-9.9 ± 0.6	7.6 ± 0.7	0.107 ± 0.007	42.7 ± 3.8
	R(7)	4.6598	3237.9	15	33.7	-8.3 ± 0.7	7.7 ± 0.8	0.112 ± 0.008	41.4 ± 6.3
	R(8)	4.6523	3281.8	17	34.1	-9.2 ± 0.4	7 ± 0.4	0.128 ± 0.006	38.9 ± 6.3
	R(9)	4.6448	3331	19	34.4	-8.6 ± 0.4	6.8 ± 0.4	0.116 ± 0.005	40.2 ± 2.5
	R(17)	4.5887	3922.5	35	36.6	-8.6 ± 0.3	6.2 ± 0.4	0.105 ± 0.005	27.6 ± 2.5
	R(18)	4.8948	4020.9	37	31.7	-7.2 ± 0.3	4.8 ± 0.4	0.086 ± 0.004	27.6 ± 2.5
	R(19)	4.9054	4124.8	39	31.4	-9.9 ± 0.8	5.2 ± 1.6	0.105 ± 0.009	30.1 ± 5.0
	R(20)	4.5694	4234.4	41	37.2	-6.3 ± 0.4	5.8 ± 0.5	0.088 ± 0.005	25.1 ± 3.8

Table 3.4: continued.

Species	Transition	λ (μm)	E_l (K)	g_l	A_{ij} (s^{-1})	v_{lsr} (km s^{-1})	Δv (km s^{-1})	τ_0	N_l/N_H ($\times 10^{-7}$)
CS v=0-1	P(8)	7.9443	84.6	17	8.1	-10.9 ± 0.5	9.7 ± 1.5	0.055 ± 0.006	12.6 ± 2.5
	R(3)	7.8212	14.1	7	7.2	-11.9 ± 0.5	8.3 ± 1.5	0.031 ± 0.004	5.0 ± 1.3
	R(4)	7.8116	23.5	9	7.4	-9.4 ± 0.5	6.2 ± 1.3	0.032 ± 0.004	5.0 ± 1.3
	R(5)	7.802	35.3	11	7.6	-10.1 ± 0.5	7.8 ± 1.3	0.039 ± 0.004	6.3 ± 1.3
	R(7)	7.7833	65.8	15	7.8	-10.4 ± 0.2	6.4 ± 0.6	0.056 ± 0.003	8.8 ± 1.3
	R(9)	7.7649	105.8	19	8	-9.5 ± 0.6	11.2 ± 1.8	0.051 ± 0.005	11.3 ± 2.5
	R(10)	7.7559	129.2	21	8	-11.1 ± 0.3	10.4 ± 0.9	0.061 ± 0.004	12.6 ± 1.3
	R(11)	7.7469	155.1	23	8.1	-12.1 ± 0.3	9.9 ± 0.8	0.06 ± 0.003	12.6 ± 1.3
	R(18)	7.6868	401.8	37	8.5	-12 ± 0.4	11 ± 1.2	0.063 ± 0.004	13.8 ± 2.5
	R(22)	7.6545	594.5	45	8.7	-12.4 ± 0.9	11.3 ± 3.7	0.081 ± 0.015	17.6 ± 6.3
	R(23)	7.6467	648.5	47	8.8	-10.3 ± 0.7	8.4 ± 1.7	0.064 ± 0.009	11.3 ± 3.8
	R(24)	7.6389	704.7	49	8.8	-5.2 ± 0.8	15.2 ± 2.2	0.06 ± 0.006	16.3 ± 5.0
	R(26)	7.6237	824.5	53	8.9	-8.4 ± 0.6	7.9 ± 2.1	0.048 ± 0.007	7.5 ± 2.5
	R(27)	7.6162	887.8	55	9	-11.2 ± 0.4	4.9 ± 1	0.076 ± 0.008	10.0 ± 2.5
	R(28)	7.6088	953.4	57	9	-10 ± 0.6	6.8 ± 1.5	0.055 ± 0.008	8.8 ± 2.5
	R(29)	7.6015	1021.5	59	9.1	-11 ± 0.4	6.7 ± 1.2	0.078 ± 0.008	12.6 ± 2.5
	]R(31)	7.5871	1164.5	63	9.2	-7.9 ± 0.9	11.5 ± 4.2	0.024 ± 0.005	5.0 ± 2.5
	R(33)	7.5731	1316.8	67	9.2	-9.1 ± 0.6	5.2 ± 1.5	0.051 ± 0.009	7.5 ± 2.5
HCN ν_2 v_2=0-1	R(11e)	13.3796	280.6	138	1.2	-11.7 ± 0.4	8.5 ± 1.1	0.098 ± 0.009	26.4 ± 3.8
	R(12e)	13.3271	331.7	150	1.2	-11.7 ± 0.7	9.4 ± 1.8	0.078 ± 0.011	23.9 ± 6.3
	R(13e)	13.275	387	162	1.3	-11.1 ± 0.3	8.7 ± 0.8	0.102 ± 0.007	28.9 ± 3.8
	R(14e)	13.2233	446.4	174	1.3	-9.5 ± 0.3	10.1 ± 0.8	0.096 ± 0.005	30.1 ± 3.8
	R(16e)	13.1213	578.2	198	1.3	-8.4 ± 0.6	9.1 ± 1.4	0.102 ± 0.012	30.1 ± 6.3
	R(17e)	13.0709	650.5	210	1.3	-7.7 ± 0.3	6.5 ± 0.8	0.07 ± 0.006	16.3 ± 2.5
	R(18e)	13.0209	727	222	1.3	-8.7 ± 0.2	8.8 ± 0.6	0.09 ± 0.004	26.4 ± 2.5
	R(19e)	12.9713	807.8	234	1.3	-7.7 ± 0.4	7.7 ± 0.9	0.077 ± 0.007	20.1 ± 3.8

Table 3.4: continued.

Species	Transition	λ (μm)	E_l (K)	g_l	A_{ij} (s^{-1})	v_{lsr} (km s^{-1})	Δv (km s^{-1})	τ_0	N_l/N_H ($\times 10^{-7}$)
	R(20e)	12.9221	892.7	246	1.3	-9.4 ± 0.2	8.5 ± 0.7	0.062 ± 0.004	17.6 ± 2.5
	R(21e)	12.8734	981.9	258	1.4	-9.4 ± 0.4	8.3 ± 1	0.058 ± 0.005	16.3 ± 2.5
	R(23e)	12.7771	1172.9	282	1.4	-8.3 ± 0.3	8 ± 0.7	0.05 ± 0.003	13.8 ± 1.3
	R(24e)	12.7295	1274.8	294	1.4	-9.5 ± 0.5	7.3 ± 1.3	0.039 ± 0.005	10.0 ± 2.5
	R(25e)	12.6823	1381	306	1.4	-8.5 ± 0.3	7 ± 0.7	0.05 ± 0.004	12.6 ± 1.3
	R(27e)	12.5891	1605.8	330	1.4	-8.2 ± 0.3	6 ± 0.9	0.034 ± 0.003	7.5 ± 1.3
	R(29e)	12.4974	1847.6	354	1.5	-6.1 ± 0.7	9.1 ± 1.7	0.028 ± 0.004	8.8 ± 2.5
	R(30e)	12.4521	1974.8	366	1.5	-8 ± 0.8	5.8 ± 2.1	0.026 ± 0.007	6.3 ± 2.5
	R(31e)	12.4072	2106.2	378	1.5	-10.3 ± 1.0	7.5 ± 2.6	0.021 ± 0.005	5.0 ± 2.5
	R(32e)	12.3627	2241.7	390	1.5	-6.4 ± 1.0	8.6 ± 2.7	0.013 ± 0.003	3.8 ± 1.3
	R(33e)	12.3185	2381.6	402	1.5	-6.3 ± 0.8	8.4 ± 2	0.013 ± 0.002	3.8 ± 1.3
	R(34e)	12.2747	2525.5	414	1.5	-9.4 ± 0.6	8.5 ± 1.5	0.015 ± 0.002	5.0 ± 1.3
HCN ν_2 v_2=0-2	P(14)	7.2923	446.4	174	1.1	-13 ± 0.4	12.7 ± 1.2	0.083 ± 0.005	208.5 ± 22.6
	P(13)	7.2775	387	162	1.1	-11.2 ± 0.4	9.3 ± 1.2	0.063 ± 0.005	126.0 ± 16.3
	P(12)	7.2627	331.7	150	1.1	-11.2 ± 0.3	10.5 ± 0.7	0.078 ± 0.003	169.6 ± 12.6
	P(10)	7.2332	233.9	126	1.1	-10.9 ± 0.6	9.8 ± 1.5	0.076 ± 0.008	154.5 ± 27.6
	P(9)	7.2184	191.4	114	1.1	-10.9 ± 0.3	12.2 ± 1	0.074 ± 0.004	189.7 ± 17.6
	P(8)	7.2037	153.1	102	1.1	-10.9 ± 0.4	12.9 ± 1.9	0.078 ± 0.007	178.4 ± 27.6
	P(6)	7.1741	89.2	78	1.2	-11.8 ± 0.4	7.9 ± 1	0.092 ± 0.007	170.8 ± 21.4
	P(5)	7.1593	63.8	66	1.2	-11.1 ± 0.3	9.1 ± 0.9	0.059 ± 0.004	126.9 ± 13.8
	P(4)	7.1445	42.5	54	1.2	-12.4 ± 0.4	13 ± 0.2	0.069 ± 0.005	197.2 ± 16.3
	P(3)	7.1297	25.5	42	1.3	-11 ± 0.6	13 ± 1.5	0.05 ± 0.004	152.0 ± 21.4
	P(2)	7.1148	12.7	30	1.4	-10.3 ± 0.8	10.6 ± 2	0.046 ± 0.006	124.3 ± 27.6
	R(0)	7.0702	0	6	0.7	-22.2 ± 0.5	5.5 ± 1.2	0.083 ± 0.01	59.0 ± 10.0
	R(2)	7.0404	12.7	30	0.9	-11.3 ± 0.9	10.1 ± 2.8	0.078 ± 0.014	139.4 ± 41.4
	R(4)	7.0106	42.5	54	1	-11.7 ± 0.4	11 ± 0.9	0.102 ± 0.006	207.2 ± 1.6

Table 3.4: continued.

Species	Transition	λ (μm)	E_l (K)	g_l	A_{ij} (s^{-1})	v_{lsr} (km s^{-1})	Δv (km s^{-1})	τ_0	N_l/N_H ($\times 10^{-7}$)
	R(5)	6.9956	63.8	66	1	-11.1 ± 0.7	13 ± 2.3	0.06 ± 0.018	147.0 ± 46.5
	R(8)	6.9509	153.1	102	1.1	-9.8 ± 0.4	5.5 ± 0.4	0.095 ± 0.009	129.4 ± 15.1
	R(9)	6.936	191.4	114	1.1	-12.7 ± 0.4	13 ± 0.5	0.08 ± 0.009	204.7 ± 25.1
	R(10)	6.9211	233.9	126	1.1	-12.9 ± 0.5	8.8 ± 1.3	0.079 ± 0.007	148.2 ± 22.6
	R(12)	6.8914	331.7	150	1.1	-13.6 ± 0.4	11.7 ± 1.2	0.096 ± 0.007	222.3 ± 25.1
	R(13)	6.8766	387	162	1.1	-13.8 ± 0.8	10.8 ± 2.6	0.067 ± 0.01	149.5 ± 36.4
	R(14)	6.8619	446.4	174	1.1	-12.6 ± 0.7	9.2 ± 1.8	0.08 ± 0.011	162.0 ± 35.2
	R(15)	6.8472	510.3	186	1.1	-11.1 ± 0.6	13 ± 0.7	0.083 ± 0.007	218.5 ± 26.4
HCN ν_1 v= 0 − 1	P(18)	3.0721	727.0	222	40.9	-9.2±0.9	4.6±2.4	0.008±0.003	–
	P(17)	3.0690	650.5	210	41.0	-9.9±0.8	4.6±0.8	0.012±0.003	–
	P(16)	3.0659	578.2	198	41.2	-9.8±0.6	4.6±0.5	0.014±0.005	–
	P(14)	3.0598	446.4	174	41.5	-9.6±0.2	5.9±0.6	0.022±0.002	–
	P(13)	3.0568	387.0	162	41.7	-9.0±0.5	5.5±1.2	0.022±0.003	–
	P(12)	3.0538	331.7	150	41.9	-9.4±0.3	5.9±0.7	0.029±0.002	–
	P(11)	3.0508	280.6	138	42.2	-10.4±0.5	7.3±1.3	0.025±0.003	–
	P(10)	3.0479	233.9	126	42.5	-9.6±0.2	5.3±0.6	0.026±0.002	–
	P(8)	3.0421	153.1	102	43.1	-9.3±0.3	7.9±0.8	0.034±0.003	–
	P(6)	3.0363	89.2	78	44.3	-10.3±0.6	9.9±1.5	0.029±0.003	–
	P(4)	3.0307	42.5	54	46.5	-9.8±0.4	8.7±1.0	0.029±0.002	–
	P(3)	3.0280	25.5	42	48.9	-10.1±0.2	5.3±0.5	0.028±0.002	–
	P(2)	3.0252	12.7	30	54.4	-9.1±0.6	6.1±1.6	0.016±0.003	–
	R(0)	3.0171	0.0	6	27.3	-10.2±0.7	4.6±1.5	0.013±0.003	–
	R(3)	3.0092	25.5	42	36.5	-8.8±0.2	6.5±0.6	0.035±0.002	–
	R(5)	3.0041	63.8	66	38.0	-8.4±0.2	5.0±0.5	0.045±0.003	–
	R(6)	3.0016	89.2	78	38.5	-9.8±0.2	6.3±0.5	0.024±0.001	–
	R(8)	2.9966	153.1	102	39.1	-10.6±0.6	8.5±1.6	0.038 ±0.005	–

Table 3.4: continued.

Species	Transition	λ (μm)	E_l (K)	g_l	A_{ij} (s^{-1})	v_{lsr} (km s^{-1})	Δv (km s^{-1})	τ_0	N_l/N_H ($\times 10^{-7}$)
	R(11)	2.9893	280.6	138	39.7	-9.5±0.4	6.7±1.1	0.015±0.002	–
	R(13)	2.9845	387.0	162	40.0	-10.6±0.8	11.1±0.5	0.022±0.004	–
p-C_2H_2 ν_5	R(10e)	13.245	186.2	21	3.5	-9.8 ± 0.3	8.4 ± 0.9	0.079 ± 0.006	7.9 ± 1.0
	R(12e)	13.1632	264.1	25	3.5	-10 ± 0.4	9.6 ± 1.1	0.073 ± 0.006	8.8 ± 1.3
	R(14e)	13.0825	355.5	29	3.6	-8.4 ± 0.3	7.9 ± 0.8	0.072 ± 0.006	8.3 ± 1.0
	R(16e)	13.0028	460.4	33	3.6	-7.7 ± 0.3	5.1 ± 0.8	0.06 ± 0.006	4.9 ± 0.8
	R(20e)	12.8466	710.8	41	3.8	-10 ± 0.5	7.3 ± 1.3	0.038 ± 0.005	4.6 ± 0.8
	R(22e)	12.77	856.2	45	3.9	-8.1 ± 0.3	6.8 ± 0.8	0.047 ± 0.003	4.1 ± 0.5
	R(24e)	12.6944	1015.2	49	3.9	-7.6 ± 0.4	7.4 ± 1.2	0.039 ± 0.004	4.1 ± 0.6
	R(26e)	12.6198	1187.6	53	4	-8.3 ± 0.5	9.4 ± 1.9	0.035 ± 0.005	4.3 ± 1.0
	R(28e)	12.5461	1373.4	57	4.1	-8.1 ± 0.5	9 ± 1.8	0.029 ± 0.004	2.6 ± 0.8
o-C_2H_2 ν_5	R(9e)	13.2862	152.3	57	3.5	-9.4 ± 0.9	6 ± 2.4	0.106 ± 0.027	7.5 ± 2.5
	R(11e)	13.2039	223.4	69	3.5	-9.9 ± 0.8	7.9 ± 3.1	0.083 ± 0.02	7.5 ± 2.5
	R(13e)	13.1227	308	81	3.6	-9.8 ± 0.3	9.6 ± 0.7	0.132 ± 0.007	13.8 ± 1.3
	R(15e)	13.0425	406.3	93	3.6	-10 ± 0.2	9.6 ± 0.5	0.133 ± 0.005	13.8 ± 1.0
	R(17e)	12.9634	517.9	105	3.7	-9.9 ± 0.3	8.8 ± 0.8	0.108 ± 0.007	10.0 ± 1.1
	R(19e)	12.8853	643	117	3.7	-9.3 ± 0.3	9 ± 0.7	0.102 ± 0.006	10.0 ± 1.1
	R(21e)	12.8082	781.7	129	3.8	-9.4 ± 0.2	10.5 ± 0.6	0.085 ± 0.004	10.0 ± 0.8
	R(23e)	12.7321	934	141	3.9	-9.1 ± 0.2	8 ± 0.5	0.072 ± 0.003	6.3 ± 0.5
	R(25e)	12.657	1099.6	153	4	-8.8 ± 0.3	7.4 ± 0.7	0.061 ± 0.004	5.0 ± 0.6
	R(27e)	12.5828	1278.8	165	4.1	-8.7 ± 0.8	11.9 ± 2.1	0.057 ± 0.007	7.5 ± 0.1
	R(29e)	12.5097	1471.4	177	4.2	-7.2 ± 0.5	8.2 ± 1.3	0.038 ± 0.004	3.8 ± 0.8
	R(31e)	12.4374	1677.5	189	4.3	-8.1 ± 0.5	8.5 ± 1.2	0.033 ± 0.003	3.8 ± 0.6
	R(33e)	12.3661	1896.9	201	4.4	-7.8 ± 0.5	7.9 ± 1.3	0.025 ± 0.003	2.5 ± 0.5
	R(35e)	12.2958	2129.8	213	4.5	-9.5 ± 0.6	8.9 ± 1.5	0.017 ± 0.002	1.3 ± 0.4
	R(37e)	12.2263	2376.1	225	4.6	-7 ± 0.8	8.1 ± 2.1	0.018 ± 0.003	1.3 ± 0.6

Table 3.4: continued.

Species	Transition	λ (μm)	E_l (K)	g_l	A_{ij} (s^{-1})	v_{lsr} (km s^{-1})	Δv (km s^{-1})	τ_0	N_l/N_H ($\times 10^{-7}$)
o-C_2H_2 $2\nu_5 - \nu_5$	R(10e)	13.2341	1235.5	63	3.6	-9 ± 0.6	8.5 ± 1.8	0.061 ± 0.009	4.6 ± 1.1
	R(11f)	13.2028	1273.6	69	4.1	-9.6 ± 0.7	7.4 ± 1.9	0.047 ± 0.008	4.4 ± 1.0
	R(12e)	13.1479	1313.4	75	3.3	-8 ± 1.2	6 ± 2.5	0.026 ± 0.019	2.9 ± 1.3
	R(14e)	13.0619	1404.7	87	3.1	-9 ± 0.4	9 ± 1	0.029 ± 0.002	4.8 ± 0.5
	R(15f)	13.0411	1457.1	93	4.1	-9.2 ± 0.4	9.6 ± 1.1	0.045 ± 0.004	4.4 ± 0.6
	R(16e)	12.9761	1509.6	99	2.9	-7.5 ± 0.5	9.9 ± 1.3	0.026 ± 0.003	4.6 ± 0.8
	R(17f)	12.9619	1569.2	105	4.1	-8.1 ± 0.4	7.7 ± 1.1	0.033 ± 0.003	2.8 ± 0.5
	R(19f)	12.8838	1694.9	117	4.2	-8.3 ± 0.5	10.2 ± 2	0.031 ± 0.004	2.6 ± 0.8
	R(21f)	12.8066	1834	129	4.3	-8.3 ± 0.3	7.4 ± 1	0.029 ± 0.003	2.8 ± 0.4
	R(23f)	12.7305	1986.9	141	4.4	-7 ± 0.4	8.4 ± 1.1	0.022 ± 0.002	2.3 ± 0.4
	R(25f)	12.6555	2153.1	153	4.5	-8 ± 0.6	8.3 ± 1.6	0.029 ± 0.004	3.0 ± 0.6
	R(27f)	12.5814	2333	165	4.6	-9.9 ± 1.3	8.3 ± 3.4	0.028 ± 0.008	2.5 ± 1.3
p-C_2H_2 $(\nu_4+\nu_5)^2 - \nu_4^1$	R(11f)	13.1697	1104.4	23	2.2	-6.3 ± 0.6	6.7 ± 1.8	0.027 ± 0.005	3.8 ± 1.3
	R(14e)	13.0289	1235.3	29	1.8	-12.8 ± 1.1	5.8 ± 2.7	0.019 ± 0.006	2.5 ± 1.3
	R(16e)	12.9437	1340.1	33	1.7	-10.6 ± 1	9.7 ± 2.8	0.017 ± 0.004	3.8 ± 1.3
	R(17f)	12.9311	1399.8	35	2.3	-7.4 ± 0.6	6.3 ± 1.6	0.02 ± 0.004	3.1 ± 0.9
	R(23f)	12.7022	1817.3	47	2.6	-9.7 ± 0.7	8 ± 2.1	0.017 ± 0.003	3.3 ± 0.9
o-C_2H_2 $(\nu_4+\nu_5)^2 - \nu_4^1$	R(10f)	13.2104	1067.1	63	2.2	-9.2 ± 0.9	10.4 ± 2.5	0.056 ± 0.01	10.0 ± 3.8
	R(11e)	13.157	1103.5	69	1.9	-8.2 ± 0.5	10.4 ± 1.3	0.043 ± 0.004	10.0 ± 1.3
	R(12f)	13.1292	1145.3	75	2.2	-9 ± 0.8	11.9 ± 2.6	0.052 ± 0.008	7.5 ± 2.5
	R(13e)	13.0715	1188	81	1.8	-6.7 ± 0.4	6 ± 1.5	0.029 ± 0.004	5.0 ± 1.3
	R(17e)	12.9012	1397.5	105	1.7	-8.5 ± 0.4	6 ± 0.5	0.04 ± 0.009	7.5 ± 1.3
	R(19e)	12.8162	1522.6	117	1.6	-7.3 ± 0.3	9.9 ± 1	0.031 ± 0.002	7.7 ± 1.1
	R(20f)	12.8155	1593.4	123	2.4	-8.3 ± 0.5	7.2 ± 1.7	0.039 ± 0.006	5.0 ± 1.3
C_2H_2 $\nu_2 + (\nu_4+\nu_5)$	P(17e)	3.0857	517.9	105	26.1	-7.1±0.9	7.8±2.2	0.014±0.003	–
	P(15e)	3.0810	406.3	93	25.9	-7.6±0.3	2.5±0.8	0.019±0.003	–

Table 3.4: continued.

Species	Transition	λ (μm)	E_l (K)	g_l	A_{ij} (s^{-1})	v_{lsr} (km s^{-1})	Δv (km s^{-1})	τ_0	N_l/N_H ($\times 10^{-7}$)
	P(13e)	3.0763	308.1	81	25.7	-7.2±0.7	5.4±1.7	0.012±0.003	–
	P(11e)	3.0717	223.5	69	25.6	-7.8±0.4	5.0±1.1	0.016±0.002	–
	P(5e)	3.0581	50.8	33	26.4	-7.1±0.4	4.2±1.0	0.012±0.002	–
	R(1e)	3.0427	3.4	9	18.9	-7.4±0.4	2.5±1.0	0.011±0.003	–
	R(11e)	3.0216	223.5	69	23.2	-7.9±0.3	3.7±1.2	0.019±0.003	–
	R(13e)	3.0176	308.1	81	23.5	-6.9±0.4	2.8±1.0	0.019±0.004	–
p-NH_3 ν_2 v_2=0-1	sP(8,2) E' E'	12.3805	1002.5	102	4.6	-6.9 ± 0.7	7.8 ± 1.7	0.024 ± 0.004	2.6 ± 0.9
	s(8,1) E" E"	12.3782	1018	102	4.8	-6.7 ± 0.9	6.2 ± 2.4	0.015 ± 0.004	1.6 ± 0.8
	aP(6,4) E' E"	12.3107	514.3	78	3.1	-8.4 ± 0.5	6.3 ± 1.2	0.02 ± 0.003	4.1 ± 0.8
	aP(6,1) E" E'	12.2491	593.5	78	5.4	-6 ± 0.3	4.5 ± 0.5	0.039 ± 0.006	3.3 ± 0.5
o-NH_3 ν_2 v_2=0-1	aP(8,3) A1" A2'	12.8487	977.2	204	4	-6.4 ± 0.4	6.1 ± 1.1	0.028 ± 0.003	2.8 ± 0.6
	aP(8,0) A1' A2"	12.8112	1023.9	204	4.7	-6.7 ± 0.2	9.5 ± 0.7	0.032 ± 0.002	3.9 ± 0.4
	aP(6,3) A1" A2'	12.2814	551.3	156	4.2	-9.4 ± 0.4	8.5 ± 1.1	0.033 ± 0.003	5.7 ± 0.9
	aP(6,0) A1' A2"	12.2451	598.7	156	5.5	-7.3 ± 0.5	7.2 ± 1.4	0.044 ± 0.006	4.4 ± 1.1

Table 3.5: Line Parameters for AFGL 2136. E_l is the energy of the lower level of the transition, g_l is the statistical weight of the lower level, A_{ij} is the Einstein A coefficient of the transition, v_{lsr} is the centroid velocity of the line, Δv is the FWHM of the line, τ_0 is the optical depth at line centre and N_l/N_H is the abundance in the lower level of the transition. Line data were taken from the HITRAN database (Gordon et al. 2017).

Species	Transition	λ (μm)	E_l (K)	g_l	A_{ij} (s^{-1})	v_{lsr} (km s^{-1})	Δv (km s^{-1})	τ_0	N_l/N_H ($\times 10^{-7}$)
$C^{18}O$ v=0-1	P(2)	4.7967	15.7	5	21.3	22.6 ± 0.1	2 ± 0.2	0.218 ± 0.01	37.7 ± 2.5
	P(1)	4.7882	5.2	3	32.2	22.1 ± 0.1	2.4 ± 0.2	0.167 ± 0.007	25.1 ± 2.5
	R(0)	4.7716	0	1	10.8	22.1 ± 0.1	2.8 ± 0.3	0.265 ± 0.015	16.3 ± 1.3
	R(3)	4.7473	31.5	7	14.7	21.9 ± 0.2	3 ± 0.5	0.198 ± 0.017	23.9 ± 3.8
	R(4)	4.7395	52.7	9	15.1	22.5 ± 0.2	1.6 ± 0.5	0.178 ± 0.019	17.6 ± 2.5
	R(5)	4.7317	79	11	15.4	22.2 ± 0.3	2.5 ± 0.8	0.151 ± 0.022	17.6 ± 3.8
	P(17)	4.9369	805.5	35	15.1	27.2 ± 0.3	11.2 ± 1	0.054 ± 0.003	18.8 ± 2.5
	P(15)	4.9168	631.9	31	15.4	27.1 ± 0.2	11.3 ± 0.7	0.061 ± 0.002	21.4 ± 1.3
	P(12)	4.8874	410.7	25	15.8	26.8 ± 0.7	12.8 ± 2.3	0.075 ± 0.009	30.1 ± 6.3
	R(6)	4.724	110.5	13	15.7	26.3 ± 0.4	9.8 ± 1.2	0.11 ± 0.009	30.1 ± 3.8
	R(11)	4.6872	347.6	23	16.5	25.9 ± 0.3	13 ± 1	0.09 ± 0.005	32.7 ± 2.5
	R(12)	4.6801	410.7	25	16.7	25.8 ± 0.7	14.3 ± 0.7	0.117 ± 0.028	47.7 ± 11.3
	R(14)	4.6662	552.9	29	16.9	27.3 ± 0.2	13.1 ± 0.8	0.08 ± 0.003	28.9 ± 2.5
	R(15)	4.6594	631.9	31	17	26.3 ± 0.1	10.9 ± 0.7	0.058 ± 0.002	15.1 ± 1.3
	R(16)	4.6527	716.1	33	17.1	27.8 ± 0.4	11.4 ± 1.1	0.06 ± 0.004	20.1 ± 2.5
	R(17)	4.6461	805.5	35	17.2	28.1 ± 0.3	11.8 ± 1.1	0.056 ± 0.003	18.8 ± 2.5
	R(18)	4.6396	900.2	37	17.3	30 ± 0.6	14.3 ± 0.8	0.046 ± 0.007	18.8 ± 2.5
	R(20)	4.6268	1105.3	41	17.5	27.8 ± 0.4	10.7 ± 1.3	0.038 ± 0.003	11.3 ± 1.3
	R(21)	4.6206	1215.6	43	17.6	27.5 ± 0.2	10.2 ± 0.7	0.034 ± 0.001	10.0 ± 1.3
	R(22)	4.6145	1331.2	45	17.7	28 ± 0.3	11.1 ± 1	0.025 ± 0.001	7.5 ± 1.3
^{12}CO v=1-2	P(19)	4.9054	4124.8	39	31.4	26.2 ± 0.2	13.4 ± 0.6	0.165 ± 0.005	36.4 ± 2.5
	P(18)	4.8948	4020.9	37	31.7	27 ± 0.3	12.6 ± 0.7	0.163 ± 0.006	25.2 ± 2.5
	P(17)	4.8843	3922.5	35	31.9	27.1 ± 0.1	11.1 ± 0.4	0.171 ± 0.004	31.4 ± 1.3
	P(16)	4.8739	3829.4	33	32.2	27.6 ± 0.2	11.8 ± 0.7	0.17 ± 0.006	33.9 ± 2.5

Table 3.5: continued.

Species	Transition	λ (μm)	E_l (K)	g_l	A_{ij} (s^{-1})	v_{lsr} (km s^{-1})	Δv (km s^{-1})	τ_0	N_l/N_H ($\times 10^{-7}$)
	P(15)	4.8637	3741.9	31	32.5	27.6 ± 0.2	12.8 ± 0.7	0.181 ± 0.006	38.9 ± 2.5
	P(8)	4.7954	3281.8	17	34.9	27.2 ± 0.2	11.7 ± 0.5	0.213 ± 0.006	41.1 ± 2.5
	P(7)	4.7861	3237.9	15	35.5	27.3 ± 0.3	11.7 ± 1	0.227 ± 0.012	44.0 ± 3.8
	P(5)	4.7678	3166.7	11	37	28 ± 0.3	12 ± 0.9	0.189 ± 0.01	42.7 ± 3.8
	P(4)	4.7589	3139.2	9	38.3	27.5 ± 0.4	10.6 ± 1	0.18 ± 0.011	35.2 ± 3.8
	P(3)	4.75	3117.3	7	40.5	28 ± 0.6	14.6 ± 1.7	0.133 ± 0.01	36.4 ± 5.0
	P(2)	4.7413	3100.9	5	45.2	27.8 ± 0.3	6.6 ± 0.7	0.129 ± 0.009	18.8 ± 2.5
	P(1)	4.7327	3089.8	3	68.2	27.1 ± 0.2	9.7 ± 0.5	0.063 ± 0.002	16.3 ± 1.3
	R(4)	4.6832	3139.2	9	32	27.8 ± 0.3	12.3 ± 0.9	0.195 ± 0.009	35.2 ± 2.5
	R(5)	4.6753	3166.7	11	32.7	27.1 ± 0.1	13 ± 0.4	0.222 ± 0.004	40.2 ± 1.3
	R(6)	4.6675	3199.5	13	33.2	26.7 ± 0.2	14 ± 0.5	0.234 ± 0.006	46.5 ± 2.5
	R(7)	4.6598	3237.9	15	33.7	28.4 ± 0.3	12.8 ± 0.9	0.223 ± 0.01	40.2 ± 3.8
	R(8)	4.6523	3281.8	17	34.1	27.2 ± 0.2	12.1 ± 0.5	0.227 ± 0.006	40.2 ± 2.5
	R(12)	4.623	3511.9	25	35.3	27.4 ± 0.4	11.7 ± 0.9	0.246 ± 0.013	41.5 ± 3.8
	R(12)	4.616	3583	27	35.6	27.5 ± 0.2	12.6 ± 0.5	0.215 ± 0.006	40.2 ± 1.3
	R(16)	4.5954	3829.4	33	36.3	28.3 ± 0.4	10.7 ± 1.2	0.191 ± 0.015	32.7 ± 3.8
	R(17)	4.5887	3922.5	35	36.6	28.1 ± 0.2	13 ± 0.5	0.192 ± 0.005	37.7 ± 1.3
	P(24)	4.9603	4726.1	49	30.3	26.5 ± 0.2	9.3 ± 0.4	0.103 ± 0.003	17.6 ± 1.3
	P(25)	4.9716	4862.7	51	30.1	27 ± 0.3	11.4 ± 0.8	0.08 ± 0.004	16.3 ± 1.3
	P(26)	4.9831	5004.6	53	29.8	27 ± 0.4	6.7 ± 0.9	0.07 ± 0.007	8.8 ± 1.3
	P(27)	4.9947	5151.9	55	29.6	26.9 ± 0.2	8.5 ± 0.6	0.064 ± 0.003	10.0 ± 1.3
	P(28)	5.0065	5304.8	57	29.4	26.2 ± 0.3	11.1 ± 0.9	0.065 ± 0.004	12.6 ± 1.3
CS v=0-1	R(2)	7.8309	7.1	5	6.9	25.7 ± 0.4	8 ± 1	0.037 ± 0.003	5.0 ± 1.0
	R(3)	7.8212	14.1	7	7.2	25.1 ± 0.5	8.7 ± 1.2	0.042 ± 0.004	6.3 ± 1.1
	R(4)	7.8116	23.5	9	7.4	25.2 ± 0.4	6.2 ± 1.1	0.044 ± 0.005	5.0 ± 1.3
	R(5)	7.802	35.3	11	7.6	25.4 ± 0.3	9.2 ± 0.8	0.057 ± 0.003	8.8 ± 1.0

Table 3.5: continued.

Species	Transition	λ (μm)	E_l (K)	g_l	A_{ij} (s^{-1})	v_{lsr} (km s^{-1})	Δv (km s^{-1})	τ_0	N_l/N_H ($\times 10^{-7}$)
	R(7)	7.7833	65.8	15	7.8	25.4 ± 0.2	8.2 ± 0.5	0.089 ± 0.003	12.6 ± 6.3
	R(8)	7.774	84.6	17	7.9	26.3 ± 0.1	7.7 ± 0.4	0.1 ± 0.003	13.8 ± 3.8
	R(10)	7.7559	129.2	21	8	26.5 ± 0.2	10.3 ± 0.5	0.112 ± 0.003	18.8 ± 6.3
	R(11)	7.7469	155.1	23	8.1	26 ± 0.3	10.3 ± 0.7	0.098 ± 0.004	16.3 ± 11.3
	R(23)	7.6467	648.5	47	8.8	25 ± 0.4	2 ± 1.1	0.059 ± 0.008	5.0 ± 0.4
	R(25)	7.6313	763.5	51	8.9	31.3 ± 1	8.6 ± 2.7	0.054 ± 0.011	7.5 ± 1.0
	R(26)	7.6237	824.5	53	8.9	27.3 ± 0.6	5.9 ± 1.6	0.053 ± 0.008	6.3 ± 0.3
	R(27)	7.6162	887.8	55	9	24.9 ± 0.5	6.5 ± 1.3	0.048 ± 0.005	6.3 ± 0.3
	R(31)	7.5871	1164.5	63	9.2	28.3 ± 0.5	4.9 ± 1.2	0.045 ± 0.006	5.0 ± 0.3
HCN ν_2 v_2=0-1	R(7e)	13.5941	119	90	1.2	26.4 ± 0.2	12.3 ± 0.7	0.155 ± 0.006	50.2 ± 3.8
	R(10e)	13.4326	233.9	126	1.2	26.3 ± 0.2	9.6 ± 0.6	0.151 ± 0.006	42.7 ± 2.5
	R(11e)	13.3796	280.6	138	1.2	26.5 ± 0.2	10.1 ± 0.6	0.156 ± 0.007	46.5 ± 3.8
	R(12e)	13.3271	331.7	150	1.2	25.3 ± 0.4	11.5 ± 1.5	0.117 ± 0.009	40.2 ± 6.3
	R(14e)	13.2233	446.4	174	1.3	27.8 ± 0.2	11.5 ± 0.6	0.145 ± 0.005	49.0 ± 2.5
	R(16e)	13.1213	578.2	198	1.3	26.7 ± 0.3	12.4 ± 0.9	0.166 ± 0.008	61.5 ± 5.0
	R(17e)	13.0709	650.5	210	1.3	27.7 ± 0.3	11.8 ± 0.8	0.106 ± 0.005	37.7 ± 2.5
	R(18e)	13.0209	727	222	1.3	27.6 ± 0.2	10.3 ± 0.5	0.121 ± 0.004	38.9 ± 2.5
	R(19e)	12.9713	807.8	234	1.3	28.2 ± 0.4	13 ± 1.2	0.085 ± 0.005	33.9 ± 3.8
	R(20e)	12.9221	892.7	246	1.3	28 ± 0.2	11.2 ± 0.6	0.079 ± 0.003	27.6 ± 1.3
	R(21e)	12.8734	981.9	258	1.4	27.2 ± 0.2	12.2 ± 0.7	0.083 ± 0.003	31.4 ± 2.5
	R(23e)	12.7771	1172.9	282	1.4	28 ± 0.2	11.6 ± 0.5	0.069 ± 0.002	25.1 ± 1.3
	R(24e)	12.7295	1274.8	294	1.4	26.5 ± 0.3	9.2 ± 0.9	0.048 ± 0.004	15.1 ± 1.3
	R(25e)	12.6823	1381	306	1.4	26.7 ± 0.2	9.7 ± 0.5	0.073 ± 0.003	22.6 ± 1.3
	R(26e)	12.6355	1491.2	318	1.4	26.5 ± 1	10.8 ± 2.7	0.036 ± 0.007	12.6 ± 3.8
HCN ν_2 v_2=0-2	P(16)	7.3219	578.2	198	1.1	27.2 ± 0.4	8.2 ± 1	0.073 ± 0.006	126.9 ± 18.8
	P(14)	7.2923	446.4	174	1.1	28.5 ± 0.3	10 ± 0.9	0.087 ± 0.005	170.8 ± 18.8

Table 3.5: continued.

Species	Transition	λ (μm)	E_l (K)	g_l	A_{ij} (s^{-1})	v_{lsr} (km s^{-1})	Δv (km s^{-1})	τ_0	N_l/N_H ($\times 10^{-7}$)
	P(13)	7.2775	387	162	1.1	25.3 ± 0.7	7.6 ± 0	0.07 ± 0.013	118.1 ± 20.1
	P(12)	7.2627	331.7	150	1.1	26.5 ± 0.3	10.8 ± 0.9	0.097 ± 0.005	207.2 ± 21.4
	P(11)	7.248	280.6	138	1.1	26.3 ± 0.5	9.9 ± 1.9	0.062 ± 0.007	118.1 ± 26.4
	P(10	7.2332	233.9	126	1.1	26.2 ± 0.6	9.4 ± 1.6	0.071 ± 0.008	133.1 ± 26.4
	P(9)	7.2184	191.4	114	1.1	25.5 ± 0.9	7.6 ± 2.8	0.068 ± 0.035	113.0 ± 71.6
	P(8)	7.2037	153.1	102	1.1	26.7 ± 0.4	8.3 ± 1	0.077 ± 0.006	136.9 ± 20.1
	P(6)	7.1741	89.2	78	1.2	25.2 ± 0.5	7.9 ± 1.1	0.064 ± 0.006	113.0 ± 20.1
	P(5)	7.1593	63.8	66	1.2	27.7 ± 0.4	8.8 ± 0.9	0.087 ± 0.006	169.6 ± 21.4
	P(4)	7.1445	42.5	54	1.2	27.3 ± 0.5	10.7 ± 1.4	0.069 ± 0.006	159.5 ± 26.4
	P(3)	7.1297	25.5	42	1.3	26.3 ± 0.4	7.6 ± 1.1	0.08 ± 0.008	149.5 ± 26.4
	P(2)	7.1148	12.7	30	1.4	26 ± 0.5	9.3 ± 1.3	0.054 ± 0.005	129.4 ± 21.4
	R(0)	7.0702	0	6	0.7	23.2 ± 0.5	7.8 ± 1.4	0.094 ± 0.011	76.6 ± 16.3
	R(2)	7.0404	12.7	30	0.9	25.8 ± 0.6	10.9 ± 2	0.086 ± 0.01	150.7 ± 32.7
	R(3)	7.0255	25.5	42	1	25.4 ± 0.3	10.6 ± 0.9	0.082 ± 0.005	149.5 ± 15.1
	R(5)	6.9956	63.8	66	1	26.7 ± 0.5	10.9 ± 3.3	0.063 ± 0.013	98.0 ± 36.4
	R(8)	6.9509	153.1	102	1.1	27.4 ± 0.4	7.7 ± 1.5	0.099 ± 0.011	153.2 ± 35.2
	R(9)	6.936	191.4	114	1.1	24.3 ± 0.4	9 ± 1	0.09 ± 0.006	162.0 ± 21.4
	R(10)	6.9211	233.9	126	1.1	28.2 ± 0.4	7.6 ± 1.3	0.082 ± 0.008	133.1 ± 26.4
	R(12)	6.8914	331.7	150	1.1	24.9 ± 0.7	9.6 ± 1.9	0.07 ± 0.009	135.6 ± 33.9
	R(13)	6.8766	387	162	1.1	24.5 ± 0.6	9.4 ± 2	0.089 ± 0.012	167.0 ± 42.7
	R(14)	6.8619	446.4	174	1.1	24.9 ± 0.6	7.6 ± 1.6	0.103 ± 0.014	173.3 ± 45.2
	R(15)	6.8472	510.3	186	1.1	26.4 ± 0.7	7.7 ± 3.5	0.078 ± 0.015	123.1 ± 61.5
	R(16)	6.8326	578.2	198	1.1	27.4 ± 0.6	7.6 ± 1.8	0.063 ± 0.009	108.0 ± 30.1
	R(17)	6.818	650.5	210	1.1	24.3 ± 1	8.2 ± 2.2	0.065 ± 0.014	116.8 ± 41.4
p-C_2H_2 ν_5	R(6e)	13.4118	71.1	13	3.4	25.4 ± 0.5	9.4 ± 1.5	0.131 ± 0.014	12.6 ± 2.5
	R(10e)	13.245	186.2	21	3.5	27 ± 0.2	11.4 ± 0.8	0.093 ± 0.004	11.3 ± 1.3

Table 3.5: continued.

Species	Transition	λ (μm)	E_l (K)	g_l	A_{ij} (s^{-1})	v_{lsr} (km s^{-1})	Δv (km s^{-1})	τ_0	N_l/N_H ($\times 10^{-7}$)
	R(12e)	13.1632	264.1	25	3.5	27 ± 0.2	11.6 ± 0.7	0.093 ± 0.004	11.3 ± 1.3
	R(14e)	13.0825	355.5	29	3.6	28.7 ± 0.4	11.4 ± 1.3	0.104 ± 0.008	12.6 ± 1.3
	R(16e)	13.0028	460.4	33	3.6	27.1 ± 0.2	10 ± 0.6	0.071 ± 0.003	10.0 ± 1.3
	R(24e)	12.6944	1015.2	49	3.9	26.4 ± 0.5	12.1 ± 1.5	0.052 ± 0.005	6.3 ± 1.3
o-C_2H_2 ν_5	Q(9e)	13.7069	152.4	57	6.1	25.8 ± 0.3	12.7 ± 1.1	0.221 ± 0.011	15.1 ± 1.3
	Q(21e)	13.6758	781.8	129	6.1	26 ± 0.4	13.3 ± 1.7	0.147 ± 0.012	11.3 ± 1.3
	R(11e)	13.2039	223.5	69	3.5	25 ± 0.9	9.6 ± 2.8	0.196 ± 0.037	20.1 ± 6.3
	R(13e)	13.1227	308.1	81	3.6	28.1 ± 0.2	11.2 ± 0.8	0.173 ± 0.008	20.1 ± 1.3
	R(15e)	13.0425	406.3	93	3.6	26.9 ± 0.2	11.9 ± 0.6	0.162 ± 0.006	20.1 ± 1.3
	R(17e)	12.9634	517.9	105	3.7	26.9 ± 0.1	12.3 ± 0.5	0.14 ± 0.003	17.6 ± 1.3
	R(19e)	12.8853	643.1	117	3.7	27.2 ± 0.1	11.4 ± 0.4	0.131 ± 0.003	15.1 ± 1.3
	R(21e)	12.8082	781.8	129	3.8	27.3 ± 0.2	10.4 ± 0.4	0.108 ± 0.003	12.6 ± 1.3
	R(23e)	12.7321	934	141	3.9	28.1 ± 0.1	10.9 ± 0.5	0.08 ± 0.002	10.0 ± 1.3
	R(25e)	12.657	1099.7	153	4	27.4 ± 0.1	10.4 ± 0.3	0.092 ± 0.002	10.0 ± 1.3
o-C_2H_2 $(2\nu_5 - \nu_5)$	R(6e)	13.4074	1120.4	39	4.1	26.3 ± 0.5	9.2 ± 2.2	0.035 ± 0.005	2.6 ± 0.8
	R(10e)	13.2341	1235.5	63	3.6	27.5 ± 0.5	9.9 ± 0.1	0.045 ± 0.007	6.7 ± 0.9
	R(14e)	13.0619	1404.7	87	3.1	25.5 ± 0.8	9.9 ± 0.9	0.019 ± 0.006	3.0 ± 1.0
	R(15f)	13.0411	1457.1	93	4.1	25.6 ± 0.3	4.6 ± 0.8	0.033 ± 0.004	3.3 ± 0.4
	R(16e)	12.9761	1509.6	99	2.9	27.6 ± 0.4	9.9 ± 0.5	0.03 ± 0.003	5.1 ± 0.6
	R(17f)	12.9619	1569.2	105	4.1	28.5 ± 0.5	10 ± 1.4	0.026 ± 0.003	2.8 ± 0.5
	R(19f)	12.8838	1694.9	117	4.2	24.9 ± 0.5	4.8 ± 1.3	0.022 ± 0.004	2.1 ± 0.4
	R(21f)	12.8066	1834	129	4.3	26.2 ± 0.6	7.8 ± 1.8	0.024 ± 0.004	2.8 ± 0.6
	R(23f)	12.7305	1986.9	141	4.4	27.2 ± 0.3	8.4 ± 1.1	0.024 ± 0.002	1.6 ± 0.3
	R(25f)	12.6555	2153.1	153	4.5	27 ± 0.4	8.3 ± 1.1	0.019 ± 0.002	1.4 ± 0.3
o-C_2H_2 $(\nu_4 + \nu_5)^2 - \nu_4^1$	R(6f)	13.3762	951.6	39	2.2	26.4 ± 0.2	7.9 ± 0.7	0.06 ± 0.004	5.5 ± 0.5
	R(9e)	13.2428	1032.4	57	2	27.3 ± 0.7	9.7 ± 1.8	0.035 ± 0.005	6.3 ± 1.3

Table 3.5: continued.

Species	Transition	λ (μm)	E_l (K)	g_l	A_{ij} (s^{-1})	v_{lsr} (km s^{-1})	Δv (km s^{-1})	τ_0	N_l/N_H ($\times 10^{-7}$)
	R(10f)	13.2104	1067.1	63	2.2	28.5 ± 0.7	8.1 ± 2	0.033 ± 0.006	4.5 ± 0.9
	R(11e)	13.157	1103.5	69	1.9	28 ± 0.6	8.9 ± 2.2	0.022 ± 0.003	0.5 ± 1.0
	R(14f)	13.0492	1236.9	87	2.2	25.9 ± 0.6	9.9 ± 1.6	0.025 ± 0.003	4.4 ± 0.6
	R(16f)	12.9702	1342.1	99	2.3	27.9 ± 0.6	4.3 ± 1.7	0.031 ± 0.007	2.8 ± 0.8
	R(18f)	12.8923	1461	111	2.3	28.6 ± 0.6	5.8 ± 1.6	0.033 ± 0.006	2.6 ± 0.8
o-C_2H_2 $(\nu_4+\nu_5)^0-\nu_4^1$	R(10f)	13.2493	1067.1	63	1.4	27.8 ± 0.8	4.7 ± 2.2	0.029 ± 0.008	5.0 ± 2.5
	R(16f)	13.007	1342.1	99	1.6	26.5 ± 0.4	9.4 ± 1.1	0.028 ± 0.002	7.9 ± 1.0
	R(18f)	12.9284	1461	111	1.6	28.6 ± 0.5	6.9 ± 1.3	0.018 ± 0.003	4.3 ± 09
	R(20f)	12.8509	1593.4	123	1.6	28.1 ± 0.4	9.5 ± 1.4	0.018 ± 0.002	5.5 ± 0.8
	R(22f)	12.7745	1739.3	135	1.6	26.9 ± 0.8	12.4 ± 3	0.012 ± 0.002	3.8 ± 1.3
	R(24f)	12.6991	1898.8	147	1.6	25.6 ± 0.7	8.2 ± 1.9	0.015 ± 0.003	4.5 ± 1.0
o-C_2H_2 $(\nu_4+\nu_5)$	P(17e)	7.7579	517.9	105	2.1	25.1 ± 0.1	6.1 ± 0.4	0.121 ± 0.004	42.7 ± 2.5
	P(15e)	7.7308	406.3	93	2.1	25.3 ± 0.4	7.4 ± 1	0.054 ± 0.004	40.2 ± 6.3
	P(11e)	7.677	223.5	69	2.2	27.3 ± 0.3	10.4 ± 2.6	0.122 ± 0.026	50.2 ± 15.1
	P(5e)	7.5966	50.8	33	2.4	24.8 ± 0.3	11.2 ± 1	0.121 ± 0.007	130.6 ± 12.6
	P(3e)	7.5698	20.3	21	2.6	24.8 ± 0.3	11.8 ± 1.2	0.084 ± 0.006	104.2 ± 12.6
	R(7e)	7.423	94.8	45	2.1	24.8 ± 0.3	9.7 ± 1	0.113 ± 0.007	96.7 ± 11.3
	R(11e)	7.37	223.5	69	2.2	25.7 ± 1.4	6.7 ± 3.4	0.064 ± 0.02	41.4 ± 21.4
	R(13e)	7.3436	308.1	81	2.2	28.2 ± 0.2	5.6 ± 0.7	0.082 ± 0.005	50.2 ± 6.3
	R(15e)	7.3174	406.3	93	2.2	29.4 ± 0.5	7.1 ± 1.3	0.075 ± 0.008	52.8 ± 10.0
	R(17e)	7.2913	517.9	105	2.2	26.5 ± 0.5	7.7 ± 1.5	0.067 ± 0.008	51.5 ± 10.0
	R(19e)	7.2654	643.1	117	2.2	23.8 ± 0.6	10.4 ± 1.5	0.051 ± 0.005	47.3 ± 8.8
	R(21e)	7.2398	781.8	129	2.2	26.4 ± 0.7	5.6 ± 1.9	0.049 ± 0.009	31.4 ± 10.0
p-NH_3 ν_2 v_2=0-1	aP(7,4) E' E"	12.5906	713.5	90	3.4	29 ± 0.5	4.2 ± 1.4	0.025 ± 0.005	2.4 ± 0.6
	sP(8,5) E" E"	12.3956	892.5	102	3.0	29.5 ± 0.3	4.6 ± 0.9	0.021 ± 0.003	2.0 ± 0.1
	sP(8,4) E' E'	12.3894	939.8	102	3.7	28.5 ± 0.4	6.9 ± 1.1	0.024 ± 0.002	3.3 ± 0.4

Table 3.5: continued.

Species	Transition	λ (μm)	E_l (K)	g_l	A_{ij} (s^{-1})	v_{lsr} (km s^{-1})	Δv (km s^{-1})	τ_0	N_l/N_H ($\times 10^{-7}$)
	sP(8,1) E" E"	12.3782	1018	102	4.8	28.4 ± 0.4	5.1 ± 1.1	0.023 ± 0.003	2.3 ± 0.3
	aP(6,5) E" E'	12.35	466.7	78	1.7	28.8 ± 0.3	6.3 ± 0.9	0.03 ± 0.003	6.9 ± 0.9
	aP(6,4) E"E"	12.3107	514.3	78	3.1	28.3 ± 0.2	6.2 ± 0.4	0.043 ± 0.002	5.5 ± 0.4
	aP(6,2) E' 'E'	12.261	577.7	78	4.9	27.1 ± 0.5	7.8 ± 1.3	0.06 ± 0.007	5.4 ± 1.0
	aP(6,1) E" E'	12.2491	593.5	78	5.4	29.7 ± 0.2	6.6 ± 0.5	0.048 ± 0.002	4.5 ± 0.5
	sP(7,5) E" E"	12.094	665.2	90	2.7	28.3 ± 0.4	5.6 ± 1.0	0.026 ± 0.003	4.0 ± 0.6
	sP(7,4) E' E'	12.089	712.7	90	3.6	28.4 ± 0.4	7.3 ± 1.0	0.032 ± 0.003	4.5 ± 0.5
	sP(7,1) E" E"	12.0797	791.4	90	5.2	29.3 ± 0.5	7.9 ± 1.5	0.026 ± 0.003	3.1 ± 0.5
	aP(5,4) E' E"	12.0387	343.4	66	2.2	28.2 ± 0.3	5.8 ± 0.8	0.03 ± 0.003	6.0 ± 0.8
	aP(5,1) E" E'	11.9786	422.8	66	5.8	28.1 ± 0.2	7.7 ± 0.5	0.054 ± 0.003	4.9 ± 0.4
	sP(6,5) E" E"	11.8057	465.6	78	1.8	26.9 ± 0.6	5.8 ± 1.6	0.024 ± 0.004	5.1 ± 1.3
	sP(6,4) E' E'	11.8017	513.3	78	3.2	28.0 ± 0.5	6.6 ± 1.4	0.032 ± 0.004	4.3 ± 0.9
	sP(6,2) E' E'	11.7958	576.8	78	5.2	27.8 ± 0.4	5.7 ± 1.0	0.045 ± 0.005	4.5 ± 0.6
	sP(6,1) E" E"	11.7942	592.6	78	5.7	29.1 ± 0.3	5.6 ± 0.9	0.046 ± 0.005	3.0 ± 0.5
	aP(4,1) E" E'	11.7158	280.3	54	6.3	28.0 ± 0.1	7.6 ± 0.4	0.065 ± 0.002	5.8 ± 0.3
	sP(5,4) E' E	11.5271	342.2	66	2.3	30.6 ± 0.1	6.9 ± 0.5	0.031 ± 0.001	6.4 ± 0.5
	sP(5,2) E' E'	11.5224	406	66	5.3	27.4 ± 0.3	6.1 ± 0.8	0.039 ± 0.004	4.9 ± 0.5
	aP(3,2) E' E'	11.4714	150.1	42	4.2	32.5 ± 0.3	4.3 ± 0.7	0.035 ± 0.003	4.1 ± 0.5
	aP(3,1) E" E'	11.4604	166.1	42	6.7	28.4 ± 0.2	7.6 ± 0.6	0.043 ± 0.002	4.3 ± 0.4
	sP(4,2) E' E'	11.2613	263.4	54	5.2	26.0 ± 0.3	6.0 ± 0.8	0.038 ± 0.003	4.6 ± 0.5
	sP(4,1) E" E"	11.2603	279.3	54	6.5	25.0 ± 0.3	6.3 ± 0.7	0.04 ± 0.003	2.9 ± 0.4
	aP(2,1) E" E'	11.2122	80.4	30	6.7	24.4 ± 0.2	7.7 ± 0.6	0.041 ± 0.002	5.4 ± 0.4
	aQ(8,7) E" E'	10.7789	766.8	102	10.4	28.9 ± 0.5	7.7 ± 1.3	0.031 ± 0.004	1.6 ± 0.3
	sQ(2,1) E" E"	10.7732	79.3	30	6.9	26.4 ± 0.5	6.5 ± 1.4	0.032 ± 0.005	3.8 ± 0.9
	aQ(5,5) E" E'	10.7671	295.3	66	12.7	25.2 ± 0.5	6.6 ± 1.4	0.068 ± 0.009	3.4 ± 0.5
	aQ(4,4) E' E"	10.7539	200.5	54	12.2	27.6 ± 0.2	9.0 ± 0.7	0.079 ± 0.004	4.4 ± 0.3

Table 3.5: continued.

Species	Transition	λ (μm)	E_l (K)	g_l	A_{ij} (s^{-1})	v_{lsr} (km s^{-1})	Δv (km s^{-1})	τ_0	N_l/N_H ($\times 10^{-7}$)
	aQ(6,5) E" E'	10.7491	466.7	78	9.1	26.3 ± 0.6	10.0 ± 1.8	0.04 ± 0.005	3.6 ± 0.6
	aQ(5,4) E' E"	10.7391	343.4	66	8.1	27.1 ± 0.4	6.0 ± 1.2	0.043 ± 0.006	3.6 ± 0.5
	aQ(1,1) E" E'	10.7339	23.2	18	7.6	25.5 ± 0.4	8.9 ± 1.2	0.047 ± 0.004	4.3 ± 0.5
o-NH_3 ν_2 v_2=0-1	aP(7,3) A1" A2'	12.5607	750.4	180	4.2	29.0 ± 0.4	6.6 ± 1.2	0.062 ± 0.007	5.1 ± 1.0
	sP(8,3) A2" A2"	12.3843	976.3	204	4.2	30.2 ± 0.3	6.1 ± 0.8	0.047 ± 0.004	4.5 ± 0.5
	aP(6,3) A1" A2'	12.2814	551.3	156	4.2	27.6 ± 0.2	8.2 ± 0.5	0.067 ± 0.003	7.7 ± 0.6
	aP(6,0) A1' A2"	12.2451	598.7	156	5.5	28.6 ± 0.2	7.8 ± 0.4	0.074 ± 0.003	6.9 ± 0.4
	sP(7,6) A2' A2'	12.0997	606.7	180	1.4	28.6 ± 0.2	5.2 ± 0.6	0.03 ± 0.002	7.9 ± 0.8
	sP(7,3) A2" A2"	12.0848	749.5	180	4.4	27.8 ± 0.3	6.7 ± 0.7	0.047 ± 0.003	4.8 ± 0.5
	sP(7,0) A2' A2'	12.0791	796.6	180	5.3	28.6 ± 0.3	5.8 ± 1	0.045 ± 0.005	2.6 ± 0.1
	aP(5,3) A1" A2'	12.0101	380.5	132	3.9	27.8 ± 0.3	9.0 ± 0.8	0.069 ± 0.004	10.9 ± 1.0
	sP(6,3) A2" A2"	11.7983	550.5	156	4.4	28.2 ± 0.2	6.3 ± 0.4	0.061 ± 0.003	6.7 ± 0.4
	aP(4,0) A1' A2"	11.7121	285.7	108	6.6	27.5 ± 0.1	8.3 ± 0.4	0.101 ± 0.003	9.0 ± 0.5
	sP(5,3) A2" A2"	11.5245	379.5	132	4.1	31.7 ± 0.2	8.0 ± 0.5	0.052 ± 0.002	7.7 ± 0.5
	aP(4,3) A2" A1"	11.2628	236.7	108	3.0	25.3 ± 0.2	8.0 ± 0.7	0.049 ± 0.003	11.1 ± 1.0
	aP(2,0) A1' A2"	11.2088	85.8	60	8.9	24.5 ± 0.1	8.4 ± 0.4	0.065 ± 0.002	7.0 ± 0.4
	aQ(3,3) A1" A2?'	10.7439	123.5	84	11.4	24.8 ± 0.3	9.9 ± 1	0.086 ± 0.006	5.3 ± 0.5
	aQ(8,6) A1' A2"	10.7397	835.6	204	7.6	26.5 ± 1	9.8 ± 3.1	0.025 ± 0.006	3.6 ± 1.1
	aQ(4,3) A1" A2'	10.7322	237.7	108	6.8	27.6 ± 0.3	10.2 ± 0.8	0.067 ± 0.004	6.8 ± 0.6
	aQ(5,3) A1" A2'	10.7182	380.5	132	4.5	26.4 ± 0.4	10.6 ± 1.4	0.05 ± 0.004	8.0 ± 1.1

4 | H_2O Absorption in Circumstellar Disks of Massive Protostars at High Spectral Resolution: Full spectral survey results of AFGL 2591 and AFGL 2136

Abstract

We have performed a high-resolution 4-13 μm spectral survey of the hot molecular gas associated with the massive protostars AFGL 2591 and AFGL 2136. Here we present the results of the analysis of the ν_2 band of H_2O, detected with the Echelon Cross Echelle Spectrograph (EXES) on board the Stratospheric Observatory for Infrared Astronomy (SOFIA) between wavelengths of 5-8 μm. All lines are seen in absorption. Rotation diagrams indicate that the gas is optically thick and lines are observed to saturate at 40% and 15% relative to the continuum for AFGL 2136 and AFGL 2591, respectively. We applied two curve of growth analyses to derive the physical conditions, one assuming a foreground origin and one a circumstellar disk origin. We find temperatures of 400-600 K. A foreground origin would require the presence of externally heated clumps that are smaller than the continuum source. The disk analysis is based on stellar atmosphere theory which takes into consideration the temperature gradient in the disk. We discuss the challenges with each model and conclude that the disk origin for the absorption lines best explains the data, where a direct prediction of the stellar atmosphere model is that absorption lines should saturate at non-zero flux. Furthermore, abundance ratios are consistent with a disk chemistry. This implies the presence of a viscously heated disk that has a temperature gradient which decreases with scale height, in order to explain the presence of absorption lines.

A. G. Barr, J. Li, A. Boogert, C. N. DeWitt, E. Montiel, M. J. Richter, N. Indriolo, Y. Pendleton, J. Chiar, A. G. G. M. Tielens
The Astrophysical Journal, In review

4.1 Introduction

Water is observed throughout the universe; from diffuse and translucent clouds to dense star forming regions, shocks, protoplanetary disks and comets, evolved stars and external galaxies (van Dishoeck et al. 2013). Its importance in the environment of star forming regions is exhibited by it being one of the most abundant molecules in both the ice and gas-phases. In warm regions, due to ice sublimation (T>100 K) and gas phase chemistry (T>250 K), all of the available oxygen that is not locked up in CO or dust grains is driven into H_2O resulting in a jump in abundance from as low as 10^{-9} with respect to H in the cold envelope, to up to 10^{-4} in the hot gas close to the protostar (Boonman et al. 2003a; Boonman & van Dishoeck 2003). It is one of the main carriers of oxygen and readily detected towards low to high mass protostars, therefore it is of fundamental importance to studies of star formation.

A massive protostar forms out of a gravitationally unstable core in a dark molecular cloud (Egan et al. 1998; Zinnecker & Yorke 2007). During this process, an accretion disk develops around the protostar through which material from the envelope can be channeled onto the forming star. Due to the high accretion rates, the disk is heated from the mid-plane by viscous processes (Dullemond et al. 2007; D'Alessio et al. 1998). The disk and protostar at this stage will still be deeply embedded in the parent molecular cloud, and will remain so until after the star reaches the main sequence (Beuther et al. 2007).

Water is very difficult to observe from the ground due to the large quantity of H_2O in the Earth's atmosphere. Ideally observations would be carried out with space based facilities, to study H_2O in depth. This is reflected in the particular success of the Infrared Space Observatory (ISO) (Cernicharo & Crovisier 2005) and the Herschel Space Observatory in observing H_2O in all of the astronomical objects previously mentioned (Melnick et al. 2010; Neufeld et al. 2011; Moreno et al. 2012; van der Tak et al. 2013; van Dishoeck et al. 2021). The Stratospheric Observatory for Infrared Astronomy (SOFIA) offers an alternative opportunity for studying H_2O, as it flies above most of the water in the Earth's atmosphere, vastly reducing interference, and allowing the opportunity to observe hundreds of ro-vibrational H_2O lines, including low energy lines, and even lines tracing the ground level (Indriolo et al. 2015a).

Gas-phase H_2O absorption towards massive protostars has been studied extensively with ISO's short wavelength spectrometer (SWS) (van Dishoeck & Helmich 1996; Cernicharo et al. 1997; van Dishoeck 1998; González-Alfonso et al. 1998; Wright et al. 2000; Boonman & van Dishoeck 2003; Boonman et al. 2003a). The cold envelope and warm protostellar environment were distinguished by a "jump" in the H_2O abundance as the temperature transitioned from low to high (Boonman & van Dishoeck 2003; Boonman et al. 2003a). The low resolution ($R \sim 1400$) of ISO/SWS, however, meant that the individual ro-vibrational H_2O transitions blended into each other, creating a single broad absorption feature. The result of this was that physical conditions had to be derived assuming a single absorbing slab model in local thermodynamic equilibrium (LTE) and adopting a simple line profile. Moreover, because of the low spectral resolution, no kinematic information could be obtained.

We have conducted the first full spectral survey of the mid-infrared (mid-IR) wavelength region at high spectral resolution of two massive protostars. Previous

papers have focused on the simple organics detected, including HCN, C_2H_2, NH_3, CS and ^{13}CO (chapters 2 and 3). All species are seen in absorption and are optically thin. Abundance/column density variations are observed in HCN and C_2H_2 with absorption bands tracing the same lower level exhibiting differences up to a factor of 10. The bands at 13 μm have a lower abundance compared to bands at 7 μm, for both AFGL 2136 and AFGL 2591. If this absorption was due to foreground gas, this would imply a smaller covering factor of the continuum source at 13 μm compared to 7 μm. Knez et al. (2009) find that absorbing gas is optically thick and lines are saturated towards NGC 7538 IRS1, however lines do not go to zero flux. They suggest that this could be due to partial covering of the continuum source, however this is highly uncertain with covering factors ranging from of a few % to 100 % across two absorbing components. Barentine & Lacy (2012) found that toward NGC 7538 IRS1, the column of C_2H_2 is higher at 7 μm compared to 13 μm. They attributed this to varying opacity in the stellar photosphere with wavelength, locating the absorption lines to probe this region, however this could only account for a factor of 2 difference in the column density.

Here we discuss H_2O in the context of this spectral survey, where the fully resolved H_2O lines allow temperatures and abundances to be derived as well as the study of kinematics in these environments. The details of the survey and analysis techniques are outlined in sections 4.2 and 4.3, respectively. In section 4.4 we present the results for the H_2O lines in the contexts of both a foreground absorbing slab and a stellar atmosphere model assuming a disk origin, and in section 4.5 we discuss these results elaborating on, and comparing, the two approaches.

4.2 Observations and Data Reduction

AFGL 2591 and AFGL 2136 were observed with the Echelon Cross Echelle Spectrograph (EXES) spectrometer (Richter et al. 2018) onboard SOFIA flying observatory (Young et al. 2012) as part of SOFIA programs 05_0041 and 06_0117. In this full spectral survey of AFGL 2591 and AFGL 2136, EXES covered the range 5.3-8 μm and required 16 wavelength settings in its HIGH-LOW mode, where the high-resolution echelon grating is cross-dispersed at the lowest practical order/angle so that the instantaneous wavelength coverage was maximised. AFGL 2591 was observed to completion in March 2017, but AFGL 2136 was observed over three flight series which spanned March 2017-April 2019. The slit width was 3.2″ for all settings, providing R=55,000 resolution. The fixed slit lengths used were either 3.1″ or 2.2″, depending on the wavelength setting. In order to remove background night sky emission and telescope thermal emission, the telescope was nodded to an off-source position 15″ away from the target coordinates every 1-2 minutes. During the flight series, the precipitable water vapour (pwv) meter on SOFIA was not working, therefore the quantity of water in the atmosphere could not be measured.

Table 4.1: Summary of Observations. V_{dop} is the Earth's velocity relative to local standard rest (LSR) at the time of the observations in the direction of the YSOs. Integration time is the time spent on source.

Source	Date (UT)	Time (UT)	Wavelength Range (μm)	V_{dop} (km s^{-1})	Integration Time (s)	Longitude (deg)	Latitude (deg)	Altitude (feet)	Zenith Angle (deg)
AFGL 2591	2017-03-23	10:06:16	7.83 - 8.01	25.8	120	-101.7	44.7	42086	53.2
	2017-03-23	09:51:47	7.67 - 7.85	25.8	240	-102.6	45.8	42066	55.0
	2017-03-17	10:34:18	7.51 - 7.69	24.4	420	-104.3	44.0	44006	51.9
	2017-03-17	10:15:14	7.34 - 7.52	24.4	300	-106.5	46.9	43043	57.1
	2017-03-22	11:47:14	7.19 - 7.37	25.6	390	-124.1	34.1	43056	54.1
	2017-03-23	09:32:32	7.02 - 7.20	25.8	330	-104.2	47.6	42069	56.9
	2017-03-21	10:14:38	6.87 - 7.05	25.3	270	-100.8	43.0	43006	51.2
	2017-03-21	09:55:52	6.69 - 6.88	25.3	300	-102.5	45.3	41998	54.4
	2017-03-23	10:14:17	6.53 - 6.71	25.8	300	-100.2	42.8	42082	50.9
	2017-03-22	12:10:50	6.36 - 6.54	25.6	180	-122.8	32.4	43058	51.3
	2017-03-22	11:23:00	6.18 - 6.37	25.6	420	-126.3	36.6	43069	58.1
	2017-03-23	09:07:04	6.01 - 6.20	25.8	420	-106.7	50.1	42065	60.6
	2017-03-22	10:50:37	5.82 - 6.02	25.6	600	-128.7	39.4	43054	63.1
	2017-03-21	09:32:06	5.65 - 5.84	25.3	330	-105.0	48.4	42001	58.6
	2017-03-21	08:45:11	5.48 - 5.67	25.3	660	-109.1	52.1	42011	62.9
	2017-03-17	09:37:31	5.35 - 5.51	24.4	660	-108.9	49.7	42996	59.2
AFGL 2136	2019-04-24	10:00:12	7.83 - 8.01	40.5	256	-104.4	36.3	43014	51.8
	2017-03-23	11:55:34	7.67 - 7.85	43.8	1170	-117.6	34.5	43063	51.3
	2017-03-17	11:13:03	7.51 - 7.69	43.5	840	-110.5	38.8	44962	60.2
	2017-03-17	11:55:32	7.34 - 7.52	43.5	660	-114.7	36.0	45008	55.7
	2017-05-25	09:57:59	7.19 - 7.37	30.0	810	-121.9	38.7	43008	51.7
	2017-05-25	10:39:58	7.02 - 7.20	30.0	840	-128.8	39.4	45012	53.1
	2017-03-21	10:47:40	6.87 - 7.05	43.7	1200	-109.3	36.5	43008	56.8
	2017-03-21	11:54:08	6.69 - 6.88	43.7	1140	-117.0	32.7	43008	50.0
	2017-03-23	10:46:19	6.53 - 6.71	43.8	1440	-110.0	37.4	43083	56.3

2017-03-16	11:34:59	6.36 - 6.54	43.4	1230	-122.4	37.2	43995	60.9
2019-04-17	10:01:58	6.18 - 6.37	41.9	256	-95.1	35.4	42997	51.7
2019-04-17	08:35:48	6.01 - 6.20	41.9	256	-83.7	39.2	43006	56.5
2019-04-17	11:10:48	5.82 - 6.02	41.9	256	-105.2	34.5	43008	47.2
2019-04-23	10:19:34	5.65 - 5.84	40.7	256	-101.1	35.9	43011	49.7
2019-04-19	10:01:54	5.48 - 5.67	41.5	256	-114.8	41.9	43012	61.4
2019-04-23	11:29:01	5.35 - 5.51	40.7	256	-112.2	35.0	43015	48.2

The EXES data were reduced with the SOFIA Redux pipeline (Clarke et al. 2015), which has incorporated routines originally developed for the Texas Echelon Cross Echelle Spectrograph (TEXES) (Lacy et al. 2003). The science frames were de-spiked and sequential nod positions subtracted, to remove telluric emission lines and telescope/system thermal emission. An internal blackbody source was observed for flat fielding and flux calibration and then the data were rectified, aligning the spatial and spectral dimensions. The wavenumber solution was calibrated using sky emission spectra produced for each setting by omitting the nod-subtraction step. We used wavenumber values from HITRAN (Rothman et a. 2013) to set the wavelength scale. The resulting wavelength solutions are accurate to 0.3 km s^{-1}.

Standard star spectra were taken for several settings but were found to be of insufficient quality to be effective. In general these spectra were too noisy such that they needed to be smoothed so much that the required telluric lines were also smoothed out, making them ineffective at dividing out the atmosphere. In some cases the standard star exhibited emission features which resulted in spurious absorption features being divided into the final spectrum. One advantage of using a standard star spectrum is that, if taken straight after the science target spectrum, the baseline is largely the same as that of the science target. This allows for efficient removal of the erratic baseline and fringing that were present. We found however that the use instead of an atmospheric model, in this case from ATRAN, proved to be much more effective in removing the atmosphere. While the ATRAN model provided a more governable way of removing the atmosphere, allowing line widths to be controlled, fringing was not removed from our data. Due to the fact that the pwv metre was not working, ATRAN models were constructed at a fixed observatory altitude of 43,000 ft, and the depths of the telluric model lines were then adapted to the observed telluric lines by multiplying the model to a power, denoted Z:

$$F = \frac{F_0}{F_m^{(AZ)}} \tag{4.1}$$

where F, F_0 and F_m are the final, original and model spectra respectively, and A is the airmass, following recommendations by the instrument team and outlined in Figure 4.1. The use of telluric model in future studies would reduce the large amount of additional time required to observe a standard star spectrum.

4.2.1 Source Description

The mid-IR continuum of AFGL 2136 and AFGL 2591 is thought to originate from a disk around these massive protostars (Preibisch et al. 2003; Monnier et al. 2009; de Wit et al. 2011; Boley et al. 2013). In the case of AFGL 2136, the mid-IR continuum has been attributed to an inner dust rim with a radius of > 125 AU. The absence of small dust grains in the inner 125 AU has been attributed to excavation by photoevaporation (Monnier et al. 2009; de Wit et al. 2011; Frost et al. 2021). For AFGL 2591, a similar scenario is suggested with an absence of grains that contribute to the mid-IR continuum in the inner 65 AU (Preibisch et al. 2003; Monnier et al. 2009), although the exact radius is not well determined due to uncertainties in the adopted distance to this source. The inner 130 AU of AFGL 2136 is observed to

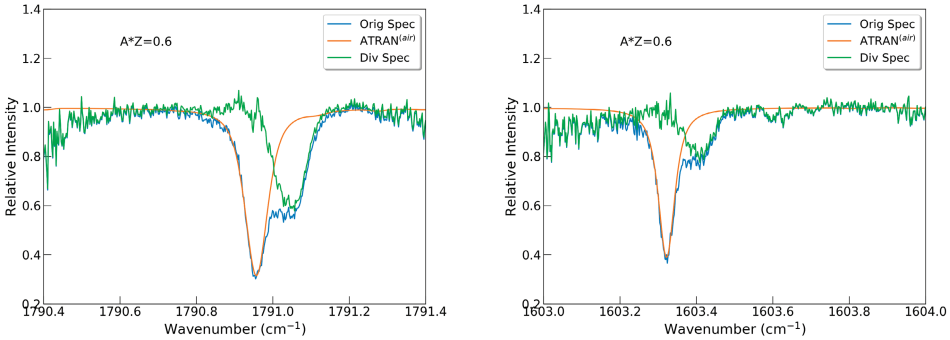

Figure 4.1: Two examples of absorption lines from AFGL 2136 from different wavelength settings illustrating the division of the telluric lines with the ATRAN model. The original spectrum is shown in blue, the ATRAN model is shown in orange, and the original spectrum divided by the ATRAN model is shown in green. The ATRAN model is scaled by multiplying the model to the power airmass to achieve a good match.

be gaseous, with a Keplerian disk observed in vibrationally excited H_2O emission detected with the Atacama Large Millimetre Array (ALMA) (Maud et al. 2019). As the emitting level is 3462 K above ground, this emission is associated with very hot gas. Coexisting with the H_2O disk are large grains (mm-size or larger) which create the sub-mm continuum and have not been photoevaporated. The sub-mm continuum is observed to cover the same extent as the gas, of around 120 AU in radius. This places the dust and gas observed at sub-mm wavelengths within the proposed dust rim responsible for the mid-IR continuum. There is evidence for a disk wind in AFGL 2136 from radial motion in the disk which could be driven by the star, supported by the detection of very compact H30α emission potentially driving an ionised disk wind (Maud et al. 2018). de Wit et al. (2011) and Frost et al. (2021) find that a hot zero-age main sequence star is too faint to provide enough N-band flux to explain the visibilities observed with the MIDI instrument on the Very Large Telescope Interferometer (VLTI). To reconcile this they propose the presence of a bloated star which contributes a few % to the total N-band flux to match the observations, in any case implying that the main source of continuum is the disk and not the central protostar. Both YSOs are associated with elongated thermal radio emission coinciding with the protostar and elongated parallel to the outflow axis (Trinidad et al. 2003; Menten & van der Tak 2004), indicative of photo-ionization of a jet-generated cone surface (Tan & McKee 2003; Tan 2008; Tanaka et al. 2016, 2017). Size estimates for these compact radio emission sources are 65 AU (Menten & van der Tak 2004) for AFGL 2136 and < 100 AU (van der Tak et al. 1999) for AFGL 2591, at the adopted distance of 3.3 kpc (Sanna et al. 2012).

4.3 Analysis

The data presented in this paper are part of a high resolution spectral survey of the 4-13 μm region of two massive young stellar objects (YSOs) AFGL 2591 VLA3 (hereafter AFGL 2591) and AFGL 2136 IRS1 (hereafter AFGL 2136). A limited set of water absorption lines in carefully selected, narrow, spectral windows has been analysed by (Indriolo et al. 2015a) and (Indriolo et al. 2020) for AFGL 2591 and AFGL 2136, respectively. In this work we build on these studies using the H_2O data from the full 5-8 μm spectral survey, containing 209 H_2O lines in AFGL 2136, and 240 lines in AFGL 2591, in the v_2=1-0 and v_2=2-1 ro-vibrational transitions of the ν_2 band. These are the numbers of lines used in this study, with many more lines having to be discarded due to the reasons outlined below.

Due to many challenges with the data reduction, the absorption lines were analysed on a line-by-line basis, instead of applying a global reduction to the spectrum as a whole. This involved normalising the science target spectrum, matching the continuum of the science spectrum and atmospheric model, and dividing the atmosphere out from each echelle order where the given absorption line was present (Fig 4.1). A first order polynomial representing the continuum was then fit over the absorption line which was then divided by this continuum to achieve a flat baseline. Naturally this introduced some systematic error in the continuum placement as not for every case was it clear where the continuum should go, and removing the baseline fluctuations was not possible since the orders could not be merged in this method. A further systematic uncertainty in the fit was poor removal of the telluric lines in places. The systematic uncertainties are estimated to be negligible to up to a factor of 0.75 of the error on the equivalent width (derived from the statistical noise) depending on the absorption line. Transitions that were blended with very deep telluric lines were discarded since it was not possible to recover the line profiles of these transitions. Likewise lines that were blended with other hot core lines were discarded.

Lines were fitted in velocity space, with either one or two gaussians depending on which was appropriate. The variables of the gaussian model were the peak velocity, v_{lsr}, velocity dispersion parameter, σ_v and the line depth. For AFGL 2136 the v_{lsr} was constrained between 24 and 28 km s^{-1} for the first component and 32 and 36 km s^{-1} for the second component. For both components, σ_v was constrained between 1 and 6 km s^{-1}. In the case of AFGL 2591, the first component was constrained to a v_{lsr} between -18 and -7 km s^{-1}. It was not possible to set the v_{lsr} of the second component as a free parameter, due to the heavy blending of the velocity components. Instead this was chosen such that it was, for all transitions, 14 km s^{-1} blue-shifted with respect to the v_{lsr} of the first component. The value of 14 km s^{-1}, however, has a certain error associated with it. This will be discussed further in section 4.4. Both components were fit with σ_v between 1 and 8 km s^{-1}. The line widths have been deconvolved with the instrument profile.

Rotation diagrams presented in section 4.4 are created using the Boltzmann equation. The column density in the lower ro-vibrational level is calculated using the optically thin relation:

$$N_i = \frac{g_l}{g_u} \frac{8\pi}{A_{ul}\lambda_{ul}^3} \int \frac{\tau_i(v)}{\phi_i(v)} dv \tag{4.2}$$

where $i = 1, 2$ for the two velocity components. N_i is the column density of the lower level, g_l and g_u are the statistical weights for the lower and upper level respectively, A_{ul} is the spontaneous emission coefficient for the transition, λ_{ul} is the wavelength of the line, $\tau(v)$ is the optical depth profile of the line in velocity space, and $1/\phi(v)$ is equal to 1 for an integrated line. If the lines are optically thin and LTE is a valid assumption, data points on the rotation diagram follow a straight line with slope -1/T_{rot}, with temperature T_{rot}.

4.3.1 Foreground Absorption

In order to attend to the effects of optical depth, we introduce a curve of growth analysis that is based on the assumption of a background light source seen through a dust-free absorbing slab of gas. The theoretical curve of growth can be approximated by:

$$\frac{W_\lambda}{b f_c \lambda} \sim \frac{\sqrt{\pi}}{c} \frac{\tau_p}{1 + \tau_p/2\sqrt{2}} \tag{4.3}$$

for $\tau_p < 1.254$ and:

$$\frac{W_\lambda}{b f_c \lambda} \sim \frac{2}{c} \sqrt{\ln[\tau_p/\ln 2] + \frac{\gamma\lambda}{4b\sqrt{\pi}}(\tau_p - 1.254)} \tag{4.4}$$

for $\tau_p > 1.254$, taken from Tielens (2021) with the additional factor $1/f_c$ to take into account a covering factor. Here W_λ is the equivalent width, λ is the wavelength, τ_p is the peak optical depth, b is the the Doppler width and γ is the damping factor. The Doppler parameter, b, is related to the velocity dispersion via $b = \sqrt{2}\sigma_v$. The expression for τ_p is given by:

$$\tau_p = \frac{\sqrt{\pi} e^2 N_l f_l \lambda}{m_e c b} \tag{4.5}$$

where N_l and f_l are the column density and oscillator strength in the lower level, respectively, e is the electron charge, m_e is the electron mass and τ_p is integrated over wavelength. In the empirical curve of growth, we introduce an additional parameter, f_c, the covering factor of the absorbing gas, which is divided into the equivalent width (e.g., the left hand side of equations 4.3 & 4.4 become $W_\lambda/b\lambda f_c$). This parameter describes the covering of the background illuminating source, where a smaller covering factor will result in a smaller observed equivalent width.

The level populations are related as follows,

$$N_l = \frac{g_l N}{Q(T)} e^{-E_l/T} \tag{4.6}$$

where Q(T) is the partition function, N is the total column density of the species, E_l is the energy of the lower level in kelvin and T is a free parameter that will be of order of T_{rot}.

4.3.2 Disk Atmosphere

Alternatively, we consider the stellar atmosphere model developed in chapter 3 and construct curves of growth in this regime also, following the stellar atmosphere theory of Mihalas (1978). Curves of growth in this approximation are constructed using the equation:

$$\frac{W}{2Y\Delta\nu} = \int_0^\infty \frac{\eta_0 H(a,v)}{1+\eta_0 H(a,v)} dv \tag{4.7}$$

where W is the equivalent width of the absorption lines in frequency space, $\Delta\nu$ is the Doppler width in units of Hz, and Y takes into account the temperature gradient in the atmosphere. For the derivation and definition of Y, see Appendix A of chapter 3. $H(a,v)$ is the Voigt profile as a function of the frequency shift, v (in velocity space and normalised to the Doppler parameter), and a the damping parameter (in Doppler units). The latter only plays a role on the square root portion of the curve of growth which is not relevant here. The right-hand side of this equation can be calculated as a function of η_0, resulting in a theoretical curve of growth. We have used the simple approximations to this provided by (Mihalas 1978). η_0 is the opacity at line centre set relative to the continuum opacity given by:

$$\eta_0 = \frac{\kappa_L(\nu=\nu_0)}{\kappa_c} = \alpha \frac{A_{ij}\lambda^3}{8\pi\sqrt{2\pi}\sigma_v} \frac{g_u}{g_l} \frac{X_l}{X_{CO}} \tag{4.8}$$

where X_l is the abundance in the lower level and α is set by the requirement that the CO abundance, X_{CO}, is 10^{-4}, which results in $\alpha = 1.3\times10^{19}$ and 2.3×10^{18} for AFGL 2136 and AFGL 2591, respectively.

As in the curve of growth for equations 4.3 to 4.5, the level populations are related by equation 4.6, with the difference that it is no longer the column density of the lower level but the abundance with respect to H nuclei; and thus N is replaced by the total abundance with respect to H, $X(H_2O)$. Adopting an abundance, temperature, and Doppler parameter for the absorbing gas, the left-hand side of equation 4.7 as well as η_0 can be calculated for each line, resulting in an empirical curve of growth.

Empirical curves of growth are created for a range of different values of T and $X(H_2O)$ and these are fit to the theoretical curve of growth. This fit is quantified by a least square process where the best combination of T and N or $X(H_2O)$ is chosen such that the reduced χ^2 is the lowest. The errors on these best fit parameters are taken from the 1σ contour in the corresponding error plot. These contour plots have been normalised to the minimum reduced χ^2 from the fitting procedure.

4.4 Results

4.4.1 AFGL 2136

For AFGL 2136 we only focus on the velocity component with peak velocity fit between 24 and 28 km s^{-1} since this is the main absorbing component seen also in HCN, C_2H_2, NH_3 and CS (chapter 3). For the v_2=1-0 band, all peak velocities are in agreement and there is no evidence for any velocity trends with opacity. We derive

an average value of 25.5±1.1 km s^{-1} for the v_{lsr}. There is however an overall increase of the line width with η_0, by a factor of 2, shown in Figure 4.2. Figure 4.3 illustrates that lines with high opacity are clearly broader.

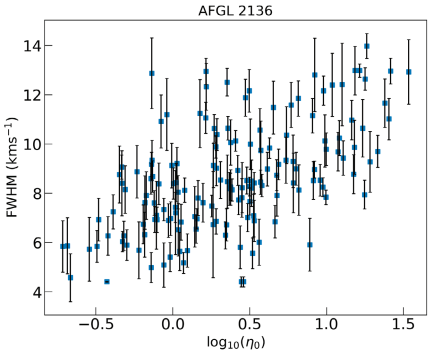

Figure 4.2: Trend between η_0 with the line width in AFGL 2136.

As was noted by Indriolo et al. (2020), the rotation diagram shows a large scatter that cannot be accounted for by the error bars (Figure 4.4). This is evident by the under-prediction of the column density of a number of lines, most prominent for those with high η_0 values i.e., high Einstein A coefficients and/or high column densities. As a result of this, the temperature and column density derived from the rotation diagram do not reflect the true physical conditions. This effect is illustrated more clearly in Figure 4.5 which shows the column density of a number of levels for which we have multiple transitions. The individual transitions should yield the same column density but as this figure illustrates, lines with high η_0 systematically yield lower column densities.

The line profiles can give further insight where, in Figure 4.6, we plot absorption lines from the $7_{2,5}$ level against an LTE model that assumes an absorbing slab of gas which is not mixed with the dust, and fully covers the background source. In this model, the equivalent width of the optically thick lines would continue to increase with column density until they saturate at zero flux. Five lines are shown with varying η_0. Observed absorption lines do not go to zero, as would be expected for very optically thick lines in the assumption of an absorbing slab, but instead saturate at 40 % relative to the continuum. Therefore lines with larger opacity exhibit a greater discrepancy with the absorbing slab model as the opacity increases. The behaviour presented in Figure 4.5 is a result of this saturation. Therefore a full curve of growth analysis is required.

We present the results of the curve of growth from the absorbing slab model for AFGL 2136 in Figure 4.7. We constrain f_c by the condition that this parameter must be equal to the depth of deepest absorption line (on a continuum-normalised flux scale). From Figure 4.6 we fix f_c to 0.4 for AFGL 2136. We then carried out the chi-squared fitting routine to find the best fit combination of T and N, for a range of different Doppler widths. We find a temperature of 457^{+13}_{-14} K and a column

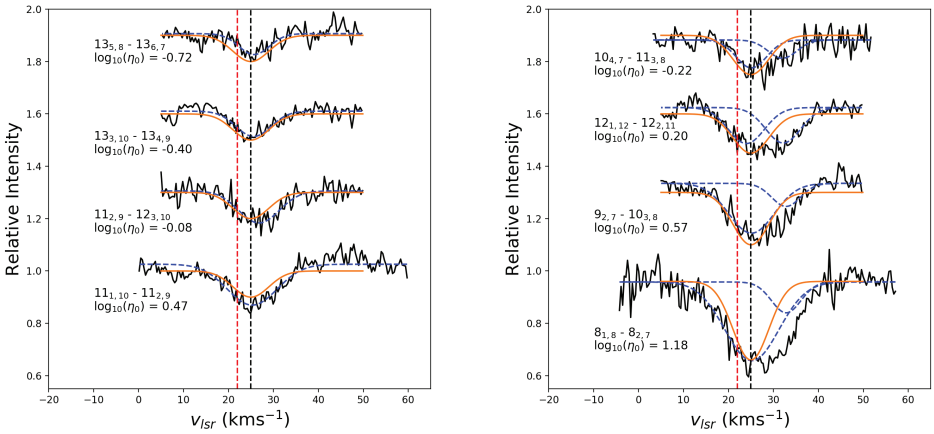

Figure 4.3: Line profiles of AFGL 2136 showing transitions of different opacity. Absorption lines are shown that exhibit one and two velocity components in the left and right panels, respectively. Shown in orange is a gaussian with a v_{lsr} of 25 km s^{-1} and a σ_v of 4 km s^{-1}. The blue dashed lines denoted the gaussian fits to each velocity component. The black dashed line at 25 km s^{-1} is added for a reference and the red dashed line at 22 km s^{-1} indicates the velocity of the gaseous envelope as observed at sub-mm wavelengths.

density $3.6^{+0.1}_{-0.1} \times 10^{18}$ cm^{-2}, for a Doppler width, b, of 3.75 km s^{-1}. This value of b corresponds to a value of 2.7 km s^{-1} for σ_v. While this is the best fit model, by eye the curve of growth does not fit well for the low opacity lines. A more linear behaviour for the low opacity lines is obtained for an excitation temperature of 600 K and a column density of $2.2{\times}10^{18}$ cm^{-2}, at the cost of an increased spread of the points around the theoretical curve of growth (and a higher chi-squared). This does not depend strongly on the adopted line width. The intrinsic σ_v may vary between 1 km s^{-1} - appropriate for thermal motion of this gas - and the observed line width of the narrowest lines (3.2 km s^{-1}), however line widths below 2.5 km s^{-1} do not fit the theoretical curve of growth. The chosen Doppler parameter introduces an uncertainty of 20% and 30% in the derived temperature and column density, respectively and does not noticeably improve the fit by eye in figure 4.7. The rotation diagram is corrected for optical depth effects by extrapolating the equivalent width for the calculated τ_p of each optically thick absorption line to a linear relation in the curve of growth. The rotation diagram is re-calculated, however the correction still shows considerable scatter (Fig 4.7).

We also pursue a curve of growth analysis based on the stellar atmosphere model presented in chapter 3. We calculate empirical curves of growth for a range of intrinsic line widths, with the constraint that σ_v must be greater than the thermal line width and less than the observed width of the optically thin lines. This sets boundaries for $1 \lessapprox \sigma_v \lessapprox 3.2$ km s^{-1}. Figure 4.8 shows the curve of growth under the assumption that lines are formed through a combination of absorption and scattering ($\epsilon = 0.5$; see chapter 3 for details). We find that the best fit value for the Doppler parameter

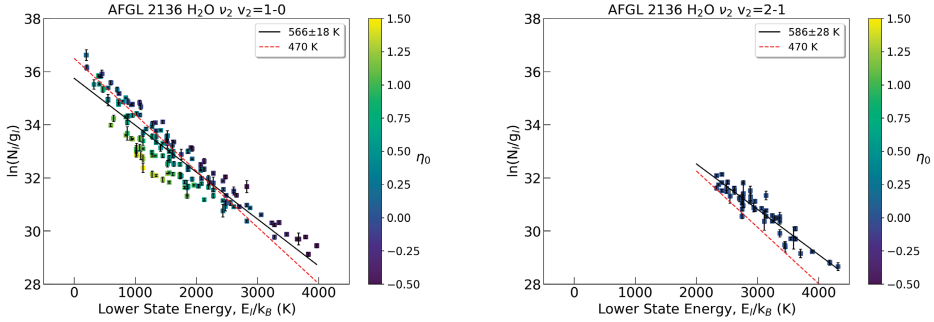

Figure 4.4: Rotation diagrams of the H_2O v=1-0 (*left*) and vibrationally excited v=2-1 (*right*) transitions of the ν_2 band in AFGL 2136. The colour bar is a function of $\log_{10}(\eta_0)$. The dashed red line denotes the temperature of 470 K derived from the curve of growth (see section 4.5.1). The solid black lines denote the fit to the rotation diagrams, and the temperatures of these fits are given in the legend.

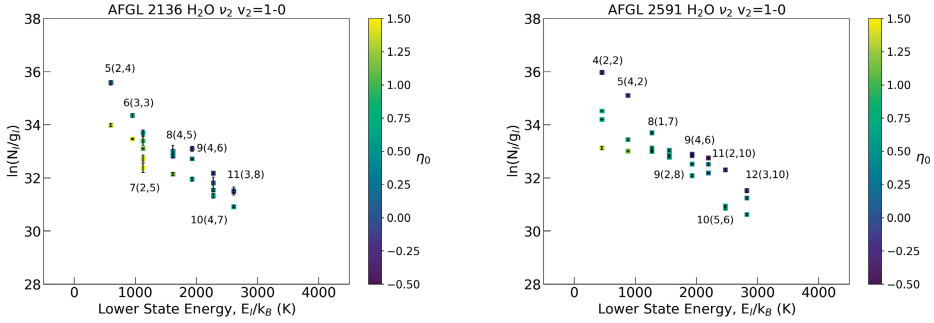

Figure 4.5: Rotation diagrams of AFGL 2136 and AFGL 2591 showing a selection of lines that have transitions out of the same lower level. These levels are indicated on the plots.

is for σ_v=3.0 km s^{-1}. The temperature and abundance with respect to CO are 470^{+24}_{-33} and $1.6^{+0.3}_{-0.1}$, respectively. This temperature is consistent with CO, CS and NH_3 in this source, whereas the temperatures of HCN and C_2H_2 are higher by 200 K (chapter 3). The cases of line formation in the approximation of pure scattering ($\epsilon = 0$) and pure absorption ($\epsilon = 1$) are also considered and shown in Figures 4.9 and 4.10 respectively. For all cases we find that σ_v of 3.0 km s^{-1} provides the best fit. The derived temperature is not very dependent on the choice of ϵ, however the abundance increases from $0.5^{+0.1}_{-0.1}$ for $\epsilon = 1$, to $1.3^{+0.1}_{-0.2}$ for $\epsilon = 0$, to $1.6^{+0.3}_{-0.1}$ for $\epsilon = 0.5$. The correction to the rotation diagram is good for all ϵ, with a closer to linear result compared to the slab model.

The temperature obtained from the slab analysis agrees with the temperature from the stellar atmosphere analysis, within the errors. The best fit value for σ_v in the stellar atmosphere model is 3.0 km s^{-1}, compared to 2.7 km s^{-1} for the slab model. We note that we cannot directly compare the column density derived from

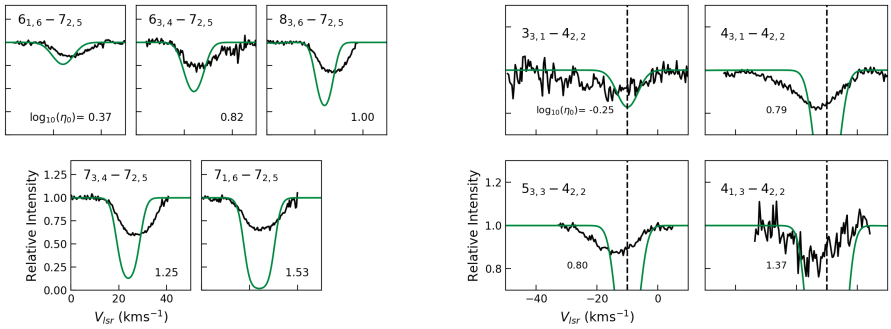

Figure 4.6: Absorption lines in AFGL 2136 of H_2O that trace the $7_{2,5}$ level (*left*) and the $4_{2,2}$ level in AFGL 2591 (*right*). The green solid line denotes a model of a background light source seen through a dust-free absorbing slab of gas, with f_c=1, generated at the physical conditions derived from the slab curves of growth. The opacities of each line, η_0, are indicated in the corresponding panels. The dashed vertical line in the plots for AFGL 2591 denotes -10 km s^{-1} for a reference.

the two methods. Goto et al. (2019) measured the ^{12}CO v=2-0 band and derived a temperature and column density of 530±80 K and 2.8±0.4 $\times 10^{19}$ cm^{-2}, respectively. With this column density we find a H_2O/CO ratio of 0.1. This is an order of magnitude lower than what we find for the H_2O abundance relative to CO from the stellar atmosphere model, however the v=2-0 band is at 2.3 μm therefore differing source sizes at difference wavelengths could have some effect. The derived physical conditions are summarised in Table 4.2 and all line parameters are given in Table 4.4 in the Appendix.

Four lines of $H_2^{18}O$ are detected in AFGL 2136 and curves of growth are shown in Figure 4.11. The temperature we derive is 252^{+7}_{-12} K and 260^{+11}_{-67}, for the stellar atmosphere and slab models respectively. This is lower than the temperature for $H_2^{16}O$ which may reflect the fact that these lines have lower energy levels, therefore probe colder gas. The abundance with respect to CO is $3.6^{+0.3}_{-0.3} \times 10^{-3}$, which results in a $^{16}O/^{18}O$ ratio of 444±83, consistent with the standard ISM value of 500 (Wilson & Rood 1994).

For the vibrationally excited v_2=2-1 band, absorption line profiles are consistent with each other and no evidence for trends in peak velocity or line width is present. The average σ_v and v_{lsr} for the v_2=2-1 band are 3.1±1.0 km s^{-1} and 25.7±1.3 km s^{-1}, respectively. This is in good agreement with the v_2=1-0 band. In the rotation diagram, all transitions can be fit with a straight line. All lines have very low values for η_0 therefore will lie on the linear part of the curve of growth. We therefore derive the temperature and abundance/column density for this band from the rotation diagram. These parameters are summarised in Table 4.2. Given the measured relative populations of the v=1-0 and v=2-1 vibrational states of H_2O, we derive a vibrational temperature of 452±57 K for H_2O, very close to the rotational temperature. The full line parameters for the v=2-1 transition are given in Table 4.4.

The ν_3=1-0 band at 2 μm was observed in absorption by Indriolo et al. (2020). All lines lie in a straight line in the rotation diagram indicative of optically thin

gas, therefore this band likely gives a reliable handle on the temperature, 502±12 K, however some lines do not reach the depth predicted by the absorbing slab model, so there are optical depth effects, also at 2 μm.

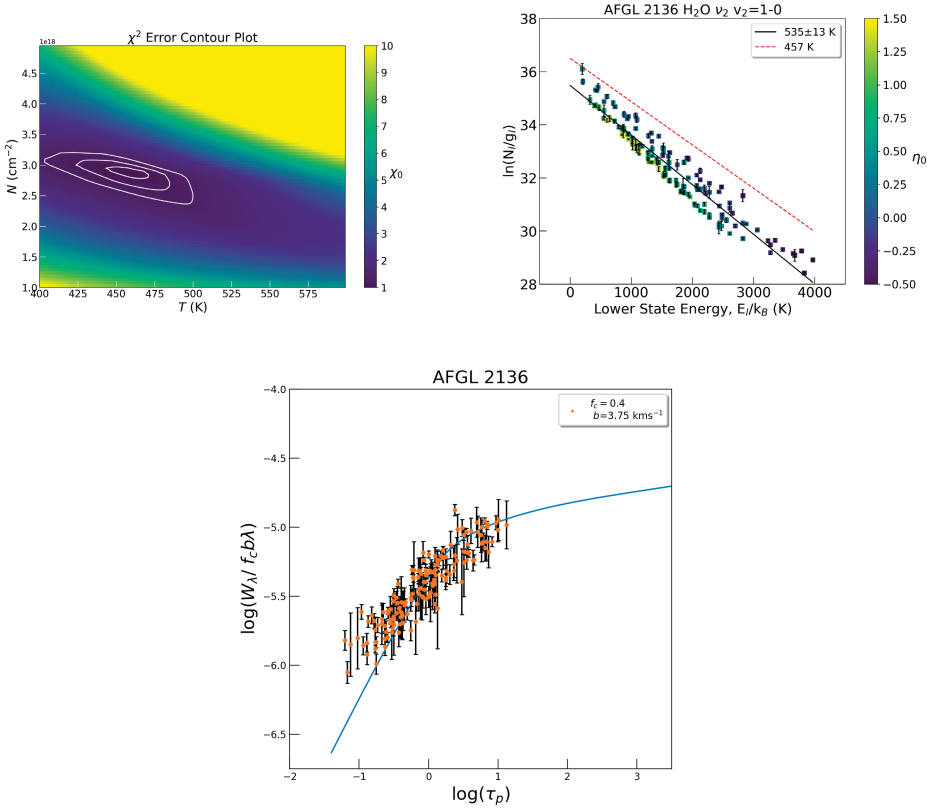

Figure 4.7: *bottom:* The curve of growth for the v=1-0 transition of AFGL 2136 for the slab model, taking a covering factor of 0.4 and b=3.75 km s^{-1}. The best fit empirical curve of growth is shown and the corresponding best fit temperature and column density are indicated. *top left*: The error on the parameters is given in the contour plot where the colour scale is the reduced χ^2 value. The contours represent the 1σ, 2σ and 3σ uncertainty levels. *top right:* The column densities for the optically thick lines were determined using the curve of growth. The best fit temperature of 457 K from the slab curve of growth is represented by the red dashed line. The black solid lines are fits to the corrected data set and the corresponding temperatures are indicated for each case.

4.4.2 AFGL 2591

The absorption line profiles in AFGL 2591 are complex. The systemic velocity of the envelope of this source is $v_{lsr} = -5.5$ km s^{-1} (van der Tak et al. 1999; Wang et al. 2012; Gieser et al. 2019). The presence of two velocity components is obvious in several examples, one at -10 km s^{-1} and one at -25 km s^{-1} (Figure 4.12) and we

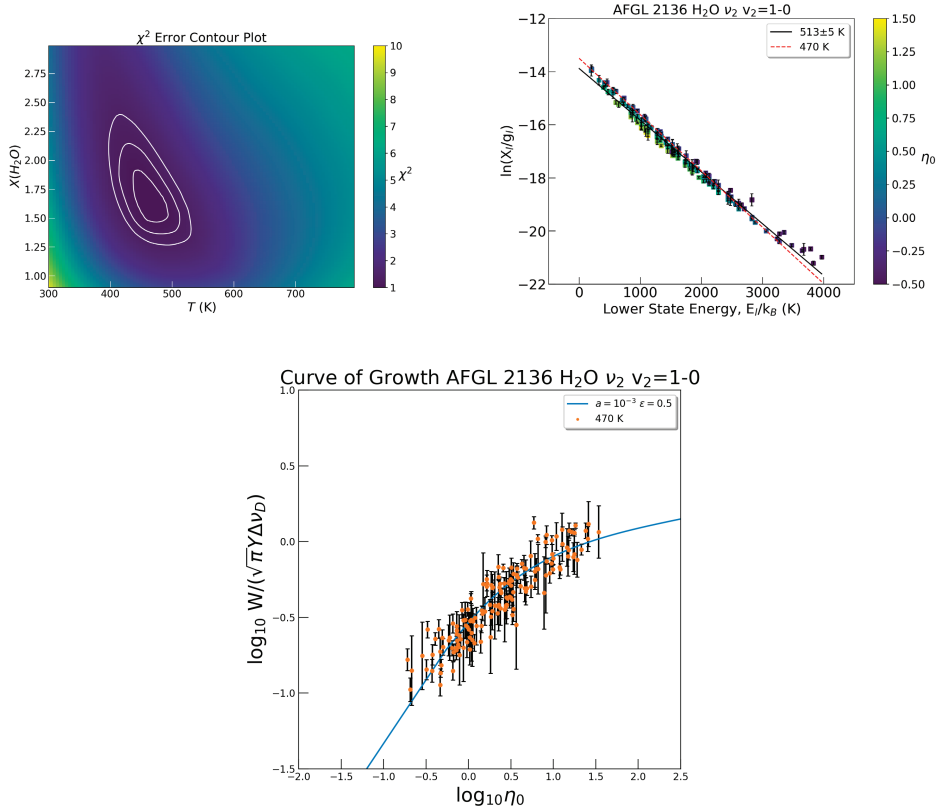

Figure 4.8: *bottom:* The curve of growth for the v=1-0 transition of AFGL 2136 for the stellar atmosphere model. The theoretical curve is for the case of a mixture of absorption and scattering. The best fit empirical curve of growth is shown and the corresponding best fit temperature and abundance are indicated. *top left*: The error on the parameters is given in the contour plot where the colour scale is the reduced χ^2 value. The contours represent the 1σ, 2σ and 3σ uncertainty levels. The H_2O abundance is quoted relative to CO. *top right:* The rotation diagram is a function of η_0 and the abundances for the optically thick lines were determined using the curve of growth. The best fit temperature of 470 K from the curve of growth is represented by the red dashed line. The black solid lines are fits to the corrected data set and the corresponding temperatures are indicated for each case. Note that the y-axis is the abundance in the lower level based on the stellar atmosphere theory.

refer to these as the major and minor components, respectively. There is no consistent trend in A or E_l for the presence and/or strength of the minor velocity component e.g. some strong lines show only one component whereas some show two, and some lines with equivalent energies show both one and two components (Figure 4.12). This may reflect different excitation conditions in the minor component compared to the major one. Due to the heavy blending of the two velocity components, in order to achieve reasonable fits the v_{lsr} of the minor component could not be left a free parameter in the fitting routine, and instead had to be fixed to a certain velocity.

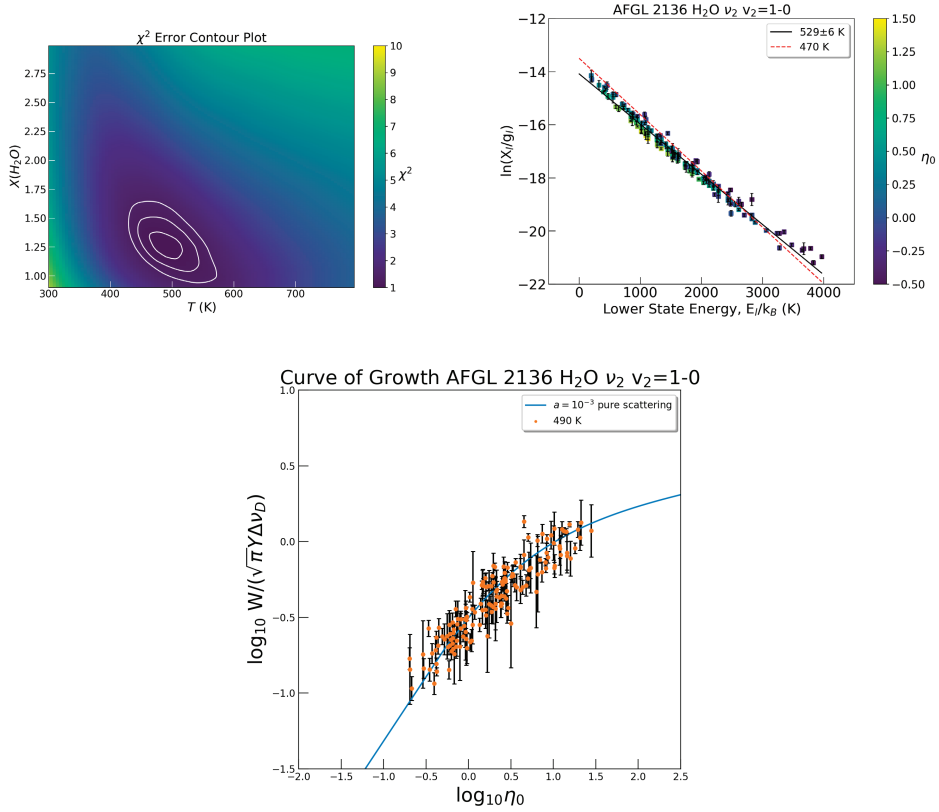

Figure 4.9: *bottom:* The curve of growth best fit for the case of pure scattering. *top left:* The error on the parameters is given in the contour plot where the colour scale is the reduced χ^2 value. The contours represent the 1σ, 2σ and 3σ uncertainty levels. The H_2O abundance is quoted relative to CO. *top right:* The rotation diagram is a function of η_0 and the abundances for the optically thick lines were determined using the curve of growth. The best fit temperature of 470 K from Table 4.2 is represented by the red dashed line. The black solid lines are fits to the corrected data set and the corresponding temperatures are indicated for each case.

In contrast to AFGL 2136, the v_2=1-0 band reveals variations in the peak velocity, with some lines appearing shifted with respect to each other. There is a general trend between the peak velocity and the opacity of the transition (Figures 4.12 & 4.13). This is the case for all lines, whether the minor component is present or not. As a result of this trend, the v_{lsr} of the minor component also changes, since it is the composite line profile that shifts. In order to minimise uncertainty of the placement of the minor component, we applied a constraint that the two velocity components should be separated by the same amount; 14 km s^{-1} for all transitions. However it is not possible to achieve this exactly, as we fix the velocity of the minor component and allow the velocity of the major component to vary. Thus the peak velocity of the major component pre-fitting was estimated by eye, looking at the composite line

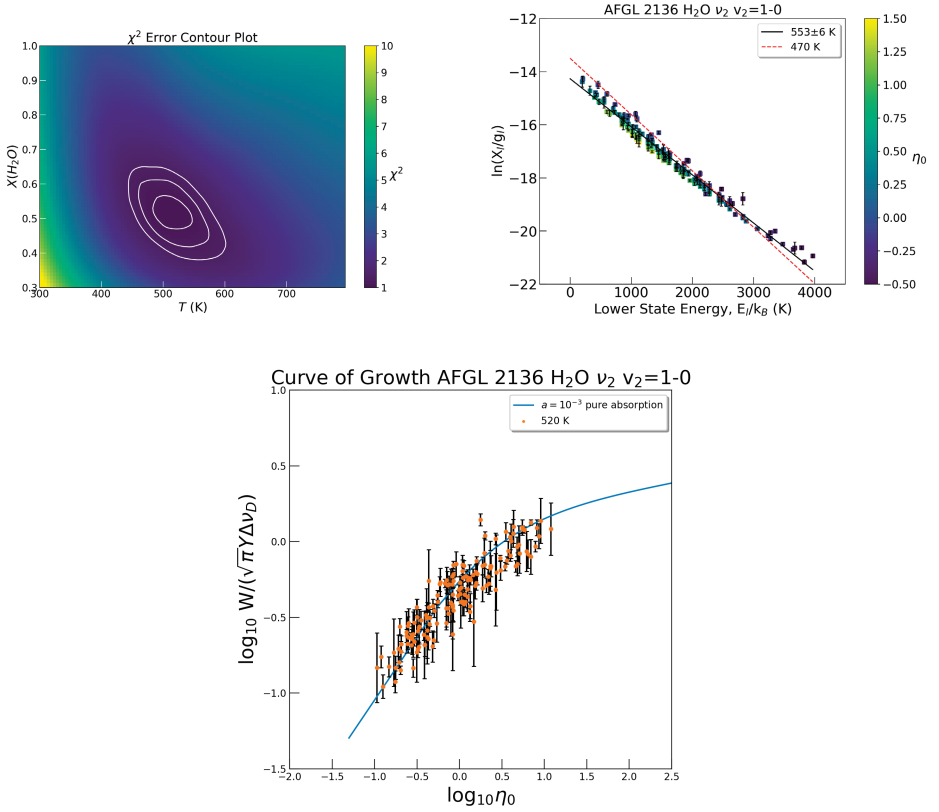

Figure 4.10: *bottom:* The curve of growth best fit for the case of pure absorption in AFGL 2136. *top left:* The error on the parameters is given in the contour plot where the colour scale is the reduced χ^2 value. The contours represent the 1σ, 2σ and 3σ uncertainty levels. The H_2O abundance is quoted relative to CO. *top right:* The rotation diagram is a function of η_0 and the abundances for the optically thick lines were determined using the curve of growth. The best fit temperature of 470 K from Table 4.2 is represented by the red dashed line. The black solid lines are fits to the corrected data set and the corresponding temperatures are indicated for each case.

profile. Then the peak velocity for the minor component to be used in the fitting was chosen based on this estimate. Naturally this leads to some uncertainties in the placement of the minor velocity component, and therefore, most importantly, the integrated line strength of the major velocity component. A separation of 14±1 km s^{-1} between the two components is more accurate, and this constraint gives a good fit to to the line profiles and curve of growths. Not accounting for the shift of the minor component introduces a large scatter in the curve of growth. Furthermore we note the lines show an overall variation in line width, illustrated in Figure 4.13. Referring to the results below, we note that this line width increases with increasing η_0.

This trend has been observed previously by Indriolo et al. (2015a), however these authors fit only 1 velocity component to every line. We have fitted two gaussian

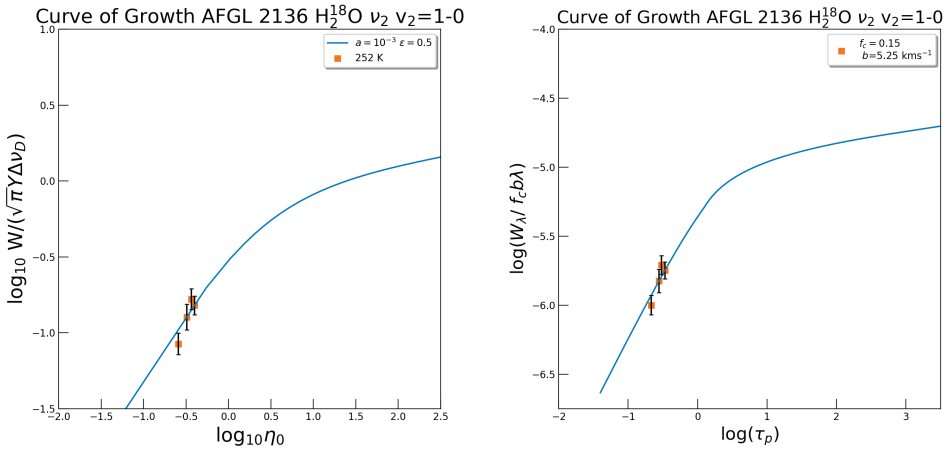

Figure 4.11: The curve of growth for $H_2^{18}O$ in AFGL 2136. The stellar atmosphere curve of growth assumes line formation by a combination of absorption and scattering.

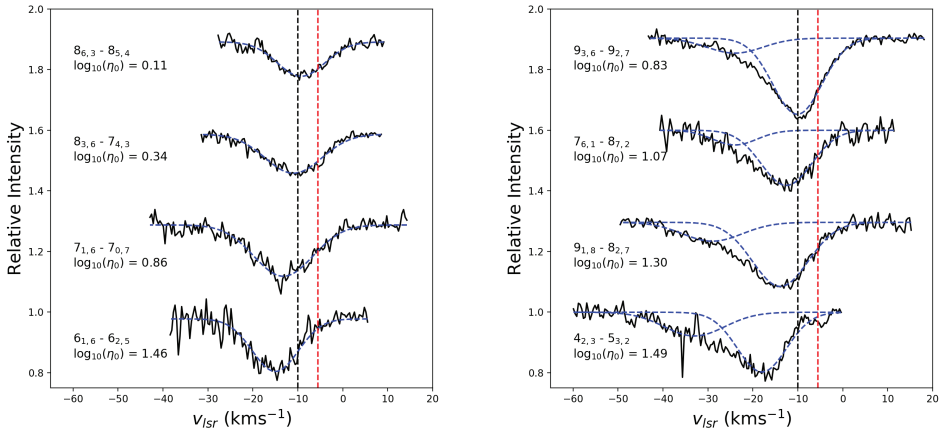

Figure 4.12: Line profiles of AFGL 2591 showing the trend in peak velocity with η_0. Transitions are shown that exhibit one and two velocity components in the left and right panels, respectively. The blue dashed lines denoted the gaussian fits to each velocity component. The black dashed line at -10 km s^{-1} is added for a reference and the red dashed line at -5.5 km s^{-1} indicates the velocity of the gaseous envelope as observed at sub-mm wavelengths.

components, but the two velocity components are not well resolved. Thus, combined with the trends in peak velocity and line width, we are limited in terms of the line fitting. It was not possible to accurately determine the physical conditions of the minor component since it is too weak and difficult to disentangle from the major component.

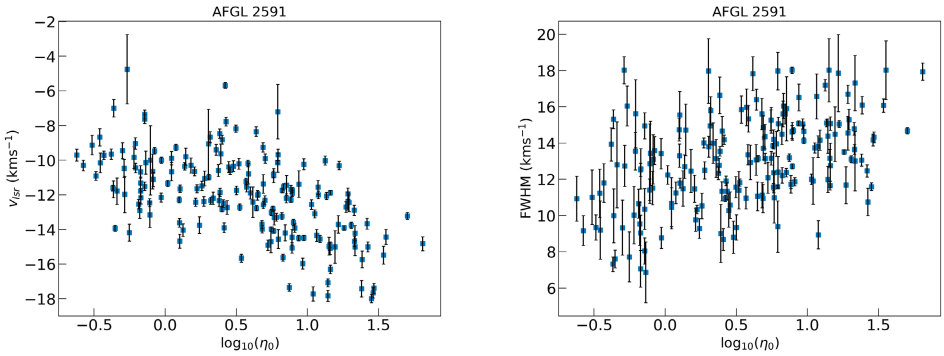

Figure 4.13: Plots illustrating the relationship between η_0 and the peak velocity and line width in AFGL 2591 on the left and right, respectively.

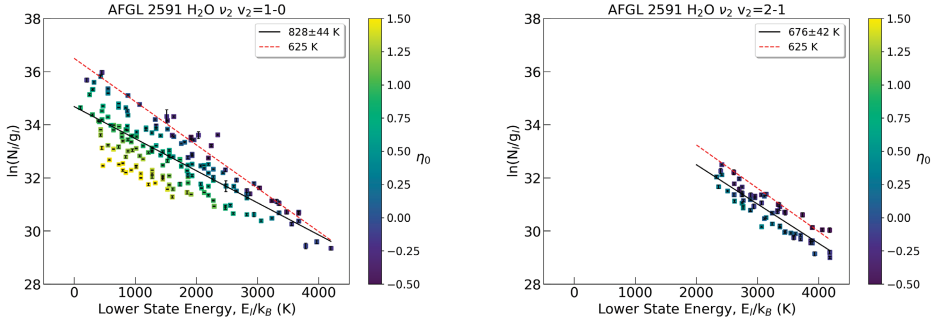

Figure 4.14: Rotation diagrams of the H_2O v=1-0 (*left*) and vibrationally excited v=2-1 (*right*) transitions of the ν_2 band in AFGL 2591. The colour bar is a function of $\log_{10}(\eta_0)$. The dashed red line denotes the temperature of 625 K derived from the curve of growth. The solid black lines denote the fit to the rotation diagrams, and the temperature of this fit is given in the legend.

The rotation diagrams for the v_2=1-0 and v_2=1-2 bands are shown in Figure 4.14. For the v_2=1-0 band, the scatter is far more accentuated compared to what is seen in AFGL 2136. Therefore the rotation diagrams do not reflect the true physical conditions and a curve of growth analysis is required. Figure 4.5 illustrates this point for levels which trace the same lower level across a range of energies.

As in AFGL 2136, Figure 4.6 shows that absorption lines do not go to zero flux, even when they have very large opacities. Four lines from the $4_{2,2}$ level are shown. These lines should have the same column density as they originate from the same lower level, however this is not the case as shown in Figure 4.5. Absorption lines saturate at 15% relative to the continuum, and therefore lines with larger and larger opacity exhibit a greater discrepancy with the absorbing slab model. Saturation occurs at a lower flux than in AFGL 2136, hence the more extreme scatter in the rotation diagram compared to AFGL 2136.

We show the results of the curve of growth analysis in the approximation of an absorbing slab for AFGL 2591 in Figure 4.16. As a result of the complexity of the line profiles, the scatter in the curve of growth for AFGL 2591 is dominated by systematic error. Therefore we determine the fit to the curve based only on lines that show a single velocity component and then apply the derived physical conditions to the data set as a whole. Again we fix the value for f_c from Figure 4.6. This sets a value of approximately 0.15 for AFGL 2591. We find a best fit temperature and column density of 541^{+1}_{-8} K and $1.5^{+0.1}_{-0.1} \times 10^{19}$ cm^{-2}, respectively. The value for b which gave the lowest chi-squared value was 5.25 km s^{-1}. This value for b corresponds to a value of 3.7 km s^{-1} for σ_v. For AFGL 2591, we fix σ_v between 1 and 4 km s^{-1}.

The curve of growth in Figure 4.17 for the stellar atmosphere model gives a temperature and abundance with respect to CO of 625^{+27}_{-22} and $7.4^{+0.5}_{-0.4}$ respectively, assuming $\epsilon = 0.5$. The best fit value for σ_v in this case is 2.75 km s^{-1}. For the other processes of lines formation we find different values of σ_v fit better, with 2.0 km s^{-1} and 1.5 km s^{-1} for $\epsilon = 0$ and $\epsilon = 1$, respectively. These curves of growth are shown in Figures 4.18 and 4.19. We also find that the abundances are different with $7.9^{+0.6}_{-0.5}$ and $4.2^{+0.3}_{-0.2}$ for ϵ of 0 and 1, respectively, while the temperature varies by only 25 K.

Comparing the slab analysis to the stellar atmosphere analysis, we find that for AFGL 2591, the temperatures are significantly different, but agree within the 3σ error bars, with 541^{+11}_{-21} K and 625^{+82}_{-70} K, respectively. Taking the column density of $9.3{\times}10^{16}$ cm^{-2} for ^{13}CO (Mitchell et al. 1990) and a ^{12}C/^{13}C ratio of 60, we find a H_2O/CO ratio of 2.7, using the water column density derived from the slab model. This is a factor of 2-4 lower than what we derive from the stellar atmosphere curve of growth, depending on the value of ϵ. The corrected rotation diagrams for the stellar atmosphere approach are better than those for the slab model, although the slab model still does a good correction. The physical conditions are summarised in Table 4.2. All line parameters are given in Table 4.7 in the Appendix.

In the v_2=2-1 band of AFGL 2591, the rotation diagram suggests that these lines are also optically thick with $\log_{10}(\eta_0)$ approaching 1. This is confirmed by the fact that there is an overall increase in the line width with η_0. We therefore carry out a curve of growth analysis using the stellar atmosphere model on this band as well to determine the physical conditions. The results are shown in Figure 4.15. There is no evidence for a velocity trend with opacity in this band and an average value of -10.2±0.4 km s^{-1} is derived for v_{lsr}. We derive a vibrational temperature of 504±61 K, for σ_v = 2 km s^{-1}. We did not consider $H_2^{18}O$ detected in our spectra of AFGL 2591. Two lines are present however were blended with other source lines, and most strong lines that should have been detected were not. All line parameters for the v=2-1 band are given in Table 4.8 in the Appendix.

H_2O line profiles agree well with those of the other molecules in this source. In a previous analysis, all species were fit with only one gaussian, assuming that absorption originated from one velocity component (chapter 3). A number of H_2O lines clearly reveal the presence of two velocity components, which is not obvious in the other molecules. If the other species were fit with two velocity components instead of one, the equivalent width of the lines would be lower and thus the abundances calculated would be reduced. We find that this is only a small effect, however, not more than a factor of 1.3. The HCN opacities are of the order of the optically thin H_2O lines. This

is reflected in the rotation diagram where the data lie along a straight line indicative of optically thin gas in LTE. Therefore the HCN lines could not have broadened after saturating at non-zero flux.

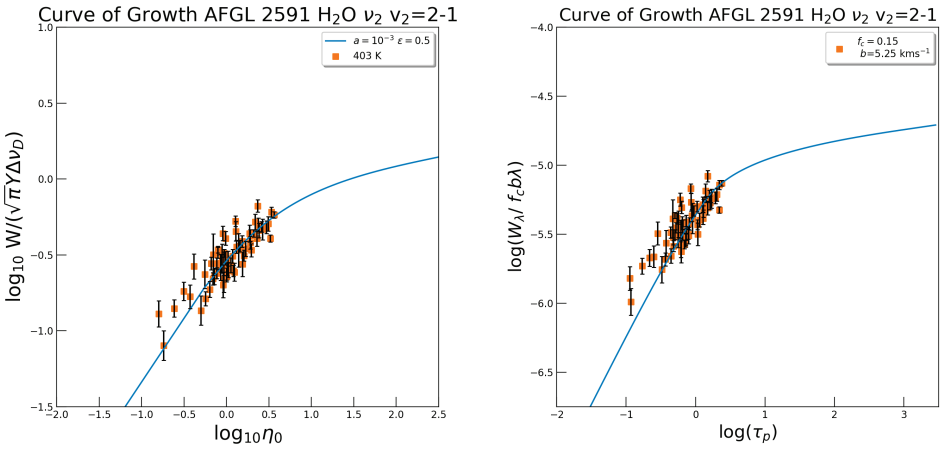

Figure 4.15: Curve of growth for AFGL 2591 v_2=2-1 band for the absorbing slab and stellar atmosphere models in the right and left panels, respectively. The best fit temperature and abundance are shown for both cases.

Table 4.2: H_2O Absorption Physical Conditions.

Source	Band	Number of Lines	Temperature (K)	Column Density (cm^{-2})	Temperature (K)	Abundance (w.r.t CO)
			Foreground Model		Atmosphere Model	
AFGL 2136	ν_2 $v_2 = 1 - 0$	154	457^{+13}_{-14}	$3.6^{+0.1}_{-0.1} \times 10^{18}$	470^{+24}_{-33}	$1.6^{+0.3}_{-0.1}$
	ν_2 $v_2 = 2 - 1$	55	585 ± 28	$3.9 \pm 0.1 \times 10^{16}$	585 ± 28	$9.2 \pm 0.4 \times 10^{-3}$
AFGL 2591	ν_2 $v_2 = 1 - 0$	177	541^{+1}_{-8}	$1.5^{+0.1}_{-0.1} \times 10^{19}$	625^{+27}_{-22}	$7.4^{+0.5}_{-0.4}$
	ν_2 $v_2 = 2 - 1$	63	418^{+28}_{-16}	$1.0^{+0.2}_{-0.2} \times 10^{17}$	403^{+27}_{-25}	$7.3^{+0.6}_{-0.4} \times 10^{-2}$

The column density and temperature derived from the slab model curve of growth are presented as well as the abundances and temperatures from the stellar atmosphere curves of growth with $\epsilon = 0.5$. Parameters of the ν_2 v_2=2-1 band in AFGL 2136 are taken from the rotation diagram. The upper and lower subscripts denote the 1σ error from the contour plots.

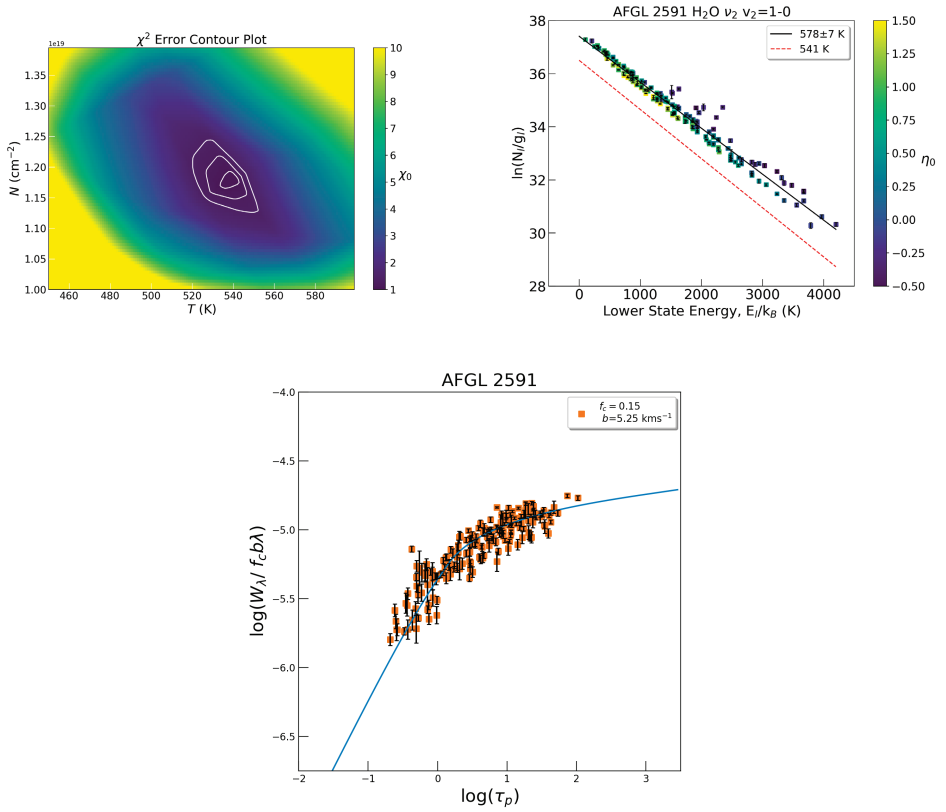

Figure 4.16: *bottom:* The curve of growth for the v=1-0 transition of AFGL 2591 for the slab model, taking a covering factor of 0.15 and b=5.25 km s^{-1}. The best fit empirical curve of growth is shown and the corresponding best fit temperature and column density are indicated. All lines are included here calculated at the conditions derived from the lines with one velocity component. *top left*: The error on the parameters is given in the contour plot where the colour scale is the reduced χ^2 value. The contours represent the 1σ, 2σ and 3σ uncertainty levels. *top right:* The best fit temperature of 541 K from the curve of growth is represented by the red dashed line. The black solid lines are fits to the corrected data set and the corresponding temperatures are indicated for each case.

4.5 Discussion

We have presented two scenarios to explain the absorption line data obtained from the spectral survey: foreground absorption and absorption in a disk atmosphere. Here, we will discuss the advantages and challenges of each model, and subsequently we will propose which model we regard as the most robust.

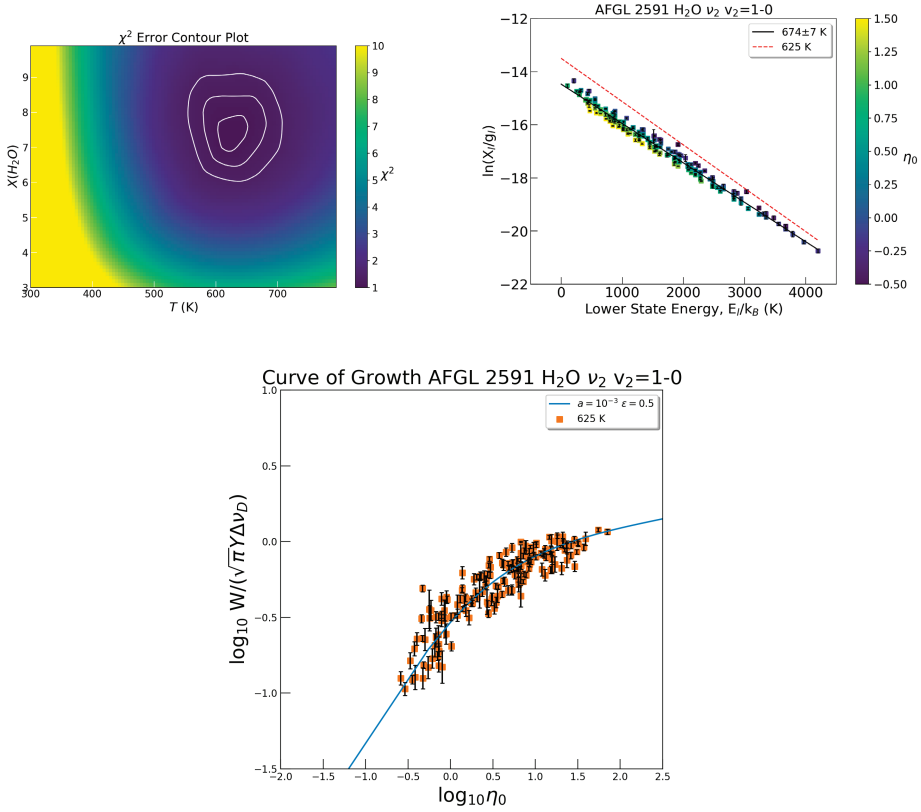

Figure 4.17: *bottom:* The curve of growth for the v=1-0 transition of AFGL 2591. The theoretical curve is for the case of $\epsilon = 0.5$. The empirical curve of growth is calculated based on the physical conditions given in Table 4.2. *top left:* The error on the parameters is given in the contour plot where the colour scale is the reduced χ^2 value. The contours represent the 1σ, 2σ and 3σ uncertainty levels. The H_2O abundance is quoted relative to CO. *top right:* The rotation diagram is a function of η_0 and the abundances for the optically thick lines were determined using the curve of growth. The best fit temperature of 625 K from the curve of growth is represented by the red dashed line. The black solid line is a fit to the corrected data set and the corresponding temperature is indicated. Note that the y-axis is the abundance in the lower level based on the stellar atmosphere theory.

4.5.1 Foreground Absorption

One explanation for the observation of absorption lines towards these massive YSOs is that these lines trace foreground absorption seen against the mid-IR continuum from the disk. This could be the sites of H_2O maser emission in these sources. H_2O masers require temperatures of around 400 K (consistent with that which we find from the curves of growth), densities of 10^8 - 10^9 cm^{-3}, and a high column density of H_2O to be produced (Elitzur et al. 1989).

H_2O masers are detected towards AFGL 2136, with the strongest maser emission coming from 27.1 km s^{-1} (Menten & van der Tak 2004), coinciding with one of

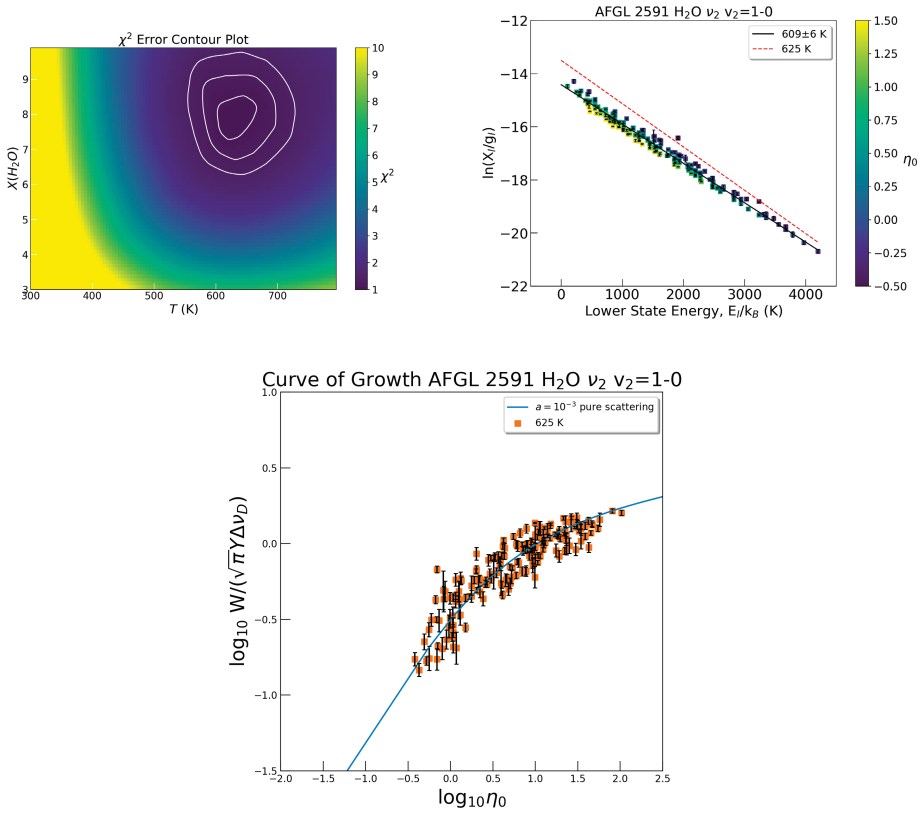

Figure 4.18: *bottom:* The curve of growth for the v=1-0 transition of AFGL 2591. The theoretical curve is for the case of $\epsilon = 0$. The empirical curve of growth is calculated based on the physical conditions given in Table 4.2. *top left:* The error on the parameters is given in the contour plot where the colour scale is the reduced χ^2 value. The contours represent the 1σ, 2σ and 3σ uncertainty levels. The H_2O abundance is quoted relative to CO. *top right:* The rotation diagram is a function of η_0 and the abundances for the optically thick lines were determined using the curve of growth. The best fit temperature of 625 K from the curve of growth is represented by the red dashed line. The black solid line is a fit to the corrected data set and the corresponding temperature is indicated. Note that the y-axis is the abundance in the lower level based on the stellar atmosphere theory.

the mid-IR H_2O velocity components seen in absorption. It should be noted that this value for the v_{lsr} has not changed in around 25 years. The maser emission arises in an area of $0.3{\times}0.5''$ (600×1000 AU) with centroid velocities ranging from 19-34 km s^{-1}. The authors find that the maser emission is coincident with the radio continuum from RS4 (in their source notation). Considering the uncertainty in the positions, AFGL 2136 IRS1 and RS4 may coincide. The authors propose that the red-shifted velocities of the H_2O maser emission suggests that it is infalling onto the protostar, and may be formed in shocked gas behind the accretion shock. The fact that we observe H_2O absorption, red-shifted with respect to the systemic velocity, would strongly support

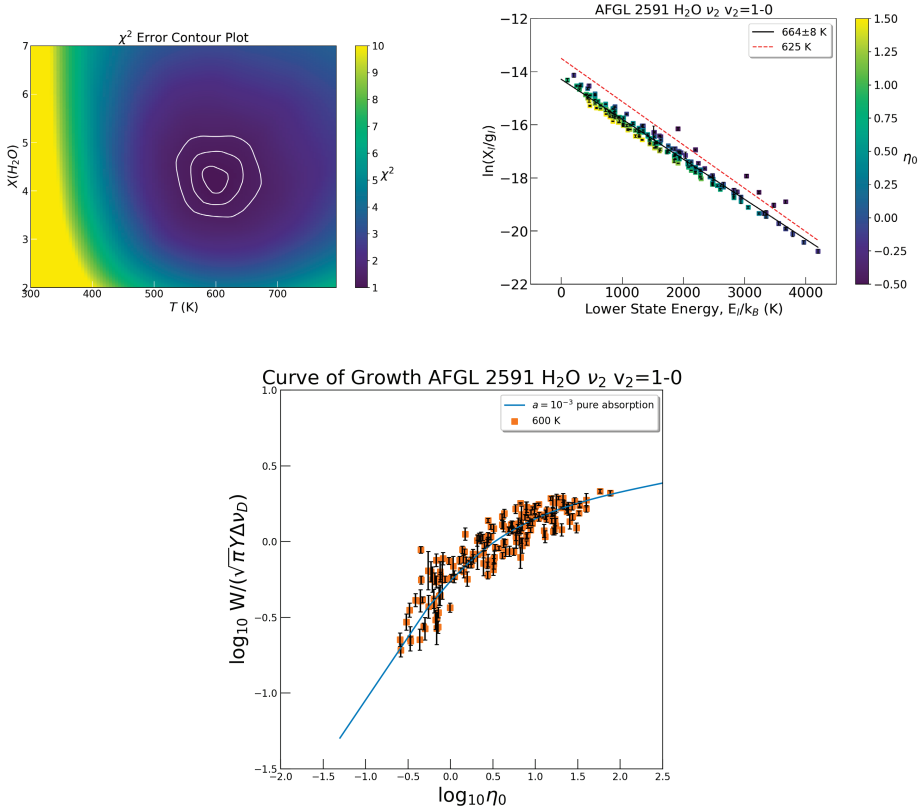

Figure 4.19: *bottom:* The curve of growth for the v=1-0 transition of AFGL 2591. The theoretical curve is for the case of $\epsilon = 1$. The empirical curve of growth is calculated based on the physical conditions given in Table 4.2. *top left:* The error on the parameters is given in the contour plot where the colour scale is the reduced χ^2 value. The contours represent the 1σ, 2σ and 3σ uncertainty levels. The H_2O abundance is quoted relative to CO. *top right:* The rotation diagram is a function of η_0 and the abundances for the optically thick lines were determined using the curve of growth. The best fit temperature of 625 K from the curve of growth is represented by the red dashed line. The black solid line is a fit to the corrected data set and the corresponding temperature is indicated. Note that the y-axis is the abundance in the lower level based on the stellar atmosphere theory.

this scenario, if the absorption came from the location of the masers.

Studies of H_2O maser emission towards AFGL 2591 conclude that it arises from the outflow cavity walls where the outflow interacts with the ambient cloud material (Trinidad et al. 2003; Torrelles et al. 2014). Sanna et al. (2012) find that the maser emission is distributed in a V-shape, opening with position angle consistent with the outflow. The velocity range of the different masers (-31 to -16 km s^{-1}; Torrelles et al. (2014)) coincides with the velocity range of the minor mid-IR H_2O absorption component. Trinidad et al. (2003) also measure 29 H_2O masers in an extended structure, and find values from -28 km s^{-1} to -9.6km s^{-1}, consistent with the range of velocities

of both the major and minor components. Thus the masers velocities also encompass the H_2O absorption line velocities in this source.

A major challenge with a foreground origin for the absorbing gas is the fact that the absorption lines do not go to zero flux, but saturate at 40 % and 15 % relative to the continuum for AFGL 2136 and AFGL 2591, respectively. If we are seeing the background source through the H_2O-rich walls of an outflow cone, then the absorbing gas must be mixed with IR emitting dust. However from models of interferometry data, the mid-IR continuum comes from ∼100 AU from the star (Monnier et al. 2009; de Wit et al. 2011; Frost et al. 2021). This is on scales sizes similar to the disk, therefore the disk is the natural source of the continuum emission.

Within the scenario of foreground absorption, a more reasonable explanation of why H_2O absorption lines do not reach zero flux is that the absorbing gas does not fully cover the infrared continuum source. This has been pursued before in several absorption line studies (Knez et al. 2009; Barentine & Lacy 2012; Indriolo et al. 2015a; Rangwala et al. 2018). We note that while the strongest maser emission in AFGL 2136 comes from two clusters that are $0.02\times0.01''$ and $0.03\times0.03''$ in size, (corresponding to ∼ 25 and 50 AU respectively, at a distance of 2 kpc) the velocity component seen in absorption at 33 km s^{-1} is not part of the strongest emission, and lies at the extremity of the maser cluster. The extent of the maser clusters is 600×1000 AU, compared to the size of the mid-IR continuum source of ∼125 AU (Monnier et al. 2009; de Wit et al. 2011; Frost et al. 2021). Thus if the H_2O absorption arises from shocked gas coinciding with the H_2O masers, in order to partially cover the source the absorbing gas must reside in blobs coinciding with the masers of corresponding velocity. This would be analogous to the scenario proposed by Knez et al. (2009), where blobs of foreground gas are seen against the circumstellar disk. These blobs would then also have to include the other molecules observed such as HCN, NH_3, CS and C_2H_2. In AFGl 2591, the masers cover a v-shape tracing the cavity walls covering only one side of the continuum, so the absorbing gas could only partially cover the source (Sanna et al. 2012).

4.5.2 Stellar Atmosphere Model

In our previous study on absorption lines of simple organic species in AFGL 2136 and AFGL 2591, we introduced an analysis based on stellar atmosphere theory under the assumption that the absorption lines originate in the disks of these protostars (chapter 3). In order to explain the presence of absorption lines, such a disk must be heated from the mid-plane such that the temperature decreases with increasing scale height. This heating is attributed to viscous accretion in the mid-plane. This same model would also apply to H_2O absorption.

The large spread in the rotation diagrams of Figures 4.4 and 4.14 is an indication that many of the H_2O absorption lines in AFGL 2136 and AFGL 2591 are optically thick. From the curves of growth we see that these lines have transitioned onto the logarithmic part of the curve of growth (Figures 4.8 & 4.17; see below). This is a consequence of the fact that these lines have saturated, resulting in the scatter in the rotation diagram.

A *direct prediction* of the stellar atmosphere model presented in chapter 3 is that

strong absorption lines will saturate at non-zero flux, therefore they may become optically thick whilst at the same time appearing as weak lines. This saturation point will be at the same flux for all lines. This is observed in both AFGL 2136 and AFGL 2591 and demonstrated in Figure 4.6, where absorption lines that trace the same lower level, but with different opacities, are compared to an absorbing slab model that fully covers the infrared source. For the low opacity lines, the absorption lines agree well with this model. However as the opacity increases, the absorption lines diverge more and more from this approximation, as the absorption lines become saturated. As discussed in section 4.5.1, fitting the data with a foreground slab necessitates the inclusion of a coverage factor less than one.

After saturation, the column density of the absorption lines are logarithmically related to the equivalent width. As a result of this, for optically thick lines, the column density will be underestimated. This is visible in Figure 4.5 where the column density of lines with higher opacity, η_0, is more underestimated than those with low opacity.

This scatter has been observed before (Indriolo et al. 2015a, 2020). Indriolo et al. (2020) noted that, in AFGL 2136, the underprediction in the column density was related to the Einstein A coefficient. Transitions with high Einstein A's and/or with large column densities will become optically thick higher up in the disk photosphere compared to optically thin lines. This translates in the rotation diagram into an apparent small column density in that level. We note that the opacity is an interplay of the Einstein A and the column density. Indeed, some lines with very similar η_0's are shifted downward in the rotation diagram by the same amount despite that they have very different Einstein A's.

In chapter 3, we located the absorbing gas to come from a clump at 50 AU, coincident with a peak in the sub-mm continuum of AFGL 2136 imaged with ALMA (Maud et al. 2019). We also adopted the same explanation for AFGL 2591. However as discussed in section 4.2, models of mid-IR interferometry observations require the continuum to originate from around 130 AU, in order to get a reasonable fit. Therefore, if the absorption lines arise in a circumstellar disk, they must probe gas beyond this radius. Such a scenario is outlined in Figure 4.20. On scales of 1000 AU, the dust is too cold to be observed at mid-IR wavelengths therefore mid-IR observations probe only a limited extent of the disk. The large grain disk in the inner 130 AU is also not seen at mid-IR wavelengths as it is optically thin.

In order to achieve a temperature structure in the disk that increases towards the mid-plane, heating of the disk has to be dominated by viscous processes in the mid-plane. Pomohaci et al. (2017) calculate the accretion rate for a sample of YSOs, estimating the accretion luminosity, L_{acc}, from Bracket γ emission, and find a low accretion rate of $1{\times}10^{-5}$ $M_\odot$/yr for AFGL 2136. AFGL 2591 has been modelled by Trinidad et al. (2003) where the authors find that the heating is dominated by stellar radiation from a radius of 20 AU, with models considered with accretion rates below $1{\times}10^{-5}$ $M_\odot/yr$. However the mass estimates for both of these YSOs of 40 $M_\odot$ (Sanna et al. 2012; Maud et al. 2019) would place these stars on the main sequence, as nuclear processes begin in the interior for masses greater than 10 $M_\odot$ during the accretion phase. Therefore their luminosity would come from hydrogen burning in the core, and accretion is not an important source of luminosity. As an aside, this does remove the need to assume a bloated star to account for the high luminosity of these

objects (de Wit et al. 2011; Frost et al. 2021). Tan & McKee (2003) developed an outflow-confined HII region model, in which high accretion rates result in a collimated morphology of the ionising radiation projected out from the star along the outflow direction, shielding the disk from protostellar feedback (Tanaka et al. 2016, 2017). The radiation from the star thus escapes through the polar direction instead of the equatorial. Because of this flashlight effect (Nakano 1989; Yorke & Bodenheimer 1999; Kuiper et al. 2016), radiation pressure does not influence the gas flow in the disk plane and massive stars can keep accreting. However, again, the star derives most of its luminosity from H-burning in the core. As a corollary, the flashlight effect prevents heating of the disk by stellar radiation. Applied to Orion Source *I* in the Orion Molecular Cloud, this model naturally explains the elongation of the radio emission from this source (Tan 2008). This model, if applied to AFGL 2136 and AFGL 2591, would explain the elongated radio emission (Trinidad et al. 2003; Menten & van der Tak 2004), and is outlined in Figure 4.20. Furthermore, it would result in the disk being shielded from stellar radiation and therefore an alternative heating mechanism for the disk is required. We note that, without external radiation heating the disk surfaces, no rim/wall would develop at the inner boundary and the mid-IR radiation would have to come from the disk surface. The scale size of this emitting surface would (still) have to be 50 AU in order to explain the visibility curves in the mid-IR (Preibisch et al. 2003; Monnier et al. 2009; de Wit et al. 2011; Frost et al. 2021).

Consider an internally heated disk. The total luminosity is given by:

$$L_{disk} = 2A < Q_p > \sigma_{sb} T_{eff}^4 \tag{4.9}$$

where A is the surface area, $< Q_p >$ the Planck averaged dust efficiency, σ_{sb} is Stefan-Boltzmann constant, and T_{eff} the effective temperature. $< Q_p >$ can be approximated as:

$$< Q_p >= 2 \times 10^{-3} \frac{a}{1\mu m} \tag{4.10}$$

for 250$<$ T $<$1000 K (cf., Chapter 5 in Tielens 2005). For a disk radius of 125 AU, a size of 50 AU and an effective temperature of 600 K, we get:

$$L_{disk} =< Q_p > 10^5 L_\odot = 10^2 \frac{a}{1\mu m} L_\odot \tag{4.11}$$

For a black body the disk would radiate 10^5 $L_\odot$, which is unrealistic. Hence the dust grains cannot be too large, the absorption/emission is not a black body, and the temperature gradient will steepen (eg., radiation escapes in frequency space rather than diffuses spatially). Taking this luminosity, we can derive the total heating of the disk in the mid-plane, or the viscous dissipation, via:

$$L_{disk} = GM_\star \dot{M}/R \tag{4.12}$$

or

$$\dot{M} = 5 \times 10^{-3} \frac{a}{1\mu m} M_\odot/yr \tag{4.13}$$

for a 40 $M_\odot$ star. The small grains in the inner disk have been removed, likely by a wind. The presence of a wind is proposed by Menten & van der Tak (2004) and Maud et al. (2018) for AFGL 2136 and Trinidad et al. (2003) for AFGL 2591. The dust inside of the rim is composed of much larger grains that have decoupled from the gas and settled in a thin layer in the mid-plane (Maud et al. 2019). Since there is still H_2O gas in the inner disk, the wind would not yet have removed all of the material. We do note that the removal of the small grains greatly reduces the dust-gas coupling to the radiation field and hence this gas has to be viscously heated as well. In the absence of small dust grains, cooling is also greatly reduced and this may lead to the high temperature required to excite the vibrationally excited H_2O line observed by ALMA (Maud et al. 2019). Detailed models will be required to assess these aspects.

Probing the Disk Wind of AFGL 2591

The presence of a velocity shift in the H_2O absorption lines with increasing opacity strongly supports the presence of a wind. Lines with higher opacity are more blue-shifted than those with lower opacities (Fig 4.12). These lines would therefore trace higher layers in a disk atmosphere that are being blown out from the disk by the wind, probing the acceleration zone. Since the orientation of AFGL 2591 is such that the disk is face on, the outflow/wind is directed towards the observer (van der Tak et al. 1999; Sanna et al. 2012), and therefore a larger blue-shift corresponds to the higher layers of the wind. Since the major and minor velocity components are separated by 14±1 km s^{-1} for every line, the velocity variation with opacity must be the same for the two components, and therefore they must both trace the same wind. These components would probe different layers of the disk however, since the peak velocities of the two components are different for the same absorption line. It is unclear however how these two components can have the same acceleration whilst arising in different layers of the disk wind. It is possible that there is a difference in the acceleration of the order of 2 km s^{-1} that cannot be detected due to the blending of the two velocity components. This could explain the scatter in the trend observed between the peak velocity and η_0 (Figure 4.13).

4.5.3 Advantages and Disadvantages

Both the foreground and disk scenarios can provide reasonable fits to the observed behaviour of the equivalent width of the H_2O lines (section 4.5.1 and 4.5.2). However, there are a number of other aspects of the observations that a model has to face. Summarising the observational characteristics of these two sources within the confines of the general structure outlined in Section 4.4, a successful model has to account for:

1) The presence of absorption rather than emission lines.

2) Non-zero saturated lines.

3) Narrow velocity components of ∼10 km s^{-1}, and peak velocities offset from sys-

temic.

4) HCN/C_2H_2 column density differences of a factor of 4 and 10 for AFGL 2136 and AFGL 2591 respectively, between 7 and 13 μm transitions from the same level (chapter 3).

5) Ortho-to-para ratios (OPRs) for C_2H_2 less than the equilibrium value of 3

6) The chemical abundance ratios.

7) The presence of 4-13 μm absorption lines for all molecules and 3 μm emission lines for HCN and C_2H_2.

8) The presence of H_2O absorption lines originating from vibrationally excited levels.

9) The velocity trend in the H_2O transitions with line opacity for AFGL 2591.

In the remainder of this subsection we will examine both scenarios - foreground absorption slab and disk absorption - against these aspects.

Foreground Absorption

As discussed in section 4.5.1, absorption by a foreground slab can readily explain the presence of narrow absorption lines that occur at a velocity offset from the systemic velocity. By associating this foreground slab with the maser emission region(s), the range of velocities observed are described by the known maser velocities.

An externally heated layer of a disk will have a surface layer that is warmer than the interior. Hence, it would show emission lines rather than absorption lines. The foreground layer could eat away this line emission, if the foreground layer and disk are at the same radial velocity. However, as the continuum source has to be only partially covered (section 4.5.1 and below), emission lines would remain and those would actually be more prominent at the longer wavelengths where, in this scenario, the coverage is very small. Hence, within this scenario, we would have to postulate that the gas in the disk surface has a very low abundance of H_2O as well as CO, C_2H_2, HCN, CS, and NH_3. As stellar EUV photons are confined to a very narrow cone, it is unlikely that photo-dissociation of these species by FUV photons plays a role in the disk surface. Moreover, ALMA has revealed the ubiquitous presence of warm H_2O in the inner 125 AU region of AFGL 2136. If this gas can be heated and remain H_2O-rich, then the dust rim or disk should contain H_2O as well.

As introduced in section 4.1, column density variations of HCN and C_2H_2 between bands at different wavelength which trace the same lower level are observed (chapter 3). In order to explain this behaviour in the context of foreground absorption, a partial covering explanation must be invoked that varies with wavelength, and can explain a difference in column density up to a factor of 4 and 10 for AFGL 2136 and AFGL 2591, respectively. This would require that the covering factor, f_c, would have to be 0.1 and 0.015 at 13 μm, for AFGL 2136 and AFGL 2591, respectively. This

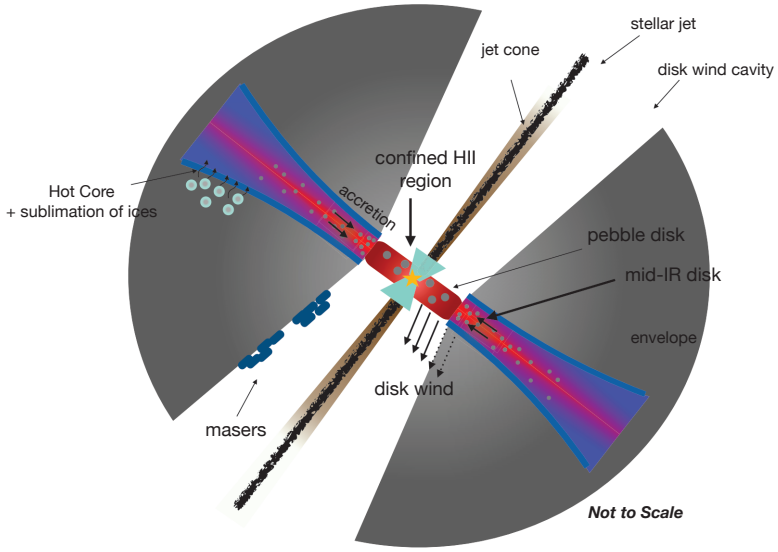

Figure 4.20: Cartoon illustration of the different physical components of the proposed disk and its surroundings (not to scale), and the mechanisms relevant to the discussion, based on observational evidence for AFGL 2136. A jet has carved a narrow channel (shown in brown) through the thick cocoon around the massive protostar. The radiation from the central star escapes through this channel, creating a flashlight effect. Near the star, the gas in the channel walls is ionised by the stellar radiation, producing a confined HII region, indicated by the green region. A disk wind, represented by the solid lines, has removed gas and small dust grains within 125 AU but leaving a thin pebble disk. The thin inner pebble disk is the source of the continuum and the vibrationally excited H_2O lines in the sub-mm while the continuum and absorption lines in the mid-IR originate from the dust disk beyond 125 AU. The disk is heated internally through viscous processes, leading to accretion. We see evidence for the wind from the mid-IR absorption lines in AFGL 2591, represented by the dotted lines. Outside of 125 AU, the disk wind is not strong enough to excavate gas and (small) grains. On a scale of 1000 AU, the disk is not warm enough to observe at mid-IR wavelengths, therefore the mid-IR disk is only observed out to a limited portion of the whole disk. At around 1000 AU, the gas is warmer than ∼100 K and ices evaporate, leading to the release of complex organic molecules (COMs) from grain surfaces as well as the gas-phase production of COMs. This is the Hot Core region. We note that there is a lack of COMs detected in a disk-like structure in AFGL 2136, but rather CH_3OH is observed in a plume structure, suggesting that this object is late on it's evolution, consistent with detection of unresolved H30α emission in a very compact region (Maud et al. 2018). AFGL 2591 on the other hand does show CH_3OH on scales of 1000 AU in a disk-like structure (Jiménez-Serra et al. 2012). The location of maser emission is located, tracing the cavity walls. The temperature and density of the disk increase towards both the mid-plane and the central star, with the colour scale representing the temperature where red is hot and blue cold. The grey-scale colour represents the surrounding envelope in which the disk is embedded. For AFGL 2591 the observer looks into the cone of the blue-shifted outflow, whereas for AFGL 2136 the observer looks more into the plane of the disk (inclination of 40°).

is, however, difficult to reconcile with a dust rim origin for the mid-IR continuum, as the whole wall would be at a very similar temperature and would not vary with wavelength. Hence, this implies that the mid-IR continuum comes from a spatially

extended disk surface, where radial distance differences will result in spatial variations in the dust temperature.

In Chapter 5 we show that HCN and C_2H_2 in AFGL 2136 are in absorption at 3 μm. Curves of growth for a foreground absorbing slab show that lines are on the linear part of the curve of growth and optically thin at all wavelengths. Thus in order to explain the observed equivalent widths, the lines at 13 μm require a partial covering factor of 0.3 and 0.25 for HCN and C_2H_2 respectively. This compares to covering factors of > 0.9 and > 0.95 for HCN and C_2H_2 respectively at both 3 μm and 7 μm, which have approximately equivalent covering factors. Thus the area of the 13 μm continuum must be three times smaller than the area of both the 3 μm and 7 μm continuum. This constraint on the covering factor of HCN and C_2H_2 means that, in the case that these species are produced in a foreground cloud, these molecules must cover the source more than H_2O, which has a covering factor of 0.4 at 6 μm. The ubiquity and high column density of H_2O in star forming regions makes this scenario highly unlikely as H_2O is very easily formed above temperatures of $\sim$250 K (Walsh et al. 2015; Agúndez et al. 2018). An OPR for C_2H_2 of 1.6 is derived, taking into consideration the partial covering factors in the curve of growth analysis.

Furthermore, the 4 to 13 μm spectral region of both sources exclusively shows lines in absorption, however the 3 μm spectrum of AFGL 2591 shows HCN and C_2H_2 lines in emission (chapter 3). AFGL 2591 is not unique in this regard with emission lines of HCN detected towards MonR2 IRS 3 at 3 μm (chapter 5). This massive YSO is another well known target that exhibits absorption lines at mid-IR wavelengths (Boonman et al. 2003a; Dungee et al. 2018). While a varying partial coverage fraction with wavelength is perhaps conceivable, that this slab would then emit in the 3 μm lines seems very unlikely.

The observations reveal absorption lines associated with v=2-1 transitions. The derived vibrational excitation temperatures of both sources are very similar to the rotational excitation temperature. This would imply densities in excess of the critical density for vibrational transitions ($\sim 10^{10}$ cm^{-3}). This is a much higher density than allowed in masers; eg., maser action requires densities below the critical density of rotational transitions and models typically yield densities of 10^9 cm^{-3} (Hollenbach et al. 2013; Neufeld & Melnick 1991). Of course, masers also require specific sight lines of high velocity coherence and so in principle the conditions in the maser spots might be different than the general region probed in absorption.

Shock heating, such as that which excites masers, cannot sustain a high enough temperature for long enough to form many of the simple organic species that are also observed in absorption (chapter 3). These include HCN, C_2H_2, NH_3 and CS, with CH_4 also being observed towards another high mass source, NGC 7538 IRS1 (Knez et al. 2009). These molecules are characteristic of disk chemistry (Walsh et al. 2015; Agúndez et al. 2018; Banzatti et al. 2017) (see Section 4.5.4). Also, by the time H_2O would form in the post-shock gas, it would have reached an equilibrium velocity and could not explain the peak velocity trend observed in AFGL 2591.

The observed OPRs of C_2H_2 are 1.8 ± 0.2 and 2.1 ± 0.3 for AFGL 2136 and AFGL 2591, respectively (chapter 3). If C_2H_2 is formed in hot gas, it should have the equilibrium OPR of 3, as opposed to cold formation on grain surfaces where the OPR is less than 3. A lower than 3 OPR, such as has been observed for C_2H_2 in Orion IRc2

(Rangwala et al. 2018), has previously been explained as gas that has been released from grain surfaces by shocks, and not had enough time to convert p-C_2H_2 to o-C_2H_2 (Timmermann 1998; Neufeld et al. 2019). This can only occur for low velocity C-type shocks with velocities ≤ 15 km s^{-1} however, since for higher velocities, large amounts of H^+ and H_3^+ rapidly convert p-C_2H_2 to o-C_2H_2, quickly achieving an OPR of 3. A shock velocity of ≤ 15 km s^{-1} is inconsistent with the J shock velocities proposed by Menten & van der Tak (2004) to explain the maser emission, therefore shocks are not a viable explanation of the low OPRs of C_2H_2.

Circumstellar Disk

Absorption lines are a natural outcome of radiative transfer in a disk atmosphere with a temperature decreasing with height. With disk densities close to or above the critical density of the levels involved, radiative transfer in the lines is dominated by absorption rather than scattering and this will lead in a natural way to saturated lines that do not go to zero. The observed velocity gradient with increasing η_0 of the H_2O lines in AFGL 2591 also fits naturally in the environment where an inner disk has been removed by a disk wind. The presence of absorption lines from vibrationally excited levels with a similar excitation temperature as the rotational population is also expected in a disk the level populations are in LTE at high densities (chapter 3).

Turning now to the challenges to the model, the difference in absorption column density between 7 and 13 μm lines of HCN and C_2H_2 originating from the same level can conceivably be explained by locating these species in a region of the disk that has the "right" conditions (i.e., temperature) to drive the chemistry to high abundances of these species (chapter 3). Indeed, the enhanced abundances of HCN and C_2H_2 are common for the inner regions of disks (Walsh et al. 2015; Agúndez et al. 2018). Therefore the abundance of HCN and C_2H_2 would be lower in the outer parts of the disk, leading to a high abundance region concentrated in the inner parts of the disk. At the longer wavelengths of 13 μm, the molecular absorption is diluted by dust emission from larger radii, where molecule formation is less efficient due to the lower temperatures, leading to the apparent column density discrepancy.

Such a thermally and chemically stratified disk may also be able to explain the presence (and characteristics) of the HCN and C_2H_2 emission lines observed in the 3 μm region of AFGL 2591. The emitting gas is cool ($\sim$200 K) and the lines are narrow. The absence of absorption lines at 3 μm implies the absence of HCN and C_2H_2 in the innermost regions of the disk where these molecules are destroyed, therefore we attributed emission lines to be produced by scattering of continuum photons higher up in the disk photosphere, thus explaining the lower temperature and narrower line width. At the longer wavelengths of 7 μm, cooler dust emission traces larger disk radii where an efficient gas phase chemistry takes place at temperatures of $\sim$600 K, which we see in absorption.

In chapter 3 we found that the low OPR of C_2H_2 could reasonably be explained by a disk atmosphere. Due to the fact that ortho lines will have three times larger column density than the para lines, these lines will become optically thick higher up in the disk photosphere compared to the para lines, thus probing a smaller column density and resulting in a slightly lower OPR than three.

The line profiles of the absorption lines present a challenge to this model however. The absorption lines of AFGL 2136 are offset from the H_2O emission line detected with ALMA, where the 232 GHz $\nu_2 = 1$ line is centred around the systemic velocity of 22 km s^{-1}. They are also around a factor of two narrower. Therefore, if the absorption lines originate in the mid-IR disk, they must only trace the red-shifted part of this disk. For AFGL 2591, the absorption lines are blue-shifted with respect to the systemic velocity. In this case they would have to probe only the blue side of the disk. This requires a specific geometry; for example a flaring disk where the completely opaque outer parts partially obscure the inner region at mid-IR wavelengths. The outer parts need to be transparent at sub-mm wavelengths, however.

In the stellar atmosphere analysis, we adopted a Doppler width based on the observed width of the optically thin lines. In this model, however, the relevant line broadening processes are thermal and microturbulent broadening. Therefore if macroscopic motions dominated the line profile, simply taking the observed line width might overestimate the Doppler width. We note that macroscopic motions such as rotation merely smear out the line profile but do not affect the equivalent width analysis (Mihalas 1978). At the temperatures we derive, the thermal contribution to the line width is around 1 km s^{-1}. Fits to the curve of growth are not possible with an intrinsic line width of < 2 km s^{-1} for any of the curves of growth, except for $\epsilon = 0$ for AFGL 2591. Therefore, microscopic turbulent processes would have to dominate the intrinsic line width, in such a way as to be greater than the sound speed (around 2 km s^{-1}). We note that dissipation of this supersonic turbulence may be a source of internal energy for the gas. As turbulence might be dissipated on a sound crossing timescale (300 yr at 100 AU), this may require a continuous replenishment of turbulence from, e.g., gravitational or magnetic energies.

The Implications for Chemistry in Disks

A CO abundance of 10^{-4} implies a dust continuum absorption of 7.7×10^{-24} and 4.3×10^{-23} cm^{-2}/g-of-gas, for AFGL 2136 and AFGL 2591, respectively. This is calculated as X_{CO}/α from equation 4.8. This is about a factor 2-10 less than in the models of Ormel et al. (2011). Overall, it seems that coagulation has proceeded to a greater extent in these disks than in the models developed by them for dense cores in molecular clouds.

The high derived abundance ratio of H_2O relative to CO implies that most of the elemental oxygen has been converted into H_2O. The dust in the region responsible for the continuum has to be warmer than 450 to 600 K and is therefore well above the ice sublimation temperature. As a result all the available oxygen will be in the gas phase. At the derived gas temperature, atomic oxygen is quickly converted into water through reactions with H_2 (Walsh et al. 2015; Agúndez et al. 2018). In our analysis, we have given abundances relative to CO, considering it likely that in the warm gas much of the available carbon has been converted into CO, resulting in an abundance of $\sim10^{-4}$ with respect to H-nuclei.

For AFGL 2591, we derive a very high H_2O/CO ratio of $7.4^{+0.5}_{-0.4}$, while typically this value is at most 2. The H_2O abundance with respect to H is also very high, ranging from 7.9×10^{-4} to 4.2×10^{-4}, as we calculate abundances under the condition

that CO to H is 1×10^{-4}. Therefore, the dust opacity implied (quoted above) is likely overestimated by around a factor of 2 or 3. This would also result in a lower CO abundance however, therefore the H_2O/CO ratio would stay the same. Whether this high abundance is due to the chemistry or an observational effect is unclear. H_2O and CO are observed at 6 and 4 μm, respectively. Since different wavelengths probe different spatial scales in the disk, spatial variations of the column densities of these molecules could lead to a difference in the abundance ratios. This would have to explain at least a factor of 2 difference, taking the H_2O abundance derived assuming $\epsilon = 1$ and taking the highest typical H_2O/CO ratio of 2. The ^{12}CO abundance of AFGL 2591 is estimated from the equivalent widths of ^{13}CO and assuming a $^{12}C/^{13}C$ ratio of 60. If this isotopologue ratio was larger than 60, this would also reduce the H_2O/CO ratio. If the ^{12}CO abundance was increased, then all the abundances quoted in Table 4.3 for AFGL 2591 would be reduced by the same factor. Alternatively CO could be depleted in this source. In AFGL 2136, the H_2O/CO abundance is within the range that would be expected for a high temperature gas-phase chemistry where a lot of water is produced. Therefore the relative abundances of the other species in AFGL 2136 are robust.

Table 4.3: Chemical Abundance Ratios.

	HCN/CO ($\times10^{-2}$)	C_2H_2/CO ($\times10^{-2}$)	NH_3/CO ($\times10^{-2}$)	HCN/C_2H_2	CS/CO ($\times10^{-3}$)	H_2O/CO
AFGL 2591	10.0	$> 0.9^a$	2.0	$< 11.2^a$	7.5	7.4^e
AFGL 2136	2.0	1.0	0.2	1.8	1.3	1.6^e
Hot Core[b]	0.03	0.02	0.02	1.5	0.1	1.7
TTauri Disk[c]	1-2	0.8-1	< 6	1-1.2	–	0.2-0.3
Herbig Disk[d]	15.0	5.0	–	3.0	3.8	1.0

[a] Upper limits are place on C_2H_2 because, while this species was detected at 13 μm in AFGL 2591, the undiluted band at 7 μm was not detected.
[b] Orion-KL observed at mm-wavelengths (Feng et al. 2015)
[c] Observations of TTauri disks by Mandell et al. (2012)
[d] Disk chemical models by Agúndez et al. (2018) assuming a H_2O/CO ratio of 1.
[e] Taking the H_2O abundance from Table 4.2.

Hot core abundance ratios of several species relevant to this discussion are summarised in Table 4.3. The abundances we derive for AFGL 2591 and AFGL 2136 are 1-2 orders of magnitude higher than what is observed in hot cores. Abundance ratios for TTauri disks calculated by Mandell et al. (2012) are consistent with other estimates of these ratios derived from disks in low mass YSOs observed with Spitzer (Salyk et al. 2011; Pontoppidan et al. 2014). These are in agreement with the abundance ratios that we derive in AFGL 2591 and AFGL 2136 (Table 4.3), as are the

abundance ratios for chemical models of Herbig disks. We caution however that the heating of Herbig and TTauri disks is by stellar radiation, therefore involves UV processing which may limit the applicability of this chemistry for the massive YSOs.

Summary

Most of the characteristics of the observed absorption lines in the mid-IR can be readily fit into the disk scenario. The most challenging aspect is the presence of narrow absorption lines shifted from the systemic velocity. This would require a specific geometry for the disk and models will have to show whether these are tenable. In contrast, absorption in foreground gas faces many challenges that are difficult to accommodate. With these considerations, we conclude that the disk origin for the absorption lines more robustly explains all of the available observational results from the spectral survey, taking into account not only absorption of H_2O, but also the other simple organics across all wavelengths. Detailed physical and chemical models for disks around massive protostars are required to fully test the disk scenario.

4.6 Conclusions

We have analysed the spectral features of H_2O in the 5-8 μm SOFIA/EXES spectral survey of the massive protostars AFGL 2136 and AFGL 2591 at a resolving power of R=50,000 (6 km s^{-1}). Our conclusions are as follows:

- Hundreds of rotational transitions of H_2O are detected in the ground and first vibrational states, as well as several lines of $H_2^{18}O$. All transitions are observed in absorption.

- Two main origins for the H_2O lines are investigated: foreground absorption against the mid-IR continuum source and an origin in the photosphere of an internally heated circumstellar disk. Using curve of growth analyses, H_2O temperatures of 457^{+13}_{-14} K and 470^{+24}_{-33} K are derived for the foreground and disk models respectively for AFGL 2136, and 541^{+1}_{-8} K and 625^{+27}_{-22} K respectively for AFGL 2591.

- We find that some lines are optically thick, even though they saturate at 40% and 15% of the continuum for AFGL 2136 and AFGL 2591, respectively, resulting in a large scatter in the rotation diagram.

- We find that, for a foreground origin for the absorption lines, the line profiles agree with H_2O maser emission in each source. However, to explain the saturation of the lines at non-zero flux, a partial covering factor must be invoked in this case. Such a covering factor must vary with wavelength by up to a factor of 10 in order to account for column density variations observed in HCN and C_2H_2 at 7 and 13 μm. Furthermore H_2O must cover the source less than HCN and C_2H_2 (chapter 5). The observed chemical abundances of HCN, C_2H_2, NH_3 and CS provide a further challenge to this interpretation. Finally, ALMA has

revealed the presence of large grains and vibrationally excited water gas in Keplerian rotation in the inner 130 AU of AFGL 2136, therefore H_2O emission lines would be expected which are not observed.

- A disk photosphere origin of the absorption lines explains in a natural way the presence of absorption lines that saturate at non zero flux. A disk origin can also account for the column density variations of HCN and C_2H_2, and low OPRs of C_2H_2, and chemical abundance ratios are characteristic of disk chemistry. However, the presence of absorption lines requires a decreasing temperature gradient with height in the disk, implying that heating of the disk is dominated by viscous dissipation in the mid-plane rather than by external illumination from the central protostar. The absence of external illumination on the disk is consistent with the flashlight effect created by the outflow cavity and the observed thermal radio morphology. Absorption lines in AFGL 2591 show velocity trends with opacity hinting at the presence of a disk wind. Finally, the peak velocities of the absorption lines are offset from the systemic velocity of the sources, and the line widths are narrower than would be expected from a disk origin, requiring a specific geometry.

- We conclude that a disk origin for the absorption lines best explains all of the available observational results from the spectral survey from water and simple organics across all wavelengths.

Acknowledgements

Based [in part] on observations made with the NASA/DLR Stratospheric Observatory for Infrared Astronomy (SOFIA). SOFIA is jointly operated by the Universities Space Research Association, Inc. (USRA), under NASA contract NNA17BF53C, and the Deutsches SOFIA Institut (DSI) under DLR contract 50 OK 0901 to the University of Stuttgart. The authors thank the anonymous referee for their very helpful and constructive input. A.G.G.M.T thanks the Spinoza premie of the NWO.

4.A Appendix

Table 4.4: Line Parameters for the v=1-0 transition of AFGL 2136. E_l is the energy of the lower level of the transition, g_l and g_u are the statistical weights of the lower and upper levels respectively, A_{ul} is the Einstein A coefficient of the transition, v_{lsr} is the peak velocity of the line, FWHM is the full width at half maximum of the line, W is the equivalent width in units of Hz and τ_p is the peak optical depth of the transition. η_0 is the opacity in the lower level of the transition calculated for $\epsilon = 0.5$. Line data were taken from the HITRAN database (Gordon et al. 2017).

Transition	λ (μm)	E_l (K)	g_l	g_u	A_{ul} (s^{-1})	v_{lsr} (km s^{-1})	FWHM (km s^{-1})	W (10^8 Hz)	$\log_{10}(\eta_0)$	$\log_{10}(\tau_p)$
$12_{2,11} - 11_{1,10}$	5.3719	2194	69	75	10.9	24.1 ± 1.8	11.2 ± 1.2	4.83 ± 0.80	0.57	0.12
$12_{1,11} - 11_{2,10}$	5.3737	2194	23	25	10.9	26.1 ± 0.7	7.9 ± 0.7	2.29 ± 0.66	0.09	-0.36
$11_{3,8} - 10_{4,7}$	5.3772	2275	63	69	3.3	26.0 ± 2.1	7.5 ± 0.9	1.64 ± 0.84	-0.06	-0.51
$9_{3,7} - 8_{2,6}$	5.3806	1414	17	19	5.0	27.2 ± 0.6	12.0 ± 0.5	4.80 ± 0.24	0.36	-0.07
$8_{3,6} - 7_{2,5}$	5.4119	1125	45	51	4.3	25.2 ± 0.6	9.6 ± 0.3	5.36 ± 0.35	1.00	0.58
$7_{6,1} - 7_{5,2}$	5.4183	1525	45	45	1.3	25.7 ± 1.8	7.9 ± 0.8	1.83 ± 0.74	0.04	-0.39
$9_{3,6} - 9_{5,4}$	5.4238	2125	57	57	1.9	26.4 ± 1.9	10.4 ± 1.1	1.82 ± 0.43	-0.23	-0.68
$11_{2,10} - 10_{1,9}$	5.4248	1860	21	23	10.2	26.7 ± 1.6	13.7 ± 0.6	5.53 ± 1.06	0.35	-0.09
$7_{3,5} - 6_{2,4}$	5.4431	867	13	15	3.9	25.6 ± 1.4	8.8 ± 0.7	3.97 ± 0.80	0.66	0.26
$10_{1,9} - 9_{2,8}$	5.4862	1554	19	21	9.5	26.7 ± 0.8	10.0 ± 0.5	4.63 ± 0.42	0.58	0.15
$10_{3,7} - 9_{4,6}$	5.4904	1929	19	21	2.6	24.9 ± 0.9	10.6 ± 0.5	1.51 ± 0.31	-0.33	-0.78
$11_{4,7} - 10_{5,6}$	5.5031	2473	63	69	1.7	25.4 ± 1.1	8.0 ± 0.6	1.14 ± 0.17	-0.49	-0.95
$9_{2,7} - 8_{3,6}$	5.5179	1447	51	57	4.6	24.3 ± 1.4	10.5 ± 0.7	5.24 ± 0.84	0.80	0.37
$11_{1,10} - 11_{0,11}$	5.5290	1909	69	69	0.8	25.2 ± 0.9	8.1 ± 0.6	1.60 ± 0.20	-0.30	-0.74
$12_{4,9} - 12_{3,10}$	5.5298	2824	75	75	2.2	24.0 ± 0.6	7.2 ± 1.0	1.12 ± 0.59	-0.67	-1.14
$10_{5,6} - 10_{4,7}$	5.5496	2275	63	63	2.7	25.2 ± 0.3	10.8 ± 0.8	1.94 ± 0.18	-0.14	-0.59
$8_{5,4} - 8_{4,5}$	5.5651	1615	51	51	2.5	25.5 ± 1.1	8.4 ± 0.6	2.65 ± 0.46	0.34	-0.09
$7_{5,3} - 7_{4,4}$	5.5670	1335	15	15	2.2	26.0 ± 0.2	9.2 ± 0.6	1.82 ± 0.15	0.02	-0.41
$5_{5,0} - 5_{4,1}$	5.5685	878	33	33	1.1	24.1 ± 1.2	8.9 ± 0.6	3.39 ± 0.57	0.49	0.08
$7_{5,2} - 7_{4,3}$	5.5775	1340	45	45	2.2	25.0 ± 0.6	9.9 ± 0.4	3.35 ± 0.24	0.50	0.07
$8_{2,7} - 7_{1,6}$	5.5836	1013	45	51	7.9	24.4 ± 2.0	12.3 ± 0.8	10.38 ± 0.71	1.40	0.99
$10_{2,9} - 10_{1,10}$	5.5870	1603	63	63	1.0	25.3 ± 2.3	8.5 ± 1.1	1.94 ± 0.82	0.03	-0.40
$8_{5,3} - 8_{4,4}$	5.5917	1628	17	17	2.6	26.2 ± 0.2	9.4 ± 0.5	1.63 ± 0.11	-0.12	-0.55

Table 4.4: continued.

Transition	λ (μm)	E_l (K)	g_l	g_u	A_{ul} (s^{-1})	v_{lsr} (km s^{-1})	FWHM (km s^{-1})	W (10^8 Hz)	$\log_{10}(\eta_0)$	$\log_{10}(\tau_p)$
$9_{3,6} - 8_{4,5}$	5.6118	1615	51	57	2.0	26.0 ± 1.4	10.2 ± 0.8	2.94 ± 1.51	0.31	-0.12
$10_{4,7} - 10_{3,8}$	5.6230	2081	63	63	2.8	25.5 ± 0.8	7.6 ± 0.4	1.65 ± 0.21	0.07	-0.38
$9_{2,8} - 9_{1,9}$	5.6485	1324	19	19	1.2	26.5 ± 0.2	10.3 ± 0.6	1.71 ± 0.13	-0.13	-0.56
$9_{1,9} - 8_{0,8}$	5.6551	1070	17	19	13.2	24.0 ± 1.8	12.3 ± 0.8	7.02 ± 2.01	1.16	0.75
$9_{4,6} - 9_{3,7}$	5.6590	1750	19	19	3.0	25.0 ± 0.8	8.8 ± 0.5	1.37 ± 0.62	-0.10	-0.54
$10_{2,8} - 10_{1,9}$	5.6645	1860	21	21	2.1	26.1 ± 0.2	8.3 ± 0.6	1.17 ± 0.11	-0.32	-0.76
$8_{4,5} - 8_{3,6}$	5.6864	1447	51	51	3.1	24.9 ± 0.7	11.3 ± 0.4	5.45 ± 0.34	0.63	0.20
$7_{4,4} - 7_{3,5}$	5.7051	1175	15	15	3.1	24.9 ± 1.1	8.7 ± 0.7	2.84 ± 0.38	0.35	-0.07
$11_{3,8} - 11_{2,9}$	5.7131	2432	69	69	3.2	28.7 ± 0.2	10.7 ± 0.5	1.95 ± 0.11	-0.14	-0.60
$6_{4,3} - 6_{3,4}$	5.7162	933	39	39	2.9	24.5 ± 4.0	10.2 ± 0.6	4.68 ± 0.71	0.96	0.55
$5_{4,2} - 5_{5,3}$	5.7217	725	11	11	2.4	24.6 ± 1.1	10.1 ± 0.4	4.61 ± 0.79	0.53	0.12
$10_{4,7} - 9_{5,4}$	5.7233	2125	57	63	1.2	26.0 ± 0.2	8.2 ± 0.4	1.03 ± 0.07	-0.33	-0.78
$8_{1,7} - 8_{0,8}$	5.7264	1070	17	17	1.4	24.1 ± 1.0	9.6 ± 0.7	2.53 ± 0.27	0.16	-0.25
$4_{4,0} - 4_{3,1}$	5.7281	552	9	9	1.6	24.5 ± 0.9	9.5 ± 0.6	2.67 ± 1.30	0.43	0.03
$8_{3,6} - 8_{2,7}$	5.7320	1274	51	51	2.7	25.2 ± 2.0	10.8 ± 0.9	6.04 ± 1.39	0.73	0.31
$9_{2,7} - 9_{1,8}$	5.7494	1552	57	57	2.6	24.6 ± 1.6	9.9 ± 0.8	3.11 ± 0.70	0.51	0.08
$6_{4,2} - 6_{3,3}$	5.7550	951	13	13	3.2	24.7 ± 1.5	10.1 ± 0.8	4.13 ± 0.70	0.51	0.10
$7_{2,6} - 7_{1,7}$	5.7735	843	15	15	1.7	25.6 ± 0.7	11.5 ± 0.4	4.99 ± 0.30	0.41	-0.01
$7_{3,5} - 7_{2,6}$	5.7792	1021	15	15	3.1	24.9 ± 1.7	11.4 ± 1.0	5.00 ± 0.73	0.50	0.09
$10_{3,7} - 10_{2,8}$	5.7995	2069	21	21	4.1	27.5 ± 0.3	8.7 ± 0.8	1.46 ± 0.17	-0.19	-0.64
$7_{1,6} - 7_{0,7}$	5.8022	843	45	45	1.8	25.0 ± 1.2	12.4 ± 0.7	7.38 ± 0.66	0.91	0.50
$11_{4,7} - 11_{3,8}$	5.8050	2609	69	69	5.3	24.7 ± 0.7	9.2 ± 0.5	2.23 ± 0.19	-0.06	-0.52
$8_{4,4} - 8_{3,5}$	5.8088	1511	17	17	4.5	26.0 ± 0.9	11.3 ± 0.5	3.65 ± 0.77	0.28	-0.15
$9_{4,5} - 9_{3,6}$	5.8280	1846	57	57	5.2	25.6 ± 0.8	8.2 ± 0.9	2.08 ± 1.40	0.56	0.12
$10_{4,6} - 10_{3,7}$	5.8289	2213	21	21	5.6	27.6 ± 0.3	8.4 ± 0.9	1.03 ± 0.14	-0.18	-0.64
$6_{2,5} - 6_{1,6}$	5.8342	643	39	39	2.1	24.0 ± 1.8	10.9 ± 0.7	7.07 ± 1.85	1.11	0.71

Table 4.4: continued.

Transition	λ (μm)	E_l (K)	g_l	g_u	A_{ul} (s^{-1})	v_{lsr} (km s^{-1})	FWHM (km s^{-1})	W (10^8 Hz)	$\log_{10}(\eta_0)$	$\log_{10}(\tau_p)$
$8_{2,6} - 8_{1,7}$	5.8380	1270	17	17	3.3	25.1 ± 1.0	9.9 ± 0.6	3.87 ± 0.38	0.37	-0.05
$6_{2,4} - 5_{3,3}$	5.8575	725	11	13	1.8	24.2 ± 0.8	9.4 ± 0.6	3.75 ± 0.33	0.50	0.10
$8_{4,5} - 7_{5,2}$	5.8656	1525	45	51	0.9	25.9 ± 1.1	9.8 ± 0.7	2.21 ± 0.96	0.03	-0.40
$9_{3,6} - 9_{2,7}$	5.8729	1729	57	57	5.2	25.0 ± 1.3	10.3 ± 0.6	4.82 ± 0.66	0.67	0.24
$8_{3,6} - 7_{4,3}$	5.8860	1340	45	51	1.0	24.9 ± 1.2	8.8 ± 0.5	2.52 ± 0.72	0.28	-0.14
$5_{2,4} - 5_{1,5}$	5.8909	470	11	11	2.5	25.6 ± 1.8	13.1 ± 0.7	7.47 ± 1.87	0.82	0.42
$7_{2,5} - 7_{1,6}$	5.9228	1013	45	45	4.4	24.5 ± 2.0	10.4 ± 0.8	5.75 ± 1.73	1.17	0.76
$8_{3,5} - 8_{2,6}$	5.9246	1414	17	17	6.1	24.5 ± 1.8	9.0 ± 0.9	3.33 ± 0.99	0.53	0.10
$7_{4,3} - 6_{5,2}$	5.9399	1278	39	45	0.6	25.1 ± 1.4	8.8 ± 0.7	2.13 ± 0.42	0.05	-0.37
$7_{3,5} - 6_{4,2}$	5.9447	1090	13	15	0.9	25.8 ± 3.0	12.5 ± 1.5	2.17 ± 0.59	-0.04	-0.46
$7_{3,4} - 7_{2,5}$	5.9507	1125	45	45	6.5	24.5 ± 1.5	9.7 ± 0.6	5.90 ± 1.79	1.25	0.83
$6_{3,3} - 6_{2,4}$	5.9530	867	13	13	6.0	24.5 ± 2.0	10.1 ± 0.8	4.28 ± 2.45	0.91	0.50
$6_{3,3} - 5_{4,2}$	5.9792	878	11	13	0.8	25.7 ± 1.1	10.0 ± 0.6	1.87 ± 0.49	0.01	-0.41
$6_{3,4} - 5_{4,1}$	6.0191	878	33	39	0.7	24.0 ± 0.5	7.1 ± 0.2	2.96 ± 0.22	0.46	0.05
$7_{2,6} - 6_{3,3}$	6.0350	951	13	15	0.6	25.2 ± 0.3	10.0 ± 0.8	1.59 ± 0.17	-0.09	-0.50
$6_{4,3} - 5_{5,0}$	6.0375	1067	33	39	0.3	25.2 ± 2.6	14.0 ± 1.4	1.94 ± 0.43	-0.14	-0.55
$5_{3,2} - 4_{4,1}$	6.0887	702	27	33	0.4	25.7 ± 1.2	12.0 ± 0.6	3.56 ± 0.76	0.27	-0.14
$5_{2,4} - 4_{3,1}$	6.0964	552	9	11	0.7	24.4 ± 0.7	9.3 ± 0.4	2.63 ± 0.22	0.25	-0.15
$4_{2,2} - 3_{3,1}$	6.1062	410	7	9	0.5	24.1 ± 0.6	8.9 ± 0.4	2.42 ± 0.16	0.16	-0.24
$4_{2,3} - 3_{3,0}$	6.1630	410	21	27	0.4	24.7 ± 0.8	10.1 ± 0.5	4.50 ± 0.35	0.57	0.18
$4_{4,1} - 5_{3,2}$	6.1698	732	33	27	0.2	24.0 ± 0.3	8.9 ± 0.5	1.37 ± 0.12	-0.12	-0.52
$3_{3,0} - 4_{2,3}$	6.2218	432	27	21	0.3	24.6 ± 1.2	10.6 ± 0.7	3.35 ± 0.38	0.28	-0.11
$3_{1,3} - 2_{2,0}$	6.2371	195	5	7	0.4	24.0 ± 3.4	12.5 ± 1.4	3.64 ± 0.55	0.18	-0.21
$5_{4,1} - 6_{3,4}$	6.2388	933	39	33	0.3	27.2 ± 0.2	9.8 ± 0.5	2.09 ± 0.13	0.08	-0.33
$2_{2,0} - 3_{1,3}$	6.2453	204	7	6	0.4	24.0 ± 1.1	7.7 ± 0.6	1.45 ± 0.34	-0.02	-0.41
$3_{2,1} - 4_{1,4}$	6.2716	323	27	21	0.3	24.0 ± 1.8	9.6 ± 0.8	2.83 ± 1.13	0.45	0.06

Table 4.4: continued.

Transition	λ (μm)	E_l (K)	g_l	g_u	A_{ul} (s^{-1})	v_{lsr} (km s^{-1})	FWHM (km s^{-1})	W (10^8 Hz)	$\log_{10}(\eta_0)$	$\log_{10}(\tau_p)$
$3_{3,1} - 4_{2,2}$	6.2827	454	9	7	0.4	25.3 ± 2.5	9.0 ± 1.4	1.59 ± 0.50	-0.11	-0.50
$4_{3,1} - 5_{2,4}$	6.2905	598	11	9	0.5	25.9 ± 1.4	8.8 ± 0.7	1.84 ± 0.36	-0.03	-0.43
$5_{3,2} - 6_{2,5}$	6.3388	795	39	33	0.5	25.3 ± 1.2	9.9 ± 0.7	3.25 ± 0.42	0.37	-0.04
$7_{4,3} - 8_{3,6}$	6.3856	1447	51	45	0.5	24.0 ± 1.5	12.2 ± 1.1	2.28 ± 0.27	-0.08	-0.50
$6_{2,4} - 6_{3,3}$	6.4531	951	13	13	11.3	24.2 ± 1.0	14.1 ± 0.3	7.35 ± 0.39	1.21	0.80
$13_{4,9} - 13_{5,8}$	6.4737	3783	81	81	15.0	25.3 ± 0.3	8.9 ± 0.9	1.66 ± 0.21	-0.48	-0.98
$9_{3,6} - 9_{4,5}$	6.4749	1957	57	57	12.7	24.4 ± 0.9	13.4 ± 0.6	6.48 ± 0.43	0.98	0.54
$3_{2,2} - 4_{1,3}$	6.5007	396	9	7	2.3	24.3 ± 0.9	12.8 ± 0.9	8.38 ± 0.77	0.77	0.37
$11_{4,7} - 11_{5,6}$	6.5067	2876	69	69	12.6	25.2 ± 1.2	14.1 ± 0.5	3.54 ± 0.24	0.22	-0.26
$9_{2,7} - 9_{3,6}$	6.5126	1846	57	57	12.2	24.0 ± 1.7	11.1 ± 0.8	4.26 ± 0.74	1.07	0.63
$7_{3,4} - 7_{4,3}$	6.5290	1340	45	45	9.5	24.3 ± 0.9	11.2 ± 0.7	5.55 ± 0.45	1.33	0.91
$13_{5,8} - 13_{6,7}$	6.5392	3966	81	81	12.5	25.7 ± 0.4	8.0 ± 1.0	1.04 ± 0.17	-0.72	-1.22
$10_{4,6} - 10_{5,5}$	6.5401	2482	21	21	11.1	25.9 ± 0.7	9.1 ± 1.7	1.21 ± 0.29	0.02	-0.44
$7_{1,6} - 7_{2,5}$	6.5474	1125	45	45	9.5	24.5 ± 3.4	14.1 ± 1.3	7.20 ± 2.86	1.53	1.12
$7_{4,4} - 8_{3,5}$	6.5818	1511	17	15	0.9	24.7 ± 0.5	10.1 ± 1.3	0.70 ± 0.12	-0.33	-0.76
$13_{3,10} - 13_{4,9}$	6.5832	3646	81	81	13.2	25.6 ± 0.2	9.1 ± 0.7	1.41 ± 0.14	-0.39	-0.89
$6_{3,4} - 6_{4,3}$	6.6007	1088	39	39	7.5	24.6 ± 3.0	14.1 ± 0.5	8.05 ± 2.75	1.42	1.00
$11_{2,9} - 11_{3,8}$	6.6594	2609	69	69	10.7	26.1 ± 0.9	10.5 ± 0.6	3.23 ± 0.28	0.42	-0.04
$9_{3,7} - 9_{4,6}$	6.6642	1929	19	19	9.4	24.8 ± 1.4	8.0 ± 0.9	2.24 ± 0.40	0.44	-0.01
$12_{4,9} - 12_{5,8}$	6.6867	3274	75	75	10.9	25.6 ± 1.1	7.4 ± 0.6	1.20 ± 0.21	-0.14	-0.63
$10_{3,8} - 10_{4,7}$	6.7052	2275	63	63	9.6	24.6 ± 2.3	12.7 ± 1.1	4.04 ± 0.76	0.65	0.20
$6_{3,4} - 7_{2,5}$	6.7146	1125	45	39	2.0	25.0 ± 2.4	9.8 ± 1.0	3.95 ± 1.49	0.82	0.40
$8_{2,7} - 8_{3,6}$	6.7157	1447	51	51	7.7	24.2 ± 2.4	12.0 ± 1.2	4.74 ± 1.03	1.23	0.81
$9_{1,8} - 9_{2,7}$	6.7288	1729	57	57	7.9	24.8 ± 2.3	13.6 ± 1.3	6.48 ± 1.37	1.04	0.60
$7_{0,7} - 7_{1,6}$	6.7731	1013	45	45	4.7	24.7 ± 1.6	12.9 ± 1.0	6.99 ± 0.83	1.38	0.97
$9_{2,8} - 9_{3,7}$	6.7826	1750	19	19	7.5	24.6 ± 1.4	8.8 ± 0.8	2.12 ± 0.40	0.53	0.09

Table 4.4: continued.

Transition	λ (μm)	E_l (K)	g_l	g_u	A_{ul} (s^{-1})	v_{lsr} (km s^{-1})	FWHM (km s^{-1})	W (10^8 Hz)	$\log_{10}(\eta_0)$	$\log_{10}(\tau_p)$
$7_{1,7} - 7_{2,6}$	6.7959	1021	15	15	4.6	24.0 ± 0.9	8.1 ± 1.1	2.71 ± 1.49	0.89	0.48
$12_{3,10} - 12_{4,9}$	6.8144	3058	75	75	9.6	25.8 ± 0.2	10.7 ± 0.7	2.48 ± 0.19	0.03	-0.45
$10_{1,9} - 10_{2,8}$	6.8251	2069	21	21	7.6	26.5 ± 0.2	11.8 ± 0.6	2.93 ± 0.19	0.29	-0.16
$13_{2,11} - 13_{3,10}$	6.8382	3475	81	81	9.8	26.1 ± 0.4	9.8 ± 1.0	1.36 ± 0.17	-0.31	-0.80
$4_{1,3} - 5_{2,4}$	6.8528	598	11	9	6.0	24.2 ± 1.8	11.3 ± 1.1	5.14 ± 0.77	1.18	0.78
$6_{0,6} - 7_{1,7}$	6.8714	843	15	13	8.1	24.9 ± 0.6	13.8 ± 0.5	6.63 ± 0.32	1.25	0.84
$8_{1,8} - 8_{2,7}$	6.8867	1274	51	51	4.4	25.2 ± 1.7	14.1 ± 1.0	6.85 ± 0.80	1.18	0.76
$11_{1,10} - 11_{2,9}$	6.9199	2432	69	69	7.3	25.3 ± 0.3	13.1 ± 0.7	3.06 ± 0.22	0.47	0.01
$11_{2,10} - 11_{3,9}$	6.9380	2439	23	23	7.2	25.8 ± 1.1	8.9 ± 0.7	1.56 ± 0.20	-0.01	-0.47
$7_{1,7} - 8_{0,8}$	6.9588	1070	17	15	7.8	25.8 ± 3.5	13.6 ± 1.7	6.83 ± 1.72	1.10	0.69
$7_{2,6} - 8_{1,7}$	6.9655	1270	17	15	5.7	25.1 ± 0.3	10.8 ± 1.1	3.19 ± 0.37	0.78	0.36
$9_{0,9} - 9_{1,8}$	6.9774	1552	57	57	4.2	24.0 ± 0.5	9.9 ± 0.4	4.08 ± 0.22	0.98	0.55
$9_{1,9} - 9_{2,8}$	6.9833	1554	19	19	4.2	27.1 ± 0.3	13.3 ± 0.9	3.20 ± 0.25	0.50	0.07
$8_{3,6} - 9_{2,7}$	7.0015	1729	57	51	3.4	25.7 ± 1.5	9.6 ± 0.8	2.65 ± 0.54	0.68	0.24
$7_{1,6} - 8_{2,7}$	7.0218	1274	51	45	5.9	24.5 ± 2.4	10.8 ± 1.2	4.27 ± 1.13	1.28	0.86
$12_{2,11} - 12_{3,10}$	7.0231	2824	75	75	7.1	24.4 ± 0.8	8.6 ± 0.6	1.56 ± 0.16	0.15	-0.32
$8_{0,8} - 9_{1,9}$	7.0559	1324	19	17	7.4	24.0 ± 0.4	10.5 ± 0.3	4.15 ± 0.19	0.92	0.50
$8_{2,7} - 9_{1,8}$	7.0617	1552	57	51	5.8	24.0 ± 1.0	11.6 ± 0.7	3.66 ± 0.32	1.08	0.65
$10_{0,10} - 10_{1,9}$	7.0818	1860	21	21	4.1	24.3 ± 1.4	10.7 ± 0.9	1.78 ± 0.23	0.26	-0.18
$10_{1,10} - 10_{2,9}$	7.0846	1861	63	63	4.1	24.6 ± 1.9	11.7 ± 1.2	2.80 ± 0.46	0.74	0.30
$10_{4,7} - 11_{3,8}$	7.0855	2609	69	63	2.2	25.1 ± 2.2	7.9 ± 1.2	1.29 ± 0.45	-0.22	-0.68
$8_{1,7} - 9_{2,8}$	7.0924	1554	19	17	5.9	24.1 ± 1.1	10.5 ± 0.7	2.82 ± 0.30	0.61	0.18
$13_{1,12} - 13_{2,11}$	7.1065	3233	81	81	7.0	25.8 ± 0.4	9.4 ± 1.1	1.59 ± 0.23	-0.18	-0.67
$9_{3,7} - 10_{2,8}$	7.1252	2069	21	19	4.0	24.5 ± 1.2	10.1 ± 0.8	1.65 ± 0.21	0.02	-0.43
$9_{2,8} - 10_{1,9}$	7.1552	1860	21	19	5.8	25.9 ± 0.7	9.8 ± 0.4	2.52 ± 0.18	0.38	-0.06
$11_{0,11} - 11_{1,10}$	7.1889	2194	69	69	4.0	24.7 ± 1.3	10.1 ± 0.5	2.98 ± 0.61	0.48	0.03

Table 4.4: continued.

Transition	λ (μm)	E_l (K)	g_l	g_u	A_{ul} (s^{-1})	v_{lsr} (km s^{-1})	FWHM (km s^{-1})	W (10^8 Hz)	$\log_{10}(\eta_0)$	$\log_{10}(\tau_p)$
$14_{2,13} - 14_{3,12}$	7.2028	3671	87	87	6.9	25.9 ± 2.8	7.9 ± 1.3	0.96 ± 0.49	-0.54	-1.04
$10_{3,8} - 11_{2,9}$	7.2356	2432	69	63	4.3	25.4 ± 3.9	8.7 ± 2.2	1.26 ± 0.69	0.26	-0.20
$9_{2,7} - 10_{3,8}$	7.2872	2081	63	57	4.5	25.1 ± 1.4	11.9 ± 0.9	3.21 ± 0.39	0.57	0.12
$12_{1,12} - 12_{2,11}$	7.3002	2554	75	75	3.9	24.0 ± 2.9	9.4 ± 0.8	1.84 ± 0.39	0.20	-0.27
$11_{2,9} - 12_{3,10}$	7.3945	2824	75	69	4.6	26.8 ± 0.3	10.7 ± 0.9	1.87 ± 0.20	-0.01	-0.48
$3_{0,3} - 4_{3,2}$	7.4108	550	27	21	0.2	26.3 ± 0.4	8.9 ± 1.2	1.13 ± 0.19	0.14	-0.26
$7_{3,4} - 8_{4,5}$	7.4618	1615	51	45	5.2	24.1 ± 1.6	11.5 ± 1.1	4.26 ± 0.63	0.99	0.56
$6_{4,2} - 7_{5,3}$	7.4654	1524	15	13	9.2	24.0 ± 2.3	10.1 ± 1.2	3.27 ± 0.89	0.78	0.35
$6_{4,3} - 7_{5,2}$	7.4708	1525	45	39	9.2	27.7 ± 0.2	15.0 ± 0.5	6.57 ± 0.26	1.26	0.83
$8_{3,5} - 9_{4,6}$	7.5193	1929	19	17	4.4	26.2 ± 0.2	12.4 ± 0.6	2.57 ± 0.16	0.21	-0.23
$13_{1,12} - 14_{2,13}$	7.5407	3350	87	81	5.1	26.3 ± 0.4	10.4 ± 1.2	1.35 ± 0.19	-0.35	-0.83
$9_{3,6} - 10_{4,7}$	7.5567	2275	63	57	3.9	24.4 ± 1.4	11.5 ± 0.9	2.39 ± 0.30	0.38	-0.08
$10_{3,7} - 11_{4,8}$	7.5802	2652	23	21	3.7	24.5 ± 0.8	7.1 ± 0.0	0.71 ± 0.12	-0.43	-0.89
$7_{4,3} - 8_{5,4}$	7.5932	1806	51	45	7.5	24.4 ± 0.9	11.2 ± 0.7	3.88 ± 0.34	1.00	0.56
$7_{4,4} - 8_{5,3}$	7.6127	1807	17	15	7.4	24.7 ± 1.0	7.8 ± 0.6	1.64 ± 0.24	0.52	0.08
$7_{5,2} - 8_{6,3}$	7.6187	2031	51	45	10.1	24.4 ± 1.6	13.9 ± 1.5	5.53 ± 0.79	0.92	0.48
$7_{5,3} - 8_{6,2}$	7.6196	2031	17	15	10.1	24.0 ± 0.4	7.1 ± 0.2	1.91 ± 0.15	0.44	-0.01
$7_{3,5} - 8_{4,4}$	7.6442	1628	17	15	4.3	25.0 ± 1.8	9.9 ± 1.0	1.91 ± 0.41	0.45	0.02
$8_{4,4} - 9_{5,5}$	7.7118	2122	19	17	6.2	26.0 ± 2.0	13.5 ± 0.9	2.60 ± 0.51	0.22	-0.23
$8_{4,5} - 9_{5,4}$	7.7676	2125	57	51	6.0	25.1 ± 1.0	10.7 ± 0.6	2.38 ± 0.25	0.69	0.24
$9_{4,5} - 10_{5,6}$	7.8122	2473	63	57	5.1	25.2 ± 2.6	10.1 ± 1.1	1.84 ± 0.73	0.35	-0.11
$15_{0,15} - 16_{1,16}$	7.8331	3829	99	93	5.1	25.1 ± 0.4	8.0 ± 1.1	0.51 ± 0.09	-0.69	-1.19
$9_{5,5} - 10_{6,4}$	7.9113	2698	21	19	7.1	24.0 ± 0.4	9.6 ± 1.0	0.88 ± 0.11	-0.17	-0.64
$11_{4,7} - 12_{5,8}$	7.9334	3274	75	69	3.7	25.0 ± 1.2	8.3 ± 0.8	0.84 ± 0.13	-0.42	-0.91
$6_{1,6} - 7_{2,5}$	7.9343	1125	45	39	0.4	24.7 ± 1.6	9.9 ± 0.7	1.71 ± 0.44	0.37	-0.04
$9_{4,6} - 10_{5,5}$	7.9452	2482	21	19	4.7	27.3 ± 0.2	10.2 ± 0.6	0.90 ± 0.07	-0.14	-0.60

Table 4.5: Line Parameters for the v=2-1 transition of AFGL 2136. E_l is the energy of the lower level of the transition, g_l and g_u are the statistical weights of the lower and upper levels respectively, A_{ul} is the Einstein A coefficient of the transition, v_{lsr} is the peak velocity of the line, FWHM is the full width at half maximum of the line, W is the equivalent width in units of Hz and τ_p is the peak optical depth of the transition. η_0 is the opacity in the lower level of the transition calculated for $\epsilon = 0.5$. Line data were taken from the HITRAN database (Gordon et al. 2017).

Transition	λ (μm)	E_l (K)	g_l	g_u	A_{ul} (s^{-1})	v_{lsr} (km s^{-1})	FWHM (km s^{-1})	W (10^8 Hz)	$\log_{10}(\eta_0)$	$\log_{10}(\tau_p)$
$4_{4,1} - 3_{3,0}$	5.4373	2745	21	27	9.8	27.5 ± 1.2	7.1 ± 3.2	1.11 ± 0.55	-0.20	-0.54
$5_{3,2} - 4_{2,3}$	5.5105	2745	27	33	6.2	24.0 ± 0.5	7.1 ± 0.5	0.73 ± 0.10	-0.31	-0.66
$6_{3,4} - 5_{2,3}$	5.5218	2955	33	39	6.9	26.6 ± 0.4	9.5 ± 1.1	1.04 ± 0.15	-0.37	-0.71
$11_{0,11} - 10_{1,10}$	5.6670	3892	63	69	27.6	27.2 ± 0.2	9.9 ± 0.6	1.18 ± 0.09	-0.32	-0.65
$3_{3,0} - 2_{2,1}$	5.6872	2507	15	21	10.9	24.9 ± 1.0	9.5 ± 1.3	1.86 ± 0.30	-0.01	-0.36
$10_{1,10} - 9_{0,9}$	5.7202	3615	57	63	26.5	26.3 ± 0.4	10.4 ± 1.1	1.64 ± 0.22	-0.13	-0.45
$6_{2,5} - 5_{1,4}$	5.7627	2879	33	39	10.9	25.5 ± 1.4	11.9 ± 3.2	2.61 ± 1.01	-0.06	-0.40
$9_{0,9} - 8_{1,8}$	5.7769	3364	51	57	25.2	27.0 ± 1.0	11.0 ± 2.8	2.83 ± 0.75	0.04	-0.29
$7_{1,6} - 6_{2,5}$	5.8206	3110	39	45	11.8	26.4 ± 0.4	11.9 ± 1.1	1.54 ± 0.18	-0.14	-0.48
$8_{1,8} - 7_{0,7}$	5.8322	3138	45	51	23.9	27.4 ± 0.2	10.7 ± 0.7	3.64 ± 0.28	0.18	-0.16
$7_{1,6} - 7_{0,7}$	5.8869	3138	45	45	3.7	26.0 ± 0.8	7.1 ± 2.2	0.90 ± 0.34	-0.68	-1.02
$7_{1,7} - 6_{0,6}$	5.8902	2938	13	15	22.4	25.2 ± 1.3	7.3 ± 2.3	1.15 ± 0.42	-0.19	-0.5
$6_{1,6} - 5_{0,5}$	5.9485	2764	33	39	20.7	25.7 ± 0.7	11.4 ± 0.7	4.25 ± 0.32	0.36	0.01
$6_{0,6} - 5_{1,5}$	5.9622	2767	11	13	20.6	25.1 ± 4.6	10.2 ± 9.2	1.58 ± 1.82	-0.12	-0.47
$4_{2,3} - 4_{1,4}$	6.0224	2621	27	27	5.9	25.0 ± 1.3	7.8 ± 2.2	1.09 ± 0.36	-0.21	-0.56
$7_{2,5} - 7_{1,6}$	6.0322	3323	45	45	9.4	26.7 ± 0.3	9.2 ± 0.7	1.04 ± 0.10	-0.38	-0.72
$4_{1,4} - 3_{0,3}$	6.0613	2492	21	27	16.7	24.7 ± 0.8	10.1 ± 0.9	2.88 ± 0.33	0.36	0.01
$5_{1,4} - 5_{0,5}$	6.0802	2764	33	33	6.4	26.5 ± 0.2	11.7 ± 0.6	1.99 ± 0.12	-0.20	-0.54
$2_{2,1} - 2_{1,2}$	6.1010	2413	15	15	5.9	26.0 ± 0.3	10.0 ± 0.7	1.16 ± 0.11	-0.26	-0.62
$3_{2,1} - 3_{1,2}$	6.1716	2550	21	21	12.5	25.8 ± 2.5	8.7 ± 3.8	1.56 ± 0.95	0.11	-0.24
$2_{1,2} - 1_{0,1}$	6.1753	2329	9	15	13.9	26.1 ± 0.8	10.4 ± 0.2	2.65 ± 0.25	0.19	-0.16
$3_{0,3} - 2_{1,2}$	6.2028	2413	15	21	11.9	25.0 ± 0.5	8.0 ± 0.7	1.78 ± 0.19	0.21	-0.15
$1_{1,0} - 1_{0,1}$	6.3157	2329	9	9	21.3	25.4 ± 0.5	7.1 ± 0.9	1.55 ± 0.29	0.19	-0.17

Table 4.5: continued.

Transition	λ (μm)	E_l (K)	g_l	g_u	A_{ul} (s^{-1})	v_{lsr} (km s^{-1})	FWHM (km s^{-1})	W (10^8 Hz)	$\log_{10}(\eta_0)$	$\log_{10}(\tau_p)$
$1_{0,1} - 1_{1,0}$	6.5149	2360	9	9	24.9	26.7 ± 0.2	10.5 ± 0.6	2.19 ± 0.17	0.27	-0.08
$3_{1,2} - 3_{2,1}$	6.5994	2618	21	21	19.1	24.0 ± 1.0	12.8 ± 1.5	3.49 ± 0.46	0.33	-0.02
$5_{1,4} - 5_{2,3}$	6.6160	2955	33	33	23.3	25.1 ± 1.5	11.1 ± 1.7	3.00 ± 0.63	0.32	-0.02
$2_{1,2} - 3_{0,3}$	6.6400	2492	21	15	13.5	24.5 ± 2.0	9.8 ± 3.3	1.76 ± 0.67	0.13	-0.22
$7_{2,5} - 7_{3,4}$	6.6462	3544	45	45	24.4	25.9 ± 0.3	8.4 ± 0.7	1.49 ± 0.16	-0.01	-0.35
$6_{2,4} - 6_{3,3}$	6.6574	3284	13	13	21.6	26.6 ± 0.3	11.0 ± 1.3	0.88 ± 0.12	-0.38	-0.72
$4_{0,4} - 4_{1,3}$	6.6674	2698	9	9	15.1	25.0 ± 1.0	7.4 ± 1.9	0.86 ± 0.26	-0.21	-0.56
$1_{0,1} - 2_{1,2}$	6.6739	2413	15	9	22.9	26.2 ± 0.2	10.4 ± 0.7	2.32 ± 0.19	0.22	-0.14
$9_{3,6} - 9_{4,5}$	6.6888	4315	57	57	23.9	24.4 ± 2.7	8.7 ± 1.9	0.69 ± 0.24	-0.56	-0.88
$9_{2,7} - 9_{3,6}$	6.6895	4180	57	57	25.5	24.5 ± 1.2	8.4 ± 1.6	0.84 ± 0.20	-0.43	-0.75
$7_{1,6} - 7_{2,5}$	6.7261	3443	45	45	20.3	24.2 ± 0.9	7.2 ± 1.8	1.02 ± 0.29	-0.01	-0.34
$3_{2,1} - 3_{3,0}$	6.7334	2745	21	21	9.2	27.7 ± 0.6	13.1 ± 2.0	1.33 ± 0.25	-0.06	-0.40
$5_{0,5} - 5_{1,4}$	6.7653	2879	33	33	12.5	26.5 ± 0.2	11.3 ± 0.7	2.33 ± 0.18	0.14	-0.21
$4_{1,4} - 4_{2,3}$	6.7857	2745	27	27	11.2	24.8 ± 0.4	9.9 ± 1.1	1.28 ± 0.18	0.13	-0.22
$5_{3,2} - 5_{4,1}$	6.7987	3240	33	33	12.1	25.6 ± 0.4	10.3 ± 1.2	1.39 ± 0.20	-0.13	-0.47
$3_{0,3} - 4_{1,4}$	6.8136	2621	27	21	17.1	25.3 ± 0.3	13.2 ± 0.9	2.98 ± 0.25	0.31	-0.04
$6_{2,5} - 6_{3,4}$	6.8285	3269	39	39	15.4	26.7 ± 0.5	11.6 ± 1.3	1.86 ± 0.26	0.01	-0.33
$4_{1,4} - 5_{0,5}$	6.8449	2764	33	27	16.0	25.5 ± 0.5	8.7 ± 1.2	2.17 ± 0.34	0.27	-0.08
$1_{1,0} - 2_{2,1}$	6.8512	2507	15	9	26.0	26.4 ± 0.3	12.1 ± 0.8	2.75 ± 0.23	0.24	-0.11
$3_{1,2} - 4_{2,3}$	7.0096	2745	27	21	13.2	24.3 ± 1.1	9.6 ± 1.6	1.79 ± 0.34	0.13	-0.21
$6_{1,6} - 7_{0,7}$	7.0362	3138	45	39	15.7	24.7 ± 0.6	10.1 ± 1.2	2.15 ± 0.28	0.13	-0.21
$2_{2,1} - 3_{3,0}$	7.0996	2745	21	15	26.7	24.3 ± 0.5	7.1 ± 0.9	1.39 ± 0.29	0.33	-0.02
$5_{1,4} - 6_{2,5}$	7.1217	3110	39	33	11.1	26.0 ± 2.0	7.6 ± 5.4	1.08 ± 0.85	-0.04	-0.38
$7_{1,7} - 8_{0,8}$	7.1324	3363	17	15	15.1	24.3 ± 1.6	7.6 ± 2.0	0.84 ± 0.33	-0.48	-0.82
$7_{0,7} - 8_{1,8}$	7.1381	3364	51	45	15.1	26.0 ± 1.5	9.4 ± 2.7	1.33 ± 0.43	-0.01	-0.34
$3_{2,1} - 4_{3,2}$	7.2050	2885	27	21	18.3	25.3 ± 1.2	13.3 ± 4.0	2.89 ± 0.89	0.21	-0.13

Table 4.5: continued.

Transition	λ (μm)	E_l (K)	g_l	g_u	A_{ul} (s^{-1})	v_{lsr} (km s^{-1})	FWHM (km s^{-1})	W (10^8 Hz)	$\log_{10}(\eta_0)$	$\log_{10}(\tau_p)$
$7_{1,6} - 8_{2,7}$	7.2245	3590	51	45	11.1	25.7 ± 4.8	9.2 ± 6.2	0.82 ± 0.78	-0.30	-0.63
$8_{1,8} - 9_{0,9}$	7.2308	3615	57	51	14.5	26.4 ± 1.4	10.4 ± 1.4	1.75 ± 0.32	-0.17	-0.50
$3_{3,0} - 4_{4,1}$	7.2937	3064	27	21	28.4	26.8 ± 0.9	13.8 ± 1.5	3.05 ± 0.37	0.29	-0.06
$4_{3,2} - 5_{4,1}$	7.4294	3240	33	27	20.9	26.1 ± 0.3	11.4 ± 0.9	1.83 ± 0.18	0.13	-0.21
$5_{3,2} - 6_{4,3}$	7.5509	3451	39	33	16.2	24.5 ± 2.3	7.9 ± 3.0	0.69 ± 0.32	-0.05	-0.39
$6_{3,4} - 7_{4,3}$	7.7350	3701	45	39	12.3	25.8 ± 1.1	7.1 ± 2.3	0.51 ± 0.19	-0.29	-0.61

Table 4.6: Line Parameters for the v=1-0 of $H_2^{18}O$ transition of AFGL 2136. E_l is the energy of the lower level of the transition, g_l and g_u are the statistical weights of the lower and upper levels respectively, A_{ul} is the Einstein A coefficient of the transition, v_{lsr} is the peak velocity of the line, FWHM is the full width at half maximum of the line, W is the equivalent width in units of Hz and τ_p is the peak optical depth of the transition. η_0 is the opacity in the lower level of the transition calculated for $\epsilon = 0.5$. Line data were taken from the HITRAN database (Gordon et al. 2017).

Transition	λ (μm)	E_l (K)	g_l	g_u	A_{ul} (s^{-1})	v_{lsr} (km s^{-1})	FWHM (km s^{-1})	W (10^8 Hz)	$\log_{10}(\eta_0)$	$\log_{10}(\tau_p)$
$2_{1,2} - 1_{0,1}$	6.0743	34	9	15.0	7.0	26.2±0.6	14.3±1.8	1.44±0.16	-0.43	-0.52
$4_{1,4} - 3_{0,3}$	5.9604	196	21	27.0	8.6	25.2±0.4	12.7±1.5	1.35±0.14	-0.39	-0.47
$5_{0,5} - 4_{1,4}$	5.9200	322	27	33.0	9.5	27.6±0.5	8.9±1.4	1.14±0.19	-0.49	-0.56
$2_{2,1} - 1_{1,0}$	5.9095	60	9	15.0	5.9	26.3±0.4	10.5±1.4	0.76±0.16	-0.58	-0.67

Table 4.7: Line Parameters for the v=1-0 transition of AFGL 2591. E_l is the energy of the lower level of the transition, g_l and g_u are the statistical weights of the lower and upper levels respectively, A_{ul} is the Einstein A coefficient of the transition, v_{lsr} is the peak velocity of the line, FWHM is the full width at half maximum of the line, W is the equivalent width in units of Hz and τ_p is the peak optical depth of the transition. η_0 is the opacity in the lower level of the transition calculated for $\epsilon = 0.5$. Line data were taken from the HITRAN database (Gordon et al. 2017).

Transition	λ (μm)	E_l (K)	g_l	g_u	A_{ul} (s^{-1})	v_{lsr} (km s^{-1})	FWHM (km s^{-1})	W (10^8 Hz)	$\log_{10}(\eta_0)$	$\log_{10}(\tau_p)$
$12_{2,11} - 11_{1,10}$	5.3719	2194	69	75	10.9	-9.7 ± 0.3	13.6 ± 0.9	3.69 ± 0.29	0.83	0.80
$12_{1,11} - 11_{2,10}$	5.3737	2194	23	25	10.9	-8.7 ± 0.3	15.9 ± 1.0	3.95 ± 0.26	0.35	0.33
$11_{3,8} - 10_{4,7}$	5.3772	2275	63	69	3.3	-10.3 ± 0.4	13.6 ± 1.2	2.08 ± 0.23	0.22	0.18
$9_{3,7} - 8_{2,6}$	5.3806	1414	17	19	5.0	-8.8 ± 0.3	15.7 ± 0.8	4.04 ± 0.21	0.44	0.50
$8_{6,3} - 8_{5,4}$	5.4172	1806	51	51	1.6	-9.3 ± 0.2	12.5 ± 0.6	2.79 ± 0.16	0.11	0.13
$4_{4,0} - 3_{3,1}$	5.4218	410	7	9	5.4	-11.7 ± 0.1	13.4 ± 0.4	3.57 ± 0.11	0.86	1.03
$9_{6,3} - 9_{5,4}$	5.4238	2125	57	57	1.9	-10.0 ± 0.2	10.4 ± 0.6	1.40 ± 0.10	0.01	-0.01
$11_{2,10} - 10_{1,9}$	5.4248	1860	21	23	10.2	-8.2 ± 0.2	12.8 ± 0.6	3.38 ± 0.15	0.54	0.54
$11_{1,10} - 10_{2,9}$	5.4285	1861	63	69	10.2	-10.2 ± 0.3	15.6 ± 0.4	6.31 ± 0.26	1.01	1.02
$7_{3,5} - 6_{2,4}$	5.4431	867	13	15	3.9	-10.2 ± 0.2	14.5 ± 0.6	3.61 ± 0.14	0.62	0.74
$11_{6,5} - 11_{5,6}$	5.4521	2876	69	69	2.4	-7.0 ± 0.5	11.4 ± 1.5	0.83 ± 0.13	-0.32	-0.43
$5_{3,2} - 4_{2,3}$	5.4641	432	27	33	3.1	-12.1 ± 0.2	16.1 ± 0.2	5.51 ± 0.14	1.17	1.34
$12_{2,11} - 12_{1,12}$	5.4689	2241	75	75	0.7	-9.7 ± 0.2	13.0 ± 1.1	1.54 ± 0.15	-0.39	-0.43
$10_{1,9} - 9_{2,8}$	5.4862	1554	19	21	9.5	-12.0 ± 0.2	14.2 ± 0.2	4.26 ± 0.12	0.69	0.73
$10_{3,7} - 9_{4,6}$	5.4904	1929	19	21	2.6	-12.2 ± 0.4	13.7 ± 1.1	1.24 ± 0.10	-0.13	-0.13
$12_{1,12} - 11_{0,11}$	5.5022	1909	69	75	15.0	-11.9 ± 0.1	16.1 ± 0.4	5.42 ± 0.15	1.20	1.20
$11_{4,7} - 10_{5,6}$	5.5031	2473	63	69	1.7	-10.4 ± 0.3	16.6 ± 1.9	1.49 ± 0.21	-0.17	-0.23
$9_{2,7} - 8_{3,6}$	5.5179	1447	51	57	4.6	-12.2 ± 0.3	13.5 ± 0.2	3.83 ± 0.15	0.89	0.94
$5_{3,3} - 4_{2,2}$	5.5229	454	9 1	1	3.9	-14.1 ± 0.1	15.2 ± 0.5	3.59 ± 0.13	0.80	0.96
$11_{2,10} - 11_{1,11}$	5.5270	1909	23	23	0.8	-9.7 ± 0.3	12.2 ± 1.2	0.80 ± 0.08	-0.58	-0.58
$11_{1,10} - 11_{0,11}$	5.5290	1909	69	69	0.8	-11.5 ± 0.2	15.9 ± 0.7	2.16 ± 0.12	-0.11	-0.10
$12_{4,9} - 12_{3,10}$	5.5298	2824	75	75	2.2	-9.4 ± 0.5	10.8 ± 1.5	0.97 ± 0.16	-0.26	-0.36
$9_{2,8} - 8_{1,7}$	5.5319	1270	17	19	8.8	-13.3 ± 0.2	15.0 ± 0.7	4.22 ± 0.19	0.82	0.89

Table 4.7: continued.

Transition	λ (μm)	E_l (K)	g_l	g_u	A_{ul} (s^{-1})	v_{lsr} (km s^{-1})	FWHM (km s^{-1})	W (10^8 Hz)	$\log_{10}(\eta_0)$	$\log_{10}(\tau_p)$
$13_{3,10} - 13_{2,11}$	5.5373	3233	81	81	2.1	-10.3 ± 0.3	10.7 ± 0.8	0.68 ± 0.07	-0.54	-0.68
$9_{1,8} - 8_{2,7}$	5.5479	1274	51	57	8.7	-13.9 ± 0.1	14.6 ± 0.1	5.95 ± 0.10	1.30	1.37
$10_{5,6} - 10_{4,7}$	5.5496	2275	63	63	2.7	-11.6 ± 0.2	13.0 ± 0.3	2.26 ± 0.09	0.14	0.11
$4_{3,1} - 3_{2,2}$	5.5567	296	7	9	4.3	-15.6 ± 0.2	16.6 ± 0.7	3.86 ± 0.17	0.87	1.04
$9_{5,5} - 9_{4,6}$	5.5599	1929	19	19	2.7	-12.5 ± 0.3	12.0 ± 0.8	1.12 ± 0.08	-0.15	-0.15
$11_{3,9} - 11_{2,10}$	5.5613	2194	23	23	1.7	-10.9 ± 0.2	10.9 ± 0.7	0.79 ± 0.05	-0.45	-0.48
$7_{5,2} - 7_{4,3}$	5.5775	1340	45	45	2.2	-12.7 ± 0.2	13.0 ± 0.2	3.17 ± 0.10	0.56	0.63
$10_{1,9} - 10_{0,10}$	5.5909	1603	21	21	1.0	-13.9 ± 0.2	9.4 ± 0.5	0.97 ± 0.05	-0.32	-0.28
$8_{5,3} - 8_{4,4}$	5.5917	1628	17	17	2.6	-12.1 ± 0.3	14.5 ± 0.8	2.00 ± 0.12	0.01	0.04
$9_{3,6} - 8_{4,5}$	5.6118	1615	51	57	2.0	-12.8 ± 0.2	12.6 ± 0.5	2.45 ± 0.12	0.44	0.47
$8_{2,6} - 7_{3,5}$	5.6208	1175	15	17	3.5	-7.8 ± 0.3	13.1 ± 0.3	3.75 ± 0.18	0.47	0.55
$7_{2,6} - 6_{1,5}$	5.6318	781	13	15	6.9	-14.5 ± 0.2	16.1 ± 0.1	5.16 ± 0.11	0.98	1.10
$9_{2,8} - 9_{1,9}$	5.6485	1324	19	19	1.2	-12.4 ± 0.2	12.7 ± 0.6	1.94 ± 0.09	-0.07	-0.01
$9_{4,6} - 9_{3,7}$	5.6590	1750	19	19	3.0	-11.3 ± 0.2	13.4 ± 0.5	2.05 ± 0.08	0.05	0.08
$10_{2,8} - 10_{1,9}$	5.6645	1860	21	21	2.1	-11.8 ± 0.3	10.6 ± 1.0	0.95 ± 0.09	-0.14	-0.13
$13_{4,9} - 13_{3,10}$	5.6840	3475	81	81	3.7	-10.2 ± 0.6	10.7 ± 1.6	0.84 ± 0.15	-0.42	-0.58
$8_{4,5} - 8_{3,6}$	5.6864	1447	51	51	3.1	-13.7 ± 0.2	16.5 ± 0.9	4.20 ± 0.26	0.72	0.77
$7_{4,4} - 7_{3,5}$	5.7051	1175	15	15	3.1	-12.2 ± 0.4	15.0 ± 1.1	2.86 ± 0.21	0.38	0.46
$10_{5,6} - 9_{6,3}$	5.7081	2347	57	63	1.0	-11.7 ± 0.5	16.3 ± 0.5	3.05 ± 0.16	-0.33	-0.37
$8_{1,8} - 7_{0,7}$	5.7096	843	45	51	12.5	-13.2 ± 0.2	15.7 ± 0.2	7.26 ± 0.22	1.74	1.86
$11_{3,8} - 11_{2,9}$	5.7131	2432	69	69	3.2	-10.3 ± 0.2	13.8 ± 0.7	2.66 ± 0.15	0.18	0.12
$6_{4,3} - 6_{3,4}$	5.7162	933	39	39	2.9	-15.1 ± 0.3	15.6 ± 0.4	5.28 ± 0.21	0.93	1.04
$5_{2,4} - 4_{1,3}$	5.7187	396	9 1	1	5.2	-16.0 ± 0.3	16.0 ± 0.3	4.74 ± 0.19	1.01	1.17
$5_{4,2} - 5_{3,3}$	5.7217	725	11	11	2.4	-13.9 ± 0.3	15.2 ± 0.3	4.30 ± 0.17	0.45	0.58
$4_{4,1} - 4_{3,2}$	5.7238	550	27	27	1.6	-14.0 ± 0.1	14.3 ± 0.4	4.21 ± 0.13	0.78	0.93
$4_{4,0} - 4_{3,1}$	5.7281	552	9	9	1.6	-12.4 ± 0.3	15.0 ± 0.3	3.52 ± 0.15	0.31	0.46

Table 4.7: continued.

Transition	λ (μm)	E_l (K)	g_l	g_u	A_{ul} (s^{-1})	v_{lsr} (km s^{-1})	FWHM (km s^{-1})	W (10^8 Hz)	$\log_{10}(\eta_0)$	$\log_{10}(\tau_p)$
$8_{3,6} - 8_{2,7}$	5.7320	1274	51	51	2.7	-13.0 ± 0.2	16.2 ± 0.7	4.16 ± 0.22	0.78	0.86
$7_{2,5} - 6_{3,4}$	5.7352	933	39	45	2.6	-13.9 ± 0.2	13.1 ± 0.2	4.39 ± 0.16	0.95	1.06
$5_{4,1} - 5_{3,2}$	5.7371	732	33	33	2.5	-13.6 ± 0.2	15.7 ± 0.2	5.57 ± 0.11	0.94	1.07
$9_{2,7} - 9_{1,8}$	5.7494	1552	57	57	2.6	-10.8 ± 0.6	16.3 ± 0.7	4.15 ± 0.33	0.62	0.67
$7_{2,6} - 7_{1,7}$	5.7735	843	15	15	1.7	-12.3 ± 0.2	16.7 ± 0.8	3.61 ± 0.17	0.36	0.48
$7_{3,5} - 7_{2,6}$	5.7792	1021	15	15	3.1	-10.6 ± 0.2	11.9 ± 0.7	2.63 ± 0.16	0.49	0.59
$9_{5,4} - 8_{6,3}$	5.7822	2031	51	57	0.7	-10.5 ± 0.5	18.8 ± 0.8	2.14 ± 0.62	-0.25	-0.26
$7_{1,6} - 7_{0,7}$	5.8022	843	45	45	1.8	-13.2 ± 0.2	15.5 ± 0.6	4.87 ± 0.22	0.86	0.98
$11_{4,7} - 11_{3,8}$	5.8050	2609	69	69	5.3	-11.5 ± 0.3	11.9 ± 0.7	2.72 ± 0.20	0.30	0.22
$6_{3,4} - 6_{2,5}$	5.8180	795	39	39	3.4	-11.6 ± 0.4	14.9 ± 0.6	5.21 ± 0.32	1.11	1.24
$6_{1,6} - 5_{0.5}$	5.8227	468	33	39	10.8	-14.8 ± 0.4	18.8 ± 0.5	6.61 ± 0.27	1.85	2.01
$9_{4,5} - 9_{3,6}$	5.8280	1846	57	57	5.2	-9.9 ± 0.3	14.3 ± 0.3	3.95 ± 0.15	0.74	0.75
$6_{2,5} - 6_{1,6}$	5.8342	643	39	39	2.1	-14.5 ± 0.2	15.2 ± 0.2	5.86 ± 0.11	1.01	1.15
$8_{2,6} - 8_{1,7}$	5.8380	1270	17	17	3.3	-8.5 ± 0.3	17.5 ± 1.0	3.19 ± 0.18	0.42	0.49
$10_{3,8} - 9_{4,5}$	5.8394	1957	57	63	0.7	-9.0 ± 0.3	14.6 ± 1.0	1.89 ± 0.16	-0.17	-0.17
$8_{4,4} - 7_{5,3}$	5.8410	1524	15	17	0.9	-11.6 ± 0.1	9.2 ± 0.4	1.37 ± 0.06	-0.33	-0.28
$5_{3,3} - 5_{2,4}$	5.8473	598	11	11	3.5	-14.0 ± 0.2	12.4 ± 0.7	2.85 ± 0.16	0.72	0.86
$9_{3,7} - 8_{4,4}$	5.8491	1628	17	19	0.9	-9.6 ± 0.3	15.0 ± 0.9	1.83 ± 0.11	-0.34	-0.31
$6_{2,4} - 5_{3,3}$	5.8575	725	11	13	1.8	-11.9 ± 0.2	14.6 ± 0.3	3.45 ± 0.14	0.42	0.56
$8_{4,5} - 7_{5,2}$	5.8656	1525	45	51	0.9	-13.6 ± 0.3	14.4 ± 0.6	2.86 ± 0.16	0.14	0.18
$4_{3,2} - 4_{2,3}$	5.8670	432	27	27	3.2	-15.1 ± 0.4	12.9 ± 0.2	4.41 ± 0.40	1.20	1.36
$9_{3,6} - 9_{2,7}$	5.8729	1729	57	57	5.2	-10.1 ± 0.1	12.8 ± 0.1	5.83 ± 0.07	0.83	0.85
$3_{3,1} - 3_{2,2}$	5.8784	296	7	7	2.4	-15.7 ± 0.2	16.8 ± 0.8	4.73 ± 0.21	0.57	0.75
$8_{3,6} - 7_{4,3}$	5.8860	1340	45	51	1.0	-11.0 ± 0.2	14.9 ± 0.6	3.44 ± 0.16	0.34	0.41
$5_{2,4} - 5_{1,5}$	5.8909	470	11	11	2.5	-12.8 ± 0.1	17.3 ± 0.6	4.27 ± 0.14	0.68	0.84
$4_{3,1} - 4_{2,2}$	5.9167	454	9	9	3.9	-12.8 ± 0.1	14.9 ± 0.1	4.45 ± 0.10	0.79	0.95

Table 4.7: continued.

Transition	λ (μm)	E_l (K)	g_l	g_u	A_{ul} (s^{-1})	v_{lsr} (km s^{-1})	FWHM (km s^{-1})	W (10^8 Hz)	$\log_{10}(\eta_0)$	$\log_{10}(\tau_p)$
$7_{2,5} - 7_{1,6}$	5.9228	1013	45	45	4.4	-10.0 ± 0.3	18.1 ± 0.3	6.21 ± 0.18	1.16	1.26
$8_{3,5} - 8_{2,6}$	5.9246	1414	17	17	6.1	-11.2 ± 0.2	12.3 ± 0.6	2.60 ± 0.13	0.61	0.66
$5_{3,2} - 5_{2,3}$	5.9383	642	33	33	5.0	-13.7 ± 0.2	14.2 ± 0.2	5.04 ± 0.12	1.35	1.49
$7_{3,4} - 7_{2,5}$	5.9507	1125	45	45	6.5	-10.3 ± 0.2	16.0 ± 0.2	6.12 ± 0.16	1.26	1.35
$6_{3,3} - 6_{2,4}$	5.9530	867	13	13	6.0	-11.5 ± 0.2	17.0 ± 0.7	4.94 ± 0.20	0.87	0.99
$6_{3,3} - 5_{4,2}$	5.9792	878	11	13	0.8	-9.5 ± 0.2	14.7 ± 0.8	2.36 ± 0.12	-0.04	0.08
$6_{2,4} - 6_{1,5}$	5.9942	781	13	13	5.8	-12.3 ± 0.2	13.0 ± 0.5	3.77 ± 0.14	0.92	1.05
$6_{3,4} - 5_{4,1}$	6.0191	878	33	39	0.7	-12.3 ± 0.4	13.9 ± 0.4	3.14 ± 0.18	0.42	0.53
$6_{4,3} - 5_{5,0}$	6.0375	1067	33	39	0.3	-11.3 ± 0.3	13.7 ± 0.4	1.81 ± 0.10	-0.14	-0.04
$5_{2,3} - 5_{1,4}$	6.0441	574	33	33	7.2	-15.5 ± 0.5	17.0 ± 0.4	5.02 ± 0.26	1.57	1.72
$5_{2,4} - 4_{3,1}$	6.0964	552	9	11	0.7	-12.3 ± 0.2	15.7 ± 0.6	2.66 ± 0.10	0.14	0.29
$4_{1,4} - 3_{2,1}$	6.2133	305	21	27	0.4	-12.7 ± 0.4	12.6 ± 0.5	3.61 ± 0.25	0.47	0.65
$3_{3,0} - 4_{2,3}$	6.2218	432	27	21	0.3	-14.7 ± 0.4	16.5 ± 1.3	3.40 ± 0.32	0.14	0.30
$2_{2,0} - 3_{1,3}$	6.2453	204	7	5	0.4	-14.2 ± 0.5	9.5 ± 1.4	0.93 ± 0.14	-0.21	-0.03
$3_{2,1} - 4_{1,4}$	6.2716	323	27	21	0.3	-13.7 ± 0.5	10.8 ± 0.5	3.08 ± 0.27	0.28	0.45
$3_{3,1} - 4_{2,2}$	6.2827	454	9	7	0.4	-12.0 ± 1.0	13.9 ± 1.1	1.69 ± 0.33	-0.25	-0.09
$2_{2,1} - 3_{1,2}$	6.3737	249	21	15	1.1	-11.4 ± 0.5	15.8 ± 0.6	4.71 ± 0.31	0.73	0.91
$1_{1,1} - 2_{0,2}$	6.3903	100	5	3	5.3	-13.3 ± 0.4	12.3 ± 1.4	2.76 ± 0.32	0.80	1.00
$4_{1,3} - 4_{2,2}$	6.4115	454	9	9	11.5	-14.2 ± 0.4	14.1 ± 1.6	3.88 ± 0.45	1.37	1.53
$7_{2,5} - 7_{3,4}$	6.4506	1212	45	45	12.5	-14.4 ± 0.4	18.8 ± 1.6	5.39 ± 0.55	1.59	1.67
$6_{2,4} - 6_{3,3}$	6.4531	951	13	13	11.3	-15.0 ± 0.5	18.8 ± 1.7	5.16 ± 0.48	1.19	1.30
$12_{4,8} - 12_{5,7}$	6.4820	3310	25	25	13.9	13.1 ± 0.7	14.0 ± 2.2	1.85 ± 0.29	-0.07	-0.22
$9_{2,7} - 9_{3,6}$	6.5126	1846	57	57	12.2	-13.7 ± 0.5	18.7 ± 2.1	5.04 ± 0.68	1.25	1.27
$13_{5,8} - 13_{6,7}$	6.5392	3966	81	81	12.5	-10.6 ± 1.0	12.8 ± 0.9	1.21 ± 0.19	-0.05	-0.27
$10_{4,6} - 10_{5,5}$	6.5401	2482	21	21	11.1	-9.1 ± 8.0	18.8 ± 1.8	2.25 ± 0.50	0.34	0.29
$7_{4,4} - 8_{3,5}$	6.5818	1511	17	15	0.9	-4.7 ± 3.9	17.0 ± 1.1	1.75 ± 0.27	-0.23	-0.18

Table 4.7: continued.

Transition	λ (μm)	E_l (K)	g_l	g_u	A_{ul} (s^{-1})	v_{lsr} (km s^{-1})	FWHM (km s^{-1})	W (10^8 Hz)	$\log_{10}(\eta_0)$	$\log_{10}(\tau_p)$
$5_{3,3} - 5_{4,2}$	6.5950	878	11	11	6.1	-14.4 ± 0.4	18.8 ± 0.2	3.73 ± 0.04	0.93	1.04
$6_{3,4} - 6_{4,3}$	6.6007	1088	39	39	7.5	-15.7 ± 0.5	17.0 ± 0.5	4.46 ± 0.25	1.42	1.51
$10_{4,7} - 10_{5,6}$	6.6409	2473	63	63	10.0	-10.9 ± 0.4	13.5 ± 1.1	2.68 ± 0.27	0.80	0.74
$9_{3,7} - 9_{4,6}$	6.6642	1929	19	19	9.4	-11.9 ± 0.3	14.1 ± 0.9	2.61 ± 0.18	0.64	0.64
$10_{3,8} - 10_{4,7}$	6.7052	2275	63	63	9.6	-11.9 ± 0.2	15.6 ± 0.5	3.47 ± 0.13	0.93	0.90
$6_{1,6} - 6_{2,5}$	6.7121	795	39	39	4.9	-15.0 ± 0.3	12.1 ± 0.8	3.39 ± 0.26	1.46	1.59
$6_{3,4} - 7_{2,5}$	6.7146	1125	45	39	2.0	-14.6 ± 0.5	16.0 ± 0.4	3.45 ± 0.17	0.83	0.92
$8_{2,7} - 8_{3,6}$	6.7157	1447	51	51	7.7	-11.9 ± 0.3	15.6 ± 0.9	4.92 ± 0.35	1.32	1.38
$8_{2,7} - 8_{3,6}$	6.7157	1447	51	51	7.7	-12.4 ± 0.5	17.6 ± 0.5	5.19 ± 0.35	1.32	1.38
$11_{3,9} - 11_{4,8}$	6.7557	2652	23	23	9.6	-10.6 ± 0.3	12.7 ± 0.7	1.89 ± 0.11	0.24	0.17
$14_{4,11} - 14_{5,10}$	6.7668	4199	87	87	11.3	-9.8 ± 0.6	11.4 ± 1.6	0.98 ± 0.17	-0.18	-0.43
$7_{0,7} - 7_{1,6}$	6.7731	1013	45	45	4.7	-14.7 ± 0.3	14.7 ± 0.3	4.53 ± 0.15	1.37	1.47
$9_{2,8} - 9_{3,7}$	6.7826	1750	19	19	7.5	-12.0 ± 0.3	12.4 ± 0.8	3.06 ± 0.20	0.69	0.71
$7_{1,7} - 7_{2,6}$	6.7959	1021	15	15	4.6	-14.2 ± 0.5	16.5 ± 0.6	4.48 ± 0.35	0.88	0.98
$12_{3,10} - 12_{4,9}$	6.8144	3058	75	75	9.6	-10.4 ± 0.3	11.7 ± 0.9	2.01 ± 0.19	0.48	0.36
$10_{1,9} - 10_{2,8}$	6.8251	2069	21	21	7.6	-10.3 ± 0.3	10.4 ± 0.9	1.77 ± 0.15	0.52	0.50
$6_{2,5} - 7_{1,6}$	6.8631	1013	45	39	5.3	-15.0 ± 0.5	18.2 ± 1.5	4.38 ± 0.44	1.37	1.47
$6_{0,6} - 7_{1,7}$	6.8714	843	15	13	8.1	-16.3 ± 0.2	13.9 ± 1.2	3.20 ± 0.28	1.20	1.32
$8_{0,8} - 8_{1,7}$	6.8749	1270	17	17	4.4	-14.9 ± 0.3	13.3 ± 0.9	2.88 ± 0.18	0.76	0.83
$8_{1,8} - 8_{2,7}$	6.8867	1274	51	51	4.4	-15.0 ± 0.9	15.5 ± 1.5	3.30 ± 0.39	1.23	1.31
$5_{1,4} - 6_{2,5}$	6.9063	795	39	33	5.8	-17.6 ± 0.3	15.2 ± 0.3	4.61 ± 0.19	1.50	1.62
$7_{1,7} - 8_{0,8}$	6.9588	1070	17	15	7.8	-14.3 ± 0.3	17.5 ± 1.2	3.86 ± 0.27	1.10	1.20
$7_{2,6} - 8_{1,7}$	6.9655	1270	17	15	5.7	-7.2 ± 1.6	18.8 ± 1.0	3.83 ± 0.49	0.83	0.90
$9_{0,9} - 9_{1,8}$	6.9774	1552	57	57	4.2	-13.1 ± 0.2	14.8 ± 0.3	3.78 ± 0.11	1.09	1.13
$9_{1,9} - 9_{2,8}$	6.9833	1554	19	19	4.2	-11.5 ± 0.3	16.9 ± 1.0	3.32 ± 0.20	0.61	0.65
$3_{2,2} - 4_{3,1}$	6.9933	552	9	7	8.6	-17.1 ± 0.2	13.2 ± 0.7	2.99 ± 0.16	1.18	1.33

Table 4.7: continued.

Transition	λ (μm)	E_l (K)	g_l	g_u	A_{ul} (s^{-1})	v_{lsr} (km s^{-1})	FWHM (km s^{-1})	W (10^8 Hz)	$\log_{10}(\eta_0)$	$\log_{10}(\tau_p)$
$8_{3,6} - 9_{2,7}$	7.0015	1729	57	51	3.4	-10.1 ± 0.5	10.9 ± 1.4	2.04 ± 0.33	0.83	0.85
$12_{1,11} - 12_{2,10}$	7.0134	2820	25	25	7.1	-9.9 ± 0.4	11.8 ± 1.1	1.46 ± 0.13	0.08	-0.01
$7_{1,6} - 8_{2,7}$	7.0218	1274	51	45	5.9	-12.4 ± 0.5	16.3 ± 0.6	4.54 ± 0.29	1.33	1.40
$12_{2,11} - 12_{3,10}$	7.0231	2824	75	75	7.1	-10.2 ± 0.3	12.7 ± 1.0	2.00 ± 0.20	0.56	0.46
$4_{2,2} - 5_{3,3}$	7.0475	725	11	9	6.8	-17.7 ± 0.4	13.1 ± 1.3	2.90 ± 0.28	1.08	1.21
$8_{1,8} - 9_{0,9}$	7.0547	1324	57	51	7.4	-13.7 ± 0.3	13.6 ± 0.3	4.51 ± 0.23	1.46	1.52
$8_{2,7} - 9_{1,8}$	7.0617	1552	57	51	5.8	-14.9 ± 0.2	14.3 ± 0.5	3.40 ± 0.14	1.19	1.24
$10_{0,10} - 10_{1,9}$	7.0818	1860	21	21	4.1	-12.5 ± 0.2	10.3 ± 0.6	1.50 ± 0.09	0.45	0.46
$10_{1,10} - 10_{2,9}$	7.0846	1861	63	63	4.1	-11.7 ± 0.2	12.9 ± 0.2	3.19 ± 0.12	0.92	0.93
$8_{1,7} - 9_{2,8}$	7.0924	1554	19	17	5.9	-12.6 ± 0.2	14.8 ± 0.6	3.29 ± 0.14	0.73	0.77
$13_{1,12} - 13_{2,11}$	7.1065	3233	81	81	7.0	-11.1 ± 0.4	13.7 ± 0.5	1.92 ± 0.12	0.32	0.18
$5_{2,3} - 6_{3,4}$	7.1175	933	39	33	5.5	-17.4 ± 0.5	14.2 ± 0.3	3.63 ± 0.18	1.42	1.53
$9_{3,7} - 10_{2,8}$	7.1252	2069	21	19	4.0	-12.4 ± 0.2	11.2 ± 0.6	1.83 ± 0.10	0.25	0.24
$4_{2,3} - 5_{3,2}$	7.1469	732	33	27	5.6	-18.0 ± 0.2	12.8 ± 0.2	3.77 ± 0.13	1.49	1.62
$9_{0,9} - 10_{1,10}$	7.1544	1603	63	57	7.1	-12.7 ± 0.3	12.9 ± 1.0	2.99 ± 0.28	1.31	1.35
$4_{3,1} - 5_{4,2}$	7.1643	878	11	9	10.4	-17.8 ± 0.3	15.4 ± 0.9	3.91 ± 0.24	1.18	1.30
$11_{0,11} - 11_{1,10}$	7.1889	2194	69	69	4.0	-12.3 ± 0.3	15.4 ± 0.7	3.13 ± 0.17	0.74	0.71
$11_{1,11} - 11_{2,10}$	7.1903	2194	23	23	4.0	-11.6 ± 0.2	11.7 ± 0.2	1.74 ± 0.08	0.26	0.24
$14_{1,13} - 14_{2,12}$	7.2001	3670	29	29	6.9	-8.7 ± 0.5	12.5 ± 1.3	0.85 ± 0.09	-0.42	-0.61
$7_{2,5} - 8_{3,6}$	7.2125	1447	51	45	4.5	-14.5 ± 0.2	15.2 ± 0.6	3.36 ± 0.15	1.13	1.18
$11_{4,8} - 12_{3,9}$	7.2383	3030	25	23	2.7	-9.1 ± 0.6	12.3 ± 1.5	0.70 ± 0.09	-0.48	-0.59
$7_{1,6} - 7_{4,3}$	7.2543	1340	45	45	0.2	-12.9 ± 0.5	11.0 ± 1.2	1.04 ± 0.14	-0.14	-0.08
$4_{1,4} - 5_{2,3}$	7.2723	642	33	27	1.2	-17.3 ± 0.2	14.3 ± 0.2	3.16 ± 0.09	0.91	1.05
$5_{3,2} - 6_{4,3}$	7.2792	1088	39	33	8.0	-17.4 ± 0.3	15.3 ± 0.3	4.12 ± 0.14	1.51	1.60
$9_{2,7} - 10_{3,8}$	7.2872	2081	63	57	4.5	-10.8 ± 0.2	12.8 ± 0.2	2.75 ± 0.10	0.80	0.78
$12_{1,12} - 12_{2,11}$	7.3002	2554	75	75	3.9	-11.7 ± 0.2	10.8 ± 0.7	1.70 ± 0.13	0.54	0.47

Table 4.7: continued.

Transition	λ (μm)	E_l (K)	g_l	g_u	A_{ul} (s^{-1})	v_{lsr} (km s^{-1})	FWHM (km s^{-1})	W (10^8 Hz)	$\log_{10}(\eta_0)$	$\log_{10}(\tau_p)$
$5_{2,4} - 6_{3,3}$	7.3389	951	13	11	3.6	-14.7 ± 0.6	16.2 ± 0.6	3.06 ± 0.25	0.78	0.89
$11_{2,9} - 12_{3,10}$	7.3945	2824	75	69	4.6	-9.4 ± 0.3	14.3 ± 1.0	2.44 ± 0.22	0.40	0.30
$12_{2,11} - 13_{1,12}$	7.4401	2939	81	75	5.4	-9.6 ± 0.6	10.6 ± 1.6	1.70 ± 0.32	0.43	0.32
$12_{1,11} - 13_{2,12}$	7.4423	2939	27	25	5.4	-11.1 ± 0.4	14.2 ± 1.4	1.82 ± 0.17	-0.05	-0.15
$7_{3,4} - 8_{4,5}$	7.4618	1615	51	45	5.2	-12.0 ± 0.2	10.5 ± 0.8	2.53 ± 0.22	1.11	1.15
$6_{4,2} - 7_{5,3}$	7.4654	1524	15	13	9.2	-11.5 ± 0.6	16.8 ± 1.8	3.78 ± 0.40	0.89	0.94
$6_{4,3} - 7_{5,2}$	7.4708	1525	45	39	9.2	-12.9 ± 0.3	15.8 ± 0.3	3.84 ± 0.15	1.37	1.41
$12_{1,12} - 13_{0,13}$	7.4744	2599	81	75	6.1	-9.3 ± 0.3	12.3 ± 0.8	2.01 ± 0.16	0.72	0.65
$8_{3,5} - 9_{4,6}$	7.5193	1929	19	17	4.4	-10.6 ± 0.3	13.5 ± 0.3	2.14 ± 0.13	0.41	0.41
$14_{1,14} - 14_{2,13}$	7.5326	3350	87	87	3.9	-10.7 ± 0.5	12.0 ± 1.4	1.57 ± 0.23	0.08	-0.07
$13_{2,12} - 14_{1,13}$	7.5396	3350	29	27	5.1	-11.8 ± 0.8	13.9 ± 2.4	0.94 ± 0.16	-0.30	-0.45
$13_{2,11} - 14_{3,12}$	7.5437	3671	87	81	4.5	-7.4 ± 0.3	9.7 ± 0.7	1.24 ± 0.11	-0.11	-0.29
$13_{2,11} - 14_{3,12}$	7.5437	3671	87	81	4.5	-7.6 ± 0.3	11.7 ± 1.1	1.72 ± 0.16	-0.11	-0.29
$9_{3,6} - 10_{4,7}$	7.5567	2275	63	57	3.9	-12.4 ± 0.9	18.7 ± 0.9	3.47 ± 0.22	0.65	0.62
$5_{1,5} - 6_{2,4}$	7.5754	867	13	11	0.7	-14.0 ± 0.4	12.7 ± 1.0	1.63 ± 0.12	0.16	0.28
$10_{3,7} - 11_{4,8}$	7.5802	2652	23	21	3.7	-10.0 ± 4.9	14.5 ± 1.8	1.26 ± 0.36	-0.07	-0.14
$6_{2,5} - 7_{3,4}$	7.5819	1212	45	39	2.2	-11.4 ± 0.8	17.4 ± 0.7	3.78 ± 0.28	0.98	1.06
$7_{6,1} - 8_{7,2}$	7.6060	2289	51	45	12.8	-12.6 ± 0.3	13.2 ± 0.3	3.37 ± 0.12	1.07	1.03
$14_{2,13} - 15_{1,14}$	7.6420	3786	93	87	4.9	-10.1 ± 0.7	8.8 ± 1.7	0.60 ± 0.15	-0.10	-0.30
$8_{4,4} - 9_{5,5}$	7.7118	2122	19	17	6.2	-5.7 ± 0.2	12.3 ± 0.2	2.97 ± 0.10	0.46	0.44
$8_{4,5} - 9_{5,4}$	7.7676	2125	57	51	6.0	-11.7 ± 0.1	13.9 ± 0.1	3.16 ± 0.06	0.93	0.91
$9_{8,2} - 10_{9,1}$	7.8054	3556	21	19	13.4	-10.7 ± 0.4	9.0 ± 1.0	0.84 ± 0.10	-0.14	-0.31
$9_{4,5} - 10_{5,6}$	7.8122	2473	63	57	5.1	-8.3 ± 0.3	14.2 ± 0.8	1.88 ± 0.14	0.68	0.62
$9_{4,6} - 10_{5,5}$	7.9452	2482	21	19	4.7	-9.8 ± 0.5	15.7 ± 1.4	1.31 ± 0.12	0.18	0.12

Table 4.8: Line Parameters for the v=2-1 transition of AFGL 2591. E_l is the energy of the lower level of the transition, g_l and g_u are the statistical weights of the lower and upper levels respectively, A_{ul} is the Einstein A coefficient of the transition, v_{lsr} is the peak velocity of the line, FWHM is the full width at half maximum of the line, W is the equivalent width in units of Hz and τ_p is the peak optical depth of the transition. η_0 is the opacity in the lower level of the transition calculated for $\epsilon = 0.5$. Line data were taken from the HITRAN database (Gordon et al. 2017).

Transition	λ (μm)	E_l (K)	g_l	g_u	A_{ul} (s^{-1})	v_{lsr} (km s^{-1})	FWHM (km s^{-1})	W (10^8 Hz)	$\log_{10}(\eta_0)$	$\log_{10}(\tau_p)$
$10_{3,8} - 9_{2,7}$	5.4015	4055	57	63.0	10.1	-8.6 ± 0.3	8.5 ± 0.9	0.81 ± 0.11	-0.62	-0.77
$4_{4,1} - 3_{3,0}$	5.4373	2745	21	27.0	9.8	-9.5 ± 0.3	11.4 ± 0.8	1.36 ± 0.12	0.01	-0.18
$5_{3,2} - 4_{2,3}$	5.5105	2745	27	33.0	6.2	-10.6 ± 0.3	10.6 ± 0.7	1.35 ± 0.11	-0.11	-0.30
$6_{3,4} - 5_{2,3}$	5.5218	2955	33	39.0	6.9	-11.1 ± 0.3	8.2 ± 0.8	1.29 ± 0.16	-0.14	-0.32
$11_{0,11} - 10_{1,10}$	5.6670	3892	63	69.0	27.6	-11.1 ± 0.3	10.1 ± 0.9	1.62 ± 0.18	0.02	-0.14
$10_{1,10} - 9_{0,9}$	5.7202	3615	57	63.0	26.5	-11.9 ± 0.3	13.3 ± 0.9	2.08 ± 0.19	0.18	0.02
$8_{1,7} - 7_{2,6}$	5.7330	3336	15	17.0	14.1	-10.1 ± 0.6	11.6 ± 1.7	0.90 ± 0.16	-0.43	-0.60
$6_{2,5} - 5_{1,4}$	5.7627	2879	33	39.0	10.9	-10.0 ± 0.3	11.5 ± 0.8	1.92 ± 0.16	0.16	-0.02
$9_{1,9} - 8_{0,8}$	5.7754	3363	17	19.0	25.2	-9.5 ± 0.4	14.1 ± 2.7	1.67 ± 0.53	-0.16	-0.32
$9_{0,9} - 8_{1,8}$	5.7769	3364	51	57.0	25.2	-11.0 ± 0.3	14.1 ± 0.2	2.32 ± 0.13	0.32	0.15
$5_{2,4} - 4_{1,3}$	5.8037	2698	9	11.0	9.7	-7.5 ± 0.5	9.8 ± 1.8	0.71 ± 0.16	-0.30	-0.49
$7_{1,6} - 6_{2,5}$	5.8206	3110	39	45.0	11.8	-7.5 ± 0.2	12.2 ± 0.8	2.75 ± 0.22	0.11	-0.07
$8_{0,8} - 7_{1,7}$	5.8353	3138	15	17.0	23.9	-7.0 ± 0.5	13.2 ± 1.2	2.28 ± 0.25	-0.04	-0.22
$3_{3,1} - 3_{2,2}$	5.9287	2610	7	7.0	4.3	-11.6 ± 0.4	8.1 ± 1.5	0.41 ± 0.09	-0.74	-0.93
$3_{3,0} - 3_{2,1}$	5.9478	2618	21	21.0	4.5	-9.2 ± 0.3	9.6 ± 0.8	0.83 ± 0.09	-0.24	-0.44
$6_{1,6} - 5_{0,5}$	5.9485	2764	33	39.0	20.7	-9.7 ± 0.2	13.6 ± 0.5	2.94 ± 0.14	0.56	0.38
$6_{0,6} - 5_{1,5}$	5.9622	2767	11	13.0	20.6	-10.1 ± 0.3	10.1 ± 0.7	1.25 ± 0.11	0.08	-0.10
$5_{3,2} - 5_{2,3}$	5.9925	2955	33	33.0	8.7	-7.3 ± 0.3	11.3 ± 0.9	1.51 ± 0.15	-0.01	-0.19
$5_{1,5} - 4_{0,4}$	6.0059	2615	9	11.0	18.8	-8.5 ± 0.4	11.1 ± 1.2	1.22 ± 0.17	0.09	-0.10
$7_{3,4} - 7_{2,5}$	6.0232	3443	45	45.0	11.8	-10.6 ± 0.3	12.3 ± 0.8	1.63 ± 0.13	-0.10	-0.27
$7_{2,5} - 7_{1,6}$	6.0322	3323	45	45.0	9.4	-10.8 ± 0.3	14.1 ± 1.0	1.38 ± 0.12	-0.11	-0.28
$2_{2,1} - 2_{1,2}$	6.1010	2413	15	15.0	5.9	-9.7 ± 0.2	13.8 ± 0.6	1.68 ± 0.09	-0.10	-0.30
$3_{0,3} - 2_{1,2}$	6.2028	2413	15	21.0	11.9	-9.8 ± 0.4	14.1 ± 0.1	3.18 ± 0.30	0.37	0.17

Table 4.8: continued.

Transition	λ (μm)	E_l (K)	g_l	g_u	A_{ul} (s^{-1})	v_{lsr} (km s^{-1})	FWHM (km s^{-1})	W (10^8 Hz)	$\log_{10}(\eta_0)$	$\log_{10}(\tau_p)$
$2_{1,1} - 2_{0,2}$	6.2878	2396	5	5.0	17.7	-9.7 ± 0.6	8.6 ± 1.5	1.40 ± 0.31	-0.05	-0.25
$1_{1,0} - 1_{0,1}$	6.3157	2329	9	9.0	21.3	-14.5 ± 0.4	10.4 ± 1.0	2.43 ± 0.29	0.34	0.14
$1_{0,1} - 1_{1,0}$	6.5149	2360	9	9.0	24.9	-9.9 ± 0.4	12.7 ± 1.7	2.08 ± 0.33	0.43	0.23
$7_{2,5} - 7_{3,4}$	6.6462	3544	45	45.0	24.4	-10.7 ± 0.3	12.3 ± 0.9	1.84 ± 0.16	0.28	0.11
$4_{0,4} - 4_{1,3}$	6.6674	2698	9	9.0	15.1	-8.3 ± 0.4	12.5 ± 1.1	1.75 ± 0.18	-0.01	-0.20
$9_{2,7} - 9_{3,6}$	6.6895	4180	57	57.0	25.5	-9.6 ± 0.5	15.0 ± 1.7	1.20 ± 0.16	-0.06	-0.21
$7_{1,6} - 7_{2,5}$	6.7261	3443	45	45.0	20.3	-11.9 ± 0.4	12.5 ± 1.0	1.63 ± 0.16	0.28	0.11
$3_{2,1} - 3_{3,0}$	6.7334	2745	21	21.0	9.2	-13.3 ± 1.0	14.1 ± 2.9	1.45 ± 0.37	0.14	-0.05
$7_{3,4} - 7_{4,3}$	6.7536	3701	45	45.0	18.0	-11.9 ± 0.4	12.4 ± 1.0	1.32 ± 0.14	0.07	-0.09
$5_{0,5} - 5_{1,4}$	6.7653	2879	33	33.0	12.5	-12.2 ± 0.5	13.1 ± 1.2	1.71 ± 0.20	0.36	0.17
$4_{2,3} - 4_{3,2}$	6.7693	2885	27	27.0	12.6	-12.1 ± 0.4	13.2 ± 1.0	1.44 ± 0.14	0.29	0.11
$5_{3,2} - 5_{4,1}$	6.7987	3240	33	33.0	12.1	-11.2 ± 0.4	11.8 ± 0.9	1.50 ± 0.15	0.12	-0.05
$4_{3,2} - 4_{4,1}$	6.8108	3064	27	27.0	7.7	-9.5 ± 0.7	13.5 ± 1.9	1.16 ± 0.21	-0.03	-0.21
$3_{0,3} - 4_{1,4}$	6.8136	2621	27	21.0	17.1	-11.9 ± 0.4	13.5 ± 1.2	2.12 ± 0.23	0.49	0.30
$8_{1,7} - 8_{2,6}$	6.8165	3735	17	17.0	18.4	-9.8 ± 0.5	10.9 ± 1.7	1.11 ± 0.21	-0.38	-0.54
$4_{1,4} - 5_{0,5}$	6.8449	2764	33	27.0	16.0	-10.1 ± 0.5	11.6 ± 0.5	2.00 ± 0.20	0.47	0.29
$1_{1,0} - 2_{2,1}$	6.8512	2507	15	9.0	26.0	-10.5 ± 0.3	13.0 ± 0.8	2.01 ± 0.16	0.41	0.22
$5_{1,5} - 6_{0,6}$	6.9411	2938	13	11.0	16.0	-11.9 ± 0.6	9.0 ± 1.5	0.90 ± 0.19	-0.03	-0.21
$7_{0,7} - 7_{1,6}$	6.9985	3323	45	45.0	10.0	-8.0 ± 0.4	13.8 ± 1.7	1.82 ± 0.27	0.11	-0.06
$6_{1,6} - 7_{0,7}$	7.0362	3138	45	39.0	15.7	-10.4 ± 0.4	15.1 ± 1.3	2.00 ± 0.20	0.38	0.20
$2_{2,0} - 3_{3,1}$	7.0934	2744	7	5.0	26.9	-10.6 ± 0.3	9.7 ± 0.9	1.07 ± 0.12	0.06	-0.13
$2_{2,1} - 3_{3,0}$	7.0996	2745	21	15.0	26.7	-11.3 ± 0.3	15.8 ± 0.9	2.39 ± 0.18	0.53	0.34
$5_{1,4} - 6_{2,5}$	7.1217	3110	39	33.0	11.1	-9.8 ± 0.2	9.8 ± 0.6	1.23 ± 0.10	0.21	0.03
$7_{0,7} - 8_{1,8}$	7.1381	3364	51	45.0	15.1	-11.3 ± 0.4	13.1 ± 1.4	1.72 ± 0.22	0.27	0.10
$8_{1,8} - 8_{2,7}$	7.1424	3590	51	51.0	9.2	-10.2 ± 0.6	9.5 ± 1.4	0.78 ± 0.15	-0.04	-0.20
$7_{1,6} - 8_{2,7}$	7.2245	3590	51	45.0	11.1	-11.8 ± 0.2	10.0 ± 0.6	0.87 ± 0.07	0.01	-0.16

Table 4.8: continued.

Transition	λ (μm)	E_l (K)	g_l	g_u	A_{ul} (s^{-1})	v_{lsr} (km s^{-1})	FWHM (km s^{-1})	W (10^8 Hz)	$\log_{10}(\eta_0)$	$\log_{10}(\tau_p)$
$8_{2,7} - 9_{1,8}$	7.2272	3868	57	51.0	10.9	-12.1 ± 0.3	10.3 ± 0.7	0.85 ± 0.08	-0.16	-0.31
$3_{2,2} - 4_{3,1}$	7.2371	2886	9	7.0	17.5	-11.4 ± 0.8	13.5 ± 2.1	1.01 ± 0.20	-0.07	-0.25
$9_{0,9} - 9_{1,8}$	7.2431	3868	57	57.0	8.9	-11.6 ± 0.3	10.2 ± 1.0	0.72 ± 0.09	-0.19	-0.35
$3_{3,0} - 4_{4,1}$	7.2937	3064	27	21.0	28.4	-11.6 ± 0.2	11.0 ± 0.5	1.54 ± 0.08	0.52	0.34
$4_{2,2} - 5_{3,3}$	7.3018	3060	11	9.0	13.7	-13.4 ± 0.2	8.2 ± 0.6	1.05 ± 0.10	-0.18	-0.36
$9_{2,8} - 10_{1,9}$	7.3255	4177	21	19.0	11.0	-14.5 ± 0.5	7.7 ± 1.2	0.49 ± 0.10	-0.80	-0.94
$9_{1,9} - 10_{0,10}$	7.3323	3892	21	19.0	13.8	-10.7 ± 0.4	9.7 ± 1.1	0.69 ± 0.10	-0.50	-0.66
$9_{0,9} - 10_{1,10}$	7.3337	3892	63	57.0	13.8	-9.5 ± 0.3	10.2 ± 0.3	1.22 ± 0.07	-0.03	-0.18
$4_{3,2} - 5_{4,1}$	7.4294	3240	33	27.0	20.9	-10.1 ± 0.4	10.9 ± 1.0	1.70 ± 0.19	0.39	0.21
$5_{3,2} - 6_{4,3}$	7.5509	3451	39	33.0	16.2	-11.5 ± 0.4	11.4 ± 1.0	1.25 ± 0.14	0.23	0.06
$5_{3,3} - 6_{4,2}$	7.5739	3452	13	11.0	16.0	-7.0 ± 0.1	10.0 ± 1.7	0.85 ± 0.18	-0.25	-0.42
$5_{5,0} - 6_{6,1}$	7.5956	3934	39	33.0	29.8	-9.2 ± 0.5	10.3 ± 1.6	0.99 ± 0.18	0.19	0.03
$6_{3,4} - 7_{4,3}$	7.7350	3701	45	39.0	12.3	-7.0 ± 0.4	10.7 ± 1.0	0.88 ± 0.10	0.03	-0.14
$6_{5,2} - 7_{6,1}$	7.7405	4181	45	39.0	24.2	-12.8 ± 0.3	13.0 ± 0.9	0.88 ± 0.08	0.01	-0.14

5 | Surveying the Inner Structure of Massive Young Stellar Objects in the L Band

Abstract

We present results from a survey of five massive protostars in the L band, conducted with iSHELL/IRTF with resolving power 6 km s^{-1}, between 2.95 and 3.25 μm. Two of our five targets show transitions from organic species, with MonR2 IRS 3 showing HCN lines in emission, and AFGL 2136 showing HCN and C_2H_2 lines in absorption. Orion BN, S140 IRS1 and MonR2 IRS 2 did not yield any detections. The velocity of the emission lines of HCN of MonR2 IRS 3A are consistent with CO emission features in lines up to J=26, as both are red-shifted with respect to the systemic velocity. CO lines also show blue-shifted absorption. This P-Cygni line profile, commonly observed towards massive young stellar objects, is likely due to an expanding shell, which is supported by sub-millimetre velocity maps of HCN. Alternatively HCN emission may arise from the upper layers of a disk photosphere. Previously HCN emission was detected at 3 μm for the first time towards a massive protostar, AFGL 2591, which was suggested to probe the upper layers of a circumstellar disk atmosphere (chapter 3). Absorption lines of HCN and C_2H_2 in AFGL 2136 show evidence for partial covering of the source, with lines at 13 μm requiring dilution factors of $\sim$0.3. This dilution fraction is three times less than at 3 μm and 7 μm; wavelengths at which the source is fully, or almost fully covered. We also conduct an analysis based on a disk origin for the absorption lines and find that HCN shows consistent physical conditions across all wavelengths, and C_2H_2 shows an increasing temperature and abundance with decreasing wavelength, indicative of a radial abundance gradient.

A. G. Barr, J. Li, A. Boogert, A. Lee, C. N. DeWitt, A. G. G. M. Tielens
Submitted to Astronomy & Astrophysics

5.1 Introduction

Circumstellar disks play a key role in the star formation process (Nakano et al. 1995; Jijina & Adams 1996; Bonnell & Bates 2006) as angular momentum conservation of a collapsing cloud leads in a natural way to a disk. Subsequent viscous dissipation, and/or a disk wind, slowly redistributes angular momentum, resulting in accretion of disk material onto the protostar. Massive protostars evolve through several stages - IR dark clouds, Hot Cores, hyper compact HII regions (HCHII), and ultracompact HII regions (UCHII) (Zinnecker & Yorke 2007; Beuther et al. 2007; Tan 2017). The Hot Core phase has been associated with the disk accretion phase (Johnston et al. 2015; Maud et al. 2019), although to what extent this is the case remains to be established.

Ro-vibrational absorption lines at infrared wavelengths trace a range of different energies and are particularly sensitive to the warm material close to protostars. These transitions are therefore a very useful tool for probing the physical and chemical conditions of massive star formation and tracing massive young stellar object (MYSO) structure on small scales. Such a tool can help to understand hot cores and the presence of potential disks, planets, outflow or winds, as well as the accretion processes of massive protostars (chapters 3 and 4).

The disk structure and evolution in low and intermediate mass stars is well understood, and significant progress continues to be made (Williams & Cieza 2011; Andrews 2020). The same cannot be said for high mass stars, where additional processes, such as photoevaporation from high radiative forces, make the picture more complicated (Zinnecker & Yorke 2007). It is expected that in these objects, disks should also play a fundamental role in the build up of the stellar mass, as in the case for low mass stars, because otherwise the high radiation pressure would halt accretion before a massive star could be formed (McKee & Ostriker 2007). Furthermore, strong evidence for the presence of disks around massive stars lies in the observation of large bipolar outflows (Shepherd & Churchwell 1996a,b; Beuther et al. 2002; Wu et al. 2005).

Cirumstellar disks are an important step in the progression from star formation to planet formation, therefore understanding them is vital to gain insight into how planets form, and what material they are made of. Near-IR observations of low mass stars have been shown to be sensitive to the inner disk on scales of a few AU (Carr & Najita 2011; Mandell et al. 2012; Gibb & Horne 2013), providing insight to the physical and chemical conditions during planet formation. Planets have yet to be detected around O-type stars with the most massive host stars observed with a planet being 3-5 $M_{\odot}$, and less discoveries as the stellar mass increases (Reffert et al. 2015; Grunblatt et al. 2019; Hollands et al. 2021). This likely reflects the short Kelvin-Helmholtz and disk dispersal timescales of massive stars compared to low mass stars, thus planets have much less time to form, as well as high radiation fields and eventual core collapse supernovae (Veras et al. 2020).

At infrared wavelengths disks of massive stars have mainly been studied through atomic line and CO bandhead emission which trace the inner disk (Bik et al. 2006; Davies et al. 2010; Cooper et al. 2013; Fedriani et al. 2020). In a survey of massive protostars, Ilee et al. (2013) modelled CO bandhead emission from 20 massive young stellar objects (YSOs) and find temperatures and densities consistent with emission from an accretion disk, close to the dust sublimation radius. The infrared spectrum

of disks around TTauri and Herbig stars is well studied compared to massive YSOs. CO has been extensively studied for both TTauri and Herbig disks (Najita et al. 2003; Blake & Boogert 2004; Salyk et al. 2009; Bast et al. 2011), with H_2O and OH also detected in TTauri disks (Pontoppidan et al. 2010; Carr & Najita 2011; Salyk et al. 2011; Banzatti et al. 2017). Herbig disks have been found to consistently exhibit a very low detection rate of H_2O compared to TTauri disks, although OH is more readily detected (Pontoppidan et al. 2010; Salyk et al. 2011; Fedele et al. 2012, 2013; Banzatti et al. 2017). Mandell et al. (2012) detected several simple species in emission towards three TTauri disks in the L band with CRIRES and NIRSPEC such as OH, HCN, H_2O and C_2H_2, also giving upper limits on CH_4 and NH_3. Simple organics have also been detected in emission in the mid-infrared (mid-IR) spectrum of TTauri and Herbig disks with *Spitzer* (Carr & Najita 2008, 2011; Pascucci et al. 2009; Pontoppidan et al. 2010; Salyk et al. 2011).

Observations of massive stars imply that the mid-IR continuum originates from the dust photosphere of the disk at distances from the star between 50 and 100 AU (Preibisch et al. 2003; Monnier et al. 2009; de Wit et al. 2011; Boley et al. 2013; Frost et al. 2021). However, at mid-IR wavelengths, water and simple organics are seen in absorption towards massive protostars (Evans, Lacy & Carr 1991; Knez et al. 2009; Barentine & Lacy 2012; Rangwala et al. 2018; Dungee et al. 2018). In chapter 3 we developed a model for AFGL 2591 and AFGL 2136 in which the absorption lines trace gas in an internally heated circumstellar disk at radii of 100-200 AU, with a temperature structure that decreases with scale height, resulting in the presence of absorption lines. We detected HCN and C_2H_2 in emission in the L band spectrum of the massive protostar AFGL 2591 and proposed it was due to scattering of continuum photons in the upper layers of the disk photosphere.

In this article we present a follow-up survey of the L band of massive protostars to investigate how widespread emission lines of organics are at these wavelengths, and to understand how they relate to the disk as probed by 4-13 μm absorption lines (chapter 3). We have selected a wide range of objects, of different masses and luminosities, and in different evolutionary stages: hot cores, ultracompact HII regions and protostars, with particular focus on MonR2 IRS 3 and AFGL 2136. MonR2 IRS 3 differs from AFGL 2591 mainly in the fact that it is a binary, and that typical temperatures are relatively cooler, being on the order of a few hundred K in MonR2 IRS 3 compared to 600-700 K in AFGL 2591. Also the luminosity and mass of MonR2 IRS 3 are an order of magnitude and a factor of 4 lower than that of AFGL 2591 respectively, which has a mass and luminosity of 40 $M_\odot$ and 10^5 $L_\odot$) respectively. AFGL 2136 is very similar to AFGL 2591 in mass, luminosity and temperature of detected molecules, although the inclination angle is 40° (Maud et al. 2019) compared to AFGL 2591 which is close to face on.

5.2 Observations and Data Reduction

All objects were observed as part of program 2021A095 with iSHELL (Rayner et al. 2016) at the Infrared Telescope Facility (IRTF) on Mauna kea. Observations were taken in the L2 mode, at a resolving power of 50,000 (6 km s^{-1}), using a slit with of

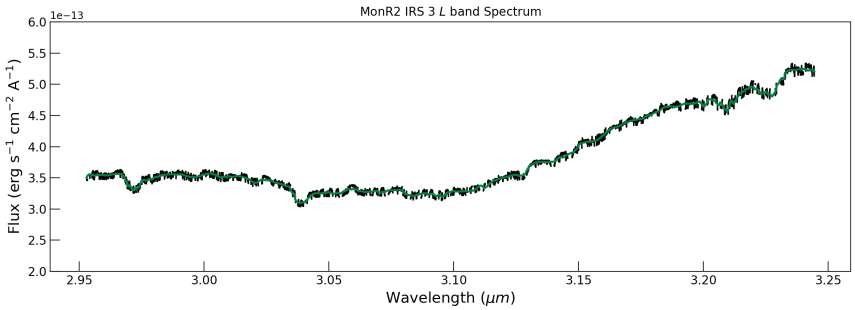

Figure 5.1: Full spectrum of the L2 setting of MonR2 IRS 3. The green line is a heavily smoothed median filter of the original spectrum used to define the baseline. The spectrum has been fully reduced, therefore the atmosphere and blaze function have been removed by division by the standard star. Regions of poor transmission have been masked out.

0.75″. Targets were nodded along the slit to allow for subtraction of sky and telescope emission. The extracted A and B spectra were then averaged. The continuum signal-to-noise (S/N) values per resolution element were > 300 for all sources except AFGL 2136 for which only a S/N of 100 was achieved. Flat fields for both science target and standard stars were taken using iSHELL's internal lamp. Details of the observations are summarised in Table 5.1.

MonR2 IRS 3 was observed on UT 2021 February 15 from 05:50 to 06:08. Seeing was on average 0.7″ and the source was observed at transit with airmass ranging from 1.13 to 1.15. HR1931 was observed as a standard star immediately before MonR2 IRS 3 from 05:24 to 05:36 at airmass 1.10 to 1.12.

MonR2 IRS 2 was observed on UT 2021 February 15 and 16 from 06:19 to 06:58 and 05:37 to 06:26 respectively. The airmass ranged from 1.1-1.2 for both nights. HR1948 was used as a standard star on the 14th and HR1931 was used on the 15th. Due to the weakness of MonR2 IRS 2, the achieved S/N was lower than MonR2 IRS 3, and a S/N of 300 was only obtained for part of the spectrum, with most of it lower.

We observed Orion BN on February 16 at two different slit angles, from 06:51 to 07:03 and 07:13 to 07:28 at 210° and 235° respectively. The airmass ranged from 1.1-1.2 and HR1948 was used as a standard star on the same night.

AFGL 2136 was observed on UT 2021 July 15 from 07:06:09 to 07:46:56 and 08:15:07 to 08:31:27, with airmass ranging from 1.4 to 1.2. HR7236 was observed in between these two acquisitions as a standard star which had an airmass of 1.3.

S140 IRS1 was observed on the same night from 08:53:38 to 09:05:19 and 09:45:41 to 09:57:22, with airmass ranging from 2.0 to 1.7. BS8585 was taken as a standard star in between these acquisitions with airmass 1.8 to 1.7. Our targeted S/N was not reached on AFGL 2136 because of forced closure of the telescope dome due to strong winds.

The data reduction was carried out using the Spextool package version 5.0.1 (Cushing et al. 2004). Wavelength calibration solutions were accurate to within 0.5 km s^{-1}. The atmospheric seeing during the observations was good, therefore the binary in MonR2 IRS 3 was resolved, allowing for separate extraction of the two binary com-

ponents. The spectra were then combined and the telluric correction was applied by dividing by the standard star, which removes the blaze function of the instrument and any fringing that was present.

The wavelength range of the L2 setting is in the middle of the H_2O ice band. The final merged spectrum therefore had large scale structure in the baseline due to the ice feature. This was removed by fitting a baseline to the spectrum using a broad median filter and dividing the spectrum by this fitted baseline (Figure 5.1). Some lines were affected by systematic error due to proximity to telluric residuals. In some cases a local continuum had to be used to achieve a flat continuum across the line by fitting a straight line across it. Many lines were lost in deep telluric lines, as the atmosphere is strong at these wavelengths.

Table 5.1: Summary of Observations.

Source	R.A (J2000)	Dec (J2000)	Date	Integration Time (s)	Airmass
MonR2 IRS 3	06:07:47.95	-06:23:01.9	14.02.21	840	1.13-1.15
MonR2 IRS 2	06:07:45.86	-06:22:59.5	14/15.02.21	3600	1.1-1.2
Orion BN	05:35:13.81	-05:22:25.9	15.02.21	720	1.1-1.2
S140 IRS1	22:19:17.65	63:18:50.7	15.07.21	1200	2.0-1.7
AFGL 2136	18:22:26.09	-13:30:08.9	15.07.21	1800	1.4-1.2

5.3 Analysis

5.3.1 Emission Lines

Emission lines are analysed following chapter 3, outlined in section 3.5.3. Transitions were fit with a single Gaussian component with peak velocity, v_{lsr}, full width at half maximum (FWHM), and line depth as free parameters. Physical conditions were calculated using the rotation diagram method, where the column density in the upper level of each transition is given by:

$$N_u = 8\pi\sqrt{2\pi}\sigma_v \frac{\tau_s}{A_{ul}\lambda^3} \tag{5.1}$$

where A_{ul} is the Einstein A coefficient of the transition, λ is the wavelength, τ_s is the scattering optical depth (see equation 3.9) and σ_v is the standard deviation of the line in velocity units. The FWHM is related to σ_v via the equation: FWHM $= \sigma_v 2\sqrt{2\ln(2)}$. For the H_2 emission lines, a single Gaussian fit was not acceptable, therefore these lines are fit with a two Gaussian model with peak velocity, FWHM and line depth as free parameters. Average line profiles for low and high J lines of HCN are created by mathematically averaging normalised line profiles of each relevant line, interpolated onto the same velocity scale.

5.3.2 Absorption Lines

Rotation Diagram

Rotation diagrams for the absorption lines are created using the Boltzmann equation. The column density in the lower ro-vibrational level is calculated using the optically thin relation:

$$N_l = \frac{g_l}{g_u} \frac{8\pi}{A_{ul}\lambda_{ul}^3} \int \frac{\tau_(v)}{\phi(v)} dv \tag{5.2}$$

N_l is the column density of the lower level, g_l and g_u are the statistical weights for the lower and upper level respectively, A_{ul} is the spontaneous emission coefficient for the transition, λ_{ul} is the wavelength of the line, $\tau(v)$ is the optical depth profile of the line in velocity space, obtained with equation 3.1, and $\phi(v)$ is the normalised line profile, where we assume a gaussian profile.

Curve of Growth for Foreground Absorption

We compare our rotation diagram analysis with a curve of growth analysis which considers a single absorbing slab of gas illuminated from behind by a background dust continuum source. The theoretical curve of growth in this way can be approximated by:

$$\frac{W_\lambda}{bf_c\lambda} \sim \frac{\sqrt{\pi}}{c} \frac{\tau_p}{1 + \tau_p/2\sqrt{2}} \tag{5.3}$$

for $\tau_p < 1.254$ and:

$$\frac{W_\lambda}{bf_c\lambda} \sim \frac{2}{c} \sqrt{\ln[\tau_p/\ln 2] + \frac{\gamma\lambda}{4b\sqrt{\pi}}(\tau_p - 1.254)} \tag{5.4}$$

for $\tau_p > 1.254$, taken from Tielens (2021) with the additional factor $1/f_c$ to take into account a covering factor. Here W_λ is the equivalent width, λ is the wavelength, τ_p is the peak optical depth, b is the Doppler width in km s^{-1} and γ is the damping factor. The expression for τ_p is given by:

$$\tau_p = \frac{\sqrt{\pi}e^2 N_l f_l \lambda}{m_e c b} \tag{5.5}$$

where N_l and f_l are the column density and oscillator strength in the lower level, respectively, e is the electron charge, m_e is the electron mass and τ_p is the peak optical depth. In the empirical curve of growth, we introduce an additional parameter, f_c, the covering factor of the absorbing gas, which is divided into the equivalent width (e.g., the left hand side of equations 5.3 & 5.4 become $W_\lambda/b\lambda f_c$). This parameter describes the covering of the background illuminating source, where a smaller covering factor will result in a smaller observed equivalent width. The level populations are related by:

$$N_l = \frac{g_l N}{Q(T)} e^{-E_l/T_{rot}} \tag{5.6}$$

where Q(T) is the partition function, N is the total column density of the species, E_l is the energy of the lower level in Kelvin and T_{rot} is a free parameter that will be of order of the kinetic temperature for LTE.

Adopting a column density, temperature, and Doppler parameter for the absorbing gas, the left-hand side of equations 5.3 and 5.4, as well as τ_p, can be calculated for each line, resulting in an empirical curve of growth. Empirical curves of growth are created from the observed equivalent widths for a range of different values of T and N, and these are fit to the theoretical curve of growth. We also vary the Doppler parameter, as discussed in section 5.4 below. The fit is quantified by a least square process where the best combination of T and N is chosen such that the reduced chi-squared is the lowest. The errors on these best fit parameters are taken from the 1σ contour.

Curve of Growth for Disk Model

We also carry out a curve of growth analysis in the approximation of absorption lines being formed in a disk atmosphere, with a temperature decreasing with altitude in the disk, based on chapter 3. Curves of growth are constructed using the equation:

$$\frac{W_\nu}{2Y\Delta\nu} = \int_0^\infty \frac{\eta_0 H(a,v)}{1+\eta_0 H(a,v)} dv \tag{5.7}$$

where W is the equivalent width of the absorption lines in frequency space, $\Delta\nu$ is the Doppler width in units of Hz, and Y is the saturation point of the lines which takes into account the temperature gradient in the atmosphere. $H(a,v)$ is the Voigt profile as a function of the frequency shift, v (in velocity space and normalised to the Doppler parameter), and a the damping parameter (in Doppler units). The right-hand side of this equation can be calculated as a function of η_0, resulting in a theoretical curve of growth. We have used the simple approximations to this provided by (Mihalas 1978). η_0 is the opacity at line centre set relative to the continuum opacity given by:

$$\eta_0 = \frac{\kappa_L(\nu=\nu_0)}{\kappa_c} = \alpha \frac{A_{ij}\lambda^3}{8\pi\sqrt{2\pi}\sigma_v} \frac{g_u}{g_l} \frac{X_l}{X_{CO}} \tag{5.8}$$

where X_l is the abundance in the lower level. The dimensionless parameter α is set by the requirement that the CO abundance, X_{CO}, is 10^{-4}, and is essentially the dust opacity, σ_c, which results in σ_c of 7.7×10^{-24} cm^{-2}/g-of-gas, or $\alpha = 1.3 \times 10^{19}$ for AFGL 2136 (section 3.5.2 in chapter 3). The level populations are related by equation 5.6, however with the column density N replaced by the abundance with respect to CO X.

The definition of Y is given in the Appendix of chapter 3 and is insensitively dependent on the temperature. The relevant temperature will be of the order of the that derived from the rotation diagram. Curves of growth are considered for line formation from pure absorption ($\epsilon = 1$), pure scattering ($\epsilon = 0$) and a combination of absorption and scattering ($\epsilon = 0.5$), where ϵ is a measure of the thermalisation of the

line, such that the fraction of scattered and absorbed photons during line formation is (1 - ϵ) and ϵ, respectively (see Appendix of chapter 3 for details).

5.4 Results

5.4.1 MonR2 IRS 3

MonR2 is a massive star forming region at a distance of 0.83±0.05 kpc (Herbst & Racine 1976). In the star forming region are several protostars associated with different stages in the high mass star formation process. The dominant source at infrared wavelengths in the region is MonR2 IRS 3, which has a luminosity of 1.5×10^4 $L_\odot$ (Henning et al. 1992). This object was itself resolved into three protostars in a deep bispectrum speckle interferometry study (Preibisch et al. 2002). MonR2 IRS 3A and MonR2 IRS 3B have masses of 12-15 $M_\odot$ and 8-12 $M_\odot$ respectively (Preibisch et al. 2002).

HCN Emission Lines

A total of 15 HCN lines from the ν_1 band are detected towards MonR2 IRS 3A. All transitions are seen in emission, spanning an energy range of ∼1000 K. Also several low energy HCN emission lines are marginally detected towards MonR2 IRS 3B.

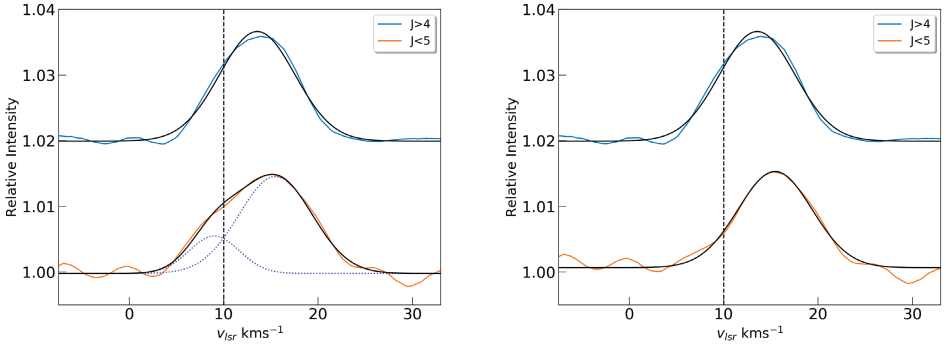

Figure 5.2: Average line profiles for low and high J in MonR2 IRS 3A, created from emission lines that have no systematic error. The high energy lines are chosen as those with J>4, shown in blue, and the low energy lines are those with J<5, shown in orange. The vertical dashed line denotes the cloud velocity of 10 km s^{-1} (van der Tak et al. 2003). *left:* Fits to the average line profiles are given in black with individual contributions to the fit as blue dotted lines. *right:* Fits to the average line profiles with the contribution at cloud velocity divided out.

Average line profiles obtained through line stacking provide useful insights for carrying out the analysis. These are constructed for both high and low J lines, with the distinction being made at J=4, and are shown in Figure 5.2. We only use lines that are not affected by systematic error and are therefore more reliable. Fitting a single Gaussian to each line profile we find that the low J line profile is broader

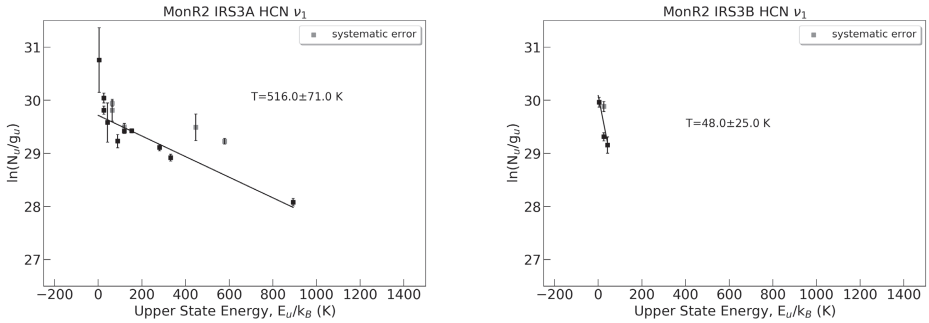

Figure 5.3: Rotation diagrams of HCN lines detected in MonR2 IRS 3A and MonR2 IRS 3B. Emission lines of which the error is underestimated from the fitting routine due to systematic error in the data reduction process are indicated in grey. These transitions are excluded from the fit used to derive the physical conditions. The column density of the low J lines in MonR2 IRS 3A is calculated using the integrated line strengths without the contribution from the cloud at 10 km s^{-1}.

than the high J profile by 2.2 km s^{-1}. Also the peak velocity is slightly red-shifted, with 14.24±0.04 km s^{-1} for the low J profile compared to 13.55±0.02 km s^{-1} for the high J profile. The low J profile appears slightly non-Gaussian with a shoulder on the blue side. The systemic velocity of the cloud is 10.0±1.0 km s^{-1} measured from submillimeter (sub-mm) observations (van der Tak et al. 2003). Therefore we fit an extra Gaussian to the low J profile and find that a weak contribution at 9 km s^{-1} fits well, likely reflecting cold gas from the cloud. In order to properly compare the high and low J lines, we therefore fit the low J lines (R1, R3, P3 and P4) with a two Gaussian model, fixing the parameters for the weak shoulder to those derived from the average line profile, and allowing the parameters of the main velocity component to be free. We then divided out this shoulder from the low J lines and re-calculated the stacked line profile, which is presented in Figure 5.2. Fitting the re-calculated average line profile we find that the deconvolved line widths of the low and high J profiles come into agreement (7.7±0.1 km s^{-1} and 7.9±0.1 km s^{-1} respectively) however the difference in peak velocity remains, with 15.44±0.04 km s^{-1} for the low J profile. This difference is a fraction 0.3 of a resolution element.

The contribution to the R(1) line at 10 km s^{-1} is very weak and only detected at 1σ. Therefore the error on this line, as well as the integrated strength of the main component, is very large. We calculate the error on this line by comparing it to the noise level at the same location in the spectrum. This is also the case for the P(4) line. We do not calculate the physical conditions of the component at 10 km s^{-1} due to the large uncertainties.

The rotation diagram of MonR2 IRS 3A is shown in Figure 5.3 where the column densities of the low J lines are calculated from the line profiles after the contribution at 10 km s^{-1} was divided out. The R(1) line is excluded from the fit to the rotation diagram due to the large uncertainty in the removal of the weak shoulder. The data can be described by a single temperature component of 516±71 K and a column density of 1.6±0.2 × 10^{16} cm^{-2}.

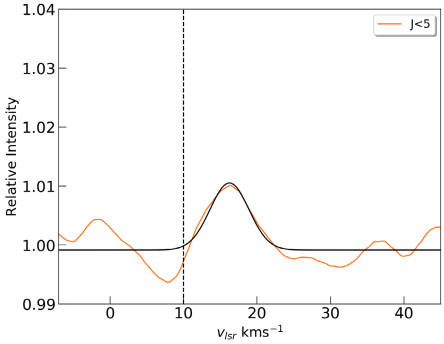

Figure 5.4: Average line profile for lines detected in MonR2 IRS 3B. The vertical dashed line denotes the cloud velocity of 10 km s^{-1} (van der Tak et al. 2003).

We also tentatively present HCN in MonR2 IRS 3B with the R(1), R(3), P(3) and P(4) lines marginally detected. The deconvolved line width and v_{lsr} are 4.4±1.2 km s^{-1} and 16.5±0.5 km s^{-1} respectively. The average line profile is shown in Figure 5.4 and shows only one velocity component. Correspondingly the rotation diagram indicates the presence of a single cold gas component at 48±25 K and is presented in Figure 5.3. The column density for this gas is $1.6\pm0.8 \times 10^{15}$ cm^{-2}.

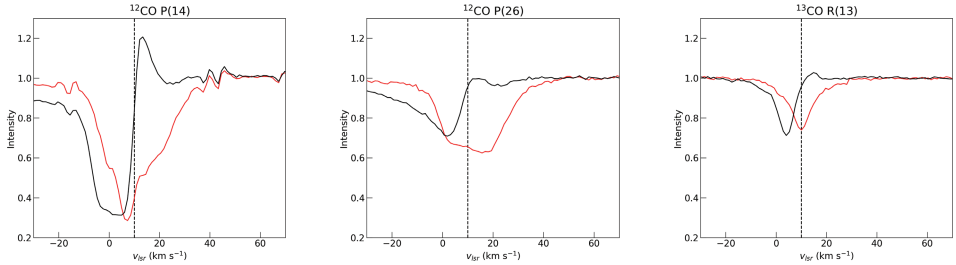

Figure 5.5: Line profiles from the ^{12}CO and ^{13}CO v=1-0 band at 4 μm (Lee et al. in preparation). The ^{12}CO P(14), ^{12}CO P(26) and ^{13}CO R(13) lines are shown in the left, middle and right panels respectively. The profiles in black and red originate from the 3A and 3B binary sources respectively. The dashed denotes the cloud velocity at 10 km s^{-1}. The P Cygni profile is quite obvious in the P(14) profile of the MonR2 IRS 3A source but actually present in all lines (Lee et al. (2021).

High spectral resolution observations of CO v=1-0 taken with iSHELL are able to resolve the binary allowing for separate extraction of the two binary sources (Lee et al. in preparation). Line profiles from the contributions of each binary component are presented in Figure 5.5. Line profiles reminiscent of P-Cygni profiles are observed in MonR2 IRS 3A, in both ^{12}CO and ^{13}CO, with absorption blue-shifted, and emission red-shifted, with respect to the systemic velocity. The red-shifted emission is centred at around 14 km s^{-1}, in agreement with the HCN emission, and persists up until high J, being still present in the P(26) ^{12}CO line, although significantly weaker than the

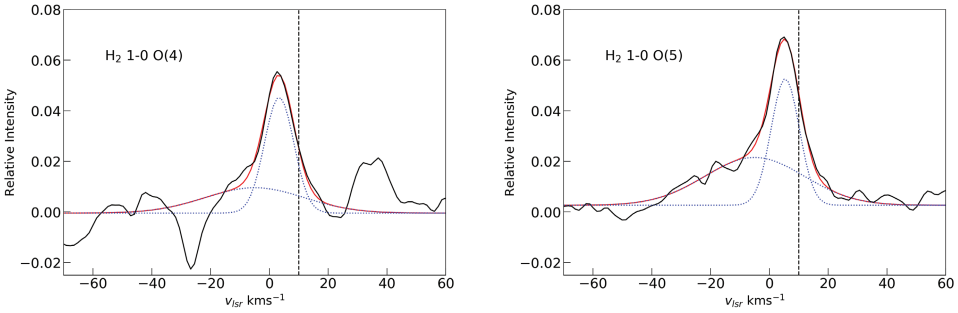

Figure 5.6: Emission lines of H_2 detected towards MonR2 IRS 3A. The global fit in indicated in red, whereas the individual Gaussian components that make up this are show as dotted blue lines. The vertical dashed line denotes the cloud velocity of 10 km s^{-1} (van der Tak et al. 2003). The feature at 35 km s^{-1} in the left panel is the HCN R(5) line.

P(14) ^{12}CO line. CO and HCN line profiles are compared in Figure 5.8.

Goto et al. (2003) observed ^{12}CO v=2-0 in absorption in MonR2 IRS 3 at a resolving power of 23,000 and found a two temperature component structure in the rotation diagram. In their study the binary components of MonR2 IRS 3 are not separated, but rather are analysed as one object. A temperature of 59±4 K to 46±3 K is found for the ^{12}CO cold component for Doppler parameters ranging between 2.5 and 4 km s^{-1}, respectively. The hot component of ^{12}CO is approximately 250 K, not varying much with the chosen Doppler parameter, with a column density of 1.2×10^{19} cm^{-2}. This compares to a value of 200 K for the hot component of ^{13}CO v=1-0 measured by Smith et al. (2020), who also do not separate the binary and observed lines in absorption.

The temperatures of the cold component of CO derived by Goto et al. (2003) are in agreement with the temperature of the HCN emission we derived for MonR2 IRS 3B. Also, Lee et al. find that the velocity of MonR2 IRS 3B is red-shifted with respect to MonR2 IRS 3A, deriving a peak velocity of 17 kms^{-1}, consistent to the velocity of HCN we observe in MonR2 IRS 3B. The temperatures derived for the blue-shifted CO absorption are significantly lower than the HCN temperature we measure in emission for MonR2 IRS 3A. The hot CO temperature is however consistent with SO_2 (225^{+50}_{-70} K), also observed in absorption (Dungee et al. 2018).

H_2 ro-vibrational lines

Two strong lines of H_2 v=1-0 are detected in MonR2 IRS 3A, the O(4) and O(5) transitions, also in emission. These are clearly non-Gaussian and are fit with a model of two combined Gaussians; a narrow component superimposed on a broad underlying component (Figure 5.6). For the narrow velocity component, the peak velocities of the O(4) and O(5) line are 3.4±0.5 km s^{-1} and 5.4±0.2 km s^{-1} respectively. The FWHM of the narrow component are 5.0±0.3 km s^{-1} and 4.8±0.2 km s^{-1} for the O(4) and O(5) lines respectively. The broad component has a FWHM and v_{lsr} of 40±2.4 km s^{-1} and -5.0±1.0 km s^{-1} respectively, for the O(5) line. The blue-shifted

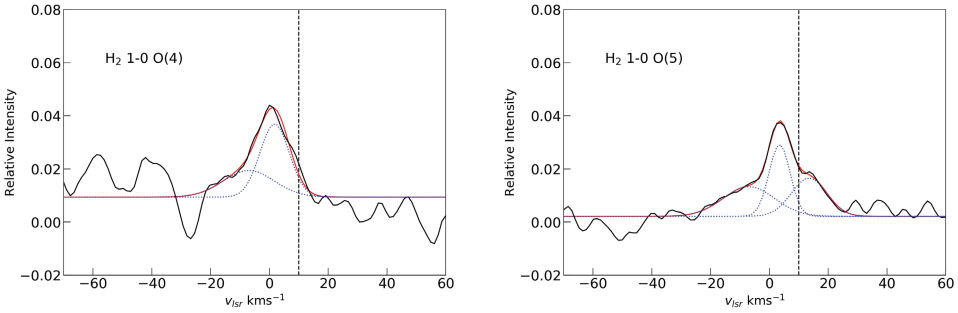

Figure 5.7: Emission lines of H_2 detected towards MonR2 IRS 3B. The global fit in indicated in red, whereas the individual Gaussian components that make up this are show as dotted blue lines. The vertical dashed line denotes the cloud velocity of 10 km s^{-1}.

wing of the broad component in the O(4) line is affected by a telluric residual which removes the edge of the wing. Therefore we use the O(5) line as a reference since this line is in a clean part of the spectrum and not affected by systematic error, and fix the line width and velocity of the broad component when fitting the O(4) line to the values of the FWHM and v_{lsr} derived from the O(5) line.

The same two lines of H_2 are also detected in MonR2 IRS 3B and presented in Figure 5.7. In this source the lines are weaker, and three velocity components are present in the O(5) line. The peak velocities of these components are -7.0±5.0 km s^{-1}, 3.5±0.6 km s^{-1} and 13.5±2.7 km s^{-1}, with respective line widths of 20.4±8.0 km s^{-1}, 8.5±1.9 km s^{-1} and 14.1±4.4 km s^{-1}. The most red-shifted velocity component is not apparent in the O(4) line however, unless it has a significantly different velocity and has blended into the neighbouring component, creating the slight shoulder on the red side of this component. As in MonR2 IRS 3A, we fix the parameters of the velocity component in the O(4) line that is affected by interference by an atmospheric residual to those of the O(5) line. The peak velocity and line width of the central component is 1.8±0.8 km s^{-1} and 11.8±1.0 km s^{-1} respectively. The H_2 lines likely trace the photon-dominated region (PDR) therefore we limit the discussion to HCN and do not analyse H_2 further.

5.4.2 Orion BN, MonR2 IRS 2 and S140 IRS1

No molecular lines were detected in the spectra of Orion BN, MonR2 IRS 2 or S140 IRS1, therefore we place upper limits on the HCN column density in these sources. Upper limits were calculated by comparing a model spectrum to the noise level at the expected location of the strongest lines for each source. Assuming a temperature of 500 K, we derive upper limits of $< 2\times10^{15}$ cm^{-2}, $< 3\times10^{16}$ cm^{-2} and $< 6\times10^{15}$ cm^{-2} on the HCN column density for Orion BN, MonR2 IRS 2 and S140 IRS1 respectively.

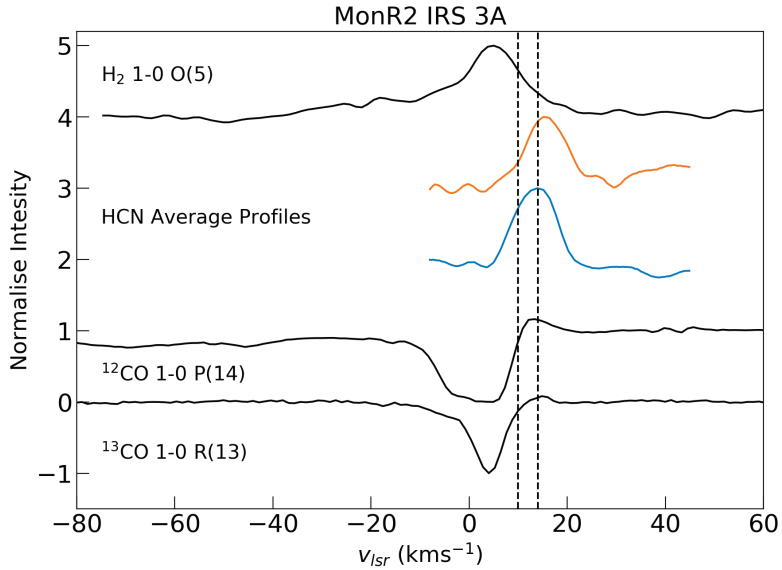

Figure 5.8: Normalised line profiles of CO, HCN and H_2 from MonR2 IRS 3A. The orange and blue lines indicate the low and high J average profiles of HCN respectively. Finally the vertical dashed lines are at 10 km s^{-1} and 14 km s^{-1}.

5.4.3 AFGL 2136

HCN Absorption

In contrast to MonR2 IRS 3, the HCN ν_1 band detected in AFGL 2136 shows transitions exclusively in absorption. We detect 32 non-blended lines of HCN, with many lines being blended with other lines from hot bands of HCN or C_2H_2. We present the full spectrum of AFGL 2136 where absorption line are detected in Figure 5.24 in the Appendix. Here we restrict our analysis to the ν_1 band, as our targeted S/N was not reached, and the weaker vibrationally excited bands are not strong enough for detailed analysis. The weighted average v_{lsr} and deconvolved line width of the ν_1 band are 27.0±0.5 km s^{-1} and 10.7±1.3 km s^{-1} respectively.

A rotation diagram analysis results in a temperature of 540±18 K and a column density of 1.4±0.5 × 10^{17} cm^{-2}, and the rotation diagram is shown in Figure 5.10. The four lowest energy lines deviate from a linear relation exhibiting a higher column than expected and are excluded from the fit. It is possible that the four lowest energy lines are slightly overestimated due to the presence of weak lines from a hot band of C_2H_2 at the same frequency. This band is not detected in other lines however, therefore it is very hard to remove. We cannot fit the four lowest energy lines to derive a temperature with a reasonable error due to the weak lines from hot bands, but it is also possible that these lines may be contaminated by cold foreground gas.

The measured line profiles for the HCN ν_1 band are consistent with those of the

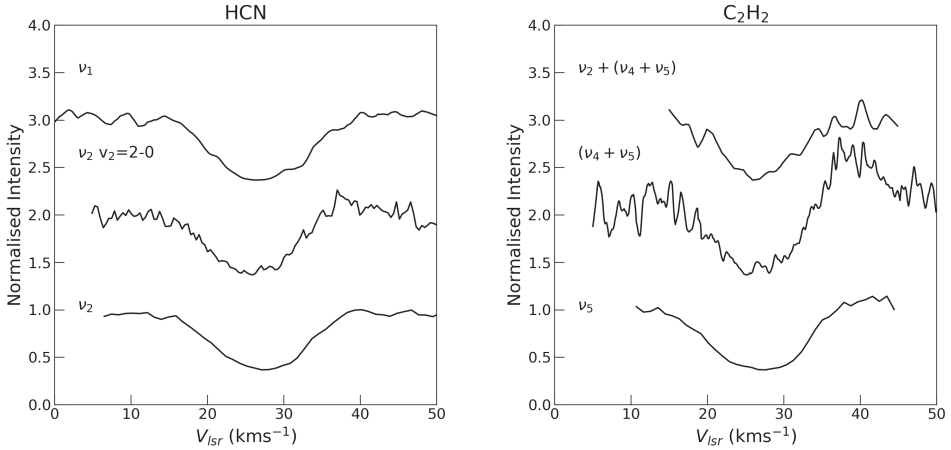

Figure 5.9: Average line profiles of the various bands of HCN and C_2H_2 detected in absorption towards AFGL 2136.

HCN v_2=2-0 band detected at 7 μm (chapter 3), and are presented in Figure 5.9. Also the physical conditions derived from the rotation diagrams are in agreement between these two bands, with a temperature and column density of 592±21 K and $1.8\pm0.2 \times 10^{17}$ cm^{-2} respectively for the v_2=2-0 band. This contrasts to the ν_2 band at 13 μm which, although having the same temperature and line profile, has a factor of 4 lower column density derived from the rotation diagram, despite all these bands probing the same lower level.

Therefore we carry out a curve of growth analysis to investigate the effects of high optical depth. Due to the uncertainty of the intrinsic line width, the curve of growth analysis is done for a range of different Doppler parameters, to explore how this parameter affects the derived physical conditions. We limit the Doppler parameter in such a way that it is less than the value consistent with the observed line width but

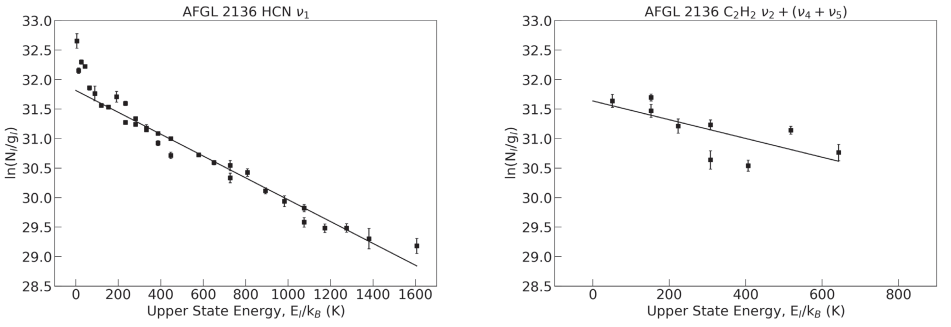

Figure 5.10: Rotation diagrams of absorption lines of HCN and C_2H_2 in AFGL 2136.

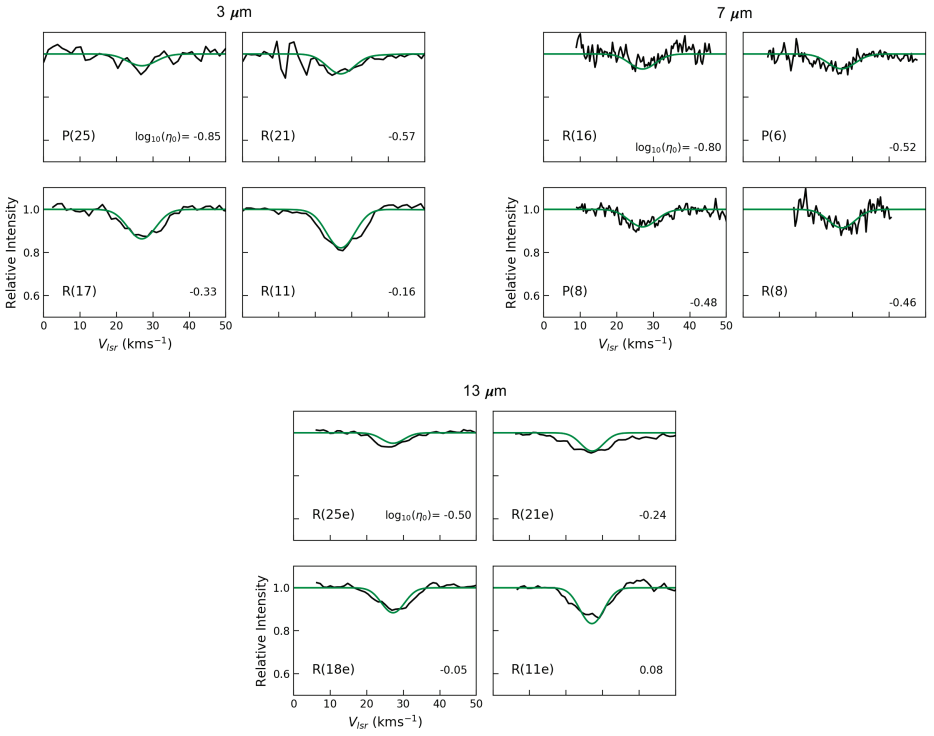

Figure 5.11: Absorption lines of varying opacity from the ν_1 (3 μm), ν_2 v$_2$=2-0 (7 μm) and ν_2 (13μm) bands of HCN (top left, top right and bottom respectively). The green solid line denotes a model of a background light source seen through a dust-free absorbing slab of gas, generated at the physical conditions derived from the curve of growth of the ν_1 band. The opacities of each line derived from the disk model curve of growth, η_0, are indicated in the corresponding panels. A covering factor of 1 is used for the 3 μm and 7 μm lines, and a covering factor of 0.3 is used for the 13 μm lines.

greater than the thermal width, resulting in a range of values for 1.5 km s^{-1} $< \sigma_v <$ 4 km s^{-1}. Fits to the curves of growth are not good for $\sigma_v <$ 3 km s^{-1} and there is not much difference between a choice of $\sigma_v >$ 3 km s^{-1}, therefore we elect to use the value that best fit the H_2O absorption lines in AFGL 2136, which was a value of 3 km s^{-1} (chapter 4).

A curve of growth analysis, presented in Figure 5.12, in the approximation of an absorbing slab of gas, for the ν_1 band at 3 μm and the ν_2=2-0 band at 7 μm, results in physical conditions that are consistent with the rotation diagrams of these bands. This can be achieved using a covering factor, f_c, equal to 1. The lines are on the linear part of the curve of growth, therefore it is not surprising that the rotation diagram and curve of growth produce consistent results as they are two versions of the same model. Comparing the line profiles with a local thermodynamic equilibrium (LTE) model at the temperature and column density derived from the 3 μm curve of growth (and $f_c = 1$), we see that the line profiles agree with the model for both bands, as illustrated in Figure 5.11.

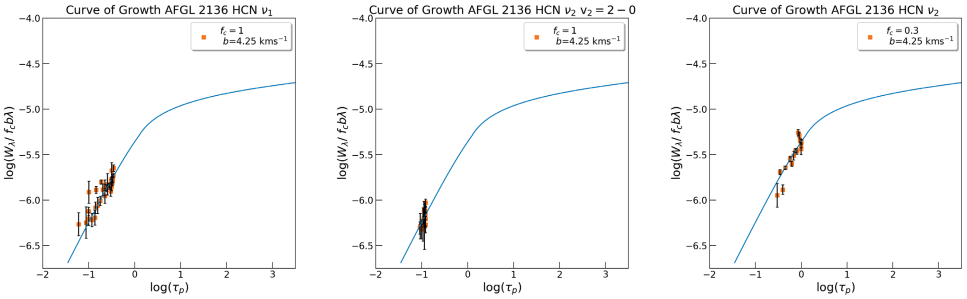

Figure 5.12: Curves of growth for the ν_1 (3 μm), ν_2=2-0 (7 μm) and ν_2 (13μm) bands of HCN in AFGL 2136, calculated using the absorbing foreground slab model. Equivalent widths for the ν_2 and ν_2 v$_2$=2-0 bands are taken from chapter 3. A covering factor of 1 is used for the 3 μm and 7 μm lines, and a covering factor of 0.3 is used for the 13 μm lines. Curves of growth are constructed for $b = 4.5$ km s^{-1} ($\sigma_v = 3$ km s^{-1}).

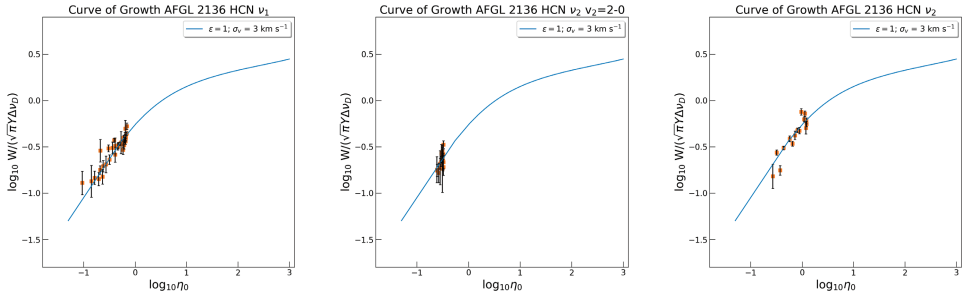

Figure 5.13: Curves of growth for the ν_1 (3 μm), ν_2 =2-0 (7 μm) and ν_2 (13μm) bands of HCN in AFGL 2136, calculated for the disk model. Equivalent widths for the ν_2 and ν_2 v$_2$=2-0 bands are taken from chapter 3. Curves of growth are constructed for a $\sigma_v = 3$ km s^{-1} and $\epsilon = 1$.

From Figures 5.11 and 5.14, we see that the absorption lines at 13 μm require the use of a covering factor in order to explain the observed equivalent widths. A covering factor of 0.3 fits the line profiles well. From a curve of growth with $f_c = 0.3$, we recover physical conditions that are in agreement with the curve of growth for the other bands. Without the use of a covering factor, the column density derived from the ν_2 band is a factor of 4 lower, reflected in the column density difference derived from the rotation diagram analysis. The lines at 13 μm have not yet transitioned onto the logarithmic part of the curve of growth. Temperatures, column densities, and beam filling factors derived for the three bands are summarised in Table 5.3.

We also considered a curve of growth analysis following the disk model developed in chapters 3 and 4 to explore other potential locations of the absorbing gas in the proximity of the star. For the analysis we elect to choose the same Doppler parameter for the slab model. Overall the resulting temperature is not very sensitive to σ_v or ϵ, however as σ_v increases, the best-fit abundance decreases, and the abundance is

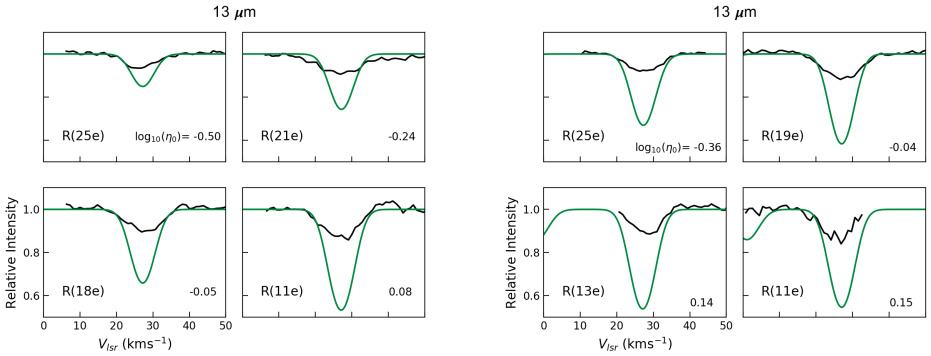

Figure 5.14: Absorption lines of varying opacity from the ν_2 band of HCN (left) and C_2H_2 ν_5 band (right). The green solid line denotes a slab model derived at the physical conditions of the respective bands at 3 μm for a covering factor of 1. The opacities of each line derived from the disk model curve of growth, η_0, are indicated in the corresponding panels.

lower for $\epsilon = 1$ compared to ϵ of 0 or 0.5. The curves with $\epsilon = 1$ give the best fits in terms of the reduced chi-squared, and these also give the best agreement for the temperature and abundance across the different wavelengths, thus we present these curves of growth in Figure 5.13 and their results in Table 5.2. The curves of growth for the other values of ϵ are given in the Appendix.

The column density difference with wavelength apparent in the rotation diagram analysis does not remain after carrying out the curve of growth for the disk model. The lines at 13 μm are beginning to transition onto the curve of growth for $\epsilon = 1$, and for ϵ of 0 or 0.5, they are on the logarithmic part of the curve of growth (Figs 5.19 to 5.22). The derived temperature of the three bands shows some variation however, as does the abundance, for a give value of ϵ. Slight differences in the location of the continuum origin at the different wavelengths could produce some difference in the derived physical conditions between the two bands. Overall the three bands of HCN seem to trace the same physical conditions.

Table 5.2: Summary of disk model curve of growth analysis for HCN in AFGL 2136.

	T (K)			X_{CO} ($\times 10^{-2}$)		
	13 μm	7 μm	3 μm	13 μm	7 μm	3 μm
$\epsilon = 1$	535^{+22}_{-17}	565^{+127}_{-97}	465^{+27}_{-28}	$1.4^{+0.1}_{-0.1}$	$3.3^{+1.6}_{-0.7}$	$1.9^{+0.1}_{-0.2}$
$\epsilon = 0.5$	395^{+9}_{-16}	505^{+100}_{-82}	460^{+12}_{-30}	$6.5^{+0.1}_{-0.3}$	$7.4^{+1.5}_{-1.5}$	$3.5^{+0.1}_{-0.3}$
$\epsilon = 0$	485^{+17}_{-18}	510^{+130}_{-71}	450^{+25}_{-22}	$4.1^{+0.1}_{-0.2}$	$6.5^{+3.4}_{-1.1}$	$3.5^{+0.2}_{-0.2}$

C_2H_2 Absorption

The $\nu_2 + (\nu_4 + \nu_5)$ band of C_2H_2 is detected towards AFGL 2136 at 3 μm. Nine lines are detected and all are in absorption. The peak velocity and deconvolved FWHM of this band are 26.4±0.7 km s^{-1} and 7.5±1.9 km s^{-1} respectively. From the rotation diagram (Fig 5.10) we find a temperature and column density of 630±235 K and 8.0±3.1 $\times$ 10^{16} cm^{-2} respectively. The line profiles are consistent with the C_2H_2 $(\nu_4 + \nu_5)$ band detected at 7 μm (Fig 5.9), as is the temperature, however the column density of the $(\nu_4 + \nu_5)$ is roughly a factor of two lower. The temperature and line profiles of the $\nu_2 + (\nu_4 + \nu_5)$ band are consistent with the 13 μm ν_5 band, however the column density of the ν_5 band is a factor of 7 lower than at 3 μm. Again, these three bands probe the same vibrational lower level.

For the curve of growth for the $\nu_2 + (\nu_4 + \nu_5)$ band with the foreground slab model, we find temperatures and column densities that are consistent with the rotation diagram, and are derived using a covering factor equal to 1. Also, the lines are on the linear part of the curve of growth and the line profiles are consistent with the LTE model in Figure 5.15, implying that the $\nu_2 + (\nu_4 + \nu_5)$ band is optically thin and in LTE. These results are summarised in Table 5.3.

As for HCN, the C_2H_2 lines at 13 μm require the use of a covering factor, as shown in Figures 5.14 and 5.15. With a covering factor of 0.25, the temperature and column density of the ν_5 band come into agreement with the other bands, and the line profiles agree with the LTE model in Figure 5.15. The lines have not yet transitioned onto the logarithmic part of the curve of growth. At 7 μm, no covering factor is needed and the column density for $f_c = 1$ is consistent with the 3 μm column, as is the line profile (Fig 5.15), although the error on the column is large. A covering factor of 0.5 would also give consistent results, therefore there is an error on f_c of the order a factor 2.

Table 5.3: Summary of Slab Curve of Growth for AFGL 2136.

Molecule	Wavelength (μm)	T (K)	N ($\times 10^{17}$ cm^{-2})	f_c
HCN	3	527^{+30}_{-80}	$1.4^{+0.1}_{-0.2}$	1.0
	7	585^{+215}_{-175}	$1.7^{+1.3}_{-0.5}$	1.0
	13	615^{+6}_{-18}	$1.8^{+0.1}_{-0.1}$	0.3
C_2H_2	3	686^{+215}_{-185}	$1.1^{+1.9}_{-0.5}$	1.0
	7	596^{+327}_{-137}	$0.37^{+0.29}_{-0.12}$	1.0
	13	485^{+54}_{-49}	$0.67^{+0.10}_{-0.07}$	0.25

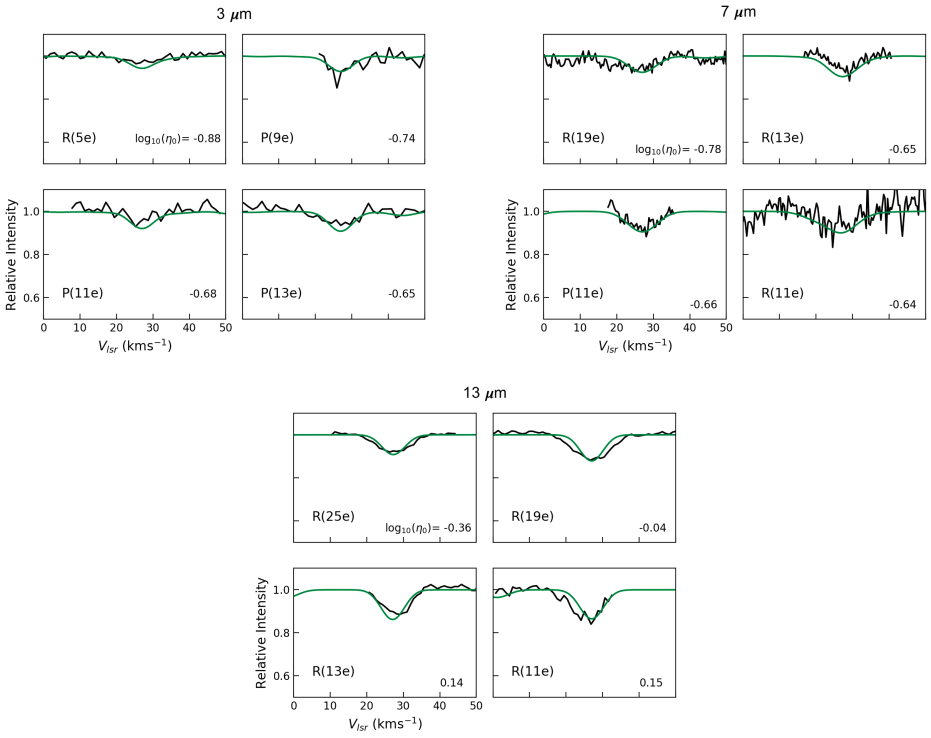

Figure 5.15: Absorption lines of varying opacity from the $\nu_2+(\nu_4+\nu_5)$ (3 μm), $(\nu_4+\nu_5)$ (7 μm) and ν_5 (13 μm) bands of C_2H_2 (top left, top right and bottom respectively). The green solid line denotes a model of a background light source seen through a dust-free absorbing slab of gas, generated at the physical conditions derived from the curve of growth of the 3 μm band. The opacities of each line derived from the disk model curve of growth, η_0, are indicated in the corresponding panels. A covering factor of 1 is used for the 3 μm and 7 μm lines, and 0.25 for the 13 μm lines.

The three lowest energy lines of the $(\nu_4+\nu_5)$ band detected at 7 μm in chapter 3 are overestimated in the rotation diagram. This is also true for the curve of growth, and the fitting does not converge with these lines included. These lines are broader than the other lines of this band by 5 km s^{-1}, therefore we leave them out of the curve of growth fitting, and attribute the larger line width to contamination by colder foreground gas along the line of sight. We also exclude the two lines that fall below the linear fit in the rotation diagram of the $\nu_2+(\nu_4+\nu_5)$ band as these are affected by telluric residuals.

In the curve of growth for the disk model we again take $\sigma_v = 3$ km s^{-1}. The best-fit curves for the $\nu_2+(\nu_4+\nu_5)$, $(\nu_4+\nu_5)$ and ν_5 bands are shown in Figure 5.17, also for $\epsilon = 1$. For C_2H_2, the curve of growth analysis only partially mitigates the column density trend observed in the rotation diagram, and we measure a temperature/abundance trend across the different bands with both increasing with decreasing wavelength (Table 5.4). This abundance/temperature trend from the curve of growth analysis is present for all values of ϵ.

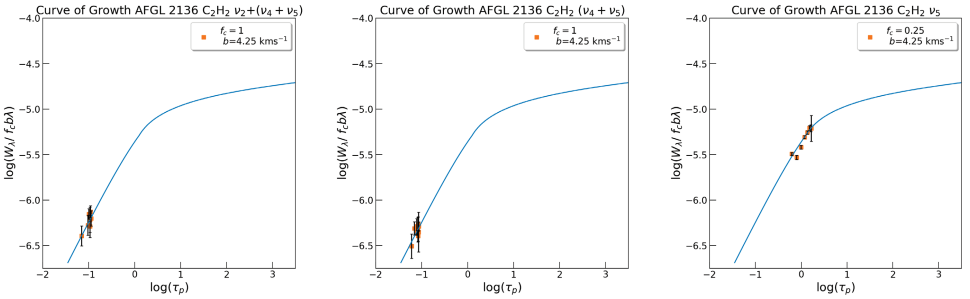

Figure 5.16: Curves of growth for the $\nu_2 + (\nu_4 + \nu_5)$ (3 μm), $(\nu_4 + \nu_5)$ (7 μm) and ν_5 (13 μm) bands of C_2H_2 in AFGL 2136, calculated using the absorbing foreground slab model. Equivalent widths for the $(\nu_4 + \nu_5)$ and ν_5 bands are taken from chapter 3. A covering factor of 1 is used for the 3 μm and 7 μm lines, and 0.25 for the 13 μm lines. A Doppler parameter of 4.25 km s^{-1} is considered, consistent with the disk model ($\sigma_v = 3$ km s^{-1}).

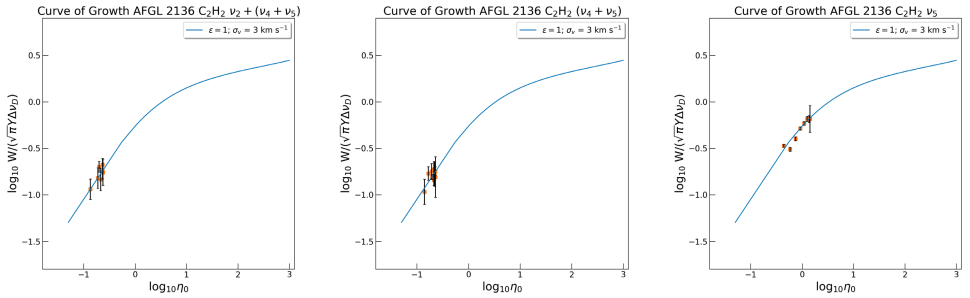

Figure 5.17: Curves of growth for the $\nu_2 + (\nu_4 + \nu_5)$ (3 μm), $(\nu_4 + \nu_5)$ (7 μm) and ν_5 (13 μm) bands of C_2H_2 in AFGL 2136, calculated for the disk model. Equivalent widths for the $(\nu_4 + \nu_5)$ and ν_5 bands are taken from chapter 3. Curves of growth are constructed for a σ_v=3 km s^{-1} and $\epsilon = 1$.

Table 5.4: Summary of disk model curve of growth analysis for C_2H_2 in AFGL 2136.

	T (K)			X_{CO} ($\times 10^{-2}$)		
	13 μm	7 μm	3 μm	13 μm	7 μm	3 μm
$\epsilon = 1$	455^{+21}_{-12}	530^{+85}_{-45}	775^{+155}_{-100}	$0.38^{+0.04}_{-0.02}$	$0.75^{+0.25}_{-0.10}$	$2.8^{+2.2}_{-1.0}$
$\epsilon = 0.5$	330^{+16}_{-10}	515^{+70}_{-30}	765^{+141}_{-93}	$1.6^{+0.1}_{-0.1}$	$1.8^{+0.3}_{-0.3}$	$4.8^{+4.1}_{-1.5}$
$\epsilon = 0$	380^{+51}_{-14}	530^{+86}_{-46}	755^{+146}_{-85}	$1.1^{+0.1}_{-0.1}$	$1.7^{+0.5}_{-0.3}$	$4.6^{+4.3}_{-1.4}$

5.5 Discussion

5.5.1 Structure of MonR2 IRS 3

MonR2 IRS 3 has been imaged at 10.7 μm using the Keck telescope (Monnier et al. 2009). These observations reveal two sources, MonR2 IRS 3A and MonR2 IRS 3B. The mid-IR continuum of MonR2 IRS 3A originates predominantly from a non-spherical structure with a major and minor size of 144±6 mas and 88±5 mas respectively (∼125×75 AU, with position angle (PA) of 41±2°). Ten times fainter, extended emission in the north-east and south-west direction traces an IR reflection nebula, presumably associated with an outflow cavity. MonR2 IRS 3B lies to the north-east at a separation of 0.87″, and appears more like a point source, or a very small compact disk on the scale of $< 0.2''$ (Monnier et al. 2009). Boley et al. (2013) find, in a very high spatial resolution interferometry study at 10.6 μm, that MonR2 IRS 3A is best described by non-spherical geometry with a major axis size of 173.0±1.8 mas. The mid IR interferometry study had limited *uv* coverage and only a 1D Gaussian was fit to the data for MonR2 IRS 3B, resulting in a size of 37.6±1.2 mas (Boley et al. 2013). MonR2 IRS 3A is clearly the dominant source of continuum with strong, extended nebulosity and K-band magnitude of 7.9 (Preibisch et al. 2002), consistent with the 10 μm relative fluxes (Monnier et al. 2009). MonR2 IRS 3B is also relatively bright in the K-band. with a magnitude of 9.1, however it is less extended than MonR2 IRS 3A.

The presence of a disk in MonR2 IRS 3A is not well established with only hints of a disk (Yao et al. 1997; Preibisch et al. 2002; Monnier et al. 2009; Kwon et al. 2016; Fuente et al. 2021). Kwon et al. (2016) and Yao et al. (1997) find evidence for an optically thick disk in MonR2 IRS 3 from polarimetry studies at 2 μm where scattered light implied a non-spherical morphology. High degrees of linear polarisation are observed perpendicular to the elongation of the MonR2 IRS 3 nebula, hinting at a circumstellar disk oriented in the southeast-northwest direction. The spatial resolution of these studies did not distinguish MonR2 IRS 3A from MonR2 IRS 3B however. Therefore these results would support a disk in MonR2 IRS 3A, assuming that it is this source which dominates the scattered light in MonR2 IRS 3. MonR2 IRS 3A is itself extended in the northeast-southwest direction with a fan-shaped bipolar near-IR nebula, supportive of a geometrically thick disk or torus in the perpendicular direction (Preibisch et al. 2002). However, Boley et al. (2013) and Monnier et al. (2009) measure a position angles of 50° and 40° for the mid-IR continuum respectively, which would set this along the same orientation as the near-IR nebula, contrary to what would be expected from a disk perpendicular to the outflow direction. Thus the near-IR reflection nebula traces the inside of the outflow cone, and the 10 μm continuum emission traces hot dust in the same region.

HCN J=3-2 sub-mm velocity maps, taken with the Atacama Large Millimetre Array (ALMA) reveal a blue-shifted, south-west extension, that coincides in position angle (60°) and size (1650 AU) with the diffuse nebulosity around MonR2 IRS 3A seen in the mid-IR (Fuente et al. 2021). There is also red shifted emission lobe which lies closer to the central object (∼1050 AU). As only one line has been measured and self absorption effects are obvious, the temperature of the J=3-2 emitting gas is not well

determined (Fuente et al. 2021). Emission from simple species such as SO_2 and OCS, as well as more complex species such as CH_3OH and CH_3OCHO, was interpreted as a disk/torus structure at ∼175 K, encapsulating both MonR2 IRS 3A and MonR2 IRS 3B. HCN was more spatially extended than all other species, ranging from -15 km s^{-1} to 22 km s^{-1}, and potentially probing outflowing material, with more extended emission being filtered out (Fuente et al. 2021).

MonR2 IRS 3B is the source of a very collimated micro-jet with three knots seen in the *K* band along the north-east south-west direction (Preibisch et al. 2002), also indicative of of a disk in this source. Collimated jets and outflows are an indication that they are in an early stage of their evolution, where the jet/outflow becomes wider with time (Beuther & Shepherd 2005), implying that any disk associated with the jet of MonR2 IRS 3B would be in an early stage of its evolution and very compact, still undergoing a period of very active accretion. Pomohaci et al. (2017) detected H_2 emission in the S(1) 2-1 line at 2.24 μm towards MonR2 IRS 3B, but not MonR2 IRS 3A, supporting the origin of these knots as shocked gas in a jet (Smith 1993; Eislöffel et al. 2000).

In Figure 5.18 we illustrate the structure of MonR2 IRS 3. The extended nebulosity from MonR2 IRS 3A along the north-east south-west direction is shown, as well as the blue and red shifted components observed in CO in the mid-IR and HCN in the sub-mm. Yet to be observed circumstellar disks are indicated where they would be expected for both MonR2 IRS 3A and MonR2 IRS 3B, perpendicular to the outflow direction. Thus we can either assign red-shifted HCN emission to the back side of an expanding shell, or to the atmosphere of a circumstellar disk, and we discuss each of these in turn below.

HCN Emission from Expanding Shell

The high temperature HCN emission from MonR2 IRS 3A is consistent in velocity with the P-Cygni emission feature of the CO profile in MonR2 IRS 3A (Fig 5.5). Lee et al. (2021, in prep) do not estimate a temperature for the emission component of CO, however the presence of this emission feature in CO up to J=26 implies that the CO gas is also hot. From the CO P-Cygni profiles, we infer that that there is an expanding shell of gas, where the blue-shifted side is seen in absorption against the continuum source, and the red-shifted side seen in emission traces the back side of the shell which is expanding away from the observer, illustrated in Figure 5.18. The HCN emission would then be associated with the back side of this shell which is illuminated by the main continuum source in the region, MonR2 IRS 3A.

The HCN emission lines of MonR2 IRS 3B are consistent in terms of the line profiles of CO absorption in this source, and the HCN temperature is consistent with the cold component of CO observed in absorption by Goto et al. (2003) and Smith et al. (2020). The temperature is 48 K, and the column density is an order of magnitude lower than MonR2 IRS 3A, therefore we locate this as cold gas in the envelope of MonR2 IRS 3B. This low temperature gas creates ro-vibrational emission lines and therefore must be caused by fluorescence from cold foreground gas.

We attribute the HCN high J ro-vibrational emission lines in MonR2 IRS 3A also to fluorescence. We consider that this gas is heated by a shock responsible for the

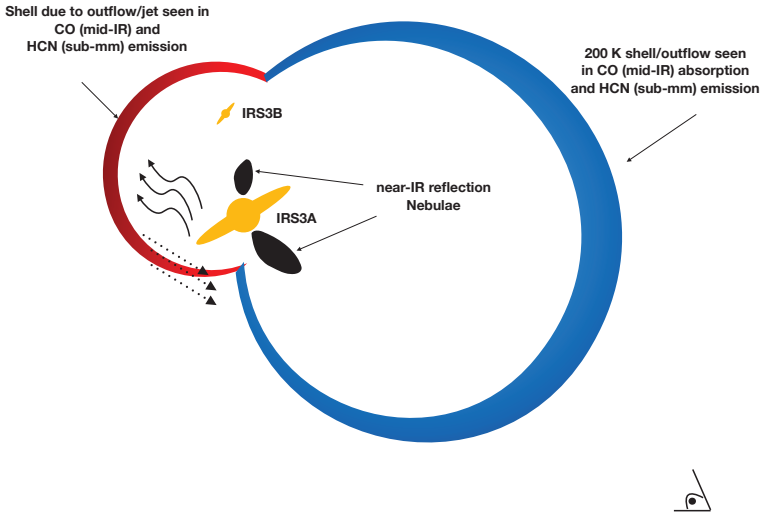

Figure 5.18: Schematic outline of the potential environment of MonR2 IRS 3 where an expanding shell of gas is irradiated by the star (wavy arrows), and traced by different molecules at different wavelengths. The individual (yet to be observed) disks of MonR2 IRS 3A and MonR2 IRS 3B are given in yellow. The infrared reflection nebulae extending from MonR2 IRS 3A are shown in black (Preibisch et al. 2002; Monnier et al. 2009). Scattering of continuum photons from MonR2 IRS 3A at 3 μm (dotted arrows) may produce the red-shifted HCN emission seen from the red side of an expanding shell, which is also evident in CO emission at 4.7 μm. The blue-side of the shell expanding towards the observer is only seen in CO absorption at infrared wavelengths, which is further away from the star and hence cooler. This side is also evident from HCN 3-2 emission at sub-mm wavelengths (Fuente et al. 2021). In this figure east is left and north is up.

red emission lobe seen in the J=3-2 map of HCN in the sub-mm. In principle, the emission lines could then represent thermal emission of HCN in the high temperature post shock gas. In a C-type shock, heating is over a long column density (10^{21} cm^{-2}) as the ionised fluid frictions itself through the neutral fluid, reaching temperatures of around 2000-3000 K (Hollenbach et al. 2013). While a J shock is instantaneously heated and then cools down over a short column (10^{18} cm^{-2}), heating due to H_2 formation could keep the postshock gas at the order of 500 K over a column of 4×10^{22} cm^{-2} (Hollenbach et al. 2013). The critical density of the ro-vibrational transitions is 2×10^{11} cm^{-3} (Hernández Vera et al. 2017), however, some six orders of magnitude higher than for the pure rotational transitions. We consider such a high density unlikely and therefore analyse the emission lines assuming a fluorescence process (cf. Chapter 3). However, to keep the HCN at 500 K via fluorescence at 1000 AU from the star (the distance of the red-shifted HCN lobe apparent from the sub-mm) is challenging, however the kinetic temperature could be much lower.

The temperature difference observed between the mid-IR CO absorption and HCN emission components in MonR2 IRS 3A likely reflects a temperature gradient that decreases as one moves away from the illuminating star. The temperature of the blue-

shifted CO absorption is ∼200 K, consistent with SO_2 absorption (230±15 K) which has comparable line profiles as CO (Dungee et al. 2018). The temperature of the absorption is comparable to the temperature of the sub-mm emission lines, 175^{+15}_{-16} K, which are described as coming from a circumbinary torus (Fuente et al. 2021). Thus the CO foreground absorption has expanded more than, and is further away from the star (∼1650 AU) than the back side of the shell (∼1050 AU), and hence cooler. We place an upper limit on the blue-shifted absorption component of $< 2 \times 10^{15}$ cm^{-2} at a temperature derived from CO absorption, 200 K, an order of magnitude lower than the column of HCN seen in emission. Taking the ^{12}CO column density from Goto et al. (2003), this corresponds to a HCN/CO abundance ratio of $< 1.7 \times 10^{-4}$. We surmise that we do not see any HCN absorption at 200 K (foreground gas evident in the CO absorption lines) because the shell has expanded too fast and the gas is too cool to form HCN in high abundance (Bast et al. 2013; Agúndez et al. 2018). Also the emission may be extended - on the scale of the redshifted lobe (∼1.3″) - so would appear brighter in the observed spectrum the more it fills the slit, whereas the absorption is only against the continuum source (∼0.144″).

The shell would then correspond to a wind blown bubble along the position angle of the reflection nebula. The difference in peak velocity observed between the low and high J HCN lines suggests that these lines are probing the acceleration zone of the expanding shell/outflow. The low J lines probe deeper into the shell and therefore trace more red-shifted velocities compared to the high J lines which become optically thick closer to the source. Since the iSHELL *L* band spectrum was extracted at the continuum peak, if the HCN emitting gas is indeed at 1000 AU (1.3″) from the continuum peak, then the actual line flux is conceivably much larger. This would imply a much higher line-to-continuum ratio and thus the derived column density is a lower limit.

For both binary components, we measure the scattering optical depth from the line-to-continuum ratio, which results in a column density of $1.6 \pm 0.2 \times 10^{16}$ cm^{-2} (chapter 3; section 3.5.3). This assumes that the 3 μm continuum flux from the top of the disk (directly seen by us) is equal to the flux from the bottom of the disk (seen by the back shell). We note that for foreground emission the natural log term in equation 9 of section 3.5.3 is not relevant, and the line-to-continuum ratio becomes $F_L/Fc = \tau_s/4\pi$. The central source by far dominates the mid-IR continuum compared to the scattering nebulosity and therefore the line to continuum ratio will give a good estimate of the scattering optical depth. For a continuum normalised spectrum, a line-to-continuum ratio of 1.02 corresponds to an optical depth is 0.01, therefore either 1 % of the fluorescing photons are scattered into out line of sight, or the size of the fluorescing region is 1 % that of the continuum. We cannot distinguish between the two of these.

P-Cygni profiles are commonly observed towards massive YSOs in CO at mid-IR wavelengths (Mitchell et al. 1990, 1991). They have also been seen in CH_4 towards the massive protostar NGC 7538 IRS 9 at 3 μm (Boogert, Blake & Öberg 2004), thus are a characteristic of these objects also in organic species. For CH_4, the temperatures are similar to what we find for HCN, with 600±100 K and 270±100 K for the emission and absorption components respectively. Cooler CH_4 could come from sublimation of ices (Boogert, Blake & Öberg 2004), however this is not to be expected for HCN

which is not observed in ices (Theulé et al. 2013; Boogert, Gerakines & Whittet 2015).

HCN Emission from a Circumstellar Disk

Alternatively, the combination of blue-shifted absorption and red-shifted emission could be fortuitous in a complex environment of star formation where many different physical components could be present. In this case, the HCN emission lines in MonR2 IRS 3A may trace a disk photosphere instead of an expanding shell or outflow, as was inferred for AFGL 2591 (chapter 3).

In order to explain the results of a high resolution spectral survey in the mid-IR, we developed a model in which absorption lines probe a circumstellar disk around massive protostars AFGL 2591 and AFGL 2136 (chapter 3). Column density variations in HCN and C_2H_2 of up to a factor of 10 were observed between ro-vibrational bands that trace the same lower level, with the bands at shorter wavelengths exhibiting a larger column. Ro-vibrational transitions of H_2O are observed to saturate at non-zero flux, a direct prediction of the proposed model (chapter 4).

HCN emission lines were also detected towards AFGL 2591 at 3 μm, in contrast to the mid-IR spectrum where all species are observed in absorption (chapter 3). The temperature derived from the emission lines was 250 K compared to 700 K in the absorption lines, and the emission lines were a factor of 2 narrower than those seen in absorption. We interpreted the emission lines to originate from scattering of continuum photons seen under an angle from higher up layers of the disk photosphere, where temperatures are lower, compared to the absorption which probes deeper into the disk. Importantly, the presence of HCN and C_2H_2 emission lines at 3 μm implied the absence of these species in the inner hot disk as otherwise we would see absorption lines (similar to the 7 μm and 13 μm HCN bands in this source).

Developing a similar scenario for Mon R2 IRS 3A, we would locate the HCN emitting gas high up in the disk photosphere where 3 μm photons from the inner disk are scattered into our beam. As the excitation temperature of the HCN emission lines is much higher than for AFGL 2591, this gas is closer to the central region. However, as for AFGL 2591, the region producing the 3 μm continuum photons cannot contain HCN. The mid-IR continuum of MonR2 IRS 3A is spatially extended along the PA of the outflow on scales of $0.2''$. Therefore any disk that is present must be smaller than these scales ($<$170 AU) and is yet to be firmly detected

Summary

We have considered two possible scenarios for the origin of the 3 μm HCN emission lines in the spectrum of MonR2 IRS 3A. The lines could result from fluorescence by gas on the backside of the source pumped by 3 μm emission from a disk, or by fluorescence of gas in the outskirts of a disk. The fact that P-Cygni profiles towards MYSOs seems common makes it less likely that it is fortuitous in MonR2 IRS 3A. Furthermore the lack of an observed disk along the direction perpendicular to the outflow makes the disk origin for HCN emission appear less likely, and the location of the HCN emission in the expanding nebula seems more attractive. However, the heating process of the HCN in the expanding shell scenario has challenges, whether

by shocks or fluorescence. Therefore we cannot make a conclusion as to the location of the HCN emission in MonR2 IRS 3A.

Multi wavelength observations of the HCN ν_2=2-0 band at 7 μm and the ν_2 band at 13 μm would allow detailed comparison of line profiles, peak velocities, temperatures and column densities. This might go far to elucidate the characteristics of the MonR2 IRS 3A system. In particular, the presence of much warmer gas in absorption - as for AFGL 2591 - would help solidify the presence of a warm disk, while dominance of absorption lines from gas with similar characteristics as CO would locate the absorption in the foreground. The spatial resolution of iSHELL is seeing limited to around 0.6″, therefore the location of the HCN emission lines relative to the continuum peak is something that could be mapped with iSHELL, which would help to understand the morphology of HCN in the infrared. Care should be taken then to avoid chopping on the array as that may lead to underestimated line fluxes for extended emission.

5.5.2 Absorption Lines in AFGL 2136

Foreground Absorption

An optically thin LTE model grossly overestimates the observed HCN and C_2H_2 lines at 13 μm, assuming a covering factor equivalent to the 3 μm and 7 μm lines. Therefore a much smaller covering factor is required for the 13 μm lines than for the other wavelengths. The results from the curve of growth analysis are in accordance with the rotation diagram analysis, which implies that the gas is optically thin. This is supported by the fact that all bands lie along the linear part of the curve of growth. The results for HCN compared to C_2H_2 are very similar, which is to be expected due to the very comparable chemistry of these two species, with HCN/C_2H_2 abundance ratios of $\sim$1 commonly observed (Salyk et al. 2011; Agúndez et al. 2018).

The quality of the data does not allow us to determine the exact value for the covering factor at 3 μm and 7 μm, however we can constrain this parameter from the 13 μm band. For a covering factor $f_c < 0.2$, the fit to the 13 μm lines for both HCN and C_2H_2 deteriorates, as the lines no longer lie along the linear part of curve of growth. This means that at 3 μm and 7 μm, the gas must at least almost fully cover the source, with $f_c > 0.9$ and $f_c > 0.95$ for HCN and C_2H_2 respectively. This constraint on the covering factor of HCN and C_2H_2 means that, in the case that these species are produced in a foreground cloud, these molecules must cover the source more than H_2O, which has a covering factor of 0.4 at 6 μm (chapter 4).

In the comparisons between the bands at different wavelengths, we only consider the ortho states of C_2H_2, since these are the only states detected at 3 μm and 7μm. Para states of C_2H_2 were detected in the ν_5 band at 13 μm however (chapter 3), therefore we can also carry out a curve of growth analysis for the para lines of C_2H_2 in this band. In doing so we derive a temperature of 566^{+68}_{-87} K, and a column density of $4.1^{+1.1}_{-1.2} \times 10^{16}$ cm^{-2}, taking $f_c = 0.25$. This results in an ortho-to-para ratio (OPR) of 1.6, which is less than the expected value of 3 (chapter 3). Therefore the curve of growth analysis and partial covering factors do not account for the low OPR observed in AFGL 2136. With the summation of the column density of both ortho and para

states, we derive a total C_2H_2 column density of 1.1×10^{17} cm^{-2} for the ν_5 band.

We conclude that the variation in the column density initially discerned from the rotation diagram analysis is due to dilution, not high optical depth effects in the 13 μm band. The coverage of the 3 μm and 7 μm bands may or may not be exactly the same, but it is very clear that the coverage of the 13 μm band is is only $\sim$0.3 of that at the shorter wavelengths. Thus the area of the 13 μm continuum must be $\sim$3 times larger than the 7 μm continuum, but the HCN/C_2H_2 containing foreground cloud must completely, or almost completely, "cover" the disk region responsible for the 3 μm and 7 μm continuum. We can estimate the size of the continuum emitting region, assuming a radial temperature gradient with an exponent in the range of -0.4 to -0.7 (Dullemond et al. 2007). Setting the temperature of the dust disk at 30 AU to 1200 K (the sublimation radius), and adopting a temperature exponent of -0.7, we find that a temperature of $\sim$500 K is reached at a radius of approximately 110 AU. This compares to the 10 μm size of AFGL 2136 of 400 AU (Monnier et al. 2009), a factor of $\sim$2 lower. High spatial resolution imaging of the dust continuum of AFGL 2136 at 3,7 and 13 μm would help to assess the reality of the foreground absorption scenario.

Disk Model

In contrast to AFGL 2591 and MonR2 IRS 3, HCN and C_2H_2 in the L band of AFGL 2136 are observed to be in absorption. The line profiles are consistent with those detected from these species at 7 μm and 13 μm. In chapter 3 we proposed that the absorption lines from this source are coming from an internally heated disk, analogous to AFGL 2591. Abundance/column density variations between the 7 μm and 13 μm bands, which probe the same lower level, were interpreted as dilution of the longer wavelength lines due to a contribution of dust emission at the longer wavelength from a region in the disk with a very low HCN and C_2H_2 abundance. These species require high temperatures ($\sim$400 K) to form in high abundances (Bast et al. 2013; Agúndez et al. 2018), therefore the high abundance material will be concentrated in the inner disk, and the outer colder parts of the disk do not contribute to the absorption lines.

In section 5.4.3. we found that the column density variations of HCN could be explained by optical depth effects with the column density of the ν_2 band at 13 μm being underestimated because it is optically thick. In the context of the circumstellar disk model, the fact that the HCN lines measure the same abundance implies that the HCN lines at 13 μm are not diluted. In this case, the high abundance HCN region in the disk must extend to the location of the 13 μm continuum origin.

While the abundances from the three bands of HCN are similar, the bands of C_2H_2 at the different wavelengths show significant difference after optical depth effects have been accounted for with the curve of growth analysis: specifically, the abundance derived from the 3 μm lines is a factor 3 and a factor 6 higher than derived from the lines at 7 and 13 μm, respectively. This implies that the high abundance C_2H_2 gas lies closer to the star compared to, and is less extended than, the high abundance HCN region. This scenario is supported by the higher temperature measured for C_2H_2 at 3 μm compared to HCN (750 K compared to 450 K), however is surprising given the similarity in the chemistry of these species (Salyk et al. 2011; Agúndez et

al. 2018). Taking the abundances from the 3 μm lines, we calculate a HCN/C_2H_2 ratio of 0.68-0.76, depending on the value of ϵ.

5.6 Conclusions

We have conducted a survey of five massive protostars from 2.95 μm to 3.25 μm to investigate how widespread transitions of organic species such as HCN and C_2H_2 are in these objects, and how they relate to potential circumstellar disks. We detected transitions towards two out of the five objects, which are the younger sources in the sample and known to exhibit hot core chemistry.

In MonR2 IRS 3, HCN transitions are detected in emission; confidently towards MonR2 IRS 3A and marginally towards MonR2 IRS 3B. A rotation diagram analysis shows that this HCN in MonR2 IRS 3A has a single temperature of 516±71 K and a column density of $1.6\pm0.2 \times 10^{16}$ cm^{-2}. The line profiles of HCN are consistent with an emission shoulder of CO in this source and are red-shifted with respect to the cloud velocity. The CO emission feature is adjacent to blue-shifted absorption, indicative of a P-Cygni profile. The CO emission feature is visible up to high energy transitions, suggesting that the temperature is high, consistent with HCN.

The HCN emission of MonR2 IRS 3A could originate either from an expanding shell of gas, or from the atmosphere of a circumstellar disk. The physical structure of HCN imaged in the sub-mm shows red-shifted emission at ∼1000 AU along the orientation of the reflection nebula, most likely probing the outflow. If the high J ro-vibrational emission comes from the outflow cavity, fluorescence of HCN due to 3 μm continuum photons is an unlikely mechanism to keep the gas at 500 K, and thermal heating due to shocks is also challenging due to the high critical densities of the ro-vibrational transitions. On the other hand, no disk has been confidently detected in MonR2 IRS 3A, and the ubiquity of P-Cygni profiles in high mass star forming regions makes it less likely that this profile is fortuitous. Therefore we cannot conclude for certain which of the proposed scenarios best fits our observations. Multi wavelength observations of HCN would help to clarify this, as absorption lines at 7 μm and 13 μm would be in strong favour for the presence of a disk, with emission lines at 3 μm probing the upper layers, analogous to AFGL 2591. Also mapping of the HCN emission with iSHELL would help to understand the location of the HCN emission lines relative to the continuum peak.

In AFGL 2136, HCN and C_2H_2 transitions are detected, exclusively in absorption. Comparing the different bands observed at 3 μm, 7 μm and 13 μm which probe the same lower level, a rotation diagram analysis reveals variations in the derived column density. We therefore conducted two separate curve of growth analyses, assuming different models to explain the absorption lines; one a stellar atmosphere model to describe a circumstellar disk, and one an absorbing slab model to describe absorption due to a foreground cloud.

The curve of growth analysis for the absorbing slab model shows that, for this model, the lines of HCN and C_2H_2 are optically thin across all wavelengths. In order to explain the observed equivalent widths, the lines at 13 μm require a partial covering factor of 0.3 and 0.25 for HCN and C_2H_2 respectively. This compares to

covering factors of > 0.9 and > 0.95 for HCN and C_2H_2 respectively at both 3 μm and 7 μm, which have approximately equivalent covering factors. Thus, while the absorbing cloud must cover the 3 μm and 7 μm emitting area equally, 3/4 of the 13 μm continuum emission does not pass through this absorbing cloud. Based on the HCN and C_2H_2 covering factors, these species must cover the source more than H_2O, assuming a foreground origin. We derive an OPR less than 3, taking into consideration the partial covering factors.

For the disk model, the HCN abundance trend with wavelength previously observed can be attributed to optical depth effects as bands across all wavelengths measure the same abundance. For C_2H_2, variations with abundance are observed after the curve of growth analysis, with higher abundances found at shorter wavelengths, consistent with a radial abundance gradient in a disk as proposed in chapter 3.

5.A Appendix

Table 5.5: Line Parameters for the HCN ν_1 band observed in emission in MonR2 IRS 3.

Source	Transition	λ (μm)	E_l (K)	g_u	A_{ij} (s)	v_{lsr} (km s^{-1})	FWHM (km s^{-1})	τ_s	N_l ($\times10^{14}$ cm^{-2})
MonR2 IRS 3A	P(20)	3.0784	893	234	41	13.1±0.5	8.5±1.3	0.012±0.001	3.7±0.6
	P(16)	3.0659	578	186	41	12.1±0.5	11.2±1.2	0.023±0.002	9.2±1.2
	P(14)	3.0598	446	162	42	15.6±0.9	15.7±5.8	0.020±0.009	10.4±6.0
	P(8)	3.0421	153	90	43	12.8±0.3	8.5±0.7	0.018±0.001	5.4±0.5
	P(7)	3.0392	119	78	44	13.6±0.2	5.9±0.5	0.020±0.001	4.0±0.4
	P(5)	3.0335	64	54	45	14.9±1.3	6.9±3.1	0.019±0.006	4.8±2.3
	P(4)	3.0307	42	42	46	13.9±0.4	4.8±1.1	0.015±0.002	3.0±1.3
	P(3)	3.0280	25	30	49	16.0±0.7	9.6±1.8	0.011±0.002	3.3±0.7
	R(1)	3.0145	4	30	33	16.9±0.4	8.3±0.9	0.017±0.001	6.9±5.7
	R(3)	3.0092	25	54	37	16.2±0.4	4.6±0.9	0.019±0.002	4.8±0.8
	R(5)	3.0041	64	78	38	14.6±0.4	9.7±1.0	0.020±0.001	7.9±1.0
	R(6)	3.0016	89	90	38	13.1±0.6	4.6±1.5	0.018±0.003	4.5±1.3
	R(7)	2.9991	119	102	39	15.2±0.5	10.0±1.4	0.016±0.002	6.6±1.0
	R(11)	2.9893	281	150	40	13.8±0.4	8.4±1.0	0.019±0.002	6.6±0.9
	R(12)	2.9869	332	162	40	14.4±0.5	9.6±1.2	0.015±0.001	5.9±0.9
MonR2 IRS 3B	P(4)	3.0307	42	42	46	14.6±0.5	4.7±1.3	0.014±0.003	1.9±0.7
	P(3)	3.0280	25	30	49	18.1±0.5	8.9±1.4	0.006±0.001	1.6±0.3
	(R1)	3.0145	4	30	33	16.6±0.4	5.5±0.9	0.013±0.002	3.1±0.7
	(R3)	3.0092	25	54	37	16.9±0.5	5.0±1.2	0.019±0.003	5.1±1.1

Table 5.6: Line parameters for the absorption lines detected in AFGL 2136 at 3 μm.

Species	Transition	λ (μm)	E_l (K)	g_u	g_l	A_{ij} (s^{-1})	v_{lsr} (km s^{-1})	FWHM (km s^{-1})	N_l ($\times 10^{15}$ cm^{-2})	W ($\times 10^{8}$ Hz)
HCN ν_1	P(27)	3.1012	1606	318	330	39.7	27.5±1.0	10.2±2.6	1.6±0.5	2.2±0.3
	P(25)	3.0945	1381	294	306	40.0	25.8±1.3	8.9±3.1	1.6±0.7	2.3±0.4
	P(22)	3.0848	1075	258	270	40.3	26.4±0.5	9.6±1.2	2.4±0.4	3.4±0.1
	P(19)	3.0752	808	222	234	40.7	27.4±0.8	16.1±2.0	3.8±0.6	5.4±0.1
	P(18)	3.0721	727	210	222	40.9	25.9±0.7	11.2±1.9	4.1±0.9	5.7±0.2
	P(14)	3.0598	446	162	174	41.5	26.2±0.4	9.1±1.0	3.8±0.5	5.2±0.1
	P(13)	3.0568	387	150	162	41.7	26.4±0.3	9.5±0.8	4.4±0.4	5.8±0.1
	P(12)	3.0538	332	138	150	41.9	27.3±0.5	11.4±1.3	5.2±0.7	7.0±0.1
	P(11)	3.0508	281	126	138	42.2	27.4±0.3	10.8±0.7	5.1±0.4	6.8±0.1
	P(10)	3.0479	234	114	126	42.5	26.7±0.3	10.1±0.7	4.8±0.4	6.4±0.1
	P(9)	3.0449	191	102	114	42.8	27.2±0.9	12.2±2.2	6.7±1.5	8.8±0.2
	P(8)	3.0421	153	90	102	43.2	27.0±0.2	9.7±0.6	5.1±0.4	6.6±0.1
	P(7)	3.0392	119	78	90	43.6	27.8±0.2	9.1±0.6	4.6±0.4	6.0±0.1
	P(6)	3.0363	89	66	78	44.3	26.1±0.9	9.2±2.3	4.9±1.5	6.3±0.3
	P(5)	3.0335	64	54	66	45.2	27.3±0.3	10.6±0.7	4.5±0.4	5.8±0.1
	P(4)	3.0307	42	42	54	46.5	26.7±0.2	11.4±0.5	5.3±0.3	6.6±0.1
	P(3)	3.0280	25	30	42	48.9	26.7±0.4	12.0±0.9	4.5±0.4	5.5±0.1
	P(2)	3.0252	13	18	30	54.4	26.4±0.4	10.5±1.0	2.8±0.3	3.2±0.1
	R(1)	3.0145	4	30	18	32.8	27.0±1.1	11.5±2.7	2.± 0.8	5.2±0.3
	R(10)	2.9917	234	138	126	40.0	28.9±0.4	14.3±1.0	6.7±0.6	9.6±0.1
	R(11)	2.9893	281	150	138	40.0	27.1±0.2	10.7±0.4	5.6±0.3	8.0±0.1
	R(12)	2.9869	332	162	150	40.0	27.8±0.3	10.8±0.7	5.1±0.4	7.3±0.1
	R(13)	2.9845	387	174	162	40.0	26.6±0.3	10.6±0.6	5.1±0.4	7.3±0.1
	R(14)	2.9822	446	186	174	40.1	26.7±0.3	11.6±0.7	5.1±0.4	7.2±0.1
	R(16)	2.9775	578	210	198	40.3	26.9±0.2	11.0±0.4	4.4±0.2	6.2±0.1
	R(17)	2.9752	650	222	210	40.3	27.3±0.3	11.0±0.8	4.1±0.4	5.8±0.1

Table 5.6: continued.

Species	Transition	λ (μm)	E_l (K)	g_u	g_l	A_{ij} (s^{-1})	v_{lsr} (km s^{-1})	FWHM (km s^{-1})	N_l ($\times 10^{15}$ cm^{-2})	W ($\times 10^8$ Hz)
	R(18)	2.9730	727	234	222	40.4	27.7±0.7	10.4±1.7	3.3±0.7	4.8±0.2
	R(20)	2.9686	893	258	246	40.5	26.6±0.4	9.7±1.0	3.0±0.4	4.2±0.1
	R(21)	2.9664	982	270	258	40.6	26.1±0.9	12.5±2.2	2.6±0.6	3.8±0.2
	R(22)	2.9642	1075	282	270	40.6	27.5±0.7	11.4±1.8	1.9±0.4	2.8±0.2
	R(23)	2.9621	1173	294	282	40.6	26.9±0.7	13.3±1.9	1.8±0.3	2.6±0.2
	R(24)	2.9599	1275	306	294	40.7	26.3±0.5	7.5±1.2	1.9±0.4	2.7±0.2
C_2H_2 $\nu_2 + (\nu_4 + \nu_5)$	P(19e)	3.0905	643	111	117	26.4	26.9±1.2	12.1±3.2	2.7±0.9	2.5±0.3
	P(13e)	3.0763	308	75	81	25.7	26.1±0.7	9.9±1.7	3.0±0.6	2.6±0.2
	P(11e)	3.0717	223	63	69	25.6	26.7±0.8	9.2±2.3	2.5±0.8	2.1±0.3
	P(9e)	3.0671	152	51	57	25.6	26.4±0.4	1.4±1.0	2.7±2.0	2.2±0.3
	R(5e)	3.0341	51	39	33	21.8	26.5±1.1	12.8±2.7	1.8±0.5	1.7±0.3
	R(9e)	3.0258	152	63	57	22.8	25.8±0.4	9.5±1.1	3.3±0.5	3.0±0.1
	R(13e)	3.0176	308	87	81	23.5	26.5±0.8	4.8±1.9	1.6±0.8	1.5±0.4
	R(15e)	3.0135	406	99	93	23.8	26.8±0.4	4.7±1.2	1.7±0.5	1.5±0.2
	R(17e)	3.0096	518	111	105	24.1	26.1±0.5	11.4±1.6	3.5±0.6	3.2±0.2

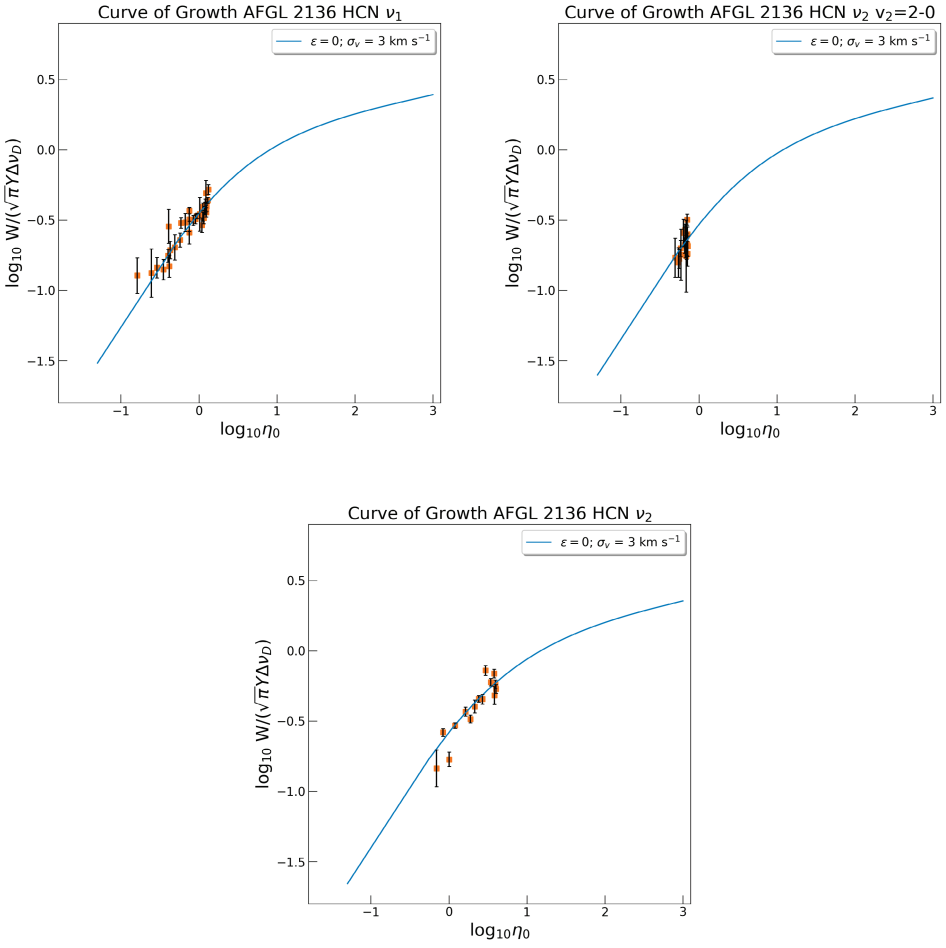

Figure 5.19: The same as Figure 5.13 but with $\epsilon = 0$.

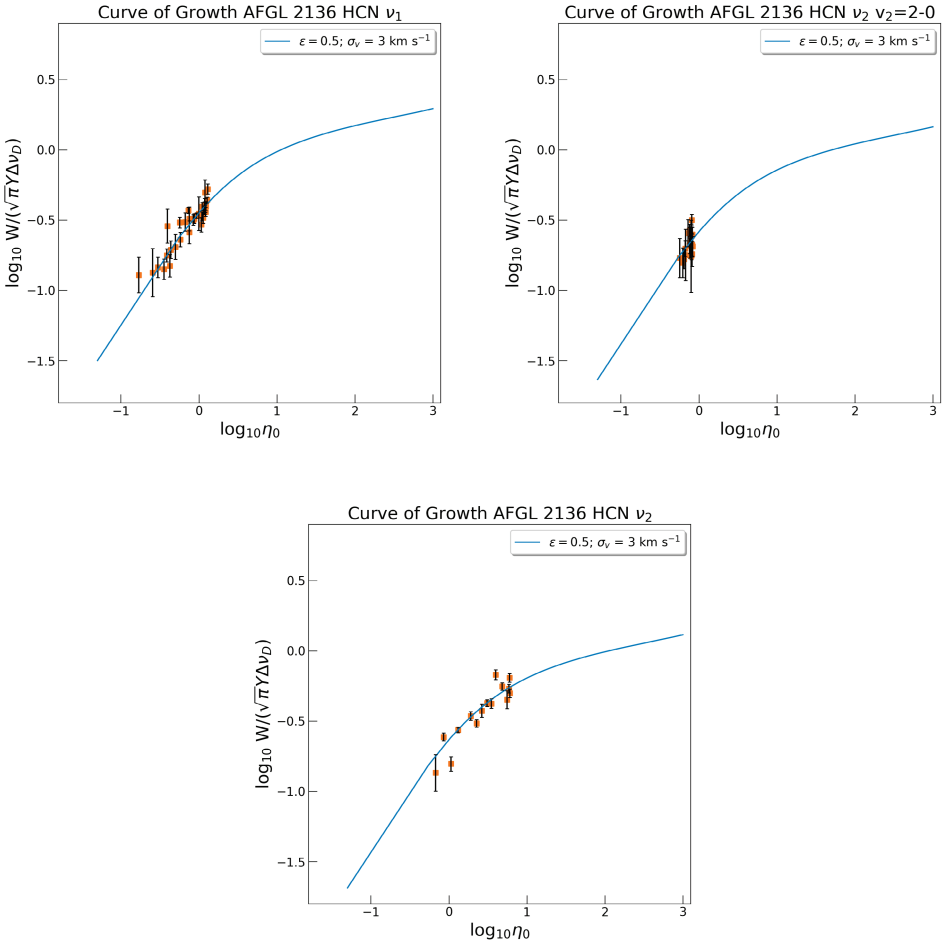

Figure 5.20: The same as Figure 5.13 but with $\epsilon = 0.5$.

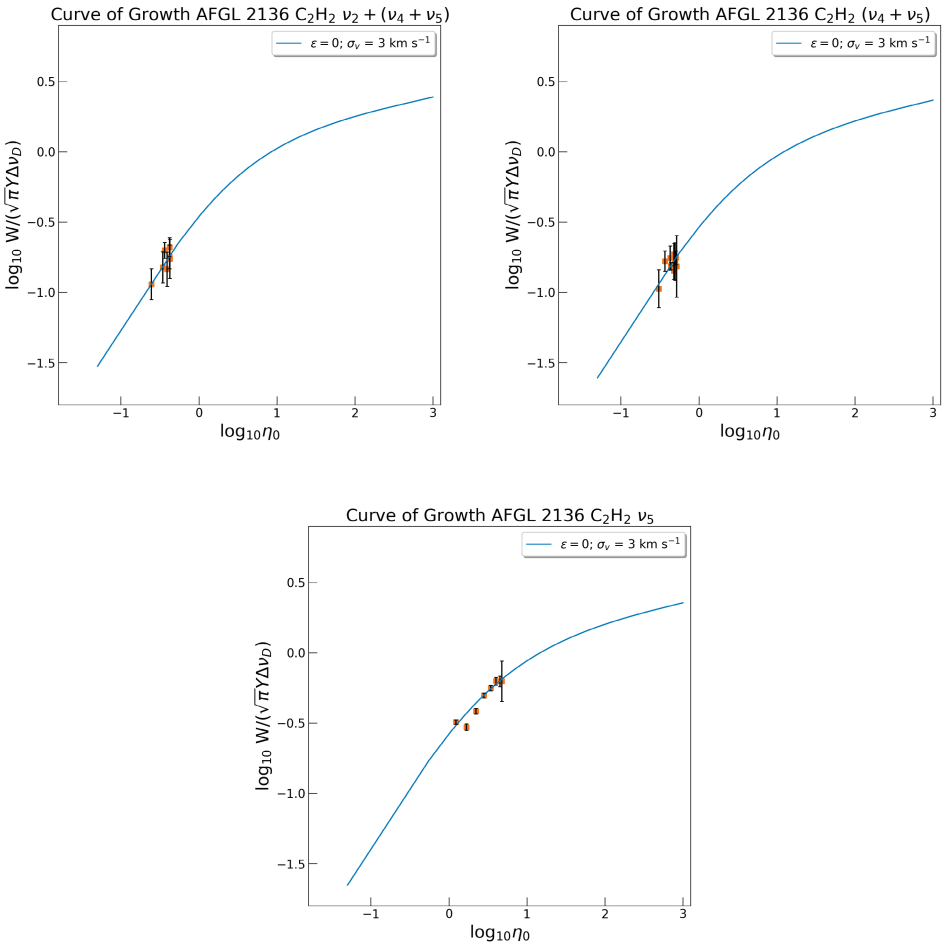

Figure 5.21: The same as Figure 5.17 but with $\epsilon = 0$.

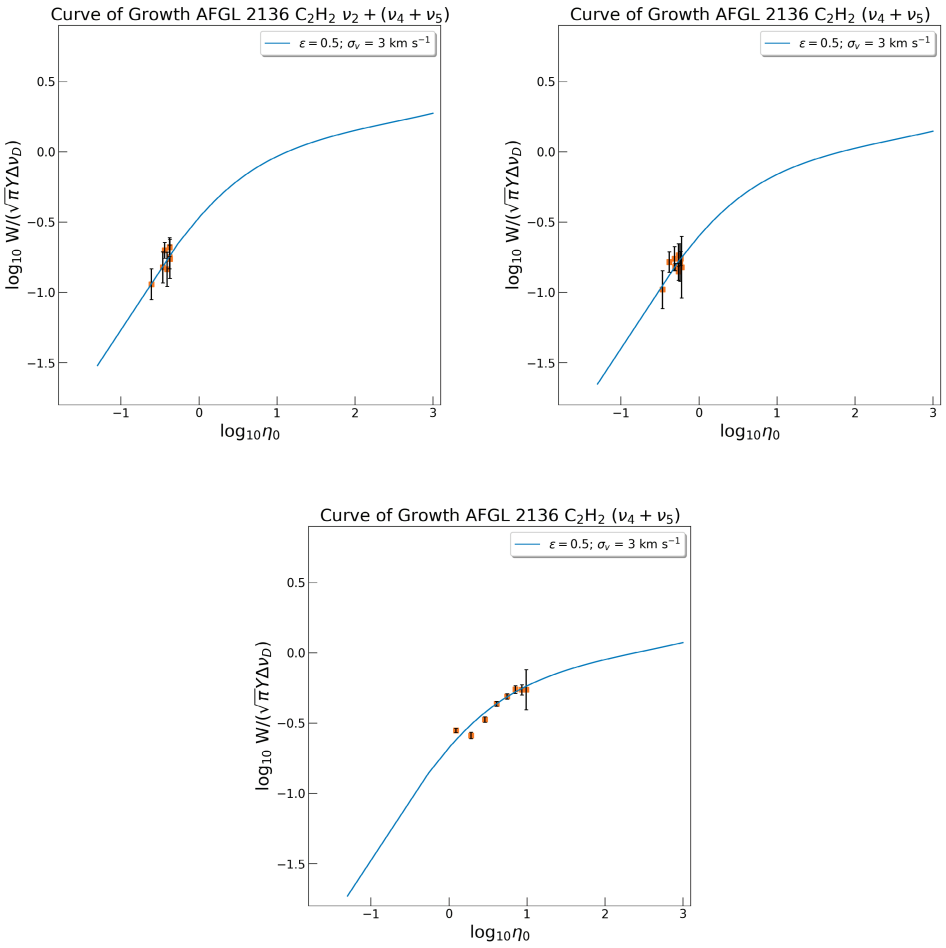

Figure 5.22: The same as Figure 5.17 but with $\epsilon = 0.5$.

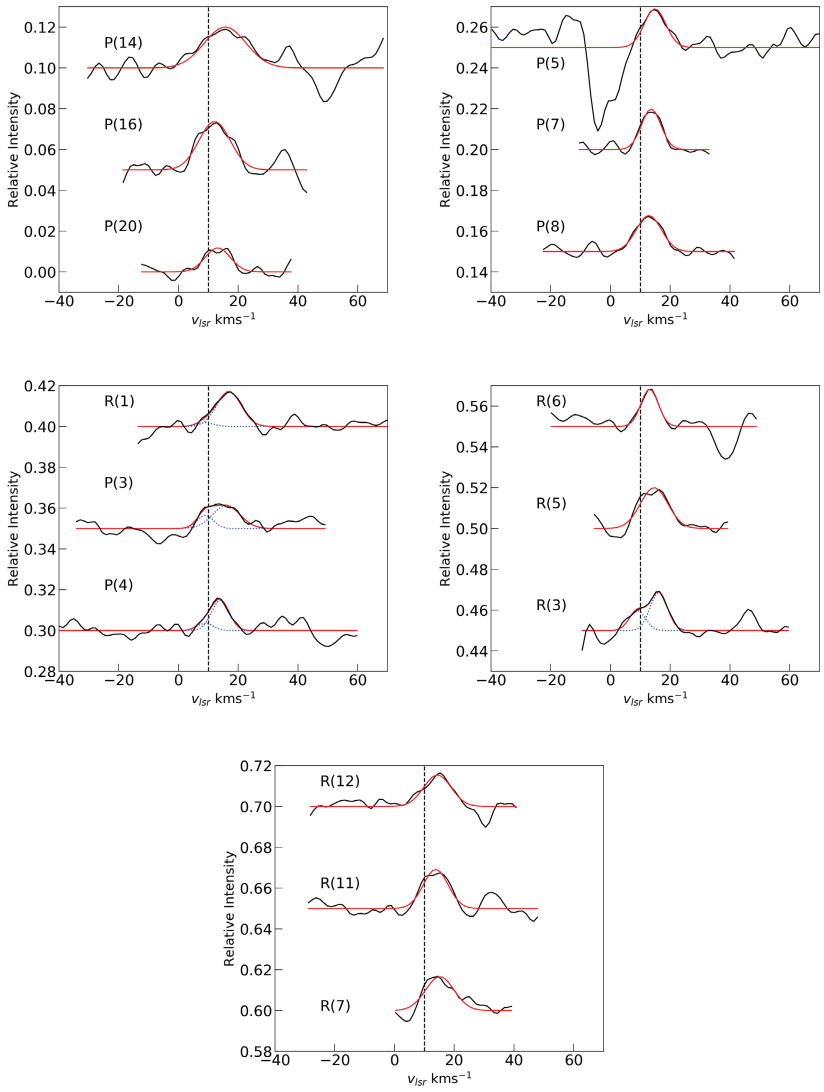

Figure 5.23: Line profiles of the detected transitions of the HCN ν_1 band of MonR2 IRS 3A. Fits are shown in red, including a two Gaussian composite fit for the P(4), P(3), R(3) and R(1) lines with individual contributions show as blue.

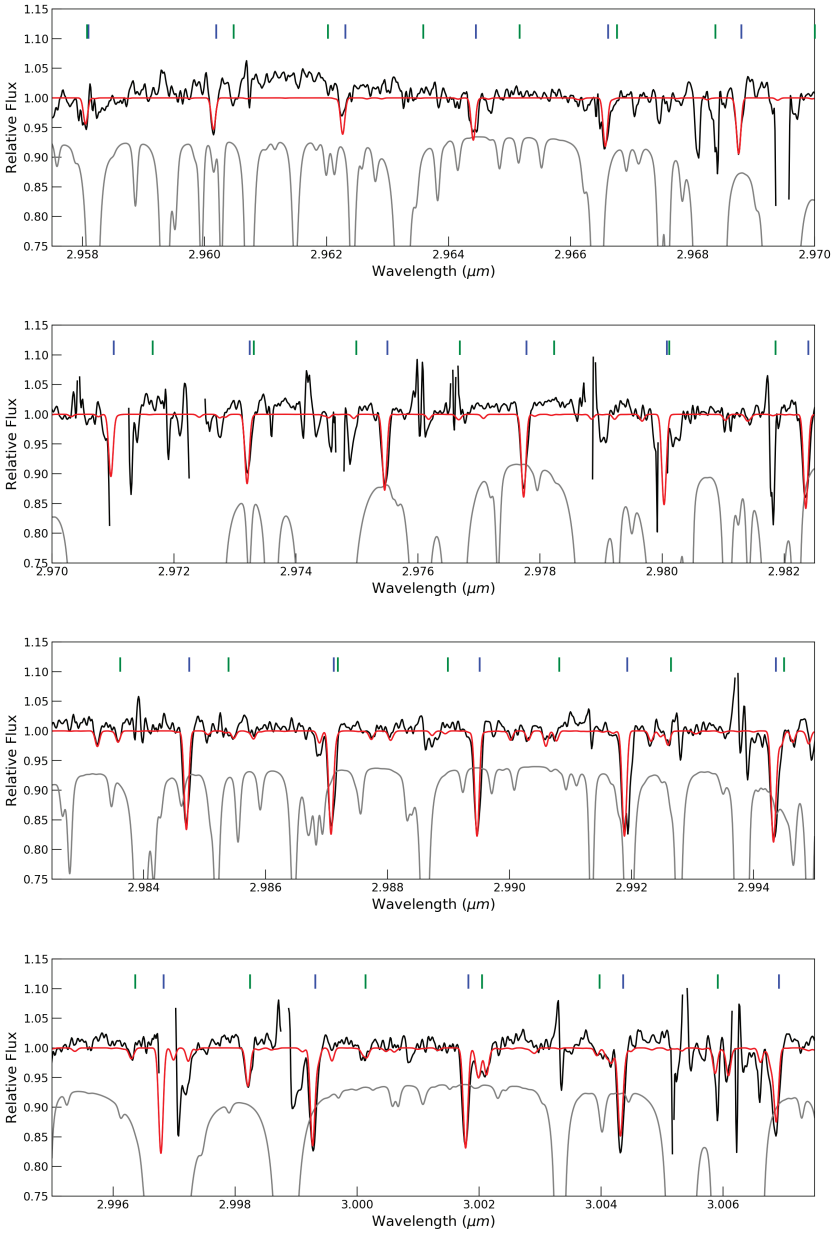

Figure 5.24: The L2 setting of AFGL 2136 in the range where absorption lines are present. In red is shown an LTE model of HCN at column density and temperature of $1{\times}10^{17}$ cm^{-2} and 500 K respectively, and C_2H_2 at column density of $8{\times}10^{16}$ cm^{-2} and 500 K respectively. The identifications of the HCN ν_1 band and C_2H_2 $\nu_2 + (\nu_4 + \nu_5)$ band are given as blue and green dashes respectively. The grey model is the atmospheric ATRAN model and regions of very bad transmission have been masked out of the science spectrum.

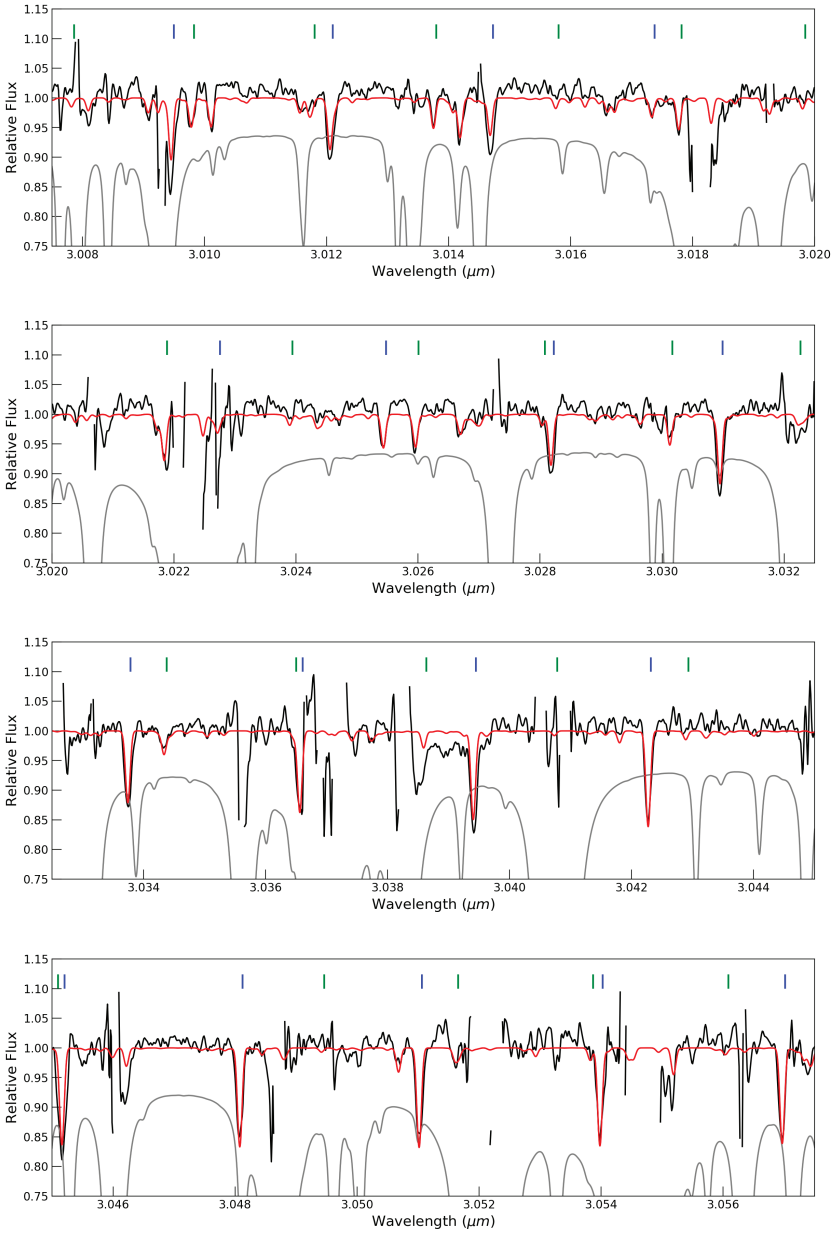
Relative Flux
Wavelength (μm)
1.15
1.10
1.05
1.00
0.95
0.90
0.85
0.80
0.75
3.008
3.010
3.012
3.014
3.016
3.018
3.020
3.022
3.024
3.026
3.028
3.030
3.032
3.034
3.036
3.038
3.040
3.042
3.044
3.046
3.048
3.050
3.052
3.054
3.056

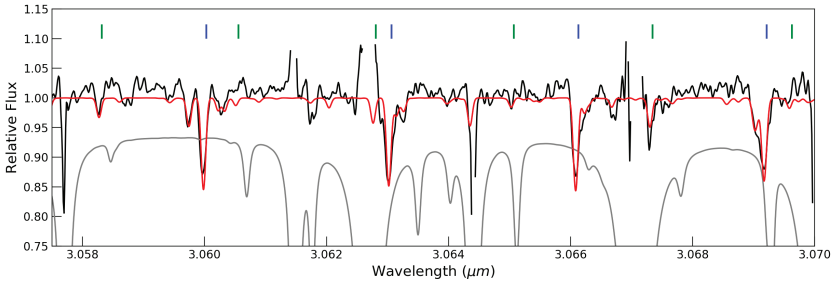
Relative Flux
1.15
1.10
1.05
1.00
0.95
0.90
0.85
0.80
0.75
3.058
3.060
3.062
3.064
3.066
3.068
3.070
Wavelength (μm)

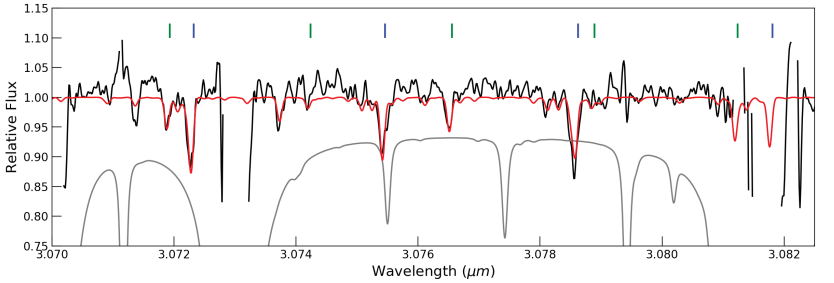
Relative Flux
1.15
1.10
1.05
1.00
0.95
0.90
0.85
0.80
0.75
3.070
3.072
3.074
3.076
3.078
3.080
3.082
Wavelength (μm)

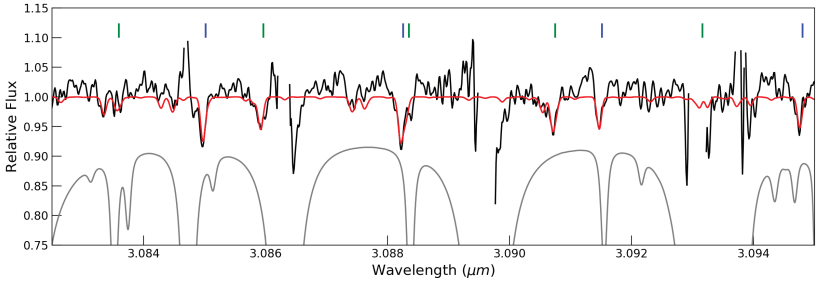
Relative Flux
1.15
1.10
1.05
1.00
0.95
0.90
0.85
0.80
0.75
3.084
3.086
3.088
3.090
3.092
3.094
Wavelength (μm)

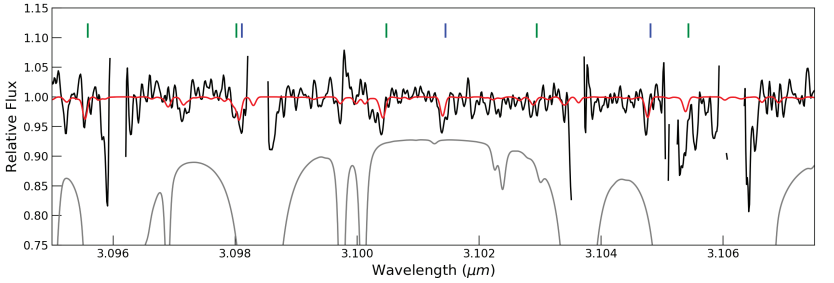
Relative Flux
1.15
1.10
1.05
1.00
0.95
0.90
0.85
0.80
0.75
3.096
3.098
3.100
3.102
3.104
3.106
Wavelength (μm)

Bibliography

Adams, S. C., Ádámkovics, M., Carr, J. S., Najita, J., & Brittain, S. D. 2019, ApJ, 871, 173

Agúndez, M., Cernicharo, J & Goicoechea, J. R. 2008, A&A, 483, 831

Agúndez, M, Roueff, E., LePetit, F & Le Bourlot, J. 2018, A&A, 616, A19

ALMA Partnership et al. 2015, ApJ, 808, L3

André, P., Di Francesco, J., Ward-Thompson, D., et al. 2014, in Protostars and Plantes VI, ed. H. Beuther, R. S. Klessen, C. P. Dullemond, & T. Henning, 27

Andrews, S. M. 2020, ARA&A, 58, 483

Asplund, M., Grevesse, N., Sauval, A. J., & Scott, P. 2009, ARA&A, 47, 481

Bally, J., Lada, C. J. 1983, ApJ, 265, 824

Banzatti, A., Pontoppidan, K. M., Salyk, C., et al. 2017, ApJ, 834, 152

Barentine, J & Lacy, J. 2012, ApJ, 757, 111

Barger, C. J., & Garrod, R. T. 2020, ApJ, 888, 38

Bast, J. E., Brown, J. M., Herczeg, G. J., van Dishoeck, E. F., & Pontoppidan, K. M. 2011, A&A, 527, A119

Bast, J. E., Lahuis, F., van Dishoeck, E. F., & Tielens, A. G. G. M. 2013, A&A, 551, A118

Beltrán M. T., Cesaroni R., Neri R., Codella C. 2004, ApJ, 601, L187

Beltrán, M. T., Cesaroni, R., Neri, R., Codella, C., at al. 2005, A&A, 435, 901

Beltrán, M. T., & de Wit, W. J. 2016, A&A Rev., 24, 6

Beltrán, M. T., Cesaroni, R., Rivilla, V. M., et al. 2018, A&A, 615, A141

Benz, A. O., Staüber, P., Bourke, T. L., van der Tak, F. F. S., et al. 2007, A&A, 475, 549

Bertoldi, F., McKee, C. F. 1992, ApJ, 395, 140

Beuther, H., Schilke, P., Sridharan, T. K., et al. 2002, A&A, 383, 892

Beuther, H. 2006, Triggered Star Formation in a Turbulent ISM Proceedings IAU Symposium, ed. Elmegreenm B. G., & Palous, J, 237

Beuther, H., Churchwell, E. B., McKee, C. F., & Tan, C. J. 2007, Protostars and Planets V, ed. Reipurth, Bo., Jewitt, David., & Keil, Klaus, University of Arizona Press, Tucson, 951

Beuther, H., Shepherd, D. S. 2005, In Cores to Clusters: Star Formation with Next Generation Telescopes, ed. MS Nanda Kumar, M Tafalla, P Caselli. Astrophys. Space Sci. Libr. 324, 105

Bik, A., & Thi, W.2004, A&A, 427, L13

Bik, A., Kaper, L., & Waters, L. B. F. M. 2006, A&A, 455, 561

Black, J. H., van Dishoeck, E. F., Wilner, S. P., & Woods, R. C. 1990, ApJ, 358, 459

Blake, G. A., Sutton, E. C., Masson, C. R., & Phillips, T. G. 1987, ApJ, 315, 621

Blake, G. A., & Boogert, A. C. A. 2004, ApJ, 606, L73

Boley, P. A., Linz, H., van Boekel, R., et al. 2013, A&A, 558, A24

Bonnell, I. A., Bate, M. R., Clarke, C. J., & Pringle, J. E. 1997, MNRAS, 285, 201
Bonnell, I. A., Bate, M. R., Zinnecker, H. 1998, MNRAS, 298, 93
Bonnell, I. A., & Bates, M. R. 2006, MNRAS, 270, 588
Boogert, A. C. A, Blake, G. A., & Öberg, K. I. 2004, ApJ, 615, 344
Boogert, A. C. A., Gerakines, P. A., & Whittet, C. B. 2015, ARA&A, 53, 541
Boonman, A. M.S., van Dishoeck, E. F., Lahuis, F., et al. 2000, ISO Beyond the Peaks: The 2nd ISO Workshop on Analytical Spectroscopy, ed. Salama, A., Kessler, M. F., Leech, K. & Schulz, B., ESA Special Publication, 456, 67
Boonman, A. M. S., Stark, R., van der Tak, F. F. S., et al. 2001, ApJ, 553, L63
Boonman,A. M. S., Doty, S. D., van Dishoeck, E. F., et al. 2003, A&A, 406, 937
Boonman, A. M. S., van Dishoeck, E. F., Lahuis, F., & Doty, S. D. 2003, A&A, 399, 1063
Boonman, A. M.S., van Dishoeck, E. F. 2003, A&A, 403, 1003
Bottinelli, S., Ceccarelli, C., Lefloch, B., Williams, J.P., et al. 2004, ApJ, 615, 354
Bruderer, S., Benz, A. O., Bourke, T. L., & Doty, S. D. 2009, A&A, 503, L13
Carey, S. J., Clark, F. O., Egan, M. P., et al. 1998, ApJ, 508, 721
Carr, J. S., Evans, N. J., Lacy, J. H., & Zhou, S. 1995, ApJ, 450, 667
Carr, J. S., & Najita, J. R. 2008, Science, 319, 1504
Carr, J. S., Najita, J.R. 2011, ApJ, 733, 102
Cassen, P., & Summers, A. 1983, Icarus, 53, 26
Cazaux, S., Tielens, A. G. G. M., Ceccarelli, C., Castets, A., et al. 2003, ApJ, 593, L51
Ceccarelli, C. 2008, Organic Matter in Space Proceedings IAU Symposium, No. 251, 2008, S. Kwok & S. Sandford, eds.
Cernicharo, J., Lim, T., Cox, P., et al. 1997, A&A, 323, L25
Cernicharo, J., & Crovisier, J. 2005, Space Sci. Rev., 119, 29
Cesaroni, R. 2005, Ap&SS, 295, 5
Cesaroni, R. 2005, in IAU Symp. 227, Massive Star Birth: A Crossroads of Astrophysics, ed. R. Cesaroni, M. Felli, E. Churchwell, & M. Walmsley (Cambridge: Cambridge Univ. Press), 59
Cesaroni, R., Galli, D., Lodato, G., Walmsley, C. M. & Zhang, Q. 2007, Protostars and Planets V, ed. Reipurth, Bo., Jewitt, David., & Keil, Klaus, University of Arizona Press, Tucson, 197
Charnley, S. B. 1997, ApJ, 481, 396
Choi, Y., van der Tak, F. F. S., van Dishoeck, E. F., Herpin, F., & Wyrowski, F. 2015, A&A, 576, A85
Clarke, C. J., Gendrin, A., Sotomayor, M. 2001, MNRAS, 328, 485
Clarke, M., Vacca, W. D., & Shuping, R. Y. 2015, Astronomical Society of the Pacific Conference Series, Vol. 495, Astronomical Data Analysis Software anSystems XXIV (ADASS XXIV), ed. A. R. Taylor & E. Rosolowsky, 355
Collins, G. W. 2003, The Fundamentals of Stellar Astrophysics, (Web Edition; pg 345)
Cooper, H. D. B., Lumsden, S. L., Oudmaijer, R. D., et al. 2013 MNRAS, 430, 1125
Cushing, M. C., Vacca, W. D., & Rayner, J. T. 2004, PASP, 116, 362
D'Alessio, P., Cantó, J., Calvet, N., & Lizano, S. 1998, ApJ, 500, 411
Davies, B., Lumsden, S. L., Hoare, M. G., et al. 2010, MNRAS, 402, 1504
de Wit, W. J., Hoare, M. G., Oudmaijer, R. D., et al. 2011, A&A, 526, L5
Doty, S. D., van Dishoeck, E. F., van der Tak, F. F. S., & Boonman, A. M. S. 2002, A&A, 389, 446
Draine, B. T./ 2003, ARA&A, 41, 241

Dullemond, C. P., Hollenbach, D., Kamp, I, & D'Alessio, P. 2007, Protostars and Planets V, ed. Reipurth, Bo., Jewitt, David., & Keil, Klaus, University of Arizona Press, Tucson, 555

Dullemond, C. P, & Monnier, J. D. 2010, ARA&A, 48, 205

Dungee, R., Boogert, A., DeWitt, C. N., Montiel, E., et al. 2018, ApJ, 868, L10

Egan, M. P., Shipman, R. F., Price, S. D., et al. 1998, ApJ, 494, L199

Eislöffel, J., Mundt, R., Ray, T. P., & Rodriguez, L. F. 2000, in Protostars and Planets IV, ed. V. Mannings, A. P. Boss, & S. S. Russel (Tucson: University of Arizona Press), 815

Elitzur, M., Hollenbach, D. J., & McKee, C. F. 1989, ApJ, 346, 983

Esplugues, G. B., Viti, S., Goicoechea, J. R., & Cernicharo, J. 2014, A&A, 567, A95

Evans, N. J., Lacy, J. H., & Carr, J. S. 1991, ApJ, 383, 674

Faure, A., Hily-Blant, P., Le Galm R., et al. 2013, ApJ, 770, l2

Favre, C., Fedele, D., Semenov, D., et al. 1018, ApJ, 862, L2

Fedele, D., Pascucci, I., Brittain, S., et al. 2011, ApJ732, 106

Fedele, D., Bruderer, S., van Dishoeck, E. F., et al. 2012, A&A, 544, L9

Fedele, D., Bruderer, S., van Dishoeck, E. F., et al. 2013, A&A, 559, A77

Fedriani, R., Caratti o Garatti, A., Koutoulaki, M., et al. 2020, A&A, 633, A128

Feng, S., Beuther, H., Henning, Th., et al. 2015, A&A, 581, A71

Feuchtgruber, H., Helmich, F. P., van Dishoeck, E. F., & Wright, C. M. 2000, ApJ, 535, L111

Frost, A. J., Oudmaijer, R. D., de Wit W. J., & Lumsden, S. L. 2021, A&A, 648, A62

Fuente, A., Treviño-Morales, S. P., Alonso-Albi, T., et al. 2021, MNRAS, 507, 1886

Gibb, E. L., Whittet, D. C. B., Boogert, A. C.. A., & Tielens, A. G. G. M. 2004, ApJS, 151, 35

Gibb, E. L., Van Brunt, K. A., Brittain, S. D., & Rettig, T. W. 2007, ApJ, 660, 1572

Gibb, K. L., & Horne, D. 2013, ApJ, 776, L28

Gieser, C., Semenov, D., Beuther, H., et al. 2019, A&A, A&A, 631, A142

Goddi, C., Ginsburg, A., Maud, L. T., Zhang, Q., & Zapata, L. A. 2020, ApJ, 905, 25

González-Alfonso, E., Cernicharo, J., van Dishoeck, E. F., et al. 1998, ApJ, 502, L169

Gordon, I. .E., Rothman, L. S., Hill, C. et al. 2017, JQSRT, 203, 3

Goto, M., Usuda, T., Takato, N., et al. 2003, ApJ, 598, 1038

Goto, M., Geballe, T. R., Harju, J., et al. 2019, A&A, 632, A29

Grunblatt, S. K., Huber, D., Gaidos, E., et al. 2019, AJ, 158, 227

Hatchell, J., Thompson, M. A., Millar, T. J., et al. 2009, A&A, 504, 853

Helmich, F. P., van Dishoeck, E. F., Black, J. H., et al. 1996, A&A, 315, L173

Hennemann, M., Motte, F., Schneider, N., Didelon, P., et al. 2012, A&A, 543, L3

Henning, Th., Chini, R., & Pfau, W. 1992, A&A, 263, 285

Henning, T., Feldt, M., & Stecklum, B. 2002, Hot Star Workshop III: The Earliest Phases of Massive Star Birth, ed. Paul A. Crowther, ASP Conference Series, Vol 267

Hall, D. N. B., Ridgway, S. T., Gillet, F. C., & Kleinmann, S. G. 1978, ApJ, 223, L47

Herbst, W., & Racine, R. 1976, AJ, 81, 840

Herbst, E., van Dishoeck, E. F. 2009, ARA&A, 47, 427

Hernández, J., Hartmann, L., Megeath, T., Gutermuth, R., Muzerolle, J., Calvet, et al. 2007, ApJ, 662, 1067

Hernández Vera, M., Lique, F., Dumouchel, F., Hily-Blant, P., Faure, A. 2017, MNRAS, 468, 1084

Hill, T., Motte, F., Didelon, P., et al. 2011, A&A, 533, A94

Hofner, P, Peterson, S., & Cesaroni, R. 1999, ApJ, 514, 899
Hollands, M., Tremblay, P. E., Gänsicke, B. T., et al. 2021, Nature, 5, 451
Hollenbach, D., Elitzur, M., & McKee, C. 2013, ApJ, 773, 70
Hunter C. 1977, ApJ, 218, 834
Ilee, J. D., Wheelwright, H. E., Oudmaijer, R. D. 2013, MNRAS, 429, 2960
Ilee, J. D., Cyganowski, C. J., Nazari, P., et al. 2016, MNRAS, 462, 4386
Indriolo, N., Neufeld, D. A., Seifahrt, A., & Richter, M. J. 2013, ApJ, 776, 8
Indriolo, N., Neufeld., D. A., DeWitt, C. N., Richter, M. J., et al. 2015, ApJ, 802: L14
Indriolo, N., Neufeld, D. A., Gerin, M., Schilke, P., et al. 2015, 800, 40
Indriolo, N., Neufeld, D. A., Barr, A. G., et al. 2020, ApJ, 894, 107
Jijina, J., & Adams, F. C. 1996, ApJ, 462, 874
Jiménez-Serra, I., Zhang, Q, Viti, S., Martín-Pintado, J., & De-Wit, W. -J. 2012, ApJ, 753, 34
Jiménez-Serra, I., Alejandro, B., Martín-Pintado, J., et al. 2020, ApJ, 897, L33
Johnston, K. G., Shepherd, D. S., Robitaille, T. P., & Wood, K. 2013, A&A, 551, A43
Johnston, K. G., Robitaille, T. P., Beuther, H., et al. 2015, ApJ, 813, L19
Jørgensen, J. K., Belloche, A., & Garrod, R. T. 2020, ARA&A, 58, 1
Kaźmierczak-Barthel, M., van der Tak, F. F. S., Helmich, F. P., et al. 2014, A&A, 567, A53
Keane, J. V., Boonman, A. M. S., Tielens, A. G. G. M., & van Dishoeck, E. F. 2001, A&A, 376, L5
Keto, E. 2007, ApJ, 666, 976
Knez, C., Lacy, J. H., Evans, N. J., van Dishoeck, E. F., & Richter, M. J. 2013, ApJ, 696, 471
Kraus, S., Hofmann, K. H., Menten, K. M., et al. 2010, Nature, 466, 339
Kress, M. ., Tielens, A. G. G. M., & Frenklach, M. 2008, 5th Spitzer Conference. New Light on Young Stars: Spitzer's View of Circumstellar Disks, poster 31
Krumholz, M. R., Klein, K. R., & McKee, C. F. 2005, in Massive Star Birth: A Crossroads of Astrophysics, Proceedings IAU Symposium, ed. R. Cesaroni, M. Felli, E. Churchwell & C. M. Walmsley, 227
Krumholz, M. R., Matzner, C. D., McKee, C. F. 2006, ApJ, 653, 361
Kuiper, R., Klahr, H., Beuther, H., & Henning, T. 2010, ApJ, 722, 1556
Kuiper, R., Turner, N. J., & Yorke, H. W. 2016, ApJ, 832, 40
Kurtz, S., Cesaroni, R., Churchwell, E., Hofner, P., & Walmsley, C. M. 2000, in Protostars and Planets IV, ed. V. Mannings, A. P. Boss, & S. S. Russell (Tucson, AZ: Univ. Arizona Press), 299
Kwon, J., Tamura, M., Hough J. H., Nagata, T., & Kusakabe, N. 2016, ApJ, 152, 67
Lacy, J, H., Evans, N. J., Achtermann, J. M., et al. 1989, ApJ, 342, L43
Lacy, J. H., Carr, J. S., Evans, N. J., et al. 1991, ApJ, 376, 556
Lacy, J. H., Knacke, R., Geballe, T. R., Tokunaga, A. T. 1994, ApJ, 428, L69
Lacy, J. H., Richter, M. J., Greathouse, T. K., Jaffe, D. T., & Zhu, Q. 2002, PASP, 114, 153
Lacy, J. H., Richter, M. J., Greathouse, T., et al. 2003, Society of Photo-Optical Instrumentation Engineers (SPIE) Conference Series, 4841, 1572
Lacy, J. H. 2013, ApJ, 765, 130
Lada, C. J., & Lada, E. A. 2003, ARA&A, 41, 57
Lahuis, F., van Dishoeck, E. F. 2000, A&A, 355, 699
Lahuis, F., van Dishoeck, E. F., Boogert, A. C. A., Pontoppidan, K. M., et al. 2006, ApJ, 636, L145

Li, J., Wang, J., Zhu, Q., Zhang, J., & Li, D. 2015, ApJ, 802, 40
Lique, F., Spielfiedel, A., Cernicharo, J. 2006, A&A, 451, 1125
Liu, H. B., Galván-Madrid, R., Jiménez-Serra, I., et al. 2015, ApJ, 804, 37
Lord, S. D. 1992, NASA Technical Memorandum 103957
Lumsden, S. L., Hoare, M. G., Urquhart, J. S., et al. 2013, ApJS, 208, 11
Lynden-Bell, D., & Pringle, J. E. 1974, MNRAS, 168, 603
Mandell, A. M., Bast, J., van Dishoeck, E. F., Blake, G. A., et al. 2012, ApJ, 747, 92
Markwick, A., Ilgner, M., Millar, T. J., & Henning, Th. 2002, A&A, 385, 632
Maud, L. T., Hoare, M. G., Galván-Madrid, R., et al. 2017, MNRAS, 467, L120
Maud, L. T., Cesaroni, R., Kumar, M. S. N., van der Tak, F. F. S., et al. 2018, A&A, 620, A31
Maud, L. T., Cesaroni, R., Kumar, M. S. N., Rivilla, V. M., et al. 2019, A&A, A&A, 627, L6
May, P. W., Pineau des Forêts, G., Flower, D. R., et al. 2000, MNRAS, 318, 809
McKee, C. F., & Ostriker, E. C. 2007, ARA&A, 45, 565
Melnick, G. J., Tolls, V., Neufeld, D. A., et al. 2010, A&A, 521, L27
Menten, K. M., & van der Tak, F. F. S. 2004, A&A, 414, 289
Mihalas, D. 1978, Stellar Atmospheres, (2nd Edition; W. H. Freeman; pg 211-213)
Mitchell, G. F., Curry, C., Maillard, J., & Allen, M. 1989, ApJ, 341, 1020
Mitchell, G. F., Maillard, J., Allen, M. 1990, ApJ, 363, 554
Mitchell, G. F., Maillard, J., & Hasewaga, T. I. 1991, ApJ, 371, 342
Monnier, J. D., Tuthill, P. G., Ireland, M., et al. 2009, ApJ, 700, 491
Moreno, R., Lellouch, E., Luisa, L. M., et al. 2012, Icarus, 221, 753
Moscadelli, L., & Goddi, C. 2014, A&A, 566, A150
Moscadelli, L., Sanna, A., Cesaroni, R., et al. 2019, A&A, 622, A206
Murakawa, K., Preibisch, T., Krau, S., & Weigelt, G./ 2008, A&A, 490, 673
Murukawa, K., Lumsden, S. L., Oudmaijer, R. D., et al. 2013, MNRAS, 436, 511
Najita, J., Carr, J. S., & Mathieu, R. D. 2003, ApJ, 589, 931
Najita, J. R., Carr, J. S., Brittain, S. D., Lacy, J. H., et al. 2021, ApJ, 908, 171
Nakano, T., Hasegawa, T., & Norman, C. 1995, ApJ, 450, 183
Nakano, T. 1989, ApJ, 345, 464
Neufeld, D. A., & Melnick, G. J. 1991, ApJ, 368, 215
Neufeld, D. A., González-Alfonso, E,. Melnick, G. J., et al. 2011, ApJ, 727, L28
Neufeld, D. A., DeWitt, C., Lesaffre, P., et al. 2019, ApJ, 878, L18
Nielbock, M., Chini, R., Hoffmeister, V. H., Scheyda, C. M., et al. 2007, ApJ, 656, L81
Öberg, K. I., Boogert, A. C. A., Pontoppidan, K. M., et al. 2008, ApJ, 678, 1032
Öberg, K. I., Guzmán, V. V., Furuya, K., et al. 2015, Nature, 520, 198
Öberg, K I. 2016, Chem. Rev, 116, 17, 9631
Olmi L., Cesaroni R., Hofner P., Kurtz S., et al. 2003, A&A, 407, 225
Ormel, C. W., Min, M., Tielens, A. G. G. M., et al. 2011, A&A, 532, A43
Osorio, M., Anglada, G., Lizano, S., & D'Alessio, P. 2009, ApJ, 694, 29
Padovani, M., Hennebelle, P., Marcowith, A., & Ferriére, K. 2015, A&A, 582, L13
Padovani, M., Hennebelle, P., Marcowith, A., & Ferriére, K. 2016, A&A, 590, A8
Palmeirim, P., André, P., Kirk, J., et al. 2013, A&A, 550, A38
Papousek, D. 1982, Molecular Vibrational-Rotational Spectra: Theory and Applications of High Resolution Infrared, Microwave, and Raman Spectroscopy of Polyatomic Molecules,

(1st Edition; Elsevier Science Pub Co)
Pascucci, I., Apai, D., Luhman, K., et al. 2009, ApJ, 696, 143
Patel, N. A., Curiel, S., Sridharan, T. K., et al. 2005, Nature, 437, 576
Peimbert, M., Luridiana, V., & Peimbert, A. 2007, ApJ, 666, 636
Pineda, J., Goodman, A., Arce, H., et al. 2010, ApJ, 712, L116
Plambeck, R. L., & Wright, M. C. H. 1987, ApJ, 317, L101
Pomohaci, R., Oudmaijer, R. D., Lumsden, S. L., et al. 2017, MNRAS, 472, 3624
Pontoppidan, K. M., Salyk, C., Blake, G. A., et al. 2010, ApJ, 720, 887
Pontoppidan, K. M., Blake, G. A., & Smette, A. 2011, ApJ, 733, 84
Pontoppidan, K. M., Salyk, C., Bergin, E. A., et al. 2014, Protostars and Planets VI, 363
Pontoppidan, K, M., Salyk, C., Banzatti, A., et al. 2019, ApJ, 874, 92
Preibisch, T., Balega, Y. Y., Schertl, D., & Weigelt, G. 2002, A&A, 392, 945
Preibisch, T., Balega, Y. Y., Schertl, D, & Weigelt, G. 2003, A&A, 412, 735
Rangwala, N., Colgan, S. W. J., Le Gal, R., Acharyya, K., et al. 2018, ApJ, 856, 9
Rathborne, J. M., Jackson, J. M., & Simon, R. 2006, ApJ, 641, 389
J. T. Rayner, A. Tokunaga, D. Jaffe, M. Bonnet, G. Ching, M. Connelley, D. Kokubun, C. Lockhart, & E. Warmbier. 2016, SPIE, 9908E, 84R
Reffert, S., Bergmann, C., Quirrenbach, A, Trifonov, T., Künstler, A. 2015, A&A, 574, A116
Richter, M. J., Ennico, K. A., McKelvey, M. E., & Seifahrt, A. 2010, in Society of Photo-Optical Instrumentation Engineers (SPIE) Conference Series, Vol. 7735
Richter, M. et al. 2018, Journal of Astronomical Instrumentation, 7,4
Rothman, L. S., Gordon, I. E., Babikov, Y., et al. 2013, J. Quant. Spec. Radiat. Transf., 130, 4
Rygl K. L. J. et al. 2012, A&A, 539, 79
Sakamoto, K., Okumura, S. K., Ishizuki, S., Scoville, N. Z. 1999, ApJS, 124, 403
Salyk, C., Blake, G. A., Boogert, A. C. A., & Brown, J. M. 2009, ApJ, 699, 330
Salyk, C., Pontoppidan, K. M., Blake, G. A., et al. 2011, ApJ, 731, 130
Sandell, G., Wright, M., Forster, J. R. 2003, ApJ, 590 L45
Sanna, A., Reid, M. J., Carrasco-González, C., et al. 2012, ApJ, 745, 191
Schneider, N., Csengeri, T., Hennemann, M., et al. 2012, A&A, 540, L11
Schilke, P., Groesbeck, T. D., Blake, G. A., & Phillips, T. G. 1997, ApJS, 108, 301
Schwarz, K. R., & Bergin, E. A. 2014, ApJ, 797, 113
Scoville, N., Klienmann, S. G., Hall, D. N. B., & Ridgway, S. T. 1983, ApJ, 275, 201
Segura-Cox, D. M., Schmiedeke, A., Pineda, J. E., et al. 2020, Nature, 586, 228
Setterholm, B. R., Monnier, J. D., Davies, C. L., Kreplin, A., et al. 2019, ApJ, 869, 164
Shakura, N. I., & Sunyaev, R. A. 1973, A&A, 24, 337
Sheehan, P. D., Tobin, J. J., Federman, S., et al. 2020, ApJ, 902, 141
Shepherd, D. S., Churchwell, E. 1996a, ApJ. 472, 225
Shepherd, D. S., Churchwell, E. 1996b, ApJ, 457, 267
Shu, F. H. 1977, ApJ, 214, 488
Shu, F. H., Adams, F. C., & Lizano, S. 1987, ARA&A, 25, 23
Šimečková, M., Jacquemart, D., Rothman, L. S., et al. 2006, Journal of Quantitative Spectroscopy & Radiative Transfer 98, 130
Smith, R. G. 1991, MNRAS, 249, 172
Smith, M. D. 1993, ApJ, 406, 520
Smith, R. L., Gudipati, M. S., Boogert, A. C. A., & Blake, G. A. 2020, Lunar and Planetary

Science Conference, 1239
Sollins P. K., Zhang Q., Keto E., and Ho P. T. P. 2005, 631, 399
Spoon H. W. W., Farrah D., Lebouteiller V., González-Alfonso E., et al. 2013, ApJ, 775, 127
Stahler, S. W., & Palla, F. 2005, The Formation of Stars, John Wiley & Sons, Ltd, 865
Tamura, M., & Yamashita, T. 1992, ApJ, 391, 710
Tan, J. C. 2008, Massive Star Formation: Observations Confront Theory, eds.Beuther, Linz, & Henning, ASP, Vol. 387
Tan, J. C. 2017, Astrochemistry VII, Proceedings IAU Symposium No. 322
Tan, J. C., & McKee, C. F. 2003, IAU Symp.221, Star Formation at High Angular Resolution, eds.Burton, Jayawardhana, & Bourke, ASP, 221 (astro-ph/0309139)
Tanaka, K. E. I., Tan, J. C., & Zhang, Y. 2016, ApJ, 8181, 52
Tanaka, K. E. E., Tan, J. C., Staff, J. E., & Zhang, Y. 2017, ApJ, 849, 133
Tercero, B., Cernicharo, J., Pardo, & J. R., Goioechea, J. R. 2010, A&A, 517, A96
Tieftrunk, A., Pineau Des Forêts, G., Schilke, P., et al. 1994, A&A, 289, 579
Tielens, A. G. G. M., & Hollenbach, D. 1985, ApJ, 291, 722
Tielens, A. G. G. M. 2005, The Physics and Chemistry of the Interstellar Medium (Cambridge University Press)
Tielens, A.G .G .M. 2021, Molecular Astrophysics, (1st Edition; Cambridge University Press pg 132
Timmermann, R. 1998, ApJ, 498, 246
Theulé, P., Duvernay, F., Danger, G., et al. 2013. Adv. Space Res, 52, 1567
Torrelles, J. M., Trinidad, M. A., Curiel, S., et al. 2014, MNRAS, 437, 3803
Trinidad, M. A., Curiel, S., Cantó, J., et al. 2003, ApJ, 589, 386
Turner, B. E., Chan, K., Green, S., & Lubowich, D. A. 1992, ApJ, 399, 114
Turner, N., Fromang, S., Gammie, C., Klahr, H., et al. 2014, Protostars Planets VI, 411
Urquhart, J. S., Hoare, M. G., Lumsden, S. L., et al. 2012, MNRAS, 420, 1656
Urquhart, J. S., Figura, C. C., Moore, T. J. T., et al. 2014, MNRAS, 437, 1791
van der Tak, F. F S., van Dishoeck, E. F., Evans, N. J., & Bakker, E. J. 1999, ApJ, 522, 991
van der Tak, F. F. S., & van Dishoeck, E. F. 2000, A&A, 358, L79
van der Tak, F. F. S. 2003, Star Formation at High Angular Resolution ASP Conference Series, ed. Jayawardhana, R., Burton, M. G., & Bourke, T. L, 221
van der Tak, F. F. S., Walmsley, C. M., Herpin, F., & Ceccarelli, C. 2006, A&A, 447, 1011
van der Tak, F. F. S., Boonman A. M. S., Braakman, R., & van Dishoeck, E. F. 2003, A&A, 412, 133
van der Tak, F. F. .S., & Menten, K. M. 2005, A&A, 437, 947
van der Tak, F. F. S., Chavarría, L., Herpin, F., et al. 2013, A&A, 554, A83
van Dishoeck, E. F., & Black, J., H. 1988, ApJ, 334, 771
van Dishoeck, E. F. 1998, in Chemistry and Physics of Molecules and Grains in Space, Faraday Discussions, 109, 31
van Dishoeck, E. F., & Blake, G. A. 1998, ARA&A, 36, 317
van Dishoeck, E. F., & Helmich, F. P. 1996, A&A, 315, L177
van Dishoeck, E. F.., Herbst, E., & Neufeld, D. 2013, Chem. Rev., 113, 9043
van Dishoeck, E. F., Kristensen, L. E., Mottram, J. C., et al. 2021, A&A, 648, A24
Veras, D., Tremblay, P. E., Hermes, J. J., McDonald, C. H., et al. 2020, MNRAS, 493, 765
Villanueva, G. L., Smith, M. D., Protopapa, S., Faggi, S., & Mandell, A. M. 2018, J. Quant. Spec. Radiat. Transf., 217, 86

Visser, R., van Dishoeck, E. F., Doty, S. D. & Dullemond, C. P. 2009, A&A, 495, 881
Viti, S., Collings, M. P., Dever, J. W., McCoustra, M. R. S., & Williams, D. A. 2004, MNRAS, 354, 1141
Vogel, S. N., Kulkarni, S. R., Scoville, N. Z. 1988, Nature, 334, 402
Walsh, C., Millar, T. J., & Nomura, H. 2010, ApJ, 722, 1607
Walsh, C., Nomura, H., & van Dishoeck, E. F. 2015, A&A, 582, A88
Walsh, C., Loomis, R. A., Öberg, K. I., et al. 2016, ApJ, 823, L10
Wang, K. S., van der Tak, F. F. .S., & Hogerheijde, M. R. 2012, A&A, 543 A22
Willacy, K., & Woods, P. M. 2009, ApJ, 703, 479
Williams, J. P., & Cieza, L. A. 2011, ARA&A, 49, 67
Wilson, T. L., & Rood, R. T. 1994, ARA&A, 32, 191
Wolfire, M. G., & Cassinelli, J. P. 1986, ApJ, 310, 207
Wright, C. M., van Dishoeck, E. F., Black, J. H., et al. 2000, A&A, 358, 689
Wu, Y., Zhang, Q., Chen, H., et al. 2005, AJ, 129, 330
Yang, B. ., Stancil, P. C., Balakrishnan, N., & Forrey, R. C. 2010, ApJ, 718, 1062
Yao, Y., Hirata, N,. Ishii, M., et al. 1997, ApJ, 490, 281
Yorke, H. W., & Bodenheimer, P. 1999, ApJ, 525, 330
Yorke, H. W., & Sonnhalter, C. 2002, ApJ, 569, 846
Young, E. T., Becklin, E. E., Marcum, P. M., et al. 2012, ApJ, 749, L17
Zapata, L. A., Garay, G., Palau, A. 2019, ApJ, 872, 176
Zinnecker, H., & Yorke H. W. 2007, ARA&A, 45, 481

Nederlandse Samenvatting

Sterren worden geboren in dichte wolken van gas en stofdeeltjes in het interstellaire medium. Met het vormen van sterren ontstaan er ook planetenstelsels. En van alle duizenden planeten die al ontdekt zijn, lijkt de Aarde uniek te zijn. Het is een planeet met de ideale omstandigheden om leven in stand te houden. Goed begrip van het stervormingsproces is van belang om te kunnen beoordelen of de Aarde volledig uniek is, of slechts zeer zeldzaam.

Het vormen van de sterren is een proces dat zich afspeelt over miljoenen jaren. Gedurende een mensenleven kunnen we enkel een momentopname van de evolutie van de geboorte van een ster waarnemen. Door het vergelijken van vele verschillende objecten en door de aanname dat alle sterren op dezelfde manier ontstaan, kunnen we een volgorde van evolutie samenstellen. De wolken waarin de sterren geboren worden hebben een dusdanige hoge dichtheid dat zij onzichtbaar zijn in het optische licht (de golflengtes zichtbaar voor het menselijk oog). Om er toch iets in te kunnen zien moeten we schakelen naar licht met een langere golflengte, vooral infrarood en sub-millimeter (sub-mm). Vandaar dat er gebruik gemaakt is van de telescoopfaciliteiten van het Stratospheric Observatory for Infrared Astronomy (SOFIA) en de Atacama Large Millimetre Array (ALMA). Deze maken het mogelijk om door de stofextinctie van de dichte wolken te kijken. Het verschil tussen optische en infrarood foto's is weergegeven in Figuur 5.25.

Een belangrijk stuk gereedschap van de astronoom is de emissie en absorptie van licht door moleculen. Een bepaald molecuul absorbeert of straalt licht uit op een unieke combinatie van discrete frequenties; deze worden lijnen genoemd. Op deze manier hebben moleculen hun eigen moleculaire vingerafdruk (zie Figuur 1.6 van deze thesis). Door gebruik te maken van een spectrale resolutie die hoog genoeg is, kunnen we al deze emissie en absorptie functies scheiden, en zo informatie afleiden zoals temperatuur, snelheid en chemische aanwezigheid. De chemische aanwezigheid maakt het mogelijk om vast te stellen hoeveel van een bepaald molecuul aanwezig is in verhouding tot een ander molecuul. Zo kunnen we informatie verkrijgen over het chemische proces dat heeft geleid tot de waargenomen aanwezigheden. De meest voorkomende moleculen in stervormende gebieden bestaan uit waterstof, koolstof, zuurstof en stikstof. Voor deze thesis zijn de volgende moleculen relevant: koolmonoxide (CO), koolmonosulfide (CS), water (H_2O), waterstofcyanide (HCN), acetyleen (C_2H_2) en ammoniak (NH_3).

Op basis van hun massa kunnen sterren in twee groepen verdeeld worden: sterren met lage massa (minder dan 8 $M_\odot$) en sterren met hoge massa (meer dan 8 $M_\odot$).

Figuur 5.25: De Taurus moleculaire wolken gezien op twee verschillende golflengtes. De foto links is gemaakt in het zichtbare gedeelte van het spectrum, de foto rechts laat dezelfde wolk zien op een golflengte van één millimeter. De wolk ziet er donker uit, maar op de langere golflengtes kunnen we zien dat er veel meer gaande is. Sterren in de maak kunnen herkend worden aan de heldere stippen in de rechterafbeelding. Bron: ESO/APEX (MPIfR/ESO/OSO)/A. Hacar et al./Digitized Sky Survey 2. Acknowledgment: Davide De Martin.

Deze twee groepen hebben vergelijkbare formatieroutes, maar er zijn belangrijke verschillen. Bijvoorbeeld dat er bij grote sterren geen planeten vlakbij zijn waargenomen, waarschijnlijk door de extreme omgeving van deze sterren. Op de kosmische schaal zijn grote sterren logischerwijs belangrijker dan sterren met weinig massa. Deze beïnvloeden het opwarmen en afkoelen van sterrenstelsels, stimuleren de productie van nieuwe sterren, en zijn de voornaamste producenten van veel van de elementen die zwaarder zijn dan koolstof.

Een belangrijk stadium in het vormingsproces van een ster van weinig massa is de schijffase. Hier kan materiaal zich hechten aan een protoster via een schijf die de ster omringt. Zo neemt de massa toe en groeit de ster. De schijf is een gevolg van het behouden van het impulsmoment, waarbij ronddraaiend en ineenstortend materiaal zich uitspreidt in een afgeplatte structuur rondom de ster, zoals afgebeeld in Figuur 5.26. Ook ontstaan er sterke wegvloeiende stromingen en winden die loodrecht op de schijf staan doordat materiaal uit het sterschijf-systeem gestuurd wordt. Zo wordt de wolk die de ster omgeeft verstrooid. Het is nog steeds een punt van debat of de schijven net zo belangrijk zijn in het vormingsproces van de sterren met hoge massa als ze zijn voor de sterren met lage massa. De theorie veronderstelt dat de schijven nodig zijn voor het maken van grote sterren, omdat er een soort mechanisme moet zijn waardoor het materiaal de grote middelpuntvliedende druk kan omzeilen zodat de ster kan blijven groeien. Een schijf is de logische oplossing, maar schijven bij sterren van hoge massa worden zeer zelden waargenomen, wat nog meer het geval is voor de nog grotere sterren.

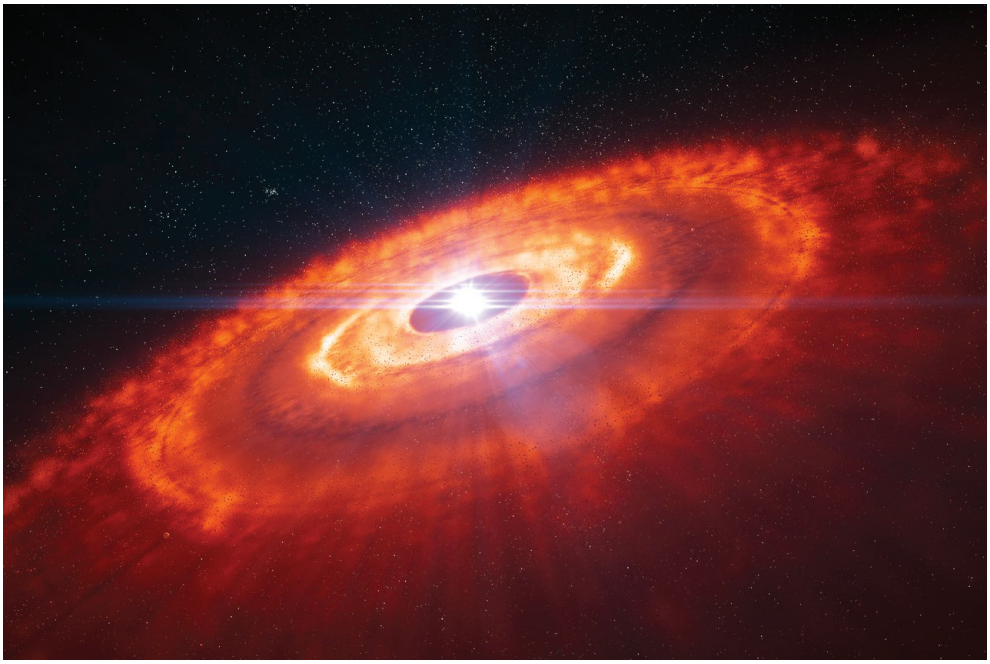

Figuur 5.26: Artist impression van een circumstellaire schijf rondom een ster in vorming. Bron: ESO/L. Calcada

Deze thesis

Door gebruik te maken van unieke observaties heeft deze thesis de vorming van grote sterren bediscussieerd, waarbij de focus ligt op de details op kleine schaal. De resultaten van het eerste spectrale onderzoek op het 3 -13 μm gebied van twee grote protosterren, AFGL 2591 en AFGL 2136, zijn gepresenteerd. De data werd verkregen van observaties van het Stratospheric Observatory for Infrared Astronomy (SOFIA) en van de Infrared Telescope Facility (IRTF) en Gemini telescopen. Onze resultaten gaan over de productie van belangrijke organische moleculen in de schijven van grote sterren, alsook over de temperatuurstructuur van de schijf.

Hoofdstuk 2 heeft het verschil in fysische condities tussen grote en kleine schalen op de plekken van stervorming laten zien, met observaties van het CS-molecuul in AFGL 2591. Pre-ALMA-observaties op submillimeter golflengtes hebben geen onderscheid kunnen maken tussen het schijfgebied en het wolkgebied van de grote protosterren. Absorptiestudies op infrarood golflengtes kunnen echter wel tot op zeer kleine schaal doordringen. Zo is er op infrarood golflengtes veel heter gas met hogere dichtheid geobserveerd dan eerder gevonden was met submillimeter studies. De hoeveelheid zwavel-bevattende moleculen die in de dichte gebieden van het sterrenstelsel geobserveerd zijn, is lager dan verwacht. Onze waargenomen CS-aanwezigheid was erg hoog, wat suggereert dat er een groot reservoir van warme zwavel-bevattende moleculen dicht bij de ster zit. Dit is nog niet eerder waargenomen. Heet gas van 700 K is gezien in CS, wat erop wijst dat dit gas waarschijnlijk geproduceerd is in de chemie

op hoge temperatuur van een schijfatmosfeer.

In hoofdstuk 3 en 4 zijn we verder gegaan met de belangrijkere vragen wat betreft de vorming van grote sterren. Hier hebben we een model gepresenteerd om de observatie van absorptielijnen in een circumstellaire schijf te kunnen verklaren. Dit model verklaart een reeks observatie-beperkingen afgeleid van verscheidene moleculen in AFGL 2591 en AFGL 2136: HCN, C_2H_2, CS, CO, NH_3 en H_2O. De formatie van zulke lijnen vereist een temperatuurgradiënt die toeneemt richting het binnenste gedeelte van de schijf. Vervolgens vereist een dergelijke temperatuurgradiënt dat het verwarmen van de schijf voornamelijk komt door viskeuze processen in het binnenste gedeelte, en niet zo zeer verwarming door stellaire straling. Deze processen leiden tot een aangroei van materiaal op de ster, waardoor de ster groter kan groeien. Enkele observatie-beperkingen zijn van belang om te vermelden, omdat deze belangrijke aandachtspunten van het model aanstippen. De aanwezigheid van HCN en C_2H_2 varieert met de golflengte, wat erop wijst dat deze soorten zich concentreren naar de binnenste 200 AU van de schijf. Vibrationeel-aangeslagen-toestand-banden van CO en C_2H_2 geven resultaten die dichtheden $> 10^{10}$ cm^{-3} vereisen. De aanwezigheden van alle moleculen zijn consistent met wat er verwacht werd op basis van chemische schijfmodellen. Tot slot, de H_2O absorptielijnen zijn verzadigd, maar gaan niet naar een flux van nul, wat normaal het geval is. Dit gedrag is een directe voorspelling van ons schijfmodel.

In hoofdstuk 5 werd het 3 μm spectrum van een reeks grote protosterren behandeld. We vonden op deze golflengte dat MonR2 IRS 3 HCN-lijnen in de straling vertoonde. Het gas was heet met een temperatuur van 500 K. Deze straling kwam overeen met óf een uitdijend omhulsel van gas, óf met de atmosfeer van een circumstellaire schijf. HCN en C_2H_2 lijnen werden gedetecteerd in absorptie in de buurt van AFGL 2136. De resultaten voor deze moleculen, samen met hoofdstuk 3 en 4, vormen een goede onderbouwing van het schijfmodel. Een alternatief voor het schijfmodel is dat het gas dichtbij de ster ligt, maar niet in een schijf. Om een dergelijk model te kunnen laten werken moet H_2O gas verder uitgerekt worden dan HCN en C_2H_2 gas. Dit bleek echter zeer onwaarschijnlijk te zijn, omdat H_2O eenvoudiger geproduceerd wordt. Het schijfmodel was daarom het voorkeursmodel omdat het beter past met al de waargenomen beperkingen.

Hoe nu verder

De detectie van honderden lijnen in het infrarood heeft groot potentieel voor het identificeren en bestuderen van schijven in grote protosterren. Om dit onderzoeksveld verder te ontdekken is het van groot belang om meer objecten op eenzelfde manier te bestuderen. Nieuwe, grotere, en betere telescopen die binnenkort beschikbaar zullen zijn, zijn de James Webb Space Telescope (JWST) en de Extremely Large Telescope (ELT). Deze thesis is van groot belang om richting te geven aan studies met de JWST, die geen observaties van hoge spectrale resolutie kunnen maken. JWST zal wel de gelegenheid bieden om objecten van lage massa te bestuderen op infrarood golflengtes vanwege de hoge kracht. Op die manier zullen we kunnen bepalen of absorptielijnen normaal zijn voor protosterren van lage massa in de vroegste fases van de vorming.

Ook is de ontwikkeling van theoretische modellen van groot belang. Op dit mo-

ment bestaan er geen modellen die circumstellaire schijven die van binnenuit verwarmd worden behandelen. Dit zal essentieel zijn voor een beter begrip en een realistischer beeld van de in deze thesis besproken schijven. Dergelijke modellen zullen ook de chemie moeten meenemen, omdat verschillende fysische processen nodig kunnen zijn om de vorming van moleculen te beginnen.

English Summary

Stars are born in dense clouds of gas and dust in the interstellar medium. With the formation of stars, comes also the formation of planetary systems. Out of the thousands of planets already discovered, the Earth appears to be unique. It is a planet that possesses the ideal conditions for the sustainment of life. To understand whether the Earth is truly unique, or just very rare, a proper understanding of the star formation process is necessary.

The star formation process occurs over timescales of millions of years. Thus, over the course of a single human lifetime, we will only observe forming stars as snapshots in their evolution. By comparing many different objects, and assuming that all stars form the same way, we can piece together an evolutionary sequence. The clouds which stars are born in are so dense that they are invisible to optical light (the wavelengths visible to the human eye). Therefore to look into them we must switch to longer wavelength light, in particular infrared and sub-millimetre (sub-mm). Hence the use of telescope facilities such as the Stratospheric Observatory for Infrared Astronomy (SOFIA) and the Atacama Large Millimetre Array (ALMA), which allow us to look through the dust extinction of dense clouds. The difference between optical and infrared images is illustrated in Figure 5.27.

One particular tool in the astronomer's toolbox is the emission and absorption of light by molecules. A certain molecule will emit or absorb light at a unique combination of discreet frequencies, called lines. In this way, a molecule owns its own molecular fingerprint (see Figure 1.6 of this thesis). Using high enough spectral resolution, we can separate all of these emission and absorption features, and derive information such as temperatures, velocities and chemical abundances. The chemical abundance allows us to determine how much of a molecule is present with respect to another. Thus we can extract information about the chemical process which led to the observed abundances. Most of the molecules in star forming regions consist of hydrogen, carbon, oxygen and nitrogen, and the relevant molecules to this thesis are carbon monoxide (CO), carbon monosulfide (CS), water (H_2O), hydrogen cyanide (HCN), acetylene (C_2H_2) and ammomia (NH_3).

Stars can be split into two groups, based on their mass: low mass stars (stars with mass less than 8 $M_\odot$) and high mass stars (stars with mass greater than 8 $M_\odot$). These two groups have similar formation routes, but there are important differences. For one, massive stars have not been observed to have planets around them, likely reflecting the extreme environment of these stars. Massive stars are arguably more important than low mass stars on cosmic scales. They influence the heating and

Figure 5.27: The Taurus Molecular cloud observed at two different wavelengths. The image on the left is taken in the visible part of the spectrum, and the image on the right is what the same cloud looks like at a wavelength of one millimetre. The cloud looks dark to us, however at longer wavelengths, we see that there is much more going on. Forming stars can be seen as bright dots in the right hand panel. Credit: ESO/APEX (MPIfR/ESO/OSO)/A. Hacar et al./Digitized Sky Survey 2. Acknowledgment: Davide De Martin.

cooling of galaxies, stimulate the production of new stars, and are the main producers of many of the elements heavier than carbon.

An important stage in the low mass star formation process is the disk phase. Here material can accrete onto the protostar via a disk which surrounds the star, thus it increases in mass and continues to grow. The disk is a consequence of the conservation of angular momentum, as rotating, infalling material spreads out in a flattened structure around the star, such as that shown in Figure 5.28. Large outflows and winds perpendicular to the disk also form as material is ejected from the star-disk system. Thus the cloud surrounding the star begins to be dispersed. It is still highly contested if disks are as important in the formation of high mass stars as they are for low mass stars. Theory predicts the need for disks in making massive stars, as some mechanism is required for material to overcome the large outward pressure so the star can continue to grow. A disk is the natural solution, however detections of disks around high mass stars are very rare, especially for the more massive stars.

This Thesis

Using unique observations, this thesis has discussed the formation of massive stars, focusing on the details at small scales. The results of the first spectral survey of the 3-13 μm region of two massive protostars, AFGL 2591 and AFGL 2136, was presented. These data were obtained from the Stratospheric Observatory for Infrared Astronomy (SOFIA) observations as well as the Infrared Telescope Facility (IRTF) and Gemini

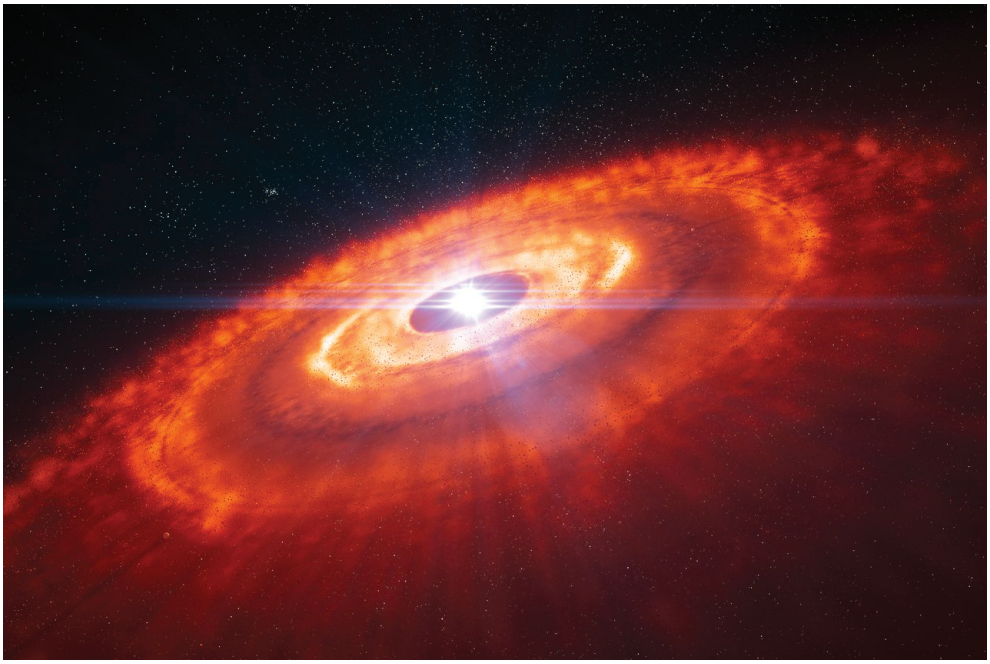

Figure 5.28: Artist's impression of a circumstellar disk around a forming star. Credit: ESO/L. Calcada

telescopes. Our results address the production of important organic molecules in the disks of massive stars, as well as the temperature structure of the disk.

Chapter 2 revealed the difference in physical conditions between large and small scales in the sites of star formation, with observations of the CS molecule in AFGL 2591. Pre-ALMA observations at sub-mm wavelengths were unable to distinguish the disk region of massive protostars from the cloud region. However absorption studies at infrared wavelengths naturally probe very small scales. Thus much hotter and denser gas is observed at infrared wavelengths compared to previous sub-mm studies. The amount of sulphur-bearing molecules observed in dense regions of the galaxy are lower than what is expected. Our detected abundance of CS was very high, suggesting that a large reservoir of warm sulphur-bearing molecules is present very close to the star, and previously unobserved. Hot gas of 700 K is observed in CS, indicating that this gas is likely produced via the high temperature chemistry in a disk atmosphere.

In chapters 3 and 4, we dug deeper into the more important questions with regards to massive star formation. Here we presented a model to explain the observation of absorption lines in a circumstellar disk. This model can account for a range of observational constraints derived from several molecules in AFGL 2591 and AFGL 2136: HCN, C_2H_2, CS, CO, NH_3 and H_2O. Such line formation requires a temperature gradient which increases towards the mid-plane of the disk. Subsequently, such a temperature gradient requires that the heating of the disk is dominated by viscous process in the mid-plane, rather than heating from stellar radiation. These processes

lead to accretion of material onto the star, and allow for the star to grow larger. Several observational constraints are worth mentioning, as they raise important points of attention in the model. The abundance of HCN and C_2H_2 vary with wavelength, implying that these species are concentrated towards the inner 200 AU of the disk. Vibrationally excited bands of CO and C_2H_2 give results that require densities $> 10^{10}$ cm^{-3}. The abundances of all molecules are consistent with what is expected from chemical models of disks. Finally, the H_2O absorption lines are saturated, but do not go to zero flux, as normally occurs. This behaviour is a direct prediction of our disk model.

Chapter 5 addressed the 3 μm spectrum for a range of massive protostars. We found that at this wavelength, MonR2 IRS 3 showed HCN lines in emission. The gas was hot with a temperature of 500 K. This emission was consistent either with an expanding shell of gas, or the atmosphere of a circumstellar disk. HCN and C_2H_2 lines were detected towards AFGL 2136 in absorption. The results for these molecules, combined with chapters 3 and 4, were strongly supportive of the disk model. An alternative to the disk model is that the gas lies close to the star but not in a disk. In order for this model to work, H_2O gas must be more extended than HCN and C_2H_2 gas. This appeared very unlikely however, as H_2O is more easily produced. The disk model was the preferred model as it more realistically fits in with all of the observed observational constraints.

Future Outlook

The detection of hundreds of lines in the infrared has great potential for identifying and studying disks in massive protostars. Extending these kinds of studies to more objects will be fundamental for opening this field further. New larger and better telescopes that will soon be available for this are the James Webb Space Telescope (JWST) and Extremely Large Telescope (ELT). This thesis will be vital to guiding studies with JWST which will not be able to take high spectral resolution observations. JWST will allow the opportunity to study low mass objects at infrared wavelengths due to the high power. Therefore we will be able to determine if absorption lines are common in low mass protostars in the earliest stages of formation.

Also of great importance is the development of theoretical models. Currently models do not exist which treat a circumstellar disk heated from the inside. These are vital for a deeper understanding, and more realistic picture, of the disks discussed in this thesis. Such models would also have to include chemistry, as different physical processes may be required to initiate the formation of molecules.

List of Publications

Refereed Publications

1. *High-resolution Infrared Spectroscopy of Hot Molecular Gas in AFGL 2591 and AFGL 2136: Accretion in the Inner Regions of Disks around Massive Young Stellar Objects*
   Barr, A. G., Boogert, A., DeWitt, C. N., Montiel E., Richter, M. J., Lacy, J. H., Neufeld, D. A., Indriolo, N., Pendleton, Y., Chiar, J., Tielens, A. G. G. M. (2020), ApJ, 900, 104

2. *The H_2O Spectrum of the Massive Protostar AFGL 2136 IRS 1 from 2 to 13 μm at High Resolution: Probing the Circumstellar Disk*
   Indriolo, N., Neufeld, D. A., **Barr, A. G.,** Boogert, A. C. A., DeWitt, C. N., Karska, A., Montiel, E., Richter, M. J., Tielens, A. G. G. M. (2020), ApJ, 894, 107

3. *Molecular complexity on disc scales uncovered by ALMA: Chemical composition of the high-mass protostar AFGL 4176*
   Bøgelund, E. G., **Barr, A. G.,** Taquent, V., Ligterink, N. F., Persson, M., Hogerheijde, M. R., van Dishoeck, E. F. (2019), A&A, 628, A2

4. *High-resolution SOFIA/EXES Spectroscopy of SO_2 Gas in the Massive Young Stellar Object MonR2 IRS3: Implications for the Sulfur Budget*
   Dungee, R., Boogert, A., DeWitt, C. N., Montiel, E., Richter, M. J., **Barr, A. G.,** Blake, G. A., Charnley, S. B., Indriolo, N., Karska, A., Neufeld, D. A., Tielens, A. G. G. M. (2018), ApJL, 868, L10

5. *Infrared Detection of Abundant CS in the Hot Core AFGL 2591 at High Spectral Resolution with SOFIA/EXES*
   Barr, A. G., Boogert, A., DeWitt, C. N., Montiel E., Richter, M. J., Indriolo, N., Neufeld, D. A., Pendleton, Y., Chiar, J., Dungee, R., Tielens, A. G. G. M. (2018), ApJL, 868, L2

Submitted Publications

1. *H_2O Absorption in Circumstellar Disks of Massive Protostars at High Spectral Resolution: Full spectral survey results of AFGL 2591 and AFGL 2136*
   Barr, A. G., Boogert, A., Li, J., DeWitt, C. N., Montiel E., Richter, M. J., Indriolo, N., Pendleton, Y., Chiar, J., Tielens, A. G. G. M. (2021), ApJ, Submitted

2. *Surveying the Inner Structure of Massive Young Stellar Objects in the L Band*
   Barr, A. G., Li, J., Boogert, A., Lee, A., DeWitt, C. N., Tielens, A. G. G. M. (2021), A&A, Submitted

Curriculum Vitae

Born in Paisley, I grew up in the neighbouring city of Glasgow, in Scotland, United Kingdom. There I attended Hutchesons' Grammar School for the entirety of my school education. Towards the end of my schooling I had yet to decide which course I wished to take at university. Enjoying the sciences, and being good at chemistry, I considered a career as a biologist; as it happened, at the last minute I decided that a career in astronomy would suit me better, although I had no real education in physics. Influenced by my father, I had a general interest in astronomy, but never really knew what it entailed to be an astronomer. In my last year of school I tried physics and found that it came naturally. So my application to the University of Glasgow to undertake a degree in Physics and Astronomy, was accepted.

Not surprisingly, at the beginning of my university degree, I struggled, after only beginning to learn physics the year before. I felt somewhat inferior in comparison to the other more vastly learned students, not realising that everyone would quickly become lifted to the same level. During the third year of my bachelor's degree, encouraged by by dad, I sent out emails approaching various astronomers at various institutes, asking if I could do a summer internship with them. I think only one of them replied: Dr Dimitris Stamatellos from the University of Central Lancashire. I am still very grateful for this, as this was a fundamental moment in my life for many reasons. There I was introduced to the topic of star and planet formation, and did a computer simulation project investigating the effect of metallicity on disk fragmentation. There I also first got the idea to come to the Netherlands, as a visiting Dutch astronomer told me how good Dutch astronomy is, particularly in education.

Still, I doubted if I would be good enough to pursue a master's degree after I completed my bachelor's (the thought of doing a PhD never crossed my mind), and indeed I graduated from my Bachelor's with a 2:2, the Scottish equivalent of a C grade. Not very impressive! Thankfully, after being rejected from the University of Amsterdam, somehow I was unconditionally accepted into a master's programme at Leiden University.

During my master's programme, I continued my interest in star and planet formation with a project with Ewine van Dishoeck. This was studying the hot core AFGL 4176 through complex organic molecules detected with the Atacama Large Millimetre Array (ALMA). For my next project I approached Xander Tielens, who would later become my PhD supervisor. I still remember one of the first things Xander said to me: 'Astronomy is all about having fun'. My thought then was, 'this is the supervisor for me!' And it hasn't changed since. Thankfully he took me under his wing and I

worked with observations from the Stratospheric Observatory for Infrared Astronomy (SOFIA), again focusing on high mass star formation, but this time on ultracompact ionised hydrogen regions and their dust properties. I enjoyed it very much and grew in confidence such that undertaking a PhD did not seem like such an insurmountable task.

One day walking into Xander's office he announced, 'I have a project'. This project eerily combined the two research projects that I had done. Studying molecules in hot cores and SOFIA observations; this time I would be working in the infrared wavelength regime, and with absorption lines instead of emission lines.

Throughout my PhD research I have analysed the first full spectral survey of the mid-infrared region of hot cores at high spectral resolution. This was for two sources, AFGL 2591 and AFGL 2136. I have also been involved in the proposal writing for the spectral surveys of W3 IRS5 and NCG 7538 IRS1, which will extend this work to more objects. In addition to this, I was the PI for the L band survey of a sample of massive protostars (chapter 5 of this thesis) after a serendipitous discovery of organic emission lines in AFGL 2591 at 3 μm.

Now that my PhD has come to an end, so has my time as an astronomer. My next ambition is to embark on a career path as a physicist outside of the area of academia.

Acknowledgements

Reflecting at the end of this PhD process, there are many people that deserve to be acknowledged and thanked for making my PhD what it was.

First I want to say thank you to my PhD supervisors, Adwin Boogert and Xander Tielens for working with me on this great project, and supporting me so well throughout it. Adwin, I have learned a lot from you over these past years; thank you for your patience and encouragement. And to Xander, what else can be said other than, 'you are so good'.

I would also like to thank the EXES Hot Core Survey team, Matt, Curtis, Ed, Nick, David, Yvonne and Jialu, for all your input into this thesis. Particular thanks go to the EXES instrument team for obtaining the EXES data, and the many hours spent trying to improve the data quality to get it to what we needed it to be. Also thanks to John Lacy for the acquirement and reduction of the TEXES data, as well as your input into the internally heated disk model.

For the smooth running of the observatory, without which would have made it impossible to get this work done, I want to thank the IT department, Erik, Eric, David and Leonardo, for always being available and finding quick solutions to every which computer problems. As important are the observatory secretaries, particularly Marjan, Evelijn and Alexandra for having answers to all my questions and being willing to accommodate any wishes.

I would like to say thank you to all the members of the ISM group (& co): Daniel, Pablo, Pedro, Kim, Mihal, Sanjana, Jordy, Dario, Cameron, Alessandra, Arthur, Cornelia, Liz, Marcelo, Morgan, Kirstin, Sasha, Olivia and Raymond. A group held together with the glue of cheese, and tomato (and pineapple for Liz), our bi-weekly pizza meetings attracted many others with an interest in the ISM (or Dominoes).

For my office mates over the past years, whether master's or PhD student, thank you for being so quiet and making the office a pleasant and productive place to work. Pablo, Christian, Merel, Martijn, Benoit, Michael, Keith, and Yu Gu, I enjoyed sharing an office with you guys. And of course, thank you to Collins and Patricia for cleaning it everyday.

For those special few at the observatory that I got to know better over the past 4 years, I want to say a particular word for. Xavier, being one of your paranymphs was really special and fun! Jordy, I enjoyed fighting over pepperoni pizza with you, and I hope your new job in Colorado will be a satisfying new chapter in your life. Mihal, I am happy that we got to start our PhDs at the same time, and after the 4 years consider you a real friend. I am glad you are staying in the Netherlands. I would also

like to remember Maolin, who very tragically passed away just as we were beginning to become friends.

Coming to the end, I of course want to thank all of my family and friends for their amazing support. Especially, thank you to Tom for the translation of my summary. And to Tjitze for being a listening ear about the stuff that's there but not really. I am very grateful for having such a great family; my mum and dad and sister Rachel. Mum and dad, without your sacrifices sending me to a good school, I doubt I would be where I am today.

And saving the best until last, my dearest wife Gerdy, truly there is no one better for me in this whole world. You know how important you were in getting this thesis finished; the endless encouragements you gave, being constant in my ups and downs, and all your very wise insights and practical advice. I am really really excited for our next season together!